博士論文

Phase ordering dynamics of colloidal suspensions

(コロイド懸濁液の秩序化ダイナミクス)

舘野 道雄

Ph.D. thesis

Phase ordering dynamics of colloidal suspensions

Michio Tateno

Abstract [*1]

コロイド懸濁液とは nm ∼ μm 程度粒子が溶媒中に分散した系の総称であり、固体・液体微粒子の懸濁液、タンパク質溶液、エマルジョンなど、ソフトマター物理学、生命科学分野でみられる系を広く含む。コロイド懸濁液の熱平衡下における挙動は、古典統計力学の枠組みでよく説明される [1]。具体的には、コロイドの自由度のみに注目し、これに対して分子系と同様の手順で統計処理を行うことで、コロイド系の熱平衡挙動を予測することが可能である。例えば、希薄なコロイド分散系の圧力 (浸透圧) や重力下のコロイドの密度分布は、理想気体の統計力学で予測されるものと同じ形となる。一方で、動力学については、コロイド系・分子系の間に全く異なる挙動を示す例が確認されている。例えば、コロイド系の臨界点近傍の密度揺らぎ [2, 3, 4] が、低分子混合系 [5] とは異なり、非指数関数的な時間減衰を示すことが、実験的に報告されている。また、剛体球系の結晶化頻度について、コロイドの光散乱実験によって得られた結果とシミュレーション結果の間に、十数桁にわたる乖離がある [6] など、ダイナミクスに関しては、様々な未解明問題が残されている。

こういった、コロイド系・分子系の間に見られる動力学の相違は、熱平衡状態を対象とする理論では無視されていた溶媒の自由度が、コロイド系の動力学においては重要な役割を演じている可能性を示唆している。しかしながら、コロイド粒子・溶媒分子という時空間スケールの全く異なる物質の運動がどのように結合するのかを物理的に把握することは難しく、コロイド懸濁液のダイナミクスを記述する構成方程式として決定的なものは得られていのが現状である。

そこで、本研究では、コロイド・溶媒間の動的結合に着目し、コロイド懸濁液の相分離動力学、剛体球コロイドの結晶化過程という、二つの基本的な自己組織化現象について、実験、数値計算を用いた研究を行った。個々の事例から得られた知見をもとに、コロイド・溶媒間の動的結合について明確な物理的描像を得ることを目標とした。

我々は、実験系として PMMA コロイド系を採用し、その相分離過程を共焦点顕微鏡により観察した。この系は、コロイドと溶媒の密度・屈折率の差を同時に最小化できるという利点を持つ。そのため、重力の影響を抑えた 3 次元剛体球系の実験観察が可能となる。個々の粒子の運動を連続的に追跡するために、運動の遅い、直径 3 μ m 程度のコロイドの合成に成功した。また、我々は、独自のセルを用い、セルへの封入時に誘起される流れによる擾乱の影響を排除することで、コロイドの凝集過程を凝集開始時刻から追跡することに成功した (第 3 章)。

また、数値シミュレーション手法として流体粒子動力学 (FPD) 法 [7, 8] を用いた。この手法は、本来固体であるコロイド粒子を、粘性の極めて高い液体粒子として近似することにより、系全体を流体として記述する。これにより、コロイド・溶媒間に課される移動境界問題という困難に煩わされることなく、問題をデカルト座標上で Navier-Stokes 方程式を数値的に解くことに帰着させることができる。我々は、この手法に fluctuating hydrodynamics という理論体系を結合させることにより、熱揺動下でコロイド・溶媒それぞれに対して要請される統計力学上の諸法則を矛盾なく満足させた状態で、コロイドの熱運動をシミュレーションすることに成功した。加えて、我々は、この手法を GPU-MPI ハイブリッド並列化により高速化することにより、大規模・

[*1] The English version is below.

長時間計算を実現した。これにより、実験結果と数値計算結果の１粒子レベルにおける直接的な比較が可能となった (第 4 章)。

まず、コロイドの相分離動力学に関する研究結果について述べる。

我々は、実験試料として、粒子サイズは異なるが、相互作用範囲がおよそ等しい２つのコロイド系 (EXP1, EXP2) を用意した。これによって、コロイドの相分離動力学の粒子サイズ依存性の有無を検証することが可能となった。実験結果を、流体力学的相互作用 (HI) を含む FPD 法、HI を完全に無視したブラウン動力学 (BD) 法による計算結果と比較したところ、時間、空間、エネルギー単位を適切にスケールすることにより、EXP1, EXP2 および FPD による結果が極めて良い一致を見せる一方で、BD は実験結果を再現できないことが分かった。これにより、コロイドの相分離動力学はスケール不変であること、また、この過程において HI が極めて重要な役割を演じることが示された (第 5 章)。

どのようなメカニズムで凝集体が成長するかを特徴づける量に、ドメインの成長指数 (α) という値がある。我々は、成長指数がコロイドの体積分率に応じてどのように変化するかを、上述の PMMA 系を用いて実験的に調べた。その結果、(A) 十分にクエンチが深い条件下では、クラスター状の構造が形成される過程では成長指数が $\alpha \sim 1/3$ に、ネットワーク状の構造が形成される場合では $\alpha \sim 1/2$ となることが分かった (第 6 章)。また、この指数は、複数のコロイド分散溶液系 [9, 10]・タンパク質溶液 [11] においても再現されることから、上記の指数は物質の詳細に依らない普遍的な指数であることを示唆している。加えて、(B) 上記の指数は HI を考慮した FPD 法では再現されるが、HI を無視した BD 法では再現されないことを確認した (第 5 章)。

クラスター構造の粗大化で確認された成長指数 $\alpha \sim 1/3$ は、水と油の相分離にも見られる。この現象では、油滴 (または水滴) はブラウン運動により輸送され、衝突・合体を繰り返すことで成長する (Smoluchowski 理論)。我々は、成長指数の類似性から、Smoluchowski 方程式をベースとした解析をコロイド系の実験・数値計算結果に適用し、衝突頻度 (K) と呼ばれる定数を測定した。その結果、抵抗係数を Stokes 則に設定した K の理論予測は BD の結果を、抵抗係数を Brenner 則に従う値に設定した理論予測は実験・FPD の結果を再現することが分かった。ここで Brenner 則とは、２つの球が接近する場合に働く粘性抵抗に関する厳密解を指す。この抵抗係数は、２つの球の重心間距離が粒子直径程度になると、急激に増大する。以上のことから、粒子の凝集過程では、近接の流体力学的相互作用、つまり潤滑効果が極めて重要な役割をすると結論付けられる (第 5 章)。

ネットワーク構造の粗大化において、成長指数 $\alpha \sim 1/2$ が見られたが、その物理的機構がなんであるかに関しては、これまでほとんど知見がなかった。我々は、上述の (A),(B) を踏まえて、熱運揺らぎを全く無視した (温度ゼロ) 状態で FPD 法による大規模シミュレーションを実行した。その結果、指数 $\alpha = 1/2$ の冪状則が、１桁を超える時空間スケールにわたって成り立つことを示すとともに、このドメインは自己相似性を保ったまま成長することが判明した。このことは、ドメインの特徴サイズがコロイドのサイズよりも十分に大きい場合においても、指数 $\alpha = 1/2$ が保持されることを意味しており、このような状況下では、連続体モデルの適用が可能となる。そこで、(B) の事実を踏まえて、コロイド・溶媒双方の自由度を扱えるモデルとして、２流体モデルに注目した。このモデルでは、コロイド・溶媒間の運動性の非対称性を反映して、コロイドのみに選択的な粘弾性応力 ($\sigma_{\rm c}$) が作用する。また、(A) の事実から、コロイド・リッチ相の粘弾性緩和速度が相分離によりもたらされる変形速度に対して十分遅いと仮定し、$\sigma_{\rm c}$ が弾性的な挙動を示すとして、理論的な解析を進めた。その結果、指数 $\alpha = 1/2$ の

導出に成功するとともに、コロイドの弾性変形に伴って、コロイド・リッチ相のドメイン内部に生じる溶媒の輸送が、ドメインの粗大化を律速するという新たな物理描像を得た (第 7 章)。

次に、剛体球コロイドの結晶化に関する研究結果について述べる。

コロイドの光散乱実験と分子シミュレーションの間に存在する何桁にもわたる結晶核形成頻度の差が、流体起因のものか否かを明らかにすべく、FPD 法を用いた数値計算を行い BD 法の結果との比較を行った。結晶核形成頻度は体積分率 ϕ の変動に対して極めて敏感に変化することから、体積分率の値を正確に把握することが、本研究を遂行するにあたって最低の条件となる。我々は、WCA 相互作用を剛体球間に働く相互作用の近似形として採用し、粒子直径に関する補正を適切に行うことにより、熱平衡下における BD 法、FPD 法を用いた数値シミュレーション結果が、剛体球系に対して知られる熱力学関数の理論予測をほぼ完全に再現することを確認した。次に、過冷却液体の長時間並進拡散係数 D_L を測定し、BD・FPD 間で比較を行ったところ、FPD における D_L は BD におけるそれの、およそ 1/4 倍程度となることが分かった。このことは、潤滑効果によりコロイドの拡散運動が抑制されていることを意味している。D_L とコロイドの直径を単位に、BD、FPD 間の結晶化頻度を体積分率 $\phi \sim 54\%$ について比較した。その結果、BD・FPD 間に見られる相違は 10% 程度で、有意のある差は認められなかった。しかし、実験・分子シミュレーション間の結晶化頻度の劇的な乖離は、これよりも数 % 低い体積分率領域で見られる。我々は、この領域を含め、今後より詳細な研究を行う予定である (第 8 章)。

以上、本研究により得られた新たな知見は、以下のようにまとめることができる。

- コロイド分散系の相分離ダイナミクスにスケール不変性がある。
- そのダイナミクス、構造形成において溶媒の流体力学的な自由度が決定的な役割を演じる。
- 潤滑効果により、クラスター間の衝突が抑制される。
- ネットワーク状の相分離構造の粗大化において、ドメイン成長指数 1/2 が、コロイド・リッチなドメイン中の溶媒の輸送に律速された弾性変形に基づく粗大化の帰結である。
- コロイド分散系の結晶化が起きる高体積分率領域においては、液体状態にあるコロイド系の並進拡散運動が、溶媒による潤滑効果により抑制される。この並進拡散係数の相違を結晶化頻度に繰り込んでしまえば、流体力学的相互は (少なくとも 54% 付近の体積分率領域では) 結晶化頻度にほとんど寄与しない。

これらの成果は、溶媒の存在によりもたらされる局所的な流体力学的相互作用が、コロイドの秩序化に多大な影響を与えることを強く示唆しており、コロイド分散系、ひいてはソフトマター系の秩序化における多体的な流体力学的相互作用の重要性を明確な形で示したものであるといえる。

Abstract

Colloidal suspensions usually stand for liquid-saturated particles whose size ranges from nm- to μm-scale, including a variety of complex fluids such as solid particles, proteins, emulsions, liquid droplets, and gas bubbles. The behaviors of colloidal suspensions in the equilibrium state are well-understood in the framework of classical statistical mechanics [1]. More specifically, we can precisely predict the thermodynamic behaviors by applying the statistical mechanical procedure to the degrees of freedom of colloids as we do for molecular systems. For example, the pressure (osmotic pressure) of a sufficiently dilute colloidal suspension and its density profile under gravity obey the same statistical mechanics laws for ideal gas. On the other hand, the dynamic behaviors of colloidal suspensions show completely different from those of molecular systems. For example, the time correlation function of concentration fluctuations of colloids in the vicinity of the critical point show nonexponential decay [2, 3, 4], contrary to the general knowledge of the dynamic critical phenomena that it should decay by a single exponential function [5]. It is also known that the crystal nucleation rate in hard-sphere-like colloids determined by scattering experiments is different from the numerical estimations by umbrella sampling and molecular dynamics simulations by many orders of magnitude [6].

These examples clearly indicate that dynamic phenomena in colloidal suspensions are intrinsically different from those in molecular systems, suggesting that dynamic coupling between colloids and solvent molecules, which does not affect static behaviors, may play a crucial role in dynamic behaviors. However, it is not easy to physically capture how the motions of colloids and solvent couple, and thus there has been no firm physical basis established with which we can comprehensively access to the various kinds of problems.

In this thesis, we specifically study two dynamical problems, gas-liquid phase separation and crystallization of hard-sphere-like colloids, as important examples. Our primary interest is how a dynamic coupling between solvent and colloids affects the colloidal dynamics. By investigating the above two problems, we aim to provide a new insight into the role of dynamic coupling between solvent and colloids in the dynamic behaviors of colloidal suspensions.

We employ suspensions of PMMA colloids as an experimental system and study the phase separation dynamics by a confocal laser scanning microscopy. In this system, we can match the density and refractive index between colloids and solvent at the same time, which allows us to observe the motions of hard-sphere like colloids in three-dimensional space while suppressing the gravitational effect. To track the trajectories of individual colloids, we synthesized rather large PMMA colloids (3 μm in diameter), whose motions are sufficiently slow to observe by confocal microscopy. By using our own protocol (salt injection method), we successfully observed the phase separation process of colloids from the very beginning without perturbation by mixing flow (Chap. 3).

We employ Fluid Particle Dynamics (FPD) method [7, 8] as a numerical simula-

tion method. This method treats a solid colloidal particle as an undeformable fluid particle, whose viscosity is much higher than the solvent viscosity and the viscosity changes smoothly across the colloid-solvent boundary. These features allow us to treat the dynamics of colloids with many-body hydrodynamic interactions simply by solving the Navier-Stokes equation in a Cartesian coordinate system without suffering from the solid-fluid boundary condition. By combining the FPD method with fluctuating hydrodynamics, we successfully reproduced the Brownian motions of colloids while satisfying the laws on statistical mechanics required both for solvent and colloids. Furthermore, we accelerated FPD simulations by GPU-MPI hybrid parallel programming and realized large-scale simulations, which allowed us to directly compare the experimental and numerical results in a single particle level (Chap. 4).

Firstly, we summarize the results on colloidal phase separation.

As a sample for experiments, we prepared the two different sizes of colloids (EXP1, EXP2), by which we can examine the dependence of the phase demixing process on the of size of colloids. Furthermore, we compared the experimental results with two different simulation methods, FPD and Brownian Dynamics (BD) method. Because the former can incorporate many-body hydrodynamic interactions (HI) properly whereas the latter completely neglect them, we can examine the effect of HI on phase separation dynamics. We found that the results obtained by EXP1, EXP2 and FPD showed almost perfect agreement after scaling the space, time and energy units, whereas BD failed to reproduce the experimental results. We also revealed that phase separation dynamics of colloidal suspensions is scale-invariant and HI plays a key role in the process (Chap. 5).

The growth exponent α is known to characterize the mechanism of domain coarsening. We experimentally studied how the exponent varies, depending on the volume fraction of colloids. As a results we found that (A) under sufficiently deep quench, α tends to be $\sim 1/3$ and $1/2$ for cluster- and network-forming phase separation, respectively (Chap. 6). Such a trend has been experimentally confirmed in colloidal suspensions [9, 10] and protein solutions [11], indicating the possibility that the above exponent is a consequence of a universal coarsening mechanism independent of material details. Moreover, we found that (B) the above trend was reproduced by simulation with HI but was not reproduced simulation without, which implies that HI plays a key role in the coarsening process (Chap. 5).

The growth exponent $\alpha \sim 1/3$ seen in cluster-forming phase separation is also seen in that of a binary liquid mixture such as water-oil mixture. In this phenomenon, oil (or water) droplets transported via thermal diffusion and grow by collision and coalescence (Smoluchowski's Brownian coagulation theory). Focusing on the commonality in the exponent, we adopted an analysis based on the Smoluchowski equation to the results of colloid suspensions obtained by our experiments and numerical simulations, and measured the constant called "collision rate" K. As a result, the theoretical prediction combining the Stokes and Brenner laws for the friction constant well reproduces BD results (simulation without HI) and the other results (EXP1, EXP2, FPD), respectively. Here the Brenner law means the exact solution for the friction constant between two colloids approaching each other,

and increases dramatically when the center-of-mass distance between the colloids becomes close to the diameter of colloids due to hydrodynamic interactions. From this, it can be concluded that the lubrication effects (or short-range HI) play a important role in the aggregation process of clusters (Chap. 5).

We mentioned in the above that the growth exponent $\alpha \sim 1/2$ appears universally in network-forming phase separation. However, there has been no serious study to figure out the coarsening mechanism behind the exponent. To reveal this, we performed large-scale FPD simulations without thermal noise (or at zero temperature), based on the point (A) and (B) described in the above. As a result, we successfully reproduced the power-law growth regime of exponent 1/2 far beyond one order of magnitude in both time and space and found that the domain grows while retaining self-similarity. This implies that the growth exponent continues to be 1/2 as long as the characteristic domain size is much larger than the particles size. In this regime, we may apply a coarse-grained description. Based on the point (B), we focused on two fluid model as a model which can deal with the degree of freedom for both colloids and solvent. In this model, a mechanical stress $\sigma_{\rm c}$ selectively acts on the colloids, reflecting the a huge gap in structural relaxation time between colloids and solvent molecules. From (A), assuming that viscoelastic relaxation in the colloid-rich domain is much slower than the characteristic time scale related to the deformation of velocity field induced by phase separation, we only focused on the elastic behavior of $\sigma_{\rm c}$. Thus, we successfully derived the growth exponent $\alpha = 1/2$ and obtained a new physical description that solvent flow inside of the colloid-rich phase induced by elastic motion of colloids limits the dynamics of the domain coarsening in network-forming phase separation (Chap. 7).

Next we summarize the results regarding crystallization of hard-sphere colloids.

In order to examine whether HI can be the origin of the huge mismatch in the crystal nucleation rate between experiments and molecular dynamics simulations, we performed FPD simulation and compared the results with those obtained by simulation without HI (BD simulation). Because the nucleation rate very sensitively changes accompanied with the change of the volume fraction of colloids ϕ, it is essential to precisely estimate the volume fraction in this study. We employed Weeks-Chandler-Andersen (WCA) potential as an approximate of the hard sphere potential and confirmed that the thermodynamic behaviors obtained by BD and FPD simulations well reproduce the theoretical prediction for hard-sphere systems, after making a correction for diameter of colloids. Then, we measured the long-time diffusion constant in supercooled liquids, $D_{\rm L}$, and found that $D_{\rm L}$ in FPD is approximately four times smaller than that in BD. This means that diffusive motion of colloids are suppressed by lubrication effects. We compared the nucleation rate at $\phi \sim 0.54$ between BD and FPD with $D_{\rm L}$ and the diameter of colloids as time and space units respectively, but no remarkable difference was confirmed. However, a huge mismatch in the crystal nucleation rate between experiments and simulations has been seen more evidently in more dilute volume fractions. Thus, to obtain a conclusive result, we need further careful study focusing on the differences in this volume fraction range (Chap. 8).

In short, we summarize the main findings in this thesis as follows.

- Phase separation dynamics of colloidal suspensions is scale-invariant.
- HI plays a key role in the phase separation kinetics.
- Collisions among clusters formed by phase separation are suppressed by lubrication effects.
- The growth exponent 1/2 seen in network-forming phase separation can be explained by a new mechanism: Coarsening proceeds by slow elastic deformation of the colloid-rich phase, which is limited by solvent transport inside it.
- In a supercooled state of hard sphere systems, the translational diffusion of colloids is suppressed by hydrodynamic lubrication effects. However, at least around 54% volume fraction, the effect of HI on crystal nucleation rate is rather minor, after normalizing the nucleation rate by the above diffusion constant.

These results indicate that short-range hydrodynamic interactions play a significant role in phase ordering kinetics of colloidal suspensions.

Acknowledgement

I would like to thank my supervisor Prof. Hajime Tanaka for supporting my Ph.D. study over five years. He always took time to have discussions despite his busy schedule. He allowed me to pursue my own research plan at my discretion, and gave me constructive advice when things were not going well. It has been an invaluable experience, conducting my research in such a free atmosphere. It was also very lucky to be able to spend my time surrounded by talented people from diverse backgrounds and abundant research facilities.

Besides my supervisor, firstly I am very grateful to Taiki Yanagishima who kindly taught me most of the experimental techniques required for this project including how to use a confocal microscope and synthesize colloids. In particular, his advice for chemical handling was essential in improving the reproducibility of the experiments. Mathieu Leocmach gave me very quick responses to a lot of questions about the image analysis, despite living far away in France. He also provided me with an internship opportunity in Lyon University. Hideyo Tsurusawa and Shunto Arai gave me a wide range of advice regarding the detailed experimental procedures. Mika Kobayashi kindly helped me the time I have trouble with experimental equipment. I am very grateful to Kyohei Takae and John Russo for imparting me so much knowledge about numerical simulations and solving computer problems. I also thank Satoko Oizumi for her extensive administration support. I sincerely thank Taiki Yanagishima, Anne-Laure Biance, Isaac Theurkauff, Nicolas Bruot and Wasim Abuillan, who I shared a lot of time with in the same office, for their friendship and stimulating discussions about science and daily life. I thank my other labmates for great times including coffee breaks, study groups, or private time.

The numerical calculations were partially performed in the Supercomputer Center at ISSP in University of Tokyo. To speed up the FPD simulations, we utilized GPGPU implementation service provided by ISSP; the project was carried out with Kyohei Takae. The contents discussed in Chapter 8 are collaborative work with John Russo and Taiki Yahagishima. I would like to express my thanks to all the related people here.

Finally, I would like to thank my parents for their understanding in allowing me to continue my academic career, their financial aid and continued encouragement.

Contents

Chapter 1

Background

1.1 Motivation

Colloidal suspensions usually stand for liquid-saturated particles whose size ranges from nm- to μm-scale. In such an intermediate length scale, which is much smaller than a macroscopic scale but much larger than the size of solvent molecules, thermal fluctuations play prominent roles. Thus, colloidal suspensions have been regarded as an ideal model system to investigate fundamental problems in statistical physics. Colloidal suspensions are a mixture of large colloidal particles and small solvent molecules, between which there is a huge gap in the length and time scales. This results in spatio-temporal hierarchy, which is a characteristic feature widely seen in soft and bio matter. Therefore, it is expected that the physical understanding of fundamental properties of colloidal suspension will greatly contribute to the understanding of soft and bio matter that also have similar spatio-temporal hierarchy. From industrial viewpoints, colloidal suspensions are also an important model system to understand the physical properties of suspensions of solid particles, proteins, liquid droplets, and gas bubbles. Typical examples seen in our daily life include milk, yoghourt, paint, cement, and so on.

Despite the importance of colloidal suspensions from both fundamental and applications viewpoints, our understanding of their dynamical properties is still far behind that of the thermodynamic properties. The examples of such dynamical phenomena in colloidal systems include phase transition kinetics (crystallization [6] and gelation [12, 13, 14]), nonlinear rheology (i.e., shear thinning/thickening [15]), self-organization dynamics (collective motion in active systems [16] and formation of biomolecular condensates [17]).

In this thesis, we specifically study two dynamical problems, gas-liquid phase separation and crystallization of hard-sphere-like colloids, as important examples. Our primary interest is how a dynamic coupling between solvent molecules and colloids affects the colloidal dynamics. By answering this question, we aim to provide a new insight into the impact of dynamic coupling between solvent and colloids on the dynamic behaviour of colloidal supensions.

In this section we briefly review some basic knowledge of colloidal suspensions including thermodynamics and dynamics.

1.2 Interparticle forces among colloids

The size of colloidal particle lies in between a macroscopic scale and molecular scale. Therefore, the motion of colloids is much slower than that of molecules, but colloids show thermal motion by exchanging the momentum with surrounding solvent molecules, unlike granular materials. If the size of colloids is larger than $\sim$ 100nm, it is possible to directly observe the thermal motion of colloids in real space with optical microscopy. Furthermore, we can artificially control the interparticle potential between colloids. These features allow us to experimentally study the structure and dynamics of colloidal particles at a single-particle level in real space, which is impossible in molecular systems. Additionally, it is known that colloidal systems in thermodynamic equilibrium behave the same as molecular systems (see section 1.3). For these reasons, colloidal systems have been studied as a model of atomic systems. In order to see the features of colloids as a model system, in this section we briefly review typical interactions between colloids.

1.2.1 Van der Waals attraction

In general, attractive interactions act on molecules and it is also the case for the molecules constituting colloidal particles. Such intermolecular attractions in a microscopic scale brings about the interparticle attraction among colloids. The intermolecular attraction between two equal-size solid spheres was frist derived by Hamaker [18] based on the assumptions that the molecules constitute the particles interact with van der Waals attraction whose the functional form is r^{-6}, in a pairwise and additive manner.

$$U_{\mathrm{vdw}} = -\frac{A}{6}\{\frac{2}{s^2-4} + \frac{2}{s^2} + \log(\frac{s^2-4}{s^2})\}, \tag{1.1}$$

where A is a constant called as the Hamaker constant and $s = (2a+h)/a$. Here a is the radius of the particles and s is the center-of-mass distance between the two particles. According to the Lifshitz theory, the Hamaker constant is given as

$$A = \frac{3}{4}k_{\mathrm{B}}T(\frac{\epsilon_{\mathrm{p}}-\epsilon_{\mathrm{s}}}{\epsilon_{\mathrm{p}}+\epsilon_{\mathrm{s}}})^2 + \frac{3h\nu_{\mathrm{e}}}{16\sqrt{2}}\frac{(n_{\mathrm{p}}^2-n_{\mathrm{s}}^2)}{(n_{\mathrm{p}}^2+n_{\mathrm{s}}^2)^{\frac{3}{2}}}, \tag{1.2}$$

where ϵ_{p} (or ϵ_{s}) and n_{p} (or n_{s}) represent the dielectric constant and the refractive index of the particles (or the solvent), respectively.

For $h/a \ll 1$, Eq. (1.1) can be approximated as $U_{\mathrm{vdw}} \sim -Aa/12h$, meaning that the van der Waals attractions are stronger for larger colloids.

1.2.2 Electrostatic repulsion

Colloids can have surface charges, which depend on a solvent, and in such a case the electrostatic repulsions act between colloids. For charged colloids, charges of opposite sign in a solvent are attracted around the colloid surfaces, which screens the

Coulomb repulsions between colloids. Thus, we cannot use bare Coulomb repulsion for this case. Such ion absorption effects can be treated as follows [18].

Denoting the concentration and valence of ions with type α as C_α and z_α respectively, the following Boltzmann distribution is to be valid under an equilibrium condition,

$$C_\alpha = C_\alpha^0 \exp\left(-\frac{z_\alpha e\psi}{k_\mathrm{B}T}\right), \tag{1.3}$$

where C_α^0 represents the concentration of ions with type α in bulk. ψ is the electrostatic potential which is determined by the Poisson equation, $\Delta\psi = -\rho_\mathrm{e}/\epsilon$, where ρ_e is the charge distribution and written as $\rho_\mathrm{e} = \sum_\alpha z_\alpha e C_\alpha$. Then, we obtain the following Poisson-Boltzmann equation:

$$\Delta\psi = -\sum_\alpha \frac{z_\alpha e C_\alpha}{\epsilon} \exp\left(-\frac{z_\alpha e\psi}{k_\mathrm{B}T}\right). \tag{1.4}$$

In the case where the electrostatic potential is sufficiently small such that $\frac{z_\alpha e\psi}{k_\mathrm{B}T} \ll 1$, Eq. (1.4) can be linearized as follows:

$$\Delta\psi = -\sum_\alpha \frac{z_\alpha e C_\alpha}{\epsilon} + \frac{e^2}{\epsilon k_\mathrm{B}T}\left(\sum_\alpha z_\alpha^2 e C_\alpha^0\right)\psi. \tag{1.5}$$

The first term in the right hand side is zero if we assume the electrical neutrality. Introducing the so-called Debye screening length κ^{-1} as $\kappa^{-1} = \sqrt{\frac{e^2}{\epsilon k_\mathrm{B}T}\sum_\alpha z_\alpha^2 C_\alpha}$, we finally obtain

$$\Delta\psi = \kappa^2\psi. \tag{1.6}$$

Based on this equation, the electrostatic interaction between two equal-size colloids with radius a, including the screening effect due to ions, is expressed [19] as the following Yukawa-type potential:

$$U_\mathrm{el} = \frac{Q^2}{4\epsilon}\left(\frac{\exp(\kappa a)}{1+\kappa a}\right)^2 \frac{\exp(-\kappa r)}{r}. \tag{1.7}$$

The theoretical framework to explain the stability of dispersion of micro-particles such as colloids and proteins by regarding their interparticle potentials as the superposition of U_vdw and U_el is widely known as the DLVO theory*1.

1.2.3 Steric repulsion

As seen in the above, the van der Waals attractions act more strongly for larger particles. Therefore, it is not so easy to disperse the μm-size particles in a solvent. As discussed in the DLVO theory, controlling the electrostatic repulsion between colloids is the one of the typical ways to realize a stable dispersion. Recently the

*1 Here we note that the pairwise additivity does not hold for charged colloids and thus it is necessary to consider many-body corrections.

attempts to reduce the Hamaker constant by matching the refractive index between colloids and a solvent also have been made (see Eq. (1.2)). If we add the sufficient amount of ions into a solvent, we can also screen out the electrostatic repulsions between the colloids. Furthermore, by chemically grafting polymer brushes on the surface of the colloids, we sterically prevent the adhesion of colloids at a very short distance. In such a condition, the interactions among colloids mentioned above (U_{vdw} and U_{el}) are negligibly small compared to the thermal energy, where we expect that colloids approximately interact with the following hard-sphere potential:

$$\begin{aligned} U_{\mathrm{hs}}(r) &= 0 \quad \text{for } \frac{r}{\sigma} > 1, \\ &= \infty \quad \text{otherwise}, \end{aligned} \tag{1.8}$$

where σ is the diameter of colloids. Such hard-sphere systems indeed have been experimentally realized and used as a fundamental model system to investigate many-body problems in statistical physics.

1.2.4 Depletion attraction

It is known that in a mixture of particles whose sizes are largely different, an effective attractive force known as "depletion force" arises among the large particles [20, 21]. In this section, we focus on a mixture of hard-sphere colloids and non-absorbing ideal polymers, especially in the case where the diameter of the colloids σ is sufficiently larger than the gyration radius of the polymers R_{g}. In such a case, since the motion of the polymers are much faster that of the colloids, we can expect that the concentration of polymers is equilibrated in the time scale of the Brownian motion of the colloids.

We consider how the spatial distribution of the concentration of the polymers $n_{\mathrm{p}} = N_{\mathrm{p}}/V_{\mathrm{f}}$ changes depending on the relative position between two colloids, where N_{p} is the number of polymers and V_{f} is the volume that polymers can freely move. There is a region surrounding a colloidal particle where the polymers cannot penetrate due to the steric repulsion between the colloid and polymers. Such a region is often called as a depletion zone. We can roughly estimate the outer shell of the depletion zone for a colloid as a sphere with diameter $\sigma + 2R_{\mathrm{g}}$ (see the region surrounded by a dotted line in Fig. 1.1) and the depletion zone excluding the part that the colloid occupies is often called as depletion layer. Because n_{p} differs between the inside and outside of the depletion zone, the surface of the depletion zone is subjective to the resulting osmotic pressure of the polymers Π_{p}. When two colloids approach within a certain distance, their depletion layers start to overlap (see the yellow region in Fig. 1.1. We denote the volume of the overlapped region as V_{overlap}). As a result, the osmotic pressure acts such that the distance between the colloids decreases. Because the resulting force acting on the colloids is to be equivalent to the sum of the osmotic pressure acting on the overlaped region, we

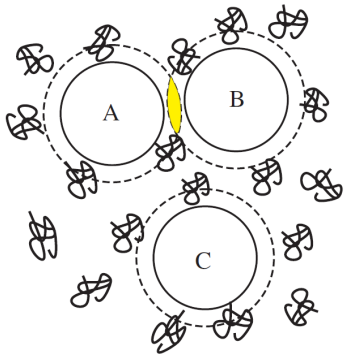

Fig. 1.1 **A schematic illustration of the depletion interaction.** The centre of a polymer molecule (coil) is excluded from coming closer than a certain distance, approximately its own radius of gyration, to the surface of a colloid (full circle) because of the high entropic cost of configurational distortion. Each colloid is therefore surrounded by a depletion zone (dotted circle) within which there is essentially no polymer centers of mass. If a colloid (such as C) is far away from other particles, the osmotic pressure of the polymer on the particle is isotropic. If, however, the surface of two colloids (such as A and B) are closer than twice the size of a depletion zone, then there is no polymer in the lens-shaped (shaded) region, and a net (osmotic) force presses the particles together—the depletion attraction. This figure and the caption are reproduced from Ref. [13].

may write the interaction potential between the two colloids $U_{\rm dep}$ as [22, 21]

$$\begin{aligned} U_{\rm dep}(r) &= 0 \quad \text{for } \frac{r}{\sigma} > 1+\Delta, \\ &= \infty \quad \text{for } \frac{r}{\sigma} < 1, \\ &= -\Pi_{\rm p} V_{\rm overlap} \quad \text{otherwise.} \end{aligned} \tag{1.9}$$

where $\Delta = 2R_{\rm g}/\sigma$ and the overlapped volume is written as

$$V_{\rm overlap} = \frac{\pi}{6}(1+\Delta)^3\sigma^3 \left[\quad 1 - \frac{3}{2}\frac{r}{(1+\Delta)\sigma} + \frac{1}{2}\left(\frac{r}{(1+\Delta)\sigma}\right)^3 \quad \right], \tag{1.10}$$

In a special case where the thermodynamic behavior of polymers can be regarded as ideal-gas like, we can write the osmotic pressure as $\Pi_{\rm p} = n_{\rm p} k_{\rm B} T$. This assumption is expected to be valid especially in a theta-solvent condition.

From the above, we find that the interaction range Δ depends on $R_{\rm g}$ and the 'depth' of the interaction (for example $U_{\rm dep}(\sigma)$) is proportional to $n_{\rm p}$. This means that the range and depth of the depletion interaction can be controlled just by changing the molecular weight and the concentration of polymers. The tunability of the intercolloid potential is one of the main reasons why collodal systems have recently attracted considerable attention as a model system. We note that a potential for depletion interaction between two colloidal spheres which takes the internal

degree of freedom of polymers into account has also been derived [23]. However, experimental results [24, 25, 26] report that the above functional form still works well at least in two-body level.

1.3 Equilibrium phase behavior

In this section we briefly review the thermodynamics of colloidal suspensions. Here we see that the thermodynamic behavior follows the classical statistical mechanics for molecular systems, which we call as colloid-atom analogy following Ref. [21]. Here we focus on only topics relevant to this thesis. We first describe the thermodynamic behavior of hard-sphere systems and then that of colloid-polymer mixture systems. Finally, we mention a scale invariant nature of equilibrium phase behaviors of colloids.

1.3.1 Hard-sphere system

In a hard sphere system, it is known that liquid-crystal transition takes place. The existence of the transition has been first discovered by simulation studies [27, 28] in 1957 and experimentally confirmed in hard-sphere-like colloidal systems [29] (see Fig. 1.2). Although no exact theoretical description of the transition has been established so far, some approximate theories precisely reproduce the thermodynamic variables observed in numerical simulations.

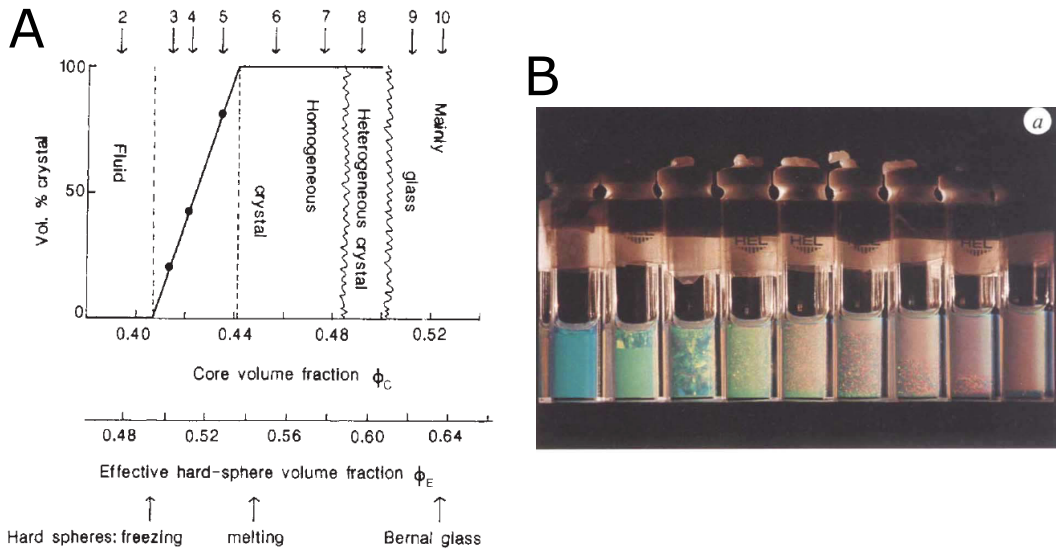

Fig. 1.2 **Experimental obervation of the phase behavior of the hard-sphere-like colloidal supensions** [29]. (A) The phase diagram of PMMA spheres. The vertical and horizontal axes represent the volume fraction of the crystal phase and that of colloids respectively. (B) The images of the actual samples. The samples are denoted from left to right by 2, 3, ... , 10, which correspond to the volume fractions indicated by the numbers in the top of panel A.

Carnahan-Staring equation of states is known as an accurate expression for the equation of states for hard-sphere liquids [30],

$$\frac{v_0 P_{\rm liq}}{k_{\rm B}T} = \frac{\phi + \phi^2 + \phi^3 - \phi^4}{(1-\phi)^3}, \tag{1.11}$$

where $P_{\rm liq}$ is the pressure, $v_0 = \pi\sigma^3/6$ is the volume of the particles, $\phi = v_0 N/V$ is the volume fraction of the particles. By using the Gibbs-Duhem equation, the chemical potential $\mu_{\rm liq}$ is given as

$$\frac{\mu_{\rm liq}}{k_{\rm B}T} = \log\left(\frac{\Lambda^3}{v_0}\right) + \log\phi + \frac{(8 - 9\phi + 3\phi^2)\phi}{(1-\phi)^3}, \tag{1.12}$$

where Λ is the de Broglie wavelength. By substituting Eqs. (1.11) and (1.12) to a thermodynamic relation of the Helmholtz free energy $F_{\rm liq} = -P_{\rm liq}V + \mu_{\rm liq}N$, we obtain

$$\frac{F_{\rm liq} v_0}{k_{\rm B}TV} = \phi\{\log(\frac{\phi\Lambda^3}{v_0}) - 1\} + \frac{4\phi^2 - 3\phi^3}{(1-\phi)^2}. \tag{1.13}$$

As a theory to describe the thermodynamics of the crystal state in hard-sphere systems, we refer to Lennard-Jones-Devonshire cell model [31]. This theory considers the motion of each particle in the region surrounded by its neighbors and estimate the average volume v of the space that the center-of-mass of the particle can access. The simplest estimation for v is given as $v = 8v_0\{(\frac{\phi_{\rm cp}}{\phi})^{1/3} - 1\} \sim \frac{8v_0}{3}(\frac{\phi_{\rm cp}}{\phi} - 1)$, where $\phi_{\rm cp}$ is the volume fraction at the closest packing and for the hard-sphere crystal we can use that of the face-centered cubic (FCC) structure ($\phi_{\rm cp} = \sqrt{2}\pi/6$). Writing the partition function Q as $Q = v/\Lambda^3$, the Helmholtz free energy $F_{\rm cry} = -k_{\rm B}T\log Q$ is calculated as

$$F_{\rm cry} = Nk_{\rm B}T\{\log(\frac{27\Lambda^3}{8v_0}) - 3\log\left(\frac{\phi_{\rm cp}}{\phi} - 1\right)\}. \tag{1.14}$$

From this expression, we can obtain the pressure $P_{\rm cry}$ and the chemical potential $\mu_{\rm cry}$ in the crystal state.

By applying the coexistence condition, $P_{\rm liq} = P_{\rm cry}$ and $\mu_{\rm liq} = \mu_{\rm cry}$, on the above results, we obtain $\phi_{\rm liq} = 0.491$, $\phi_{\rm liq} = 0.541$ and $P_{\rm coex} = 6.01$, which are very close to the values observed in numerical simulation, $\phi_{\rm liq} = 0.494$, $\phi_{\rm cry} = 0.545$, and $P_{\rm coex} = 6.12$ respectively [32].

1.3.2 Colloid-polymer mixture

In this section we briefly explain the phase behaviors of colloidal suspensions in the presence of interparticle attractions. In the above section we have seen that a hard-sphere system has liquid and crystal phases as thermodynamically stable states. It is a well-known fact that systems generally shows at least three phases, gas, liquid and crystal states, in the presence of interparticle attractions. However, how the three phases are located in an equilibrium phase diagram strongly depends

on the details of the interaction potential (e.g., the interaction range Δ in the below case).

As a theory relevant to our study, we refer to the free volume theroy in Ref. [1], which describes an equilibrium phase behavior of a colloid-polymer mixture. In this theory, the free energy for a colloid-polymer mixture $F_{\rm tot}$ is given as the sum of the free energy for colloids $F_{\rm c}(N_{\rm c}, V)$ and that for polymers $F_{\rm p}(N_{\rm p}, V_{\rm f})$. Then, it is assumed that $F_{\rm p}$ and $F_{\rm c}$ are given by that for an ideal gas (i.e., $F_{\rm p} = N_{\rm p} k_{\rm B} T \log(N_{\rm p}/V_{\rm f}) + \cdots$) and the one for a hard-sphere system (see section 1.3.1), respectively. Here, $N_{\rm c}$ and $N_{\rm p}$ represent the numbers of colloids and polymers respectively. V and $V_{\rm f}$ are the total volume of the system and the volume in which polymers can freely move. We denote the ratio of these volumes as "free-volume fraction" $\alpha = V_{\rm f}/V$ and assume that α only depends on the volume fraction of colloids $\phi = \pi\sigma^3 N_{\rm c}/6V$ and the size ratio $\Delta = 2R_{\rm g}/\sigma$, where σ and $R_{\rm g}$ are the diameter of colloids and the gyration radius of polymers respectively.

Then, $F_{\rm tot}/V$ is designated by a pair of two intensive properties, (ϕ, $n_{\rm p}$), where $n_{\rm p} = N_{\rm p}/V$ is the concentration of polymers. By differentiating $F_{\rm tot}$ by $N_{\rm p}$, we obtain the chemical potential for polymers $\mu_{\rm p}$ as

$$\mu_{\rm p} = k_{\rm B} T \log n_{\rm p} - k_{\rm B} T \log \alpha + \cdots . \tag{1.15}$$

The first term represents the chemical potential in the absence of the colloids and the second therm ($W \equiv -k_{\rm B} T \log \alpha$) corresponds to the work required to insert one polymer to the bath of the colloids. By using the Widom's insersion method, a specific expression of $\alpha(\phi, \Delta)$ can be calculated as (see [21] for the detail calculation):

$$\alpha = (1 - \phi) \exp\left[-A\gamma - B\gamma^2 - C\gamma^3\right], \tag{1.16}$$

where $\gamma = \phi/(1-\phi)$, $A = 3\Delta + 3\Delta^2 + \Delta^3$, $B = 9\Delta^2/2 + 3\Delta^3$ and $C = 3\Delta^3$.

In the first row of Fig. 1.3, we show the phase diagrams computed by using to the above free energy $F_{\rm tot}$. The third row in Fig. 1.3 shows experimental results [33, 34], where we can see a good agreement between the theoretical prediction and experimental results on a quantitative level. Panels (a), (b) and (c) correspond to the phase diagrams for various size ratios, $\Delta = 0.08, 0.33$ and 0.57, respectively (ξ in the figure corresponds to Δ). We can see that the topology of the phase diagram significantly depends on Δ. For example, we can see the gas-fluid coexistence and critical point exist in the equilibrium phase diagram for large Δ, whereas they are hidden behind the gas-crystal coexistence region for small $\Delta(= 0.08)$. Such an interaction-range dependence of the shape of the phase diagram is also observed exprimentally in protein solutions [35] and by numerical simulations [36, 37].

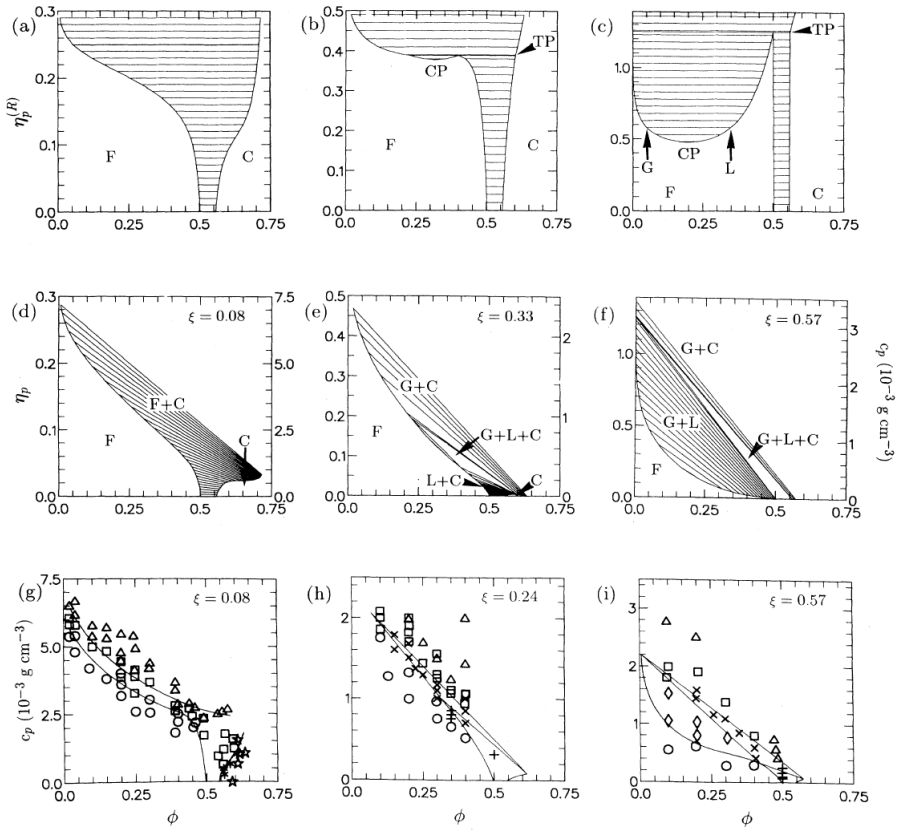

Fig. 1.3 (a)-(c) Theoretical phase diagrams, calculated according to the method in [1], plotted in the (ϕ, $\eta_{\rm p}^{(R)}$) plane for size ratios ($\xi = 0.08, 0.33,$ and 0.57. The horizontal axis is the colloid volume fraction ϕ and the vertical axis is the effective polymer volume fraction in a reservoir in osmotic equilibrium with the sample [$\eta_{\rm p}^{(R)}$; see Eq. (12) in the text]. In (a), only the fluid, the fluid plus crystal, and the crystal are predicted. In (c), a region of gas-liquid coexistence is also predicted; the critical point and triple line are indicated. In (b), the critical point and triple line almost coincide. The symbols denote the following: CP, critical point; TP, triple line; F, fluid; G, gas; I, liquid; C, crystal; F+C, Fluid plus crystal. (d)-(f) Theoretical phase diagrams, according to [1], in the (ϕ, $\eta_{\rm p}^{(R)}$) plane for the same size ratios: the horizontal axis is again ϕ; the vertical axis plots the effective volume fraction of polymers in the *sample* volume. Vertical axes in units of g per cm are also given on the right of each figure to facilitate comparison with experimental data. The symbols are the same as in (a)-(c). (g)-(i) Experimental phase diagrams for size ratios ($\xi = 0.08, 0.25,$ and 0.57); the vertical axes plot the polymer concentration in g per cm. (g) is taken from [33]. All lines on (g)-(i) are drawn in as guides to the eye, except for the triangular regions in (h) and (i), which have been located with the aid of experimentally determined colloid concentrations in the three coexisting phases (see text). The symbols denote the following: circle, fluid; diamond, gas plus liquid; crass, gas plus liquid plus crystal; plus sign, liquid plus crystal; square, gas plus crystal; triangle, gel (for $\xi = 0.08$) or no visible crystallites (for $\xi = 0.33$ and 0.57); stars, glass. This figure and caption are reproduced form Ref. [34].

1.3.3 Law of corresponding states

When we say colloidal suspensions, their macroscopic properties depend on the microscopic details such as chemical structures of materials forming colloids, the type of molecules constituting the solvent that in which colloids are suspended, and the intermolecular interactions among them. In the above examples, we have seen that the static phase behaviors of colloidal suspension can be understood by classical statistical mechanics. Here we mention that this is a very powerful tool to comprehensively classify the colloidal systems. In the framework of the statistical mechanics, all we need to know is the interaction among the colloids and we may ignore all the microscopic details beside it. For example, if we express the intercolloid potential U by a scaling function f with an energy unit ϵ and a length unit σ as $U(r) = \epsilon f(r/\sigma)$, we can calculate the thermodynamic functions and determine the phase diagram only with two control parameters, the potential depth scaled by the thermal energy, $\beta\epsilon$, and the volume fraction of colloids, ϕ. In this case, the phase diagrams of colloidal systems whose interaction potentials are scaled as above can be mapped on a single phase diagram. Roughly speaking, if materials whose interaction potentials have a similar shape, the phase diagrams are almost the same. This is widely known as the law of corresponding states [38, 39, 40].

Such a scale-invariant nature of the static phase diagram has been originally found in molecular systems whose interparticle potential can be expressed as Lennard-Jones potential [38, 39]. In colloidal systems, whose the interaction potentials can be artificially control, there may be various functional forms for the scaling function of the interaction potential f. Thus, how to characterize the function f is an important problem. As Δ in the depletion interaction (see Eq. 1.9), f is to be a function of at least a parameter characterizing the interaction range. A way to quantify the effective range of attraction via the reduced second virial coefficient b_2 (see section 5.2.2 for the detail) was suggested in Ref. [40] and the validity of the method for short range attraction ($\Delta < 0.1$) was confirmed experimentally [41, 42].

1.4 Colloidal dynamics

As explained above, the static behavior of colloids is explained in a very clear manner by the same theoretical framework of classical statistical mechanics developed for molecular systems. The problem here is whether such a colloid-atom analogy is also valid in dynamical phenomena. In fact, some experimental studies suggested that the colloidal systems show dynamic behaviors different from those in molecular systems. For example, for protein solutions [2, 3] and a microemulsion [4], the time correlation function of concentration fluctuations in the vicinity of the critical point show nonexponential decay, contrary to the general knowledge of the dynamic critical phenomena that it should decay by a single exponential function. It is also known that the crystal nucleation rate in hard-sphere-like colloids determined by scattering experiments is different from the numerical estimations by umbrella sam-

pling and molecular dynamics simulations by many orders of magnitude [6].

Here we mention that the success of the colloid-atom analogy in the thermodynamic behavior also implies that the solvent molecules in colloidal suspensions have almost no effect on the static behavior of colloidal particles. In dynamical phenomena, it is not clear at all whether we can neglect the dynamic degrees of freedom of solvent molecules. Indeed, the nonequilibrium phenomena where the hydrodynamic degrees of freedom of the solvent plays a crucial role are known. For example, in the formation process of colloidal gels, it has been shown that the hydrodynamic interactions between colloids mediated by the solvent assists the percolation of colloids [7, 43, 44, 45, 46].

These examples clearly indicate that dynamic phenomena in colloidal suspensions are intrinsically different form those in molecular systems, suggesting that dynamic coupling between colloids and solvent molecules, which does not affect static behaviors, plays a crucial role in dynamic behaviors. However, there has been no firm physical basis established with which we can comprehensively access to the various kinds of problems, mainly because of the difficulty associated with many-body nature of hydrodynamic interactions .

In this section, we review some basic knowledge about colloidal motion and see difficulties in dealing with dynamic coupling between colloids and solvent.

1.4.1 How to describe colloidal dynamics

As there is a huge gap in length and time scales between colloids and solvent molecules it is difficult to theoretically access the dynamic problem of colloids while describing a solvent on a molecular level. Thus, a coarse-grained description is necessary to deal with slow colloidal dynamics. On the other hand, there has been no reliable theoretical model that coarse-grain the degrees of freedom of both solvent molecules and colloids. In other words, there has been no consensus about the form of the constitutive relation of colloidal suspensions. For these reasons, models that coarse-grain the solvent molecules and treat colloids as particles are often used. Thus, we focus on such an approach in the following.

1.4.2 Brownian motion of a free colloid

For the thermal motion of an isolated colloid in a solvent, such a coarse-grained description for solvent works very well. For example, as will be shown below, an analytic solution for such motion was derived and the validity was experimentally confirmed.

Langevin equation with a white noise

The most fundamental and well-used coarse-grained model for a free colloid is the Langevin equation with a white noise expressed as

$$M\frac{d\boldsymbol{V}}{dt} = -\zeta\boldsymbol{V} + \boldsymbol{F}^{\mathrm{R}}, \tag{1.17}$$

where M and $\boldsymbol{V}$ are the mass and the velocity of the colloid respectively. $\boldsymbol{F}^{\mathrm{R}}$ is a random force exerted by collisions with surrounding molecules and is related with the viscous drag coefficient ζ via the fluctuation-dissipation theorem as

$$\langle F_i^{\mathrm{R}}(t) F_j^{\mathrm{R}}(t') \rangle = 2k_{\mathrm{B}}T\zeta\delta_{ij}\delta(t-t'), \tag{1.18}$$

where the symbol $\langle A \rangle$ represents the ensemble average of A. As a basic quantity characterizing the colloid dynamics, the velocity auto-correlation (VACF) function is calculated as

$$\langle \boldsymbol{V}(0) \cdot \boldsymbol{V}(t) \rangle = \frac{3k_{\mathrm{B}}T}{M} e^{-\frac{t}{\tau}}, \tag{1.19}$$

where we put $\tau = M/\zeta$. Another well-used quantity is the mean square displacement (MSD) of a particle. Denoting the center-of-mass position of the colloid as $\boldsymbol{V}(t)$, the MSD is given as

$$\langle |\boldsymbol{R}(t) - \boldsymbol{R}(t)|^2 \rangle = 6Dt\{1 + \frac{\tau}{t}(e^{-\frac{t}{\tau}} - 1)\}, \tag{1.20}$$

where D is the diffusion constant of the particle and given by $D = k_{\mathrm{B}}T/\zeta$. The short time and long time behaviors of MSD are respectively approximated as $\sim \sqrt{\frac{3k_{\mathrm{B}}T}{M}}t^2$ ($t/\tau \ll 1$) and $6Dt$ ($1 \ll t/\tau$), which are known as ballistic and diffusive motion respectively. From MSD, a typical time scale of diffusive motion is evaluated, for example, by using the radius of the colloid a, as $\tau_{\mathrm{B}} = a^2/6D$. τ_{B} is often called as Brownian time. If we adopt the Stokes relation for the drag coefficient, i.e., $\zeta = 6\pi\eta a$ (η is the viscosity of the solvent), we obtain $\tau_{\mathrm{B}} = \pi a^3\eta/k_{\mathrm{B}}T$. This means that Brownian motion is faster for a smaller particle size, higher temperature, and lower viscosity.

Langevin equation of a free colloid including a hydrodynamic memory effect

*2 FDT in Eq. (1.18) assumes that there is no time correlation in the random force (i.e., Markovian white noise) and the resulting VACF shows an exponential decay as in Eq. (1.25). Such an exponential decay is also seen in molecular motion in a dilute fluid [47]. However, it is known that a liquid medium constituting the solvent of colloids shows collective motions in a nonlocal and non-instantenous manner. For example, in general, VACF of a liquid show a power-law decay of $\propto t^{-3/2}$, which is different from exponential decay as seen in Eq. (1.25). Such a power-law decay is known as long-time tail, which became widely recognized since a seminal molecular dynamics simulation work by Alder and Wainwright in 1970 [48] and was theoretically confirmed later (see e.g., Refs. [30, 49]). For Brownian motion of a

*2 The hydrodynamic effects that we discuss here is about inertia effects, i.e., the dynamical crossover of a free colloid from ballistic to diffusive motion. In real experiments of colloidal suspensions (especially many-body problems such as phase ordering dynamics), such effects are considered to be negligible. However, in some hydrodynamic simulation methods for colloids, it is required to perform computations while incorporating the inertia term, which is also the case with the method that we use in our study (FPD method). This is the main reason why we introduce the inertia effects here, but we also believe that this is a good example to see one aspect of complexities in the dynamics of colloidal suspensions.

free colloid, the existence of such a hydrodynamic mode has been experimentally observed recently [47].

As a theoretical expression for a free colloid including a hydrodynamic memory effect, we refer to the following Langevin equation in the frequency space ω [*3],

$$-i\omega M\boldsymbol{V}(\omega) = -\zeta(\omega)\boldsymbol{V}(\omega) + \boldsymbol{F}^{\mathrm{R}}(\omega), \tag{1.21}$$

with

$$\zeta(\omega) = 6\pi\eta_{\mathrm{s}}a\{1 + (-i\omega)\frac{a^2}{9\nu} + (1-i)\sqrt{\frac{a^2\omega}{2\nu}}\}, \tag{1.22}$$

$$\langle F_i^{\mathrm{R}}(\omega)F_j^{\mathrm{R}}(\omega')\rangle = 2k_{\mathrm{B}}T\mathrm{Re}\zeta(\omega)\delta_{ij}\delta(\omega-\omega'), \tag{1.23}$$

where ν is the kinetic viscosity of a solvent ($\nu = \eta_{\mathrm{s}}/M$). The first term in Eq. (1.21) means resistance generated by a solvent in nonsteady flow, which can be derived from the Navier-Stokes equation for a viscous fluid [50]. This force is often called as the Boussinesq-Basset force and separated into three terms as in the right hand side of Eq. (1.22). The first term is the viscous force in a steady states ($\omega = 0$), which is consistent with the Stokes law. The second term is a force required for a colloid to push the surrounding solvent away and can be rewritten as $i\omega M\boldsymbol{V}(\omega)/2$, which is equivalent to the increase of the effective mass of colloid by $M/2$. The last term represents a non-steady effect, which is responsible for a hydrodynamic memory effect.

VACF of the above equation is known to be expressed as

$$\langle \boldsymbol{V}(t)\cdot\boldsymbol{V}(0)\rangle = \frac{3k_{\mathrm{B}}T}{M_{\mathrm{eff}}}\psi^{\mathrm{T}}(\frac{t}{\tau_{\mathrm{a}}}). \tag{1.24}$$

Here $\tau_{\mathrm{a}} = a^2/\nu$, where a is the hydrodynamic radius of a colloid. $M_{\mathrm{eff}} = 3M/2$ is the effective colloid mass and the increment of mass originates from the second term in the right hand side of Eq. (1.22). ψ^{T} is the memory function including hydrodynamic effect (see Eq. (4.20) for the functional form). The asymptotic behavior of ψ^{T} in the large x (or, long-time) limit is given by $\psi^{\mathrm{T}}(x) \sim \frac{1}{6\sqrt{\pi}}x^{-3/2}$, which reproduces the long-time tail.

The corresponding translational mean square displacement was also derived as

$$\langle|\boldsymbol{R}(t) - \boldsymbol{R}(t)|^2\rangle = 6Dt\ h(\frac{t}{\tau_a}) \tag{1.25}$$

where $h(x)$ is a function characterizing the crossover behavior from ballistic to diffusive motion and has a complicated functional form (see Eq. 4.23) and compare it with Eq. (1.25). The asymptotic behavior of $h(x)$ is given by $h(x) \to 3x/2$ ($x \to 0$) and $h(x) \to 1$ ($x \to \infty$) for the ballistic and diffusive regimes, respectively.

[*3] Here we only consider the case where the mass densities of the colloid and solvent are the same.

DFT in Eq. (1.23) is derived [51, 52, 53] by imposing the boundary condition for the surface of a colloid in the Navier-Stokes equation for a viscous fluid with the thermal fluctuations [50, 54],

$$\rho\frac{\partial \boldsymbol{v}}{\partial t} = -\nabla p + \eta_{\mathrm{s}}\nabla^2\boldsymbol{v} + \nabla\cdot\sigma^{\mathrm{R}}, \tag{1.26}$$

where $\boldsymbol{v}$ is the velocity field and p is the pressure determined such that the incompressibility condition $\nabla\cdot\boldsymbol{v}=0$ is to be satisfied. σ^{R} is the random stress tensor and follows the DFT for an incompressible fluid,

$$\langle\sigma^{\mathrm{R}}_{ij}(\boldsymbol{r},t)\sigma^{\mathrm{R}}_{mn}(\boldsymbol{r}',t')\rangle = 2k_BT\eta_{\mathrm{s}}(\delta_{im}\delta_{jn}+\delta_{in}\delta_{jm})\delta(\boldsymbol{r}-\boldsymbol{r}')\delta(t-t').$$

This approach based on fluctuating hydrodynamics are also developed for other problems such as the rotational Brownian motion [55] and the translational Brownian motion of a liquid droplet [56].

We have introduced a Langevin equation with a hydrodynamic memory effect so far, but here we note that it is unfortunately difficult to study many-body problems of colloids with Eq. (1.21) as a starting point. In Eq. (1.23), we can clearly see that the random force is no longer white noise and has a memory effect. This is a consequence of thermal fluctuations at different points in the fluid being coupled with each other through the Navier-Stokes equation. Thus, it is difficult to reproduce the resulting hydrodynamic memory effects properly by applying stochastic forces locally; more specifically, it is hard to constitute such a special random number sequence.

1.4.3 Many-body problems

In studying colloidal dynamics based on a hydrodynamic description for solvent (see Sec. 1.4.1), we inevitably encounter a complicated moving boundary problem, since the non-slip solid-fluid boundary condition has to be satisfied for all the surfaces of colloidal particles. Such a problem can be solved analytically only when the flow profile of solvent has high symmetry. Therefore, many-body problems in a colloidal suspension are basically to be discussed only under significant approximations.

Point-particle approximation

The simplest treatment for the boundary problems between colloids and solvent is to regard colloids as points. Denoting the force acting on colloid n at position $\boldsymbol{R}_n$ with velocity $\boldsymbol{V}_n$ as $\boldsymbol{F}_n$, the Navier-Stokes equation under the Stokes approximation can be written as

$$-\nabla p + \eta_{\mathrm{s}}\nabla^2\boldsymbol{v} = -\sum_n \boldsymbol{F}_n\delta(\boldsymbol{r}-\boldsymbol{R}_n), \tag{1.27}$$

where $\boldsymbol{v}$ is flow field of solvent and η_{s} is the viscosity of solvent. p is the pressure, which is determined such that the imcompressibility condition $\nabla\cdot\boldsymbol{v}=0$ is to be satisfied. Equation 1.27 can be solved as [57]

$$\boldsymbol{v}(\boldsymbol{r}) = \sum_n \boldsymbol{T}(\boldsymbol{r}-\boldsymbol{R}_n)\cdot\boldsymbol{F}_n, \tag{1.28}$$

where $\boldsymbol{T}$ is the so-called Oseen tensor:

$$T_{ij}(\boldsymbol{r}) = \frac{1}{8\pi\eta_{\rm s} r}(\delta_{ij} + \frac{r_i r_j}{r^2}). \tag{1.29}$$

Assuming the Stokes law between the force and the relative velocity between colloids and solvent, i.e, $\boldsymbol{F}_n = 6\pi\eta_{\rm s} a(\boldsymbol{V}_n - \boldsymbol{v}(\boldsymbol{R}_n))$, we obtain

$$\boldsymbol{V}_n = \sum_m \boldsymbol{T}_{nm} \cdot \boldsymbol{F}_m, \tag{1.30}$$

where we denote $\boldsymbol{T}_{nm} = \boldsymbol{T}(\boldsymbol{R}_n - \boldsymbol{R}_m)$ for $n \neq m$ and $\boldsymbol{T}_{nn} = 1/6\pi\eta_{\rm s} a$. The set of equations that incorporate the thermal noise following the fluctuation-dissipation theorem to the above equation is know as the simplest version of Stokesian Dynamics [58, 59]. The above equation is correct only if the interparticle distance is sufficiently larger than the particle diameter. In other words, lubrication effects, or hydrodynamic interactions at short distance is not properly incorporated in the above equation.

Hydrodynamic interaction at short distance

Here we consider the situation where two spherical equal-size colloids with radius a approach with the same velocity V along the line connecting their center-of-mass positions. In this problem, the exact solution for the friction coefficient is known [60]. Denoting the distance between the surfaces of the two colloids as u and the frictional force acting on the sphere as $F = -6\pi\eta_{\rm s} a C_2(u) V$, C_2 is given as

$$C_2(u) = \frac{4}{3}\sinh\alpha \sum_{n=1}^{\infty} \frac{n(n+1)}{(2n-1)(2n+3)} \{ \frac{4\cosh^2((n+1/2)\alpha) + (2n+1)^2\sinh^2\alpha}{2\sinh((2n+1)\alpha) - (2n+1)\sinh(2\alpha)} - 1 \} \tag{1.31}$$

where α is determined by $\cosh(\alpha) = u/2 + 1$. The asymptotic behavior of C_2 for $u \to \infty$ is $1 + 3/2u \sim 1 + 3a/2r$, which reproduces the expression for hydrodynamic interaction by the Oseen tensor (Eq. 1.30). For a short distance ($u \to 0$), $C_2 \sim 1/2u = (2(r/a - 2))^{-1}$, which is a different functional form from $1 + 3a/2r$.

Based on the asymptotic behavior of C_2 for small u, we may express a hydrodynamic force that colloid n experiences as a result of the relative motion between n-th and m-th colloids as

$$\boldsymbol{F}_{nm} = -\frac{3\pi\eta_{\rm s} a}{2(R_{nm}/a - 2)}(\boldsymbol{V}_{nm} \cdot \hat{\boldsymbol{R}}_{nm})\hat{\boldsymbol{R}}_{nm}, \tag{1.32}$$

where $\boldsymbol{R}_{nm} = \boldsymbol{R}_n - \boldsymbol{R}_m$, $\boldsymbol{V}_{nm}$ is the derivative of $\boldsymbol{R}_{nm}$. $\hat{\boldsymbol{R}}_{nm}$ is the unit vector parallel to $\boldsymbol{R}_{nm}$. Such kinds of formula are used in some hydrodynamic models for complementing a short range hydrodynamic interaction that is missed in the original model. However, it is hard to evaluate how precisely the superposition of such a two-body expression can describe many-body hydrodynamic interactions.

Direct numerical simulation

It is not easy to contract the hydrodynamic degrees of freedom of a solvent into the interaction tensor acting among colloids [*4], but it is possible to numerically treat

[*4] An exact expression of a high rank tensor is known. See, e.g. [61].

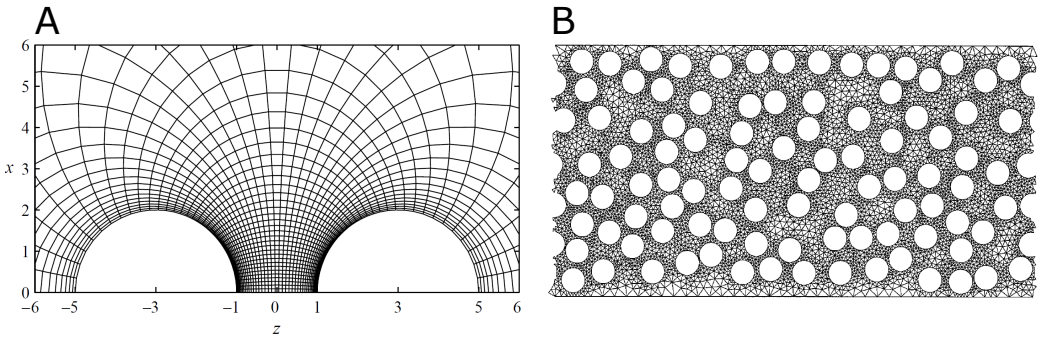

Fig. 1.4 **Moving boundary problems in colloidal suspensions**. **A.** Finite difference grid in bispherical coordinates [62]. **B.** Two-dimensional finite-element mesh in a channel flow with 100 circular disks [63].

the time evolution of the corresponding Navier-Stokes equation. To realize direct numerical simulation, we need to consider how to deal with the moving boundary problems between colloids and solvent again. If we try to straightforwardly deal with the problem, we need to generate complicated adaptive mesh for every time steps (see Fig. 1.4), which is numerically costly.

To overcome these difficulties, a new simulation method called Fluid Particle Dynamics (FPD) method [7] has been developed in 2000, which can perform direct numerical simulation on the Cartesian coordinate without suffering from the moving boundary problems (see Sec. 4.2.1 for the detail). This method approximates a solid colloidal particle as a shape-fixed liquid droplet whose viscosity is much higher than the solvent viscosity. This assumption allows us to treat the whole system including colloids as fluid body. The singularity on the colloid-solvent interface is avoided by introducing a finite thickness between liquid droplets and solvent, with which we can sustain the numerical stability. This idea of embedding the solid-fluid boundary conditions into the Navier-Stokes equation by smoothly connecting the solid body and fluid body with finite-thickness interface have been adopted to various hydrodynamic simulation methods [64, 65, 66].

Chapter 2

Relevant theory and previous study

The subjects of our study are (1) the structural formation process of colloidal suspensions undergoing phase separation and (2) crystallization dynamics of hard sphere colloids. In this section, we introduce the basic theories which are relevant to these two phenomena and review previous researches.

2.1 Phase separation in binary mixtures of simple liquids

2.1.1 Phase behavior

A mixture of two liquids, which is homogeneously mixed at a high temperature, often phase separates upon cooling. To comprehend the thermodynamic behavior of such a mixture, we consider the following Ginzburg-Landau-type free energy:

$$f(\phi) = \frac{1}{2}r\phi^2 + \frac{1}{4}u\phi^4 - h\phi, \tag{2.1}$$

where ϕ is the composition of the one of the components, $r = r_0(T - T_\mathrm{c})/T_\mathrm{c}$ (T_c being the critical temperature) and h is the external field. r_0 and u are positive constants. In Fig. 2.1, we show the functional form of Eq. 2.1. Here we can see that f has a single minimum for $T > T_\mathrm{c}$, whereas for $T < T_\mathrm{c}$ f has two minima. From the material conservation, the average of ϕ over the whole system, ϕ_0, is constant. Under a certain condition specified by ϕ_0 and T, the state where the system is decomposed into two phases with compositions of ϕ_a and ϕ_b (shown in the figure) can be more stable than the homogeneous state of composition ϕ_0. More specifically, the free energy at the red circle point is larger than that at the red star point, i.e. $F(\phi_0) > [(\phi_\mathrm{b} - \phi_0)F(\phi_\mathrm{a}) + (\phi_0 - \phi_\mathrm{a})F(\phi_\mathrm{b})]/(\phi_\mathrm{b} - \phi_\mathrm{a})$. Such a situation is realized when $T < T_\mathrm{c}$ and $\phi_\mathrm{a} < \phi_0 < \phi_\mathrm{b}$.

We can understand this behavior on the basis of the phase diagram in the $\phi - T$ plane (see Fig. 2.2a). The solid line in the figure is called as "binodal line" and the composition of the two coexisting phases are given by ϕ_a and ϕ_b. The two phases can coexist in a thermodynamically equilibrium state. However, the phase separation dynamics can be classified into three types (see the three colored regions in Fig. 2.2a). The dashed line is called as "spinodal line", which is determined by the compositions at which the second derivative of the free energy, f'', is zero (see

also the blue points in Fig. 2.1). Depending on whether f'' is positive or negative, phase separation dynamics is classified into nucleation-growth (NG)-type (see the yellow region) or spinodal-decomposition (SD)-type respectively. The former takes place in the metastable region, and thus phase separation is initiated by overcoming a free-energy barrier by an activated process. On the other hand, the latter proceeds in the unstable region, and thus the initial mixed state is absolutely unstable and phase separation starts without any free energy barrier.

Furthermore, the pattern formation of SD-type phase separation depends on the initial composition ϕ_0. Near the symmetric composition (i.e., near 50:50 mixture, the blue region in Fig. 2.2a) a bincontinuous pattern (Fig 2.2b) is formed, whereas in an off-symmetric composition (which corresponds to the green region) a droplet pattern (see Fig 2.2c) is formed.

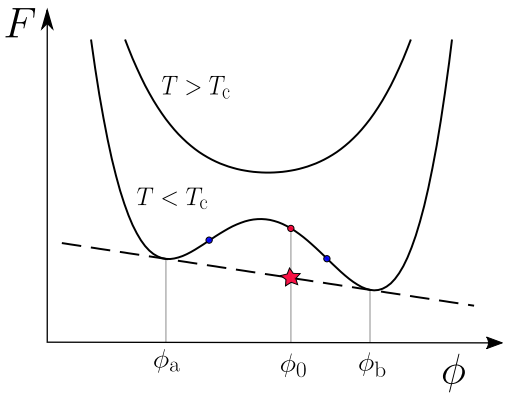

Fig. 2.1 Typical free energy curves for a binary mixture of simple liquids for $T > T_c$ and $T < T_c$ (see the solid curves). The dashed line is the common tangent for the free energy curve at $T < T_c$ and we denote ϕ at the two contacts as ϕ_a and ϕ_b ($\phi_a < \phi_b$).

2.1.2 Kinetic theory of phase separation of a binary mixture: Model H

Model H

Phase separation dynamics in a binary mixture of simple liquids is well-understood, based on a coarse-grained model called "model H". In this model, the order parameter ψ is chosen as the composition of the one of the components. The temporal change of ψ is to be induced by either diffusion or hydrodynamic convection (flow velocity $\boldsymbol{v}$). The corresponding conservation laws for composition and momentum are given by the following set of equations:

$$(\frac{\partial}{\partial t} + \boldsymbol{v} \cdot \nabla)\psi = L_\psi \nabla^2(\beta\mu_\psi) + \theta_\psi, \tag{2.2}$$

$$\rho(\frac{\partial}{\partial t} + \boldsymbol{v} \cdot \nabla)\boldsymbol{v} = -\nabla \cdot \boldsymbol{\Pi} - \nabla p + \eta\nabla^2\boldsymbol{v} + \boldsymbol{\zeta}, \tag{2.3}$$

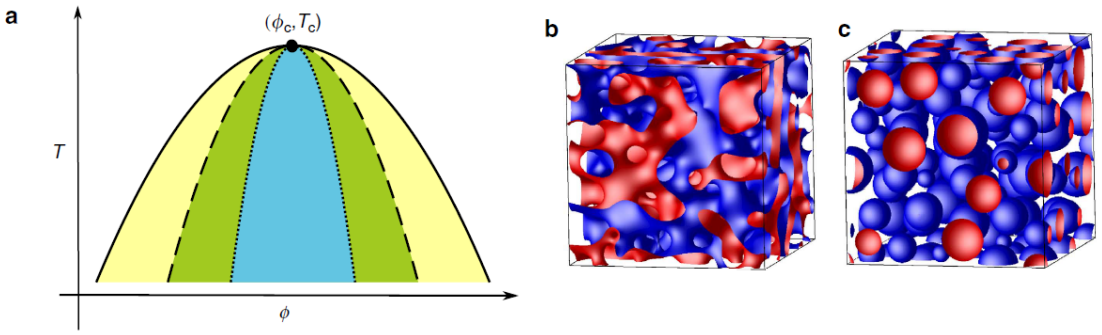

Fig. 2.2 **a,** Schematic figure of the phase diagram of a binary mixture. The solid and dash curves represent binodal and spinodal lines. In the yellow region, NG-type phase separation takes place. Inside of the spinodal line, SD-type phase separation takes place, but the type of pattern formation depends on the initial composition ϕ_0. Near the symmetric composition (50:50 mixture: see the green region) a bincontinuous pattern (**b**) is formed, and at an off-symmetric composition (which corresponds to the blue region), a droplet pattern is formed (**c**). Blue and red color in **b** and **c** represent the outer and inner sides of the domain interfaces, respectively. This figure is reproduced from Ref. [67].

where ρ is the mass density and η is the viscosity [*1]. μ is the osmotic pressure regrading ψ and given as $\mu_\psi = \delta\mathscr{F}/\delta\psi$. Here $\mathscr{F}$ is the free energy functional expressed as

$$\mathscr{F}(\psi) = \int d\boldsymbol{r} \left[f(\boldsymbol{r}) + \frac{1}{2} C |\nabla\psi|^2 \right], \tag{2.4}$$

where the second term represents the gradient term and C is a positive constant. f is the bulk free energy for which we assume the Ginzburg-Landau type as before:

$$f = \frac{1}{2} r\psi^2 + \frac{1}{4} u\psi^4 - h\psi. \tag{2.5}$$

The last term in the right hand side of the above equation represents the change of free energy by an external field, but we do not consider it in this section (or, we assume $h = 0$). In Eq. 2.3, $\boldsymbol{\Pi}$ is the osmotic stress tensor, which is related to the thermodynamic force $\boldsymbol{F}_\psi$ as $\boldsymbol{F}_\psi = -\nabla \cdot \boldsymbol{\Pi} = -\psi\nabla\mu_\psi$. p is the pressure introduced such that the hydrodynamic flow satisfies the incompressible condition $\nabla \cdot \boldsymbol{v} = 0$. θ and $\boldsymbol{\zeta}$ represent thermal fluctuations of ψ and $\boldsymbol{v}$ respectively, satisfying the fluctuation-dissipation relations with the transport coefficient regarding material diffusion constant L_ψ and the viscosity η respectvely: $\langle \theta_\psi(\boldsymbol{r}, t)\theta_\psi(\boldsymbol{r}', t')\rangle = -2k_\mathrm{B}TL_\psi\nabla^2\delta(\boldsymbol{r} - \boldsymbol{r}')\delta(t - t')$, $\langle \zeta_i(\boldsymbol{r}, t')\zeta_j(\boldsymbol{r}', t)\rangle = -2k_\mathrm{B}T\eta\nabla^2\delta(\boldsymbol{r} - \boldsymbol{r}')\delta(t - t')\delta_{ij}$.

Under the Stokes approximation ($\rho D\boldsymbol{v}/Dt = 0$), Eq. (2.3) with $\nabla \cdot \boldsymbol{v} = 0$ can be

[*1] For simplicity, we assume that the mass density and viscosity are the same between the two liquids.

transformed as

$$\begin{aligned}\boldsymbol{v} &= \int d\boldsymbol{r}\boldsymbol{T}(\boldsymbol{r}-\boldsymbol{r}')\cdot(\boldsymbol{F}_\psi(\boldsymbol{r}')+\boldsymbol{\zeta}(\boldsymbol{r}')) \\ &= \int d\boldsymbol{r}\boldsymbol{T}(\boldsymbol{r}-\boldsymbol{r}')\cdot[\mu(\boldsymbol{r}')\nabla\psi(\boldsymbol{r}')+\boldsymbol{\zeta}(\boldsymbol{r}')],\end{aligned} \tag{2.6}$$

where $\boldsymbol{T}$ is the Oseen tensor (see Eq. 1.29).

Early stage of spinodal decomposition

First we examine the stability of Eq. 2.2. For simplicity, here we neglect the convective term and the thermal noise. We decompose the order parameter ψ into the average concentration, ψ_0, and the deviation from it, $\delta\psi$. Supposing that $\delta\psi$ is sufficiently small, we can linearize Eq. 2.2. Then, the time-correlation function in the wave number space, $S_q(t) = \langle\delta\psi_q(t)\delta\psi_q(0)\rangle$ can be calculated as

$$S_q(t)/S_q(0) = e^{-2\Gamma_q t}, \tag{2.7}$$

where $\Gamma_q = Lq^2[(\frac{\partial^2 f}{\partial\psi^2})_0 + Cq^2]$ is called "the decay rate of the order-parameter fluctuations". If $(\frac{\partial^2 f}{\partial\psi^2})_0 < 0$, infinistimaly small fluctuations exponentially grow with time, which is widely known as "spinodal instability".

Late stage of spinodal decomposition

When a certain period of time has elapsed after the linear regime, the order parameters inside of the domains are almost saturated to the equilibrium values $\psi = \pm\psi_\mathrm{e} \equiv \pm|r|/u$. In such a late stage of phase separation, thus, the bulk free energy f does not play a dominant role and the domain coarsening proceeds such that the total interfacial energy is to be minimized. During the coarsening process, it has been confirmed by many experimental and numerical studies that the phase-separated structure evolves in a self-similar manner, i.e., the statistical function to characterize the domain pattern can be scaled by the characteristic domain size, ℓ. For example, the structure factor can be scaled as

$$S_{\boldsymbol{q}}(t) = \ell(t)^d g(\boldsymbol{q}\ell), \tag{2.8}$$

where g is a scaling function and d is the spatial dimension. Furthermore, it has also been established that ℓ grows with time obeying a power law as $\ell \propto t^\alpha$, which is known as a dynamic scaling law.

The above exponent α is called "growth exponent". The value of α depends on the physical mechanisms of coarsening. In ordinary binary mixtures, the following three mechanisms are widely recognized: the first is the evaporation-condensation (or, Lifshitz-Slyozov-Wagner) mechanism [68] (Fig. 2.3C), which is observed in a mixture with a strongly asymmetric composition (1:99 or more asymmetric mixture, for example). In this mechanism, molecules in small droplets are transported to nearby larger droplets by thermal diffusion, because smaller droplets have larger chemical potential due to the larger interfacial curvature. For a more symmetric composition, collisions among droplets due to their Brownian motions become a major coarsening

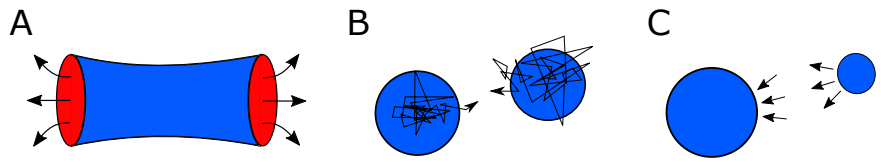

Fig. 2.3 Illustrative diagram of coarsening mechanisms of a binary liquid mixture: **A**. Tube hydrodynamic instability. **B**. Brownian coagulation mechanism. **C**. Evaporation-condensation mechanism.

mechanism, which is known as Smoluchwski's Brownian coagulation mechanism (Fig. 2.3B). The growth exponents of the above two mechanisms are commonly $\alpha = 1/3$. As we mentioned in Sec. 2.1.1, a bicontinuous structure is formed near the symmetric composition. In such a structure, the spatial fluctuations in the interface curvature of a bicontinuous structure creates the gradient of Laplace pressure along liquid tubes, leading to hydrodynamic flow inside of the tubes. For example, a tube structure shown in Fig. 2.3A is thus unstable. This instability of a fluid tube is known as Rayleigh instability. The fluid inside of the tube is squeezed out and then the tube eventually breaks up and is disconnected. This coarsening mechanism is called "Siggia's hydrodynamic mechanism" [69]. The growth exponent of this mechanism is $\alpha = 1$.

Below, we explain how to derive the growth exponents for the latter two coarsening mechanisms of a binary liquid mixture, which are relevant to our study of colloidal phase separation.

2.1.3 Coarsening mechanism of bicontinous structure

Near the symmetric composition, a bicontinuous structure is formed. The coarsening mechanism of such a structure is understood by focusing on the motion of the interface of the bicontinuous structure [69, 5].

To consider this, let us first check an interfacial profile in the equilibrium state, where $\mu = r\psi + u\psi^3 - C\nabla^2\psi = 0$. Provided that the flat interface between the different phases perpendicular to the x axis is located at $x = 0$ and $\psi = \pm\psi_{\mathrm{e}}$ is satisfied for $x \to \pm\infty$, we obtain the following composition profile, $\psi = \psi_{\mathrm{int}}$:

$$\psi_{\mathrm{int}}(x) = \psi_{\mathrm{e}} \tanh(\sqrt{\frac{|r|}{2C}}x). \tag{2.9}$$

The increment of the free energy per unit area resulting from the presence of interface, or the interfacial tension is introduced as,

$$\gamma = \int dx C(\frac{d\psi_{\mathrm{int}}}{dx})^2. \tag{2.10}$$

In the case in which the interface has a finite curvature, we may approximate ψ as $\psi(\boldsymbol{r}) \sim \psi_{\mathrm{int}}(\zeta)$. Here $\zeta = \boldsymbol{n}(\boldsymbol{r}_{\mathrm{a}}) \cdot (\boldsymbol{r} - \boldsymbol{r}_{\mathrm{a}})$, where $\boldsymbol{r}_{\mathrm{a}}$ represents the position on the interface that is closest from $\boldsymbol{r}$ and $\boldsymbol{n}(\boldsymbol{r}_{\mathrm{a}})$ is the unit normal vector of the

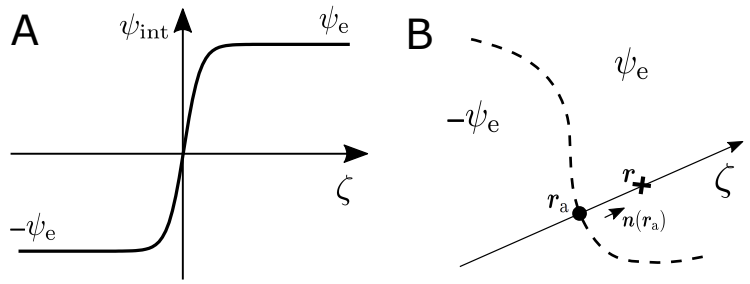

Fig. 2.4 **A**. The composition profile at the interface, $\psi_{\rm init}$. **B**. Approximation of the phase field ϕ by using $\psi_{\rm init}$. The dashed line in this figure represents the position of the interface between two domains.

interface at that point. Denoting the derivative of $\psi_{\rm int}$ in terms of ζ as $\psi'_{\rm int}$, we have the following relations: $\nabla\psi_{\rm init} = \psi'_{\rm init}\boldsymbol{n}$ and $\nabla^2\psi \sim \psi''_{\rm int} + (\nabla\cdot\boldsymbol{n})\psi'_{\rm int}$. From $\nabla\cdot\boldsymbol{n} = (1/R_1 + 1/R_2)$ (R_1 and R_2 are the principal curvatures), the chemical potential is given by $\mu_\psi \sim -C(1/R_1+1/R_2)\psi'_{\rm int}$. Accordingly, $\mu_\psi\nabla\psi = -C(1/R_1+1/R_2)(\psi'_{\rm int})^2\boldsymbol{n}$. Since $(\psi'_{\rm int})^2$ has a very sharp peak at $\zeta = 0$, it can be approximated by a delta function. By comparing it to Eq. (2.10), we obtain $(\psi'_{\rm int})^2 \sim \gamma\delta(\zeta)/C$. Substituting the above result into Eq. (2.11), we have

$$\boldsymbol{v}(\boldsymbol{r}) = -\gamma\int d\boldsymbol{r}_{\rm a}\boldsymbol{T}(\boldsymbol{r}-\boldsymbol{r}_{\rm a})\cdot\boldsymbol{n}(\boldsymbol{r}_{\rm a})(\frac{1}{R_1(\boldsymbol{r}_{\rm a})}+\frac{1}{R_2(\boldsymbol{r}_{\rm a})}). \tag{2.11}$$

Here we do not consider the thermal fluctuation for simplicity. Denoting $\ell(t)$ as the characteristic domain size at time t, the above relation can be simplified as $\ell/t \propto \gamma\ell^2(1/\eta\ell)(1/\ell) \propto \gamma/\eta$. Finally we obtain the domain growth law of $\ell \propto \gamma t/\eta$. This coarsening law characterized by the growth exponent $\alpha = 1$ is widely known as Sigaa's hydrodynamic mechanism [69] and the validity has been confirmed by experimental [70] and simulation [71, 72] studies.

2.1.4 Smoluchwski's Brownian coagulation theory

In a binary mixture with an off-symmetric composition, spherical droplets are formed. These droplets move via Brownian motion due to thermal force noise and grow wit time by collisions and coalescence among the droplets. Here let us call a droplet containing i elements (e.g., the number of molecules) i-cluster and denote the number of i-clusters per unit volume as n_i.

The Smoluchowski's coagulation euqation is an equation describing the time evolution of n_i and given by [73]

$$\frac{\partial}{\partial t}n_i = \frac{1}{2}\sum_{j=1}^{i-1}K_{i-j,j}n_{i-j}n_j - \sum_{j=1}^{\infty}K_{i,j}n_in_j, \tag{2.12}$$

where $K_{i,j}$ is a constant often called "coagulation rate" and describes the frequency at which i-cluster coagulates with j-cluster. This equation is based on the

assumption that the number of particles per unit volume is sufficiently small so that collisions involving more than three clusters are negligible. Also it dose not take the effect of break-up of clusters into account, which is valid if the interparticle attraction of colloids is strong enough compared to the thermal energy.

Coagulation rate in the Smoluchowski theory

To evaluate the time evolution of the above coagulation equation, we need to model the form of the coagulation rate $K_{i,j}$. Smoluchwski assumed that the transport of clusters takes place only by their Brownian motions and considered the relative diffusion equation for i-cluster and j-cluster. First let us denote the number density of i-clusters around j-cluster as $n_{i,j}(\boldsymbol{r}, t)$, where $\boldsymbol{r}$ represents the relative position vector whose origin is at the center-of-mass position of the j-cluster. Then, we can write the diffusion equation as $\partial_t n_{i,j}(\boldsymbol{r}, t) = -\nabla \cdot \boldsymbol{j}_{i,j}$ and $\boldsymbol{j}_{i,j} = -D_{i,j}\nabla n_{i,j}$. Here $D_{i,j}$ is the relative diffusion constant between i-clusters and j-clusters. Assuming the isotropy with respect to the radial angle,

$$\frac{\partial}{\partial t} n_{i,j}(r, t) = r^{-2} \frac{\partial}{\partial r}[r^2 \frac{\partial}{\partial r}(D_{i,j} n_{i,j})]. \tag{2.13}$$

Supposing that the coagulation takes place when the distance between the center-of-mass position of i-cluster and that of j-cluster is below $r = R_{i,j}$ ($R_{i,j}$ is often called "collision radius"), a natural boundary condition is $n_{i,j} = 0$ at $r = R_{i,j}$ and $n_{i,j} = n_i$ at $r = \infty$. With this boundary condition, we can solve Eq. (2.13) and obtain the following result:

$$n_{i,j}(r, t) = n_i(t)(1 - \frac{R_{i,j}}{r} + \frac{2R_{i,j}}{\sqrt{\pi r^2}} \int_0^{\frac{r-R_{i,j}}{\sqrt{4D_{i,j}t}}} e^{-\xi} d\xi). \tag{2.14}$$

$K_{i,j} n_i n_j$ corresponds to the number of collisions per unit time between clusters with size i and j. Thus, we can write $K_{i,j} n_i n_j = n_j \int_{r=R_{i,j}} \boldsymbol{j}_{i,j} \cdot d\boldsymbol{s}$. By substituting Eq. (6.4), we obtain

$$K_{i,j} = 4\pi R_{i,j} D_{i,j} (1 + \frac{R_{i,j}}{\sqrt{\pi D_{i,j} t}}). \tag{2.15}$$

In a long-time regime ($t \gg R_{i,j}^2 / D_{i,j}$), in other words, in the case in which the equilibration of $n_{i,j}$ toward the steady state is sufficiently fast compared to the frequency of collisions, the above result can be simplified as

$$K_{i,j} = 4\pi R_{i,j} D_{i,j}. \tag{2.16}$$

In the case in which the cluster shape can be regarded as sphere, the coagulation radius is simply given as $R_{i,j} = a_i + a_j$, where a_i is the radius of i-cluster. If we write the relative diffusion constant as the sum of the free diffusion constant of spherical solid particle, i.e., $D_{i,j} = \frac{k_B T}{6\pi\eta}(a_i^{-1} + a_j^{-1})$, the collision rate becomes

$$K_{i,j} = \frac{2k_B T}{3\eta}(a_i + a_j)(a_i^{-1} + a_j^{-1}). \tag{2.17}$$

Additionally, if the fluctuation of the distribution of cluster size is small ($a_i \sim a_j$ for all i, j), one finds that the collision rate becomes a constant that dose not depend on the size of clusters,

$$K_{\mathrm{s}} \equiv K_{i,j} = \frac{8k_{\mathrm{B}}T}{3\eta}. \tag{2.18}$$

In the presence of viscous force and interparticle attraction

The above theory assumes that the relative diffusion coefficient is written by the sum of the free diffusion constant of spherical particles. However, it is known that the relative diffusion motion between two particles is significantly suppressed as two particles get close, which can be understood from the fact that the velocity field of a solvent generated around the two particles is strongly deformed compared to that around an isolated particle.

A modified version of the Smoluchowski theory that takes such an effect of viscous force into account is known [74]. This theory considers the effect of the interaction potential between i and j-cluster, $U_{i,j}$, as well. Because the interparticle force transports the number density $n_{i,j}$ with the relative velocity between the two clusters, $u_{i,j}$, the flux $\boldsymbol{j}_{i,j}$ has an additional term of $-n_{i,j}u_{i,j}$. Since we are focusing on the viscous regime, the interparticle force is to be balanced with the viscous force generated by squeezing flow between the clusters, i.e., $-\frac{\partial U_{i,j}}{\partial r} = \zeta(r/R_{ij})u_{i,j}$, where $\zeta(r/R_{ij})$ is the viscous drag coefficient between two clusters whose center-of-distance is r and given as $\zeta = k_BT/D_{i,j}$. From the above, we obtain $\boldsymbol{j}_{i,j} = -D_{i,j}(\nabla n_{i,j} + \frac{n_{i,j}}{k_{\mathrm{B}}T}\nabla U_{i,j})$. Under the same condition as in the preceding section (the assumption of isotropy, a steady state, and the same boundary condition), we obtain

$$n_{i,j}(r,t) = \frac{\int_{R_{i,j}}^{r} D_{i,j}^{-1} e^{U_{i,j}/k_{\mathrm{B}}T} r^{-2} dr}{\int_{R_{i,j}}^{\infty} D_{i,j}^{-1} e^{U_{i,j}/k_{\mathrm{B}}T} r^{-2} dr} e^{-U_{i,j}/k_{\mathrm{B}}T} n_i. \tag{2.19}$$

If we can assume that clusters are spherical and that the deviation of the distribution of cluster size is small ($a \sim a_i$ for all i), we can obtain

$$\frac{K}{K_{\mathrm{s}}} = [\int_2^{\infty} C_2(s) e^{U(s)/k_{\mathrm{B}}T} \frac{ds}{s^2}]^{-1}, \tag{2.20}$$

where $s = r/a$ and $C_2(s)$ is given by the viscous drag coefficient between two clusters divided by that of a free cluster. For the drag coefficient for two spherical particles, an exact solution is known (see Eq. 1.31).

A solution under a constant coagulation rate

In the condition where the coagulation rate is constant ($K \equiv K_{i,j}$), we can get the following analytic solution for Eq. (6.4), under the initial condition of $n_i(t) = n_{\mathrm{p}}$ for $i = 0$ and $n_i(t) = 0$ for otherwise:

$$n_i = n_{\mathrm{p}}(\frac{t}{t_{\mathrm{h}}})^{i-1}/(1 + \frac{t}{t_{\mathrm{h}}})^{i+1}, \tag{2.21}$$

$$n_{\rm c} \equiv \sum_i n_i = (1 + \frac{t}{t_{\rm h}})^{-1} n_{\rm p}, \tag{2.22}$$

where $n_{\rm tot}$ is the total number density of clusters and $t_{\rm h}$ is a half-life period for $n_{\rm c}$ that is related to the coagulation rate as $t_{\rm h} = 1/n_{\rm p}K$.

The asymptotic behavior of $n_{\rm c}$ in a long-time regime is $n_{\rm c} \sim 1/Kt$. In the case where the shape of clusters is spherical, we may take the mean radius of cluster $R(t)$ as the characteristic domain size $\ell(t)$. Since $R(t)$ obeys the relation of $n_{\rm c}R(t)^d \propto$ const, we obtain $R(t) \propto t^{1/d}$, indicating that the growth exponent of the Brownian coagulation mechanism is $1/d$ ($1/3$ in three dimensions).

2.2 Phase separation of complex fluids

In this section, we consider the phase separation dynamics of complex fluids. In the above, we have discussed the phase separation dynamics of a binary mixture of simple liquids, where we have seen that the material transport by fluid flow plays an essential role in addition to material diffusion. This implies that the degrees of freedom of fluid flow should play a key role also in phase separation of complex fluids. Complex fluids such as colloids, polymers, liquid crystals, etc., show complex rheological behavior depending on the kinds or composition of the materials. Therefore, it is possible that such viscoelastic behavior has a significant influence on the pattern formation process during phase separation. However, for colloidal systems, which is the target of our study, there has so far been no successful rheological description of colloidal suspensions and developing the constitutive equation is actually one of the central topics of colloidal science [75]. To see the viscoelastic effects on phase separation of complex fluids, in the following we first review phase separation of polymer solutions, and then introduce the previous studies of colloidal phase separation.

2.2.1 Two fluid model for a polymer solution.

Two fluid model

Before getting to the topic of the phase separation, we introduce the two fluid model for polymer solutions [76, 77]. This model considers the time evolution of the local volume fraction of polymer ϕ, and the average local velocity field of polymers and solvent, $\boldsymbol{v}_{\rm p}$ and $\boldsymbol{v}_{\rm s}$. The basic set of kinetic equations for these variables are given by

$$\frac{\partial \phi}{\partial t} = -\boldsymbol{\nabla} \cdot (\phi \boldsymbol{v}_{\rm p}) = \boldsymbol{\nabla} \cdot ((1-\phi)\boldsymbol{v}_{\rm s}), \tag{2.23}$$

$$\boldsymbol{v}_{\rm s} - \boldsymbol{v}_{\rm p} = \frac{(1-\phi)}{\zeta_R}[\boldsymbol{\nabla} \cdot \boldsymbol{\Pi} - \boldsymbol{\nabla} \cdot \boldsymbol{\sigma}_{\rm p}], \tag{2.24}$$

$$\rho \frac{\partial \boldsymbol{v}}{\partial t} = -\boldsymbol{\nabla} \cdot \boldsymbol{\Pi} + \boldsymbol{\nabla} \cdot \boldsymbol{\sigma}_{\rm p} - \nabla p + \eta \nabla^2 \boldsymbol{v}, \tag{2.25}$$

$$\boldsymbol{\nabla} \cdot \boldsymbol{v} = 0, \tag{2.26}$$

where $\boldsymbol{v}$ is the average velocity given as $\boldsymbol{v} = \phi\boldsymbol{v}_{\rm p} + (1-\phi)\boldsymbol{v}_{\rm s}$, ζ_R is the effective friction constant related to the relative motion of polymers and the solvent after coarse-graining, and η is the solvent viscosity. Eq. (7.5), (7.7) and (7.8) represent the material conservation law, the momentum conservation law, and the incompressible condition, respectively. Eq. (7.6) means that the friction force arising from the relative velocity between polymers and solvent is to be mechanically balanced with the osmotic force generated by the osmotic stress tensor $\boldsymbol{\Pi}$ and the viscoelastic force generated by the mechanical stress tensor $\boldsymbol{\sigma}_{\rm p}$. Here we note that $\boldsymbol{\Pi}$ is related to the thermodynamic force $\boldsymbol{F}_\phi$ as $\boldsymbol{F}_\phi = -\boldsymbol{\nabla}\cdot\boldsymbol{\Pi} = -\phi\nabla(\delta\mathscr{F}_\phi/\delta\phi)$, where $\mathscr{F}_\phi$ is the free energy functional and we use the same functional form as in Eq. 2.1.2. In the two fluid model, the evolution of $\boldsymbol{\sigma}_{\rm p}$ is assumed to be expressed by the following Maxwell equation with a single relaxation mode,

$$\frac{\partial}{\partial t}\sigma_{{\rm p}ij} + (\boldsymbol{v}_{\rm p}\cdot\nabla)\sigma_{{\rm p}ij} = G\left[\frac{\partial v_{{\rm p}i}}{\partial x_j} + \frac{\partial v_{{\rm p}j}}{\partial x_i} - \frac{2}{3}(\nabla\cdot\boldsymbol{v}_{\rm p})\right] - \frac{1}{\tau}\sigma_{{\rm p}ij} \tag{2.27}$$

where G and τ are the shear modulus and the relaxation time. The above constitutive equation can be derived from the equation of motion for the individual polymers [57, 15].

The point of the model is that the mechanical stress $\boldsymbol{\sigma}_{\rm p}$ selectively acts on polymers and the time evolution of $\boldsymbol{\sigma}_{\rm p}$ is solely determined by the deformation rate tensor of polymers, which reflects the difference in the structural relaxation times between solvent molecules and polymers. We note that the model without the mechanical stress term is physically equivalent to model H.

Density fluctuation in linear regime

The above equation for mass conservation can be rewritten as

$$\frac{\partial\phi}{\partial t} = -\nabla\cdot(\phi\boldsymbol{v}) + \nabla\cdot\left[\frac{\phi(1-\phi)^2}{\zeta_{\rm R}}(\nabla\cdot\boldsymbol{\Pi} - \nabla\cdot\boldsymbol{\sigma}_{\rm p})\right]. \tag{2.28}$$

By mean-field approximation, we can obtain the following linearized equation for ϕ and $Z = \nabla\nabla:\boldsymbol{\sigma}_{\rm p}$ in wavenumber space,

$$\frac{\partial}{\partial t}\begin{pmatrix}\phi_q\\ Z_q\end{pmatrix} = \begin{pmatrix}-\Gamma_q & -\frac{L}{\phi}\\ -\frac{4Gq^2\Gamma_q}{3\phi} & -\frac{1+q^2\xi_{\rm ev}}{\tau}\end{pmatrix}\begin{pmatrix}\phi_q\\ Z_q\end{pmatrix}, \tag{2.29}$$

where $L = (1-\phi)^2\phi^2/\zeta_{\rm R}(\phi)$ is the transport coefficient, $\xi_{\rm ev} = (4LG\tau/3\phi^2)^{1/2}$ is the length scale known as viscoelastic length and $\Gamma_q = Lq^2[(\frac{\partial^2 f}{\partial\phi^2}) + Cq^2]$ is the decay rate in the absence of the mechanical stress. From Eq. 2.29, the time-correlation function for ϕ_q, $S_q(t) = \langle\phi_q(t)\phi_{-q}(0)\rangle$ can be computed as

$$S_q(t)/S_q(0) = A_{\rm s}e^{-\Gamma_{{\rm s}q}t} + (1-A_{\rm s})e^{-\Gamma_{{\rm f}q}t}, \tag{2.30}$$

where $\Gamma_{{\rm s}q}$ and $\Gamma_{{\rm f}q}$ are the solution of the quadratic equation which satisfies $\Gamma_{{\rm s}q} + \Gamma_{{\rm f}q} = \Gamma_q + (1+q^2\xi_{\rm ev}^2)/\tau$ and $\Gamma_{{\rm s}q}\Gamma_{{\rm f}q} = \Gamma_q/\tau$, and $A_{\rm s} = \frac{\Gamma_{{\rm s}q}\tau - (1+q^2\xi_{\rm ev}^2)}{(\Gamma_{{\rm f}q}-\Gamma_{{\rm s}q})\tau}$. In the case

where the diffusive relaxation is much slower than the stress relaxation ($\tau\Gamma_q \ll 1$), the concentration fluctuation relaxes with the decay rate into which the viscoelastic effect is renormalized, $\bar{\Gamma}_q = \Gamma_q/(1+\xi_{\rm ev}^2 q^2)$:

$$S_q(t)/S_q(0) \sim e^{-2\bar{\Gamma}_q t}. \tag{2.31}$$

From this, we find that the functional form of $S_q(t)$ is crucially different form the one for model H at a small length scale, which is due to a coupling between diffusion and stress modes, but for a large length scale $\xi_{\rm ev} \gg q^{-1}$, $S_q(t)$ recovers the same q-dependence as in model H. In the opposite case ($\tau\Gamma_q \gg 1$), the stress and diffusive relaxations are decoupled:

$$S_q(t)/S_q(0) \sim e^{-\Gamma_q t} + \frac{\xi_{\rm ev}^2 q^2}{\Gamma_q \tau} e^{-t/\tau}. \tag{2.32}$$

The above behavior under the linear approximation is justified by comparison with experiments (see e.g., [78]).

2.2.2 Viscoelastic phase separation

Viscoelastic phase separation of polymer solutions

The phase separation dynamics of polymer solutions has been believed to be universally expressed by model H, although the free energy is modified by the polymerization degree of polymers N [57]. However, it has been experimentally discovered that the pattern formation processes which cannot be understood in the framework of model H take place in a polymer solution with large N [79]. Figure 2.5 show an example of the typical phase separation process observed in a polystyrene/diethyl malonate mixture. The pattern evolution proceeds as follows:

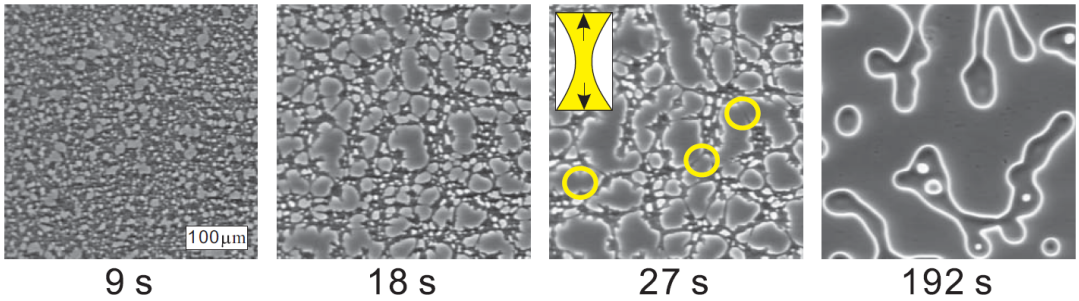

Fig. 2.5 Time evolution of viscoelastic phase separation in a polystyrene/diethyl malonate mixture [80].

1. Gel-like domain is formed over the space after the growth of composition fluctuation.
2. The solvent in the polymer-rich domain is squeezed out and the volume of polymer-rich domain shrinks.

3. During the volume shrinking process, the polymer-rich domain coarsens while pulling each other. In this process, rupture of the thin arms of the polymer-rich domain is observed.
4. In the late stage, fluid-like coarsening as seen in ordinary binary mixtures proceeds (the domain coarsens to decrease the interfacial area).

This behavior implies that rheological characteristics of the polymer-rich phase has a significant effect on the phase separation dynamics. For this reason, this phenomena was named as "viscoelastic phase separation" [81, 82]. In viscoelastic phase separation, the mechanical balance dominates the pattern formation and the self-similarity dose not hold, which is in contrast to the phase separation of ordinary binary mixtures.

Importance of bulk stress and the physical meaning

One of the striking point of viscoelastic phase separation is that the polymer-rich phase can form the percolating pattern even when the composition of polymer is minority, and the phase inversion phenomena [*2] became the central issue to understand the new type of the phase separation process.

As we mentioned in the last section, one of the crucial features of polymer solutions compared to ordinary binary mixtures is the huge gap in the structural relaxation time between different components, which is expected to be a key to approach the above problem. As examples of the studies focusing on this point, we mention several works that examined the difference in material diffusion [83, 84] and viscosity [85, 86, 87], and parts of the studies report that these gaps between two phases actually enhance the percolation of the minority phase. However, since the behavior that the polymer domain are pulling each other is experimentally observed, one may consider that the mechanical stress in polymer-rich phase is responsible for this phenomena.

The viscoelastic effects have been first examined by Taniguchi and Onuki [88] by numerical simulation using two fluid model. They successfully reproduced the formation of the network pattern and revealed an importance of viscoelastic effect in stabilizing the network pattern. After that, Tanaka and Araki [89] reported the simulation result by two fluid model but with a different constitutive equation. Specifically, they described the mechanical stress as $\boldsymbol{\sigma}_{\mathrm{p}} = \boldsymbol{\sigma}_{\mathrm{S}} + \boldsymbol{\sigma}_{\mathrm{B}}$, where $\boldsymbol{\sigma}_{\mathrm{S}}$ is shear stress and follows the same time evolution as in Eq. 2.27. The point of their formulation is additionally including *bulk stress* $\boldsymbol{\sigma}_{\mathrm{B}}$, which is usually neglected in polymer physics since longitudinal deformation (extension and compression along the polymer chain, in a microscopic viewpoint) relaxes with a much faster speed than that of the transverse mode (shear deformation of tube in a language of reptation theory) [57]. They introduce the volume-fraction dependent bulk modules $G_{\mathrm{B}}(\phi)$ as $G_{\mathrm{B}} = G_{\mathrm{B}}^{0}\Theta(\phi - \phi_{\mathrm{r}})$ [*3] (Θ being the step function). Under the consti-

[*2] Except that, this system shows a various types of pattern formations that cannot be observed in ordinary binary mixtures such as moving droplet phase, fracture phase separation and so on [80]. We focus on the phase inversion here for the relevance of the topics discussed later.

[*3] We also need to consider the volume fraction dependence of shear modulus and relaxation time. See the original paper [88, 89] for this point.

tutive equation, they demonstrated that the bulk stress has a greater impact on the emergence of phase-inversion pattern than the shear stress. This argument has been supported by other numerical studies afterward [90, 91].

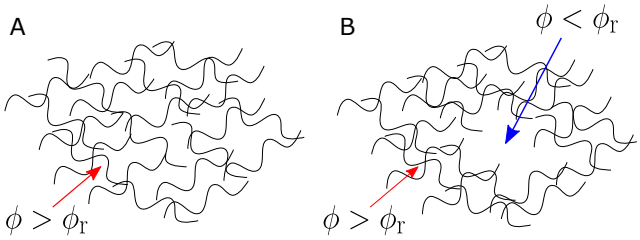

Fig. 2.6 Illustrative figure for the expression of bulk modulus $G_B = G_B^0 \Theta(\phi - \phi_r)$. In the early stage of phase separation, a transient gel with almost uniform concentration is formed (**A**) and later it becomes inhomogeneous by volume shrinking (**B**).

In [80, 89], they describe the physical origin of this term as rupture of transient gel [*4]. In Fig. 2.6, we show a schematic figure for a transient gel. In the early stage of phase separation, a transient gel with almost uniform composition is formed (Fig. 2.6A). After that, spacial heterogeneity in the composition is induced toward the equilibrium composition. In this process, as described in the above, volume shrinking of the polymer-rich phase (by squeezing out of the solvent from the polymer-rich phase) takes place. In order to increase the local polymer composition at a certain position, we need to break a transient network of polymers, which is expected to emerge as slow stress relaxation after coarse-graining. Of course, this viscoelastic effect does not play a role in a region sufficiently dilute polymer composition (i.e., $\phi < \phi_r$, see Fig. 2.6B), where there is no connectively of polymers. This is why the composition dependence is introduced by a step-like function. We note that there has not been no microscopic derivation of the bulk stress, and it is an open question how to rationalize this concept on a microscopic basis.

Dynamic asymmetry and universality of viscoelastic phase separation

In the above, we have seen that the condition that mechanical stress (especially, bulk stress) selectively acts on one phase (i.e., stress division) is essential in viscoelastic phase separation. This in turn implies the possibility that viscoelastic phase separation universally takes place as long as the above condition is satisfied. Such a situation is expected to be realized by just mixing the different liquids whose structural relaxation times are drastically different. In other words, we can expect that mixtures of liquids with large *dynamic asymmetry* belong to the class of viscoelastic phase separation [81, 82].

Indeed, it has been demonstrated that two-component polymer blends under the situation where temperature is set to be inbetween the glass transition tempera-

[*4] Note that "transient gel" mentioned here means network-like topology in a *microscopic scale* as in a network structure of a polymer gel (not the macroscopic network structure that we can see in Fig. 2.6)

tures of the two components [92] shows the pattern formation process as Fig. 2.5. Furthermore, the similar pattern formation is widely observed in phase separation of various complex fluids such as emulsions [93], colloids [94, 9] and proteins [11].

Clarifying whether colloidal phase separation belongs to the same dynamical class of viscoelastic phase separation of polymer solutions and if not, what is the the similarity and difference between them, is one of the main aims of our study.

2.2.3 Colloidal phase separation

Colloidal suspensions can be classified into two categories depending on the interaction among colloids. One is the case where colloids stick each other by chemical bonds. Aggregation kinetics under such irreversible interactions (especially in dilute suspensions) is rather well-understood by growth of fractal-like clusters [95, 14]. The other case is the systems where colloids aggregate by reversible (physical) interactions, whose ordering dynamics is the subject of our study.

Colloidal self-assembly processes under physical interactions are triggered by phase separation in most cases. However, in colloidal suspensions, unlike ordinary binary mixtures and polymer solutions, there is no common consensus regarding how the composition fluctuation grows and decays, or how the rheological behavior is expressed. For this reason, there has been no well-established framework (or, a coarse grained model) for colloidal phase separation. Thus, in this section, we provide an overview of a part of recent experimental and numerical results.

Effect of attraction range

Kinetic pathway of colloidal phase separation depends on the range of intercolloid attractions Δ. In Sec. 1.3.2, we have seen the case of colloid-polymer mixtures and found that the topology of the equilibrium phase diagram is significantly influenced by Δ. Such a change in thermodynamically stable states as a function of Δ is not limited to depletion interaction. We can find the similar Δ dependence in systems with other types of interactions (see, e.g., [36]).

The remarkable points for the attraction-range dependence of the phase diagram may be the following two cases: one important value is $\Delta \sim 0.3$: for $\Delta \lesssim 0.3$, the gas-liquid coexistence region (including the critical point) is hidden beneath the liquid-crystal coexistence region [21]. The other is $\Delta \lesssim 0.1$. In this region, the phase diagram is known to be almost independent of the details of the potential (i.e., sticky hard sphere limit) [40, 42]. As will be mentioned later, for a sufficiently short range attraction, the attractive glass transition line also plays an important role in determination of the stable states (including nonequilibrium states).

It has been also reported that the attraction range significantly affects the morphology of aggregates. Lu, et al [96] experimentally studied how the attraction range affects the morphology of aggregates. Figure 2.7 shows the confocal images of colloidal clusters with different attraction ranges, where we can see the more elongated and ramified structures for small Δ whereas more compact and spherical structures for large Δ. The formation of anisotropic clusters for small Δ has been supported by simulation studies [41, 97].

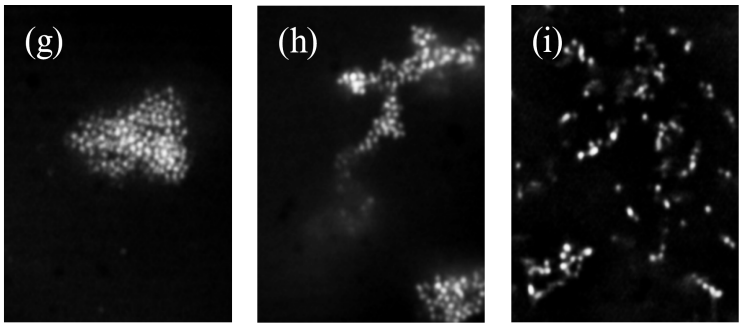

Fig. 2.7 The attraction-range (Δ) dependence of aggregates in colloid-polymer mixtures [96]. The images are obtained by confocal microscopy. (g), (h), (i) correspond to $\Delta = 0.11$, 0.04, and 0.02 respectively. The volume fraction is commonly set as $\phi \sim 0.04$. See the original paper for the interaction strength.

Percolation

Whether colloidal aggregates have connected-network or disconnected-cluster structures has a strong impact on the macroscopic physical properties such as elastic, transport, and surface properties [98]. Thus, revealing the mechanism of percolation is one of the important issues.

When a suspension is dense enough ($\phi \gtrsim 0.2$, for example), particles can form a structure percolating transiently even in a single liquid phase [99, 100]. From this, we can expect that it is possible to produce network-like aggregates by quenching such a percolated liquid into the liquid-gas coexistence region. However, network structures have been observed experimentally even in a much more dilute region ($\phi \gtrsim 0.05$) than the expectation from this argument (see, e.g., [42, 101]).

Regarding this, a role of hydrodynamic interactions (HI) has been pointed out recently. Furukawa and Tanaka [43] found that colloids tend to form more elongated aggregates upon phase separation in simulations with HI than those without (see Fig 2.8), which further affects whether the system forms a percolated-network or a disconnected-cluster pattern upon phase separation. This trend has been confirmed by various simulation methods later [44, 45, 46, 102]. However, a specific role of HI in percolation is not so clear for now. In the above work, Furukawa and Tanaka mentioned that squeezing of a solvent accompanied by aggregation of colloids (in other ward, many-body short-range HI) is responsible for the formation of elongated aggregates. Later, the importance of long-range HI for percolation is also confirmed by Varga et al. [46]. Specifically, in this work, the border between cluster and network formations was compared between experiments and simulations with long-range HI (Rotne-Prager-Yamakawa tensor) and a relatively good agreement was observed [46].

Besides HI, as mentioned in the last section, the range of intercolloid attraction is also important for the formation of elongated clusters and percolation. For example, according to a numerical study by Griffiths et al, percolation takes places at $\phi = 0.015$ in the case of very short-range attraction $\Delta = 0.04$.

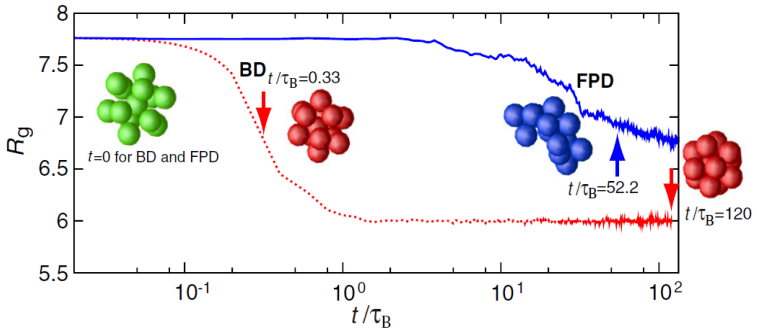

Fig. 2.8 The time evolution of the gyration radius R_g of 13 particles, which are initially at vertices of a regular icosahedron with the edge length 8.08. FPD and BD correspond to the results by simulation with HI and without [43]. The similar test is performed in other hydrodynamic models later [103, 104].

Gelation resulting from dynamic arrest of spinodal decomposition

Network-like structures formed during phase separation process are sometimes retained over an experimental time scale. This indicates that such a formation of physical gel (or, gelation [*5]) results from freezing of phase separation dynamics. Revealing the physical origins of dynamic arrest is one of the central issues.

The vitrification of the colloid-rich phase is viewed as one of the most promising scenarios [105, 14, 42]. Slow dynamics of supercooled liquids are mostly triggered by steric hindrance among particles and the effect of attraction is considered to play a rather minor role in dense systems. However, it turned out by analysis based on Mode Coupling Theory that when the attraction is sufficiently strong and short-range another type of glassy states induced by attractive interaction appears, which is called as attractive glass [106]. A numerical study has shown that the attractive glass line obtained by this theory goes across the gas-liquid spinodal line [107]. From this, we can expect that in a phase separation process, the volume fraction inside of colloid-rich phase reaches to the glass transition point, leading to dramatic slowing down of phase separation dynamics (see Fig. 2.9A). This mechanism is supported by experimental [108, 42] and numerical [109, 110] studies.

The above mechanism is the case when the characteristic size of the domain ℓ is sufficiently larger than the particle size σ, since the glass transition is a concept in bulk [110]. On the other hand, we can find the experimental studies reporting the gel structures with $\ell/\sigma = \mathcal{O}(1)$. Hence it is questionable whether we can apply the idea of glass transition to such a "thin" gel (see Fig. 2.9B). Locally Favored Structure (LFS) is known as a scenario to explain the formation mechanism of thin gels. LFS is the energetically most stable structures that a small number of particles form. For example, icosahedral structure is the LFS for 13 particles. The importance of LFS for gelation has been first pointed out by Royall et al, and LFS

[*5] In this thesis, we suppose that "gel" means a network structure where coarsening is arrested. We do NOT call a network structure still in coarsening regime as "gel".

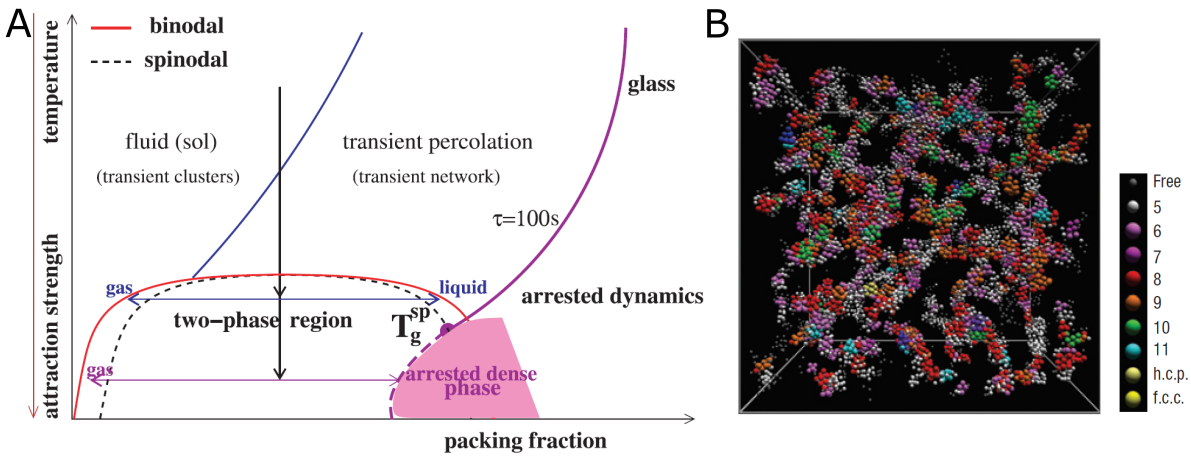

Fig. 2.9 **A** Schematic picture of dynamic arrest due to attractive glass transition. [14]. **B** Colloidal gel with thin arms [101].

is now recognized as one direction to explain the physical origins of slow dynamics in colloidal gel [111, 101].

As the other scenarios regarding gelation due to dynamic arrest, we refer to those based on jamming transition [112] and rigidity percolation [113, 114]. We also mention that the gels where the inner structure is crystallized are reported [115, 116] and there is the issue of what is the difference between attractive glasses and gels with very high volume fractions [117]. When we say physical gels, they have a wide variety of structures and there can be different mechanisms of dynamic arrest for different gels. Such a classification of the gelation mechanisms is still in developing.

We finally stress again that our interest in the thesis lies not in the physical properties of gel or mechanism of gelation, but rather in *phase separation dynamics* of colloidal suspensions.

Coarsening

One of the aims of our study is to reveal the role of dynamic coupling between colloids and solvent during a phase separation process. Therefore, investigating the coarsening mechanism of colloidal phase separation is a central issue in this thesis. Here, we briefly review the experimental results [*6] on the coarsening process, particularly focusing on what kind of growth exponents have been observed under what circumstances.

As an early work, we first refer to a small angle light scattering (SALS) experiment performed by Poon et al. [120]. They observed the spinodal decomposition of colloids interacting with short-range attraction ($\Delta \sim 0.10$) under a shallow quench,

[*6] In numerical studies, various values of the growth exponent have been reported depending on simulation methods (see [118, 43, 119], for example). However, we do not dwell into this issue here, because it requires in-depth discussion about the difference in various numerical models, which is beyond the scope of the thesis.

and found that the domain size increases with the growth exponent of $\alpha \sim 1/4$ and 1 for short and long time windows. The growth exponent $\alpha = 1$ known for the coarsening of a bicontinous fluid structure has also been reported by recent studies: food colloids (casein micelles, $\Delta \sim 2$) [121] and silicon-oil droplets [122] ($\Delta \sim 0.5$). This coarsening law is considered to belong to Siggia's hydrodynamic mechanism. Verhaegh et al. also performed SALS for a colloidal suspension with long-range attraction $\Delta \sim 1.0$ [123] and observed $\alpha \sim 1/3$ under shallow quench. From this, they thought that the coarsening is dominated by the Brownian coagulation mechanism [*7].

On the other hand, Bailey et al. [10] studied phase separation in a *deeply quenched* colloidal suspension ($\Delta \sim 0.6$) under microgravity and successfully observed the coarsening of a bicontinuous structure more than 5 decades in time. The short-time behavior determined by SALS shows $\alpha \sim 1/2$ and the long time behavior observed by direct imaging shows $\alpha \sim 1$. The similar exponent $\alpha \sim 1/2$ in network-forming phase separation under deep quench has been reported in polystyrene colloid [9], protein (lysozyme) solution [11] and lyotropic liquid crystal [125]).

From the above, the coarsening process under shallow quench can be explained by an analogy of the one in ordinary binary liquid mixtures. On the other hand, for the coarsening process under deep quench, the growth exponent $\alpha \sim 1/2$ has been reported and there has so far been no theoretical explanation for this coarsening law. In such a deeply quenched case, it is expected that the rheological behavior of colloidal suspension may play a crucial role in phase separation. This implies the necessity of a new description of phase separation dynamics beyond model H, focusing on viscoelastic characteristics of colloids.

2.3 Crystallization kinetics of hard-sphere colloids

To clarify the impact of a hydrodynamic degree of freedom of solvent on the crystallization kinetic of colloids is the second subject of this thesis. In this section, we provide a brief overview of this phenomenon. We first explain the Classical Nucleation Theory (CNT), which is one of the most fundamental phenomenological theory to generally describe a homogenous nucleation process. Then we introduce a kinetic equation for a nucleation process called as the Becker-Döring equation. Finally, we review recent studies regarding the microscopic kinetics of crystallization and explain what is the central issue in this phenomenon.

2.3.1 Classical Nucleation Theory

The energy cost to form a nucleus consisting of n particles in the metastable bulk phase, whose pressure and chemical potential are p and μ respectively, is given as

[*7] In this paper, it is also reported that the growth rate observed in a linear regime shows the completely different functional from one predicted in binary mixture of simple liquid (see Eq. 2.7). Later Tanaka revealed that the data can be fitted by the growth rate of a two fluid model (see Eq. 2.31) [124].

[126],

$$\Delta F = \gamma A + (p - p')V' + n[\mu'(T, p') - \mu(T, p)], \tag{2.33}$$

where A is the interfacial area between the bulk phase and the nucleus, V' is the nucleus's volume, p' and μ' are the pressure and the chemical potential inside the nucleus, and γ is the surface tension. By expanding μ' by $p' - p$

$$\mu'(T, p') - \mu'(T, p) \simeq \left(\frac{\partial \mu'}{\partial p'}\right)_T (p' - p) = v'(p' - p) \tag{2.34}$$

where $v' = V'/n$. This is a good approximation when the nucleus is incompressible (or, when v' is hardly dependent on the change of p'). As a result, we obtain

$$\Delta F = \gamma A + n\Delta\mu, \tag{2.35}$$

where $\Delta\mu = \mu'(T, p) - \mu(T, p) < 0$ is the difference in the chemical potential between the stable and the metastable states. Since the interfacial area should be proportional to $n^{2/3}$ we denote $A = a(nv')^{2/3}$ (a is a constant which depends on the morphology of the nucleus) and then we can rewrite the above relation as

$$\Delta F = |\Delta\mu| n^{2/3} (\frac{3}{2} n_{\rm c}^{1/3} - n^{1/3}), \tag{2.36}$$

where $n_{\rm c} = (2av'^{2/3}\gamma/3|\Delta\mu|)^3$ is the critical nucleus size and ΔF takes a maximum value at $n = n_{\rm c}$. When this energy barrier $\Delta F(n_{\rm c})$ is sufficiently larger than the thermal energy $k_{\rm B}T$, the metastable phase is retained for a long time, but once n exceeds $n_{\rm c}$ the nucleus spontaneously starts to grow and the stable phase eventually covers the whole system. Denoting the rate to form such a nucleus larger than the critical size as I and assuming that the critical-size dependence of I is determined by the Boltzmann weight, we can obtain the following formula for the nucleation rate:

$$I = I_0 \exp\left[-\beta \Delta F(n_{\rm c})\right], \tag{2.37}$$

where I_0 is a constant, which can be determined by the kinetic theory.

In the case where the nucleus has a spherical shape, choosing the radius of the droplet R as the key parameter instead of n, we can rewrite Eq 2.35 as

$$\Delta F = 4\pi R^2 \gamma - \frac{4\pi}{3} R^3 \rho' |\Delta\mu|, \tag{2.38}$$

where $\rho' = 1/v'$. Then the radius of the critical nucleus is expressed as $R_{\rm c} = 2\gamma/\rho'|\Delta\mu|$.

2.3.2 Derivation of nucleation rate from a kinetic theory

In this section, we explain how the kinetic factor of the nucleation rate (I_0 in Eq. 2.37) can be determined. There are several ways for the derivation [5], but here we employ an approach based on the Becker-Döring equation.

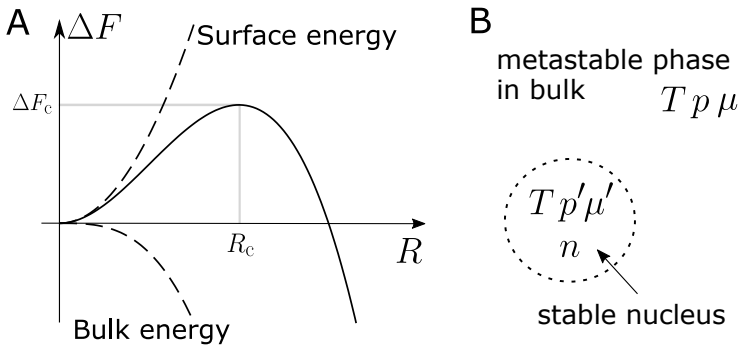

Fig. 2.10 **A**. The functional profile of the free energy in the Classical Nucleation Theory. **B**. Formation of a stable nucleus in the bulk of the metasbale phase.

First we denote the density of nucleus with n particles as $\rho(n,t)$ and assume that the time evolution of $\rho(n,t)$ obeys the following master equation:

$$\frac{\partial}{\partial t}\rho(n,t) = f_+(n-1)\rho(n-1,t) - f_-(n)\rho(n,t) - f_+(n)\rho(n,t) + f_-(n+1)\rho(n+1,t), \tag{2.39}$$

where $f_+(n)$ and $f_-(n)$ are the transition rates that a nucleus of n particles gains or loses a particle, respectively. For this process, we assume the detailed balance:

$$f_+(n-1)\rho_0(n-1) = f_-(n)\rho_0(n), \tag{2.40}$$

where $\rho_0(n)$ is the density of nucleus of n particles in the vicinity of metastable state and determined by the Boltzmann weight, i.e., $\rho_0(n) = \rho_0(1)\exp\left(-\beta\Delta F(n)\right)$. $\rho_0(1)$ is equivalent to the density of metastable liquid ρ'. f_- in Eq. 2.39 can be erased by using Eq. 2.40. By serializing n for the resulting equation, we obtain the following Fokker-Plank equation:

$$\frac{\partial}{\partial t}\rho(n,t) = \frac{\partial}{\partial n}\left[f_+(n)\rho_0(n)\left(\frac{\partial}{\partial n}\frac{\rho(n,t)}{\rho_0(n)}\right)\right]. \tag{2.41}$$

Denoting the density in a steady state as $\rho_{\rm s}(n)$, the steady flux of the above equation is $I \equiv -f_+(n)\rho_0\partial_n[\rho_{\rm s}(n)/\rho_0(n)]$ (= const.). Then, the formal solution of ρ_s is

$$\rho_{\rm s}(n) = I\rho_0(n)\int_{n'}^{\infty}\frac{dn'}{f_+(n')\rho_0(n')}. \tag{2.42}$$

Since $\rho_{\rm s}(n) \to \rho_0(n)$ for $n \to 0$, the above relation becomes

$$I = \left[\int_0^{\infty}\frac{dn}{f_+(n)\rho_0(n)}\right]^{-1}. \tag{2.43}$$

Since ΔF has a sharp peak around $n \sim n_c$, we can use the saddle point analysis for the above integral, and the result is

$$I = Z f_+(n_c)\rho' \exp\left[-\beta \Delta F(n_c)\right], \tag{2.44}$$

where $Z = \sqrt{\beta|\Delta F''(n_c)|/2\pi}$ is the so-called Zeldovich constant ($\Delta F''$ being the second derivative of ΔF).

To compute the nucleation rate, we need to know $\Delta F(n_c)$, $\Delta F''(n_c)$ and $f_+(n_c)$. In numerical simulations, $\Delta F(n)$ can be determined by the Umbrella Sampling method. On the other hand, $f_+(n_c)$ can be measured as follows. First we introduce the Langevin equation corresponding to Eq. 2.41,

$$\frac{\partial}{\partial t} n(t) = -f_+(n) \frac{\partial}{\partial n}(\beta \Delta F) + \theta(n,t), \tag{2.45}$$

where θ is the thermal noise satisfying $\langle \theta(n,t)\theta(n,t')\rangle = 2f_+(n)\delta(t-t')$. Here, considering the time evolution of nuclei whose size is initially $n(0) = n_c$, $n(t)$ for a short time follows $\partial_t n \sim \theta(n_c, t)$ since $\partial_n(\beta\Delta F) \sim 0$ for $n \sim n_c$. Thus, the mean square displacement of n satisfies the following relation [127, 128]:

$$\langle |n(t) - n_c|^2 \rangle \sim 2 f_+(n_c) t, \tag{2.46}$$

From this relation. we can measure $f_+(n_c)$ by tracking the microscopic change of a nucleus near the critical size. This procedure allow us to determine the nucleation rate without any adjustable parameters [127, 128].

2.3.3 Crystallization of hard-sphere colloids

Characterization of the nucleation frequency is one of the most important issues in material sciences ranging from metallic materials, pharmaceuticals, to foods. However, although one may say that phenomenological theory such as CNT qualitatively captures the trend of crystallizations, no common consensus regarding the general understanding of this phenomenon has yet been reached [6, 129]. To develop a better understanding, the studies based on the microscopic pathway of particles in the crystallization process have been actively performed recently. Colloidal suspensions have aroused great interest in this context, since it is an experimental system that shows the same thermodynamical behavior as atomic systems but can be observed with optical microscopy in a single-particle resolution, which is impossible in atomic systems [130]. Among them, hard-sphere colloids have been intensively studied as one of the most fundamental systems which show a liquid-crystal transition. In 2001, Auer and Frenkel pointed out [127] a huge mismatch in the crystal nucleation rate between light scattering experiments and numerical prediction based on Umbrella Sampling method (see Fig. 2.10). Revealing what is the physical origin behind this huge discrepancy is one of the central issues in this field [6, 129].

The huge discrepancy in the nucleation rate between experiments and simulations implies the possibility that there exist any unexpected nucleation pathway that efficiently form large nucleus. For example, unlike the assumption of CNT, a three-dimensional observation by confocal microscopy reports that nucleus with critical

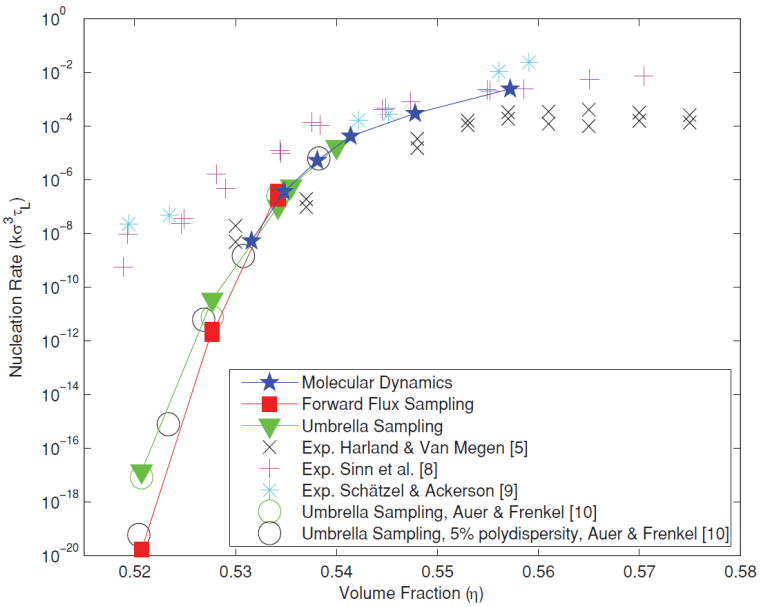

Fig. 2.11 Comparison of the crystal nucleation rate in hard-sphere colloids between experiments and simulations [131]. Here we can see in both experiments and simulations that the nucleation rate dramatically decreases as the volume fraction of colloids ϕ decreases. However, the decreasing tendency is much stronger in simulations. For example, at $\phi = 52\%$, we can see that the degree of the mismatch between experiments and simulations reaches more than 8 orders of magnitude.

size have nonspherical shape on average [132]. Also a simulation study [133] claims that it is important to consider the morphology of the crystal nucleus and the type of crystal structures in the nucleus.

Furthermore, the emergence of dense precursors has been pointed out by light-scattering experiment [134] and interpreted as the indication of translational ordering (or, density increase), which was claimed to be confirmed by numerical simulation of a hard-sphere system [135]. However, this scenario was challenged by numerical simulations of the same hard sphere system [136, 137]. The issue here is whether precursors have translational order signalled by an increase in density [135] or have only orientational order without any density change [136, 137]. The latter scenario emerges from the structural formation in a metastable supercooled state of a glass-forming system [138, 139], for which it is natural to assume that there is no development of translational order. Later this scenario was confirmed for hard spheres [140] and soft spheres [141]. Furthermore, these studies showed that crystalline polymorphs are also selected by the symmetry of precursors (see also a review [129]). It has recently confirmed also by experiments of charged colloidal systems [142, 143] that particles with high orientational order rather than translational order (or density) act as precursors of crystal nucleus by charged colloids.

Besides that, the effects of the non-ideal features in experiments such as polydispersity of size of colloids [144], gravity (or, density mismatch between colloids and

a solvent) [145, 146] have been pointed out.

On the other hand, there is a potentially important effect that most of the simulation methods have neglected: hydrodynamic degrees of solvent. Indeed, as far as we know, simulation studies that take the hydrodynamic interactions (HI) among colloids are limited to the following two cases. One is a work by Radu and Schilling [147], where they examined the effect of HI by Multiple Particle Collision Dynamics. They obtained the result that simulations with larger viscosity shows a larger nucleation rate and concluded that HI may speed up nucleation. The other is a numerical study on crystal growth by Roehm, et al., using Fluctuating Lattice Boltzmann method, where they reported that HI slows down the speed of crystallization [148]. These results seem conflicting and further investigations are necessary. We note that examining such an effect is crucial not only for crystallization of hard-sphere systems but also for fundamental understanding of the kinetics of the systems where crystallization proceeds in a liquid such as protein solutions.

Chapter 3

Experimental method

3.1 Experimental method

3.1.1 Three-dimensional observation by confocal microscopy

To capture the precise positions of colloids in three-dimensional (3D) space, we use a confocal laser scanning microscopy (Leica SP5). This method allows us to measure the intensity of a specific fluoresce light only from a point only on a focal plane, which is realized by rejecting off-focal lights from other locations by a spatial optical pinhole. The sample stage can be scanned along the z(optical)-axis by a piezo device and the focus point can be scanned on the xy plane by a mirror. Thus, we can obtain a stack of two-dimensional images on the xy planes along z-axis in a rather short time. So, if we use rather large-size colloidal particles, we are able to take a 3D image of a colloidal suspension before colloidal particles move via Brownian motion. This method also allows to follow dynamical evolution of 3D structures of colloidal suspensions with a particle-level resolution, typically with a time resolution less than $\sim$ 30 s. From a confocal microscopy image, we can reconstruct the three-dimensional structures of the samples with a microscopic resolution by extracting the center-of-mass positions of all colloidal particles. We used the algorism in Ref. [149] to make such 3D reconstruction from a confocal microscopy image.

3.1.2 Samples

In our experiments, we prepared two different sizes of poly methyl methacrylate (PMMA) colloids sterically stabilized with polyhydroxyl steric acids and labelled with fluorescent dye (rhodamine). See Appendix A for synthesis method for PMMA paritlces. The average diameter of colloids are $\sigma = 1.9$ μm (EXP1) and 2.9 μm (EXP2), and both have approximately 3% size polydispersity.

To closely match the density and refractive index of colloids with those of a solvent, we used a mixture of cis-decalin and cyclohexyl bromide (CHB) as the solvent. Because of the nearly perfect refractive index matching, the van der Waals interaction between colloids can be safely neglected. We regarded the samples as density matched when we cannot see sediment or float of colloids after 10 min of

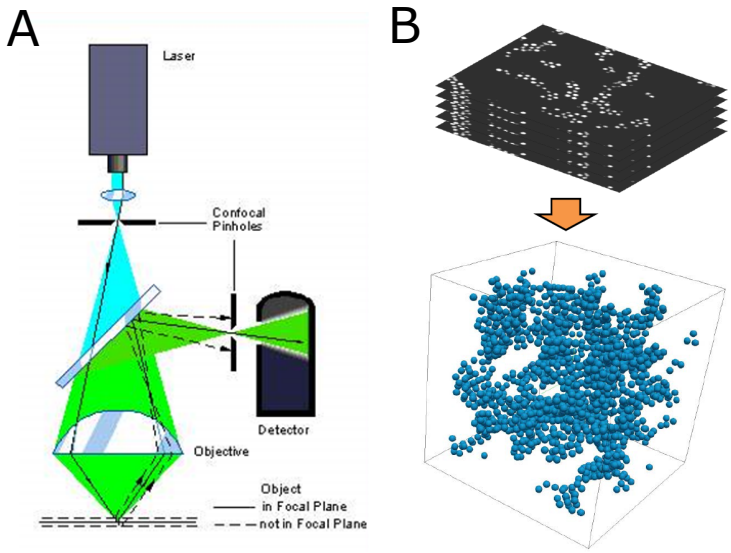

Fig. 3.1 **A.** Schematic figure of the principle of confocal microscopy (http://www.nhm.ac.uk). **B.** 3D reconstruction from a confocal image

centrifuge with 10,000 rpm. In the matching point, the weight fraction of CHB was roughly 74%. It is known that CHB absorbs moisture as an impurity in contact with air, which is expected to lead to the loss of stability of the ion concentration in CHB. In order to avoid this effect, we purified CHB by mixing calcium chloride for 1 hour and then filtering it out. We also cleaned cis-decalin with aluminium oxide. Preparation of samples and sealing them into the cells were performed in a glove box filled with dry nitrogen. The Debye screening length in the mixture was approximately 2 μm. We determined it by first measuring the radial distribution function $g(r)$ of a dilute colloidal suspension (0.5% volume fraction) by confocal microscopy, and then by comparing the interaction potential $u(r)$ obtained from the relation $u(r) \sim k_{\mathrm{B}}T \log g(r)$ with the Yukawa potenital [26]. PMMA has charges in the mixture of CHB and cis-decalin, which were determined as 210 e for EXP1 and 350 e for EXP2, by performing electrophoresis following Ref. [150, 151]. We controlled the Debye screening length of the electric repulsion by adding a salt (tetra-butylammonium bromide: TBAB).

In order to induce short-range attractive interactions between colloids (depletion interactions [20, 21]), we dissolved polystyrene with a molecular weight of 8.4×10^6 Da for EXP1 and 2.0×10^7 Da for EXP2. The gyration radius of the polymer in the solvent is estimated as $R_{\mathrm{g}} \cong 120$ nm in EXP1 and $R_{\mathrm{g}} = 180$ nm in EXP2. Thus, the characteristic range of the depletion interaction, $\Delta = 2R_{\mathrm{g}}/\sigma$, is approximately 0.13 for both EXP1 and EXP2, which can be regarded to be short-range. The concentration of the polymer, C_{p}, is used as a control parameter to change the strength of the attraction between colloids, or the depth of the potential, $\beta\epsilon$. The polymer concentration, C_{p}, also changes the viscosity of the solvent, which affects the Brownian time of colloids. Thus, we measured the viscosity of the solution of the polymer in the closely matched solvent at $T = 26$ °C by rheometer and obtained

the relation: $\eta = 2.25 + 2.7C_{\rm p}$ for EXP1 and $2.25 + 4.8C_{\rm p}$ for EXP2 (here the units of η and $C_{\rm p}$ are g/L and mPa.s respectively).

We set different scanned box sizes depending on samples, which are summarize in Table 3.1.

Sample	σ	$\tau_{\rm B}$	Q	L^3	Δt
EXP1	1.9 μm	2.3 s	210 e	$107^3\mu{\rm m}^3$	24.8 s
EXP2	2.9 μm	7.1 s	350 e	$145^3\mu{\rm m}^3$	18.2 s

Table 3.1 **Properties of samples and settings of confocal observation.** σ: the diameter of colloids; $\tau_{\rm B}$: the Brownian time of a free colloidal particle; Q: the average number of surface charges of colloids per particle; L^3: the size of the scanned box; Δt: the time resolution for a 3D image acquisition. Here we show τ_B in $C_{\rm p} = 0.50$ g/L for EXP1, and that in $C_{\rm p} = 0.30$ g/L for EXP2. The temperature is commonly 26 °C in both experiments. The pixel resolutions of images are 0.21 μm for EXP1 and 0.38 μm for EXP2.

3.1.3 Initiation of phase demixing by salt injection

In order to observe the aggregation process of colloids from the very beginning without any perturbation by mixing flow, we used the following special protocol. As mentioned in the main text, the control parameters of our experiment are the volume fraction of colloids ϕ and the effective temperature $\beta\epsilon$. Since the temperature change results in the mismatch of the density and refractive index between the colloids and the solvent, we need to change either ϕ or the polymer concentration $C_{\rm p}$ to initiate phase demixing. However, it is almost impossible to change these quantities rapidly. Thus, we used a unique method to change the Debye screening length of electrostatic repulsions of colloids by salt injection [9]. We contact our sample cell, whose volume is roughly 8 mm×5 mm×100σ, with a reservoir cell, whose volume is about 500 times larger than the sample cell for observation, through a membrane filter (Fig. 3.2). Since the pore size of the membrane filter used is roughly 0.1 μm (Wahtman Anodisc 47), we expect that components in the sample except for colloids (solvent molecules, salt ions, and polymers) can pass through the filter. Thus, by loading a solvent different from that in the sample, we can quickly change the physical state of the sample since the salt diffusion takes place much faster than colloid phase separation.

First we insert a colloidal suspension together with polymers into the sample cell. In this condition, direct contacts between colloids are hardly observed due to long-range Coulomb repulsions (Fig. 3.3A). Then we insert a solvent saturated with salt (TBAB) into the reservoir cell. Just after the contact of the two cells, salt ions are gently injected to the sample cell by diffusion and screen the electric repulsions, which allows us to bring the sample from a stable one-phase state (Fig. 3.3A) to an unstable two-phase state (Fig. 3.3B). Once the electrostatic interaction is screened by salt injection, the depletion attractions by polymers become dominant in the interactions between colloids. If the quench is deep enough, colloids start

to aggregate due to the attractive interaction (Fig. 3.3C-E). Note that the solution used for salt injection contains colloids and the same concentration of polymers as in the sample cell with density and refractive index matching (in Fig. 3.2 we do not draw colloids and polymers in the reservoir cell just for simplicity). This unique protocol allows us to avoid harmful macroscopic perturbations on the system such as hydrodynamic flow and mechanical vibrations, upon the initiation of demixing.

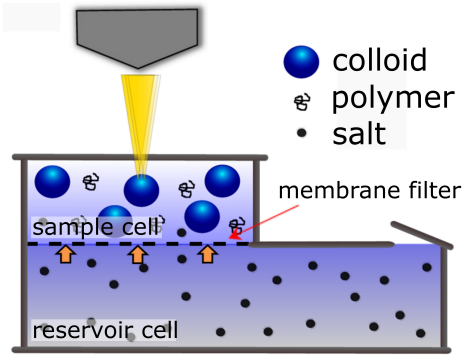

Fig. 3.2 **Schematic figure of the cell used in our experiments.** The cell is composed of the sample cell and the reservoir cell separated by a membrane filter. In this image, we do not draw colloids and polymers in the reservoir cell just for simplicity.

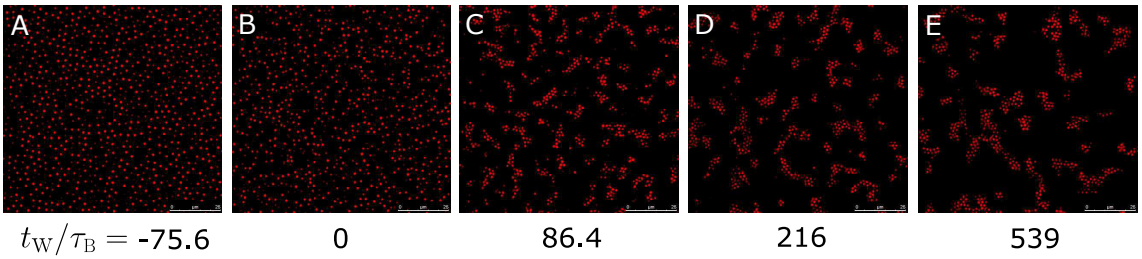

Fig. 3.3 **A process of colloidal phase separation.** Here we show examples of 2D confocal images in EXP1 at the polymer concentration, $C_p = 0.50$ g/L, and the volume fraction, $\phi \sim 10$ % at various scaled times t_w/τ_B (τ_B is the Brownian time). In this sample, a kinetically arrested network structure (gel) is seen at the end of the observation $t_w/\tau_B \sim 500$. The length of the side of the images corresponds to 107 μm.

3.1.4 Definition of the onset of demixing

Here we explain how we separate the screening process of the electrostatic repulsion and the aggregation process in an unambiguous manner. To evaluate the validity of our method quantitatively, we now show in Fig. 3.4 the temporal change of the radial distribution function $g(r)$ (r: distance) in EXP1 for a condition ($C_p = 0.50$ g/L, $\phi \sim 10\%$). In the very beginning of observation, we can see that the position

of the first peak of $g(r)$ shifts and approaches $r/\sigma = 1$. This is the screening process of the electric repulsion induced by the salt injection. After this process, we see that the height of the first peak begins to grow. In this work, we define the onset time of the aggregation of colloids, $t_{\rm w} = 0$, as the time when the first peak of the radial distribution function starts to grow rapidly. To confirm the reproducibility of our method, we show the results of three different runs in Fig. 3.4. We confirm that by using the onset time defined above, the radial distribution functions of the three independent runs can be overlapped almost perfectly. The slight mismatch may be due to the finite time resolution of our 3D scan ($\sim 10.8\tau_{\rm B}$).

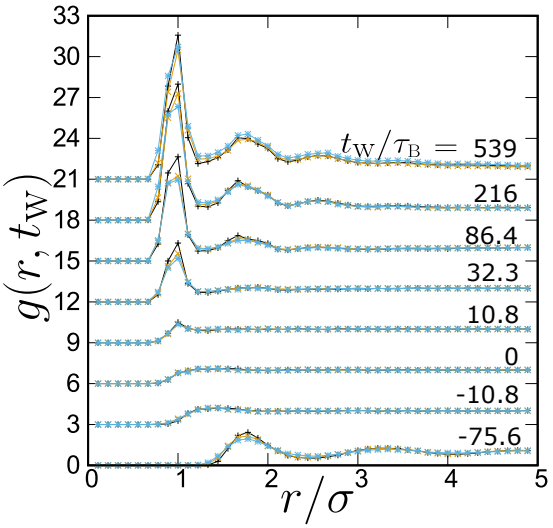

Fig. 3.4 **Temporal change of the radial distribution function** $g(r, t_{\rm w})$. The result is for a sample in EXP1 of $C_{\rm p} = 0.50$ g/L and $\phi \sim 10\%$. Three colors correspond to three independent observations. The agreement of the three results show reproducibility of our measurements.

3.1.5 Analysis of the temporal growth of the scattering function during demixing

We calculate the scattering function $S(q, t_{\rm w})$ from the 3D power spectrum of the density correlation function as $S(\boldsymbol{q}, t_{\rm w}) = \rho_{\boldsymbol{q}}(t_{\rm w})\rho_{-\boldsymbol{q}}(t_{\rm w})/N$. Here the density field is defined as $\rho(\boldsymbol{r}, t_{\rm w}) = \frac{6}{\pi\sigma^3}\sum_n \Theta(\sigma/2 - |\boldsymbol{r} - \boldsymbol{R}_n(t_{\rm w})|)$, where Θ is the step function and $\{\boldsymbol{R}_n\}$ is the set of the center-of-mass positions of colloids.

To analyse the temporal change of $S(q, t_{\rm w})$ during phase separation, we calculate the growth rate of composition fluctuations at wave number q as $R(q, t_{\rm w}) = \frac{\tau_{\rm B}}{2t_{\rm w}}\log(S(q, t_{\rm w})/S(q, 0))$. In Fig. 3.5A, we show its temporal change. We can see that $R(q, t_{\rm w})$ shows little change in the early stage ($t_{\rm w} < 100\tau_{\rm B}$). At $t_{\rm w}/\tau_{\rm B} = 10.8$, $R(q, t_{\rm w})$ looks quite noisy simply because $R(q, t_{\rm w})$ at early times is sensitive to the noise in $S(q, 0)$. When $R(q, t_{\rm w})$ is independent of time, i.e., $R(q) \equiv R(q, t_{\rm w})$, we can have the following relation: $S(q, t_{\rm w}) = S(q; 0)\exp(2tR(q)/\tau_{\rm B})$ ($R(q)$: the growth rate), which is known to be valid for Cahn's linear regime of spinodal de-

composition [5]. Such behavior can be seen in the early stage (see Fig. 3.5A). The presence of Cahn's linear regime in the early stage of aggregation can also be confirmed from the exponential growth behavior of the peak (or integrated) intensity, $I(t_{\rm w}) = \int d(q\sigma/2\pi) S(q, t_{\rm w})$ (see the inset in Fig. 3.5A).

The temporal change in $S(q)$ is shown in Fig. 3.5B, where we can see the shift of the peak wave number to a smaller value as phase separation proceeds.

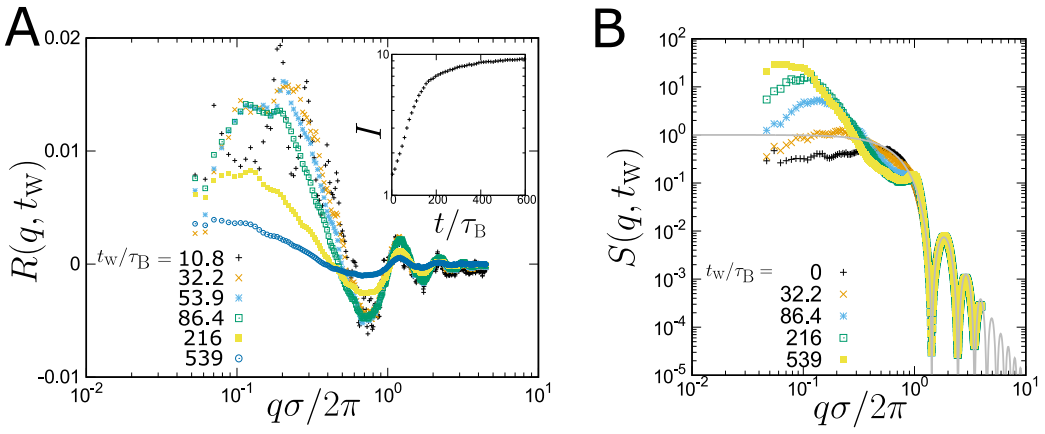

Fig. 3.5 **A**. Temporal change of the growth rate. The result is for a sample of $C_{\rm p} = 0.50$ g/L and $\phi \sim 10$ %. Inset: Temporal change of the intensity of composition fluctuations at the same state point. **B**. Temporal change of $S(q, t_{\rm w})$. The result is for a sample of $C_{\rm p} = 0.50$ g/L and $\phi \sim 10$ %. The gray line represents the form factor for a sphere whose radius is σ.

Chapter 4

Simulation method

Here we explain numerical simulation methods that we use in our study. To see how the hydrodynamic degrees of freedom affect colloidal dynamics, we use two different simulation methods: Brownian Dynamics (BD) method and Fluid Particle Dynamics (FPD) method. Since the former completely neglects the hydrodynamic interactions (HI) among colloids and the latter can incorporate HI, we can examine how HI affects colloidal dynamics.

4.1 Brownian dynamics method

In Brownian Dynamics (BD) simulations, we use the following Langevin equation, which describes the relation among the center-of-mass position, $\boldsymbol{R}_n(t)$, and the velocity, $\boldsymbol{V}_n(t)$, of particle n ($n = 0, 1, .., N-1$), and the force acting on particle n, $\boldsymbol{F}_n(t)$:

$$\frac{d\boldsymbol{R}_n(t)}{dt} = \boldsymbol{V}_n(t) = \zeta^{-1}(\boldsymbol{F}_n + \boldsymbol{F}_n^{\mathrm{R}}), \tag{4.1}$$

where ζ is the friction constant between colloids and the solvent. $\boldsymbol{F}_n^{\mathrm{R}}$ is the random thermal force acting on particle n, which satisfies the following fluctuation-dissipation relation:

$$\langle \boldsymbol{F}_n^{\mathrm{R}} \rangle = \boldsymbol{0}$$

and

$$\langle F_{ni}^{\mathrm{R}}(t) F_{mj}^{\mathrm{R}}(t') \rangle = 2k_{\mathrm{B}}T\zeta\delta_{nm}\delta_{ij}\delta(t-t').$$

In this simulation, we set the space unit as the colloid diameter σ and the time unit as $\tau = \sigma^2/D$ where D is the free diffusion constant of an isolated colloid: $D = k_{\mathrm{B}}T/\zeta$. The Brownian time in BD simulation is defined as $\tau_{\mathrm{B}} = (\frac{\sigma}{2})^2/6D$. The time step used is $\Delta t = 1.0 \times 10^{-5}\tau$.

4.2 Fluid particle dynamics method

In order to deal with the hydrodynamic degrees of freedom in colloidal suspensions by numerical simulation, we need to solve the moving boundary problem for all colloidal particles if we treat colloids as solids, since the (nonslip) solid-fluid

boundary condition should be satisfied on the surfaces of all colloid particles. The Fluid Particle Dynamics (FPD) method [7] treats a solid colloidal particle as an undeformable fluid particle, whose viscosity is much higher than the solvent viscosity and the viscosity changes smoothly across the colloid-solvent boundary. These features allow us to treat the dynamics of colloids with many-body hydrodynamic interactions simply by solving the Navier-Stokes equation in a Cartesian coordinate system without suffering from the solid-fluid boundary condition. We explain the detail of the simulation method here.

4.2.1 The fundamentals of FPD method

Basic set of equations

We express the center-of-mass position of particle n as $\boldsymbol{R}_n$. By introducing a phase field $\phi_n \in [0,1]$ as below, we distinguish whether the position $\boldsymbol{r}$ is inside ($\phi_n \sim 1$) or outside ($\phi_n \sim 0$) of the particle,

$$\phi_n(\boldsymbol{r}) = \frac{1}{2}\Big\{\tanh\Big[\frac{1}{\xi_n}(a_n - |\boldsymbol{r} - \boldsymbol{R}_n|)\Big] + 1\Big\}, \tag{4.2}$$

where a_n is a parameter to characterize the size (radius) of particle n and ξ_n is the interfacial thickness. See Fig. 4.1 for the functional form. Depending on $\phi = \sum_n \phi_n$, we define viscosity feild $\eta(\boldsymbol{r})$ as follows,

$$\eta(\boldsymbol{r}) = \eta_{\rm c}\phi(\boldsymbol{r}) + \eta_{\rm s}(1 - \phi(\boldsymbol{r})), \tag{4.3}$$

where $\eta_{\rm c}$ and $\eta_{\rm s}$ is the viscosity of the colloidal particles and the liquid in which colloids are suspended. Here the summation is taken over all N particles.

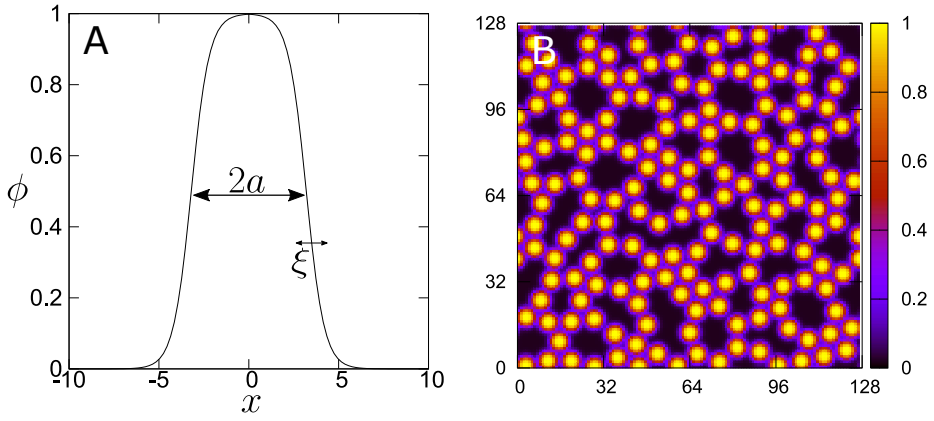

Fig. 4.1 **A.** The functional profile of $\phi(x) = \frac{1}{2}\{\tanh(\frac{a-|x|}{\xi}) + 1\}$. **B.** An example of ϕ in 2D. Here we set $a \equiv a_n = 3.2$ and $\xi \equiv \xi_n = 1.0$ for all n.

The key points of this method are that (i) the particle rigidity is approximately sustanined by large viscosity difference, $(\eta_{\rm c} - \eta_{\rm s})/\eta_{\rm s} \gg 1$, and (ii) a rigid solid-liquid boundary is replaced by a smooth interface with thickness ξ_n. When there is no other gross (or hydrodynamic) variable than the velocity field $\boldsymbol{v}(\boldsymbol{r})$, the dynamics of

colloidal particles with hydrodynamic interactions can be approximately described by solving the Navier-Stokes equation with Eqs. (4.3) and (4.2). It is worth noting that with decreasing ξ_n/a_n and increasing η_c/η_ℓ the method is expected to become asymptotically exact [152].

In FPD method, as we numerically solve the Navier-Stokes equation in a direct manner, it is possible to rather straightforwardly incorporate the internal degree of freedom of a solvent such as ion density [153, 154, 155] and orientational [156] field. In this thesis, we consider the simplest case, where colloid particles are immersed in a simple liquid. Then the equation of motion to be solved is

$$\rho\big(\frac{\partial}{\partial t} + \boldsymbol{v}\cdot\nabla\big)\boldsymbol{v} = \boldsymbol{f} - \nabla\cdot[\boldsymbol{\sigma} - \boldsymbol{\sigma}^{\mathrm{R}}] \tag{4.4}$$

with

$$\boldsymbol{\sigma} = p\boldsymbol{I} - \eta(\nabla\boldsymbol{v}^{\dagger} + \nabla\boldsymbol{v}),$$

where $\boldsymbol{I}$ is the unit tensor. In the above, ρ is the mass density, and we assume that the density of the liquid is the same as that of particles. $\boldsymbol{v}(\boldsymbol{r})$ is the velocity field, and the pressure p is determined to satisfy the incompressibility condition $\nabla\cdot\boldsymbol{v} = 0$. $\boldsymbol{\sigma}^{\mathrm{R}}$ is the random stress noise, which we will discuss in detail in Sec. 4.2.1.

In the above, $\boldsymbol{f}(\boldsymbol{r})$ is the interparticle force density, which is obtained by distributing the force $\boldsymbol{F}_n$ and torque $\boldsymbol{N}_n$ acting on the center of mass of particle n to the lattice with the weight of ϕ_n. Here we decompose the force density to the translational and rotational components: $\boldsymbol{f}(\boldsymbol{r}) = \boldsymbol{f}^{\mathrm{T}}(\boldsymbol{r}) + \boldsymbol{f}^{\mathrm{R}}(\boldsymbol{r})$. The first and second terms of the right-hand side is the force density corresponding to $\boldsymbol{F}_n$ and $\boldsymbol{N}_n$ respectively and expressed as

$$\boldsymbol{f}^{\mathrm{T}}(\boldsymbol{r}) = \sum_n^N \phi_n(\boldsymbol{r})\boldsymbol{F}_n \Big/ \int d\boldsymbol{r}\phi_n(\boldsymbol{r}), \tag{4.5}$$

$$\boldsymbol{f}^{\mathrm{R}}(\boldsymbol{r}) = \sum_n^N \phi_n(\boldsymbol{r})\boldsymbol{r}_{\mathrm{on}}\times(\boldsymbol{N}_n\times\boldsymbol{r}_{\mathrm{o}i}) \Big/ \int d\boldsymbol{r}\phi_n(\boldsymbol{r})|\hat{\boldsymbol{N}}_n\times\boldsymbol{r}_{\mathrm{on}}|^2, \tag{4.6}$$

where the rotation center of particle n is located at its center-of-mass, $\boldsymbol{r}_{\mathrm{on}} = \boldsymbol{r} - \boldsymbol{R}_n$, and $\hat{\boldsymbol{N}}_n$ is the unit vector along $\boldsymbol{N}_n$.

We determine the center-of-mass velocity $\boldsymbol{V}_n$ and angular velocity $\boldsymbol{\Omega}_n$ from $\boldsymbol{v}$ as

$$\boldsymbol{V}_n = \int d\boldsymbol{r}\boldsymbol{v}\phi_n \Big/ \int d\boldsymbol{r}\phi_n(\boldsymbol{r}) \tag{4.7}$$

$$\boldsymbol{\Omega}_n = \int d\boldsymbol{r}\phi_n(\boldsymbol{r})(\boldsymbol{r}_{\mathrm{on}}\times\boldsymbol{v}) \Big/ \int d\boldsymbol{r}|\hat{\boldsymbol{n}}\times\boldsymbol{r}_{\mathrm{on}}|^2\phi_n(\boldsymbol{r}) \tag{4.8}$$

where $\hat{\boldsymbol{n}}$ is a unit vector along the rotational axis.

In practical numerical calculations, the on-lattice velocity field, $\boldsymbol{v}(\boldsymbol{r}, t+\Delta t)$, is evaluated from the physical quantities at time t by Eq. (B.1). Then we move the position of particle n off-lattice as a rigid body by $\boldsymbol{R}_n(t+\Delta t) = \boldsymbol{R}_n(t) + \Delta t\boldsymbol{V}_n(t+\Delta t)$, where Δt is the time increment of the numerical integration. We aslo update

the orientational vectores of colloids depending on the angular velocities following the explicit forward difference Euler scheme, but we need to take special care for the time evolution since orientational vector is pseudovector. Sepcifically, here we use normalized quaternion but see other documents for further details (e.g. [157]).

The correction factors originating from the finite interface thickness

By multiplying both sides of Eq. (B.1) by $\phi_n(\boldsymbol{r})$ and then performing its spatial integration, we can straightforwardly obtain an approximate equation of translational motion of particle n:

$$M_n \frac{d\boldsymbol{V}_n}{dt} = \boldsymbol{F}_n + \boldsymbol{K}_n^{\mathrm{T}}, \tag{4.9}$$

where $M_n = \lambda_n^{\mathrm{T}} \rho \int d\boldsymbol{r} \phi_n(\boldsymbol{r})$ is the mass and the velocity of particle n. Here we note that the time derivative of the particle velocity can be approximated as

$$d\boldsymbol{V}_n/dt \cong \int d\boldsymbol{r}(\partial/\partial t + \boldsymbol{v}\cdot\nabla)\boldsymbol{v}\phi_n / \int d\boldsymbol{r}\phi_n(\boldsymbol{r}). \tag{4.10}$$

λ_n^{T} is a correction factor resulting from the introduction of the smooth interface and given by

$$\lambda_n^{\mathrm{T}} = \int d\boldsymbol{r}\phi_i(\boldsymbol{r}) / \int d\boldsymbol{r}\phi_i^2(\boldsymbol{r}). \tag{4.11}$$

In the sharp-interface limit $\xi_n/a_n \to 0$, λ_n^{T} tends to $\to 1$. For the correction factor arising from the finite interface thickness ξ_n, see also the discussion in Sec. 4.2.1. The second term of the right-hand side of Eq. (4.9) is the force exerted by the fluid, which is given by

$$\boldsymbol{K}_n^{\mathrm{T}} = -\lambda_n^{\mathrm{T}} \int d\boldsymbol{r}\phi_n \nabla\cdot[\boldsymbol{\sigma} - \boldsymbol{\sigma}^{\mathrm{R}}] \cong -\lambda_n^{\mathrm{T}} \int dS_n \hat{\boldsymbol{n}}_n \cdot [\boldsymbol{\sigma} - \boldsymbol{\sigma}^{\mathrm{R}}]. \tag{4.12}$$

Here we use the following approximate relation

$$\int d\boldsymbol{r}\nabla\phi_n \cdot \boldsymbol{Q} \cong -\int_{S_n} \hat{\boldsymbol{n}}_n dS_n \cdot \boldsymbol{Q}, \tag{4.13}$$

for an arbitrary tensor $\boldsymbol{Q}(\boldsymbol{r})$, where S_n is the surface of particle n and $\hat{\boldsymbol{n}}_n$ is the unit outward normal vector to S_n.

Similarly, the equation of rotational motion of particle n can be obtained by operating $\phi_n(\boldsymbol{r})\boldsymbol{r}_{on}\times$ on the both sides of Eq. (B.1) and then performing its spatial integration:

$$I_n \frac{d\boldsymbol{\Omega}_n}{dt} = \boldsymbol{N}_n + \boldsymbol{K}_n^{\mathrm{R}}, \tag{4.14}$$

where $I_n = \lambda_n^{\mathrm{R}} \rho \int d\boldsymbol{r} |\hat{\boldsymbol{n}} \times \boldsymbol{r}_{\mathrm{on}}|^2 \phi_n(\boldsymbol{r})$ is the moment of inertia of particle n, respectively. λ_n^{R} is the correction factor regarding rotational motion and given as

$$\lambda_n^{\mathrm{R}} = \int d\boldsymbol{r} |\hat{\boldsymbol{n}} \times \boldsymbol{r}_{\mathrm{on}}|^2 \phi_n(\boldsymbol{r}) / \int d\boldsymbol{r} |\hat{\boldsymbol{n}} \times \boldsymbol{r}_{\mathrm{on}}|^2 \phi_n^2(\boldsymbol{r}). \tag{4.15}$$

The last term in Eq. 4.14 is the torque exerted by the fluid, which can be approximated in the same way as the case of translational motion:

$$\begin{aligned} \boldsymbol{K}_n^{\mathrm{R}} &= -\lambda_n^{\mathrm{R}} \int d\boldsymbol{r} \phi_n \boldsymbol{r}_{\mathrm{on}} \times \nabla \cdot [\boldsymbol{\sigma} - \boldsymbol{\sigma}^{\mathrm{R}}] \\ &\cong -\lambda_n^{\mathrm{R}} \int dS_n \hat{\boldsymbol{n}}_n \cdot (\boldsymbol{r}_{\mathrm{on}} \times [\boldsymbol{\sigma} - \boldsymbol{\sigma}^{\mathrm{R}}]) \end{aligned} \tag{4.16}$$

Introduction of thermal stress noise

In the FPD, there can be two ways to incorporate thermal noise. One is to introduce the thermal force noise to the center of mass of a particle as in Brownian dynamics simulation. Since the particle is treated as a solid particle for the motion of its center of mass, this is certainly a candidate. However, as we have seen in Eq (1.23), the random force has a memory effect. This is a consequence of thermal fluctuations at different points in the fluid being coupled with each other through the Navier-Stokes equation. Indeed, it is difficult to reproduce the resulting hydrodynamic memory effects properly by applying stochastic forces only at certain points; more precisely, it is hard to constitute such a random number sequence [158]. So only the part of thermal noise acts as the noise, which leads to an obscurity in the temperature, as mentioned in the introduction. Furthermore, the rotational Brownian motion is not naturally introduced. The other is to introduce the thermal stress noise directly in the fluid to satisfy the fluctuation-dissipation theorem with the nonlocal viscosity $\eta(\boldsymbol{r})$ [43]. This should properly reproduce both translational and rotational Brownian motion with a full statistical mechanical consistency [53, 55, 56]. This theoretical framework is widely known as fluctuating hydrodynamics. Thus, we introduce the random stress noise, $\boldsymbol{\sigma}^{\mathrm{R}}(\boldsymbol{r})$, which satisfies the fluctuation-dissipation relation [50, 54]:

$$\langle \sigma_{ij}^{\mathrm{R}}(\boldsymbol{r}, t) \sigma_{mn}^{\mathrm{R}}(\boldsymbol{r}', t') \rangle = 2k_B T \eta(\boldsymbol{r}) (\delta_{im}\delta_{jn} + \delta_{in}\delta_{jm}) \delta(\boldsymbol{r} - \boldsymbol{r}') \delta(t - t').$$

The variance of the particle velocity at equilibrium is given by

$$\begin{aligned} \langle |\boldsymbol{V}_n|^2 \rangle &= \int d\boldsymbol{r} d\boldsymbol{r}' \phi_n(\boldsymbol{r}) \phi_n(\boldsymbol{r}') \langle \boldsymbol{v}(\boldsymbol{r}) \cdot \boldsymbol{v}(\boldsymbol{r}') \rangle / [\int d\boldsymbol{r} \phi_n(\boldsymbol{r})]^2 \\ &= 2k_{\mathrm{B}} T / M_n. \end{aligned}$$

Here we make use of the relation $\langle \boldsymbol{v}(\boldsymbol{r}) \cdot \boldsymbol{v}(\boldsymbol{r}') \rangle = (2k_{\mathrm{B}}T/\rho)\delta(\boldsymbol{r} - \boldsymbol{r}')$. The relation $\langle |\boldsymbol{V}|^2 \rangle = 2k_B T / M_n$ also represents the equipartition theorem for the kinetic energy with respect to the translational motion of the particle: $M_{\mathrm{eff}n} \langle |\boldsymbol{V}_n|^2 \rangle / 2 = 3k_B T/2$, where $M_{\mathrm{eff}n} = 3M_n/2$ is the effective mass [50] (see also Eq. (1.22)). Regarding the angular velocity, we also obtain the equipartition theorem: $\langle |\boldsymbol{\Omega}_n|^2 \rangle = 3k_{\mathrm{B}}T/I_n$.

Here it may be worth commenting on the correction factor introduced above. Our basic set of kinetic equations exactly satisfy the fluctuation-dissipation relation. In our method, however, we need to cut out a high-viscosity region represented by our shape function ϕ_n and regard it as a solid particle (the transformation from a fluid particle to a solid one). This process inevitably suffers from an artificial

effect coming from the finite thickness of the interface. This inevitably leads to the necessity to introduce the correction factor. However, this effect must disappear in the sharp interface limit: $\xi_n/a_n \to 0$. What is important is that before the transformation from a fluid particle to a solid one our FPD method satisfies both thermodynamic and mechanical principles in an exact manner and even after the transformation this also holds with the correction factors (see the next section).

Setting of numerical simulations

In our simulation, the units of length ℓ and time τ are related as $\tau = \ell^2/(\eta_s/\rho)$, which sets both the scaled density and viscosity of the fluid region to unity. This τ is a time required for the fluid momentum to diffuse over a lattice size ℓ. The units of stress and energy are $\bar{\sigma} = \rho(\ell/\tau)^2$ and $\bar{\epsilon} = \bar{\sigma}\ell^3$, respectively. Furthermore, we set $\eta_c/\eta_s = 50$, $\Delta t = 0.0025$ and $\xi = \ell = 1$, and $a = 3.2$. We solve the equation of motion [Eq. (B.1)] by the Marker-and-Cell (MAC) method with a staggered lattice under the periodic boundary condition. For implementation of FPD method in more detail, see Appendix B, where we describe the detailed procedure of the computation and the notes for parallel computing.

4.2.2 Verification of FPD method in a dilute limit

In this section, we check the validity of our simulation method incorporating thermal fluctuation effects, by examining the Brownian motion of particles and fluid motion at a low volume fraction of colloids Φ. Hereafter we consider a monodisperse system and thus omit the particle intex n.

Here we put 100 of colloidal particles in the cubic simulation box whose side length is $L = 256$ and apply the thermal noise such that $k_BT = 14.3$. We assume that colloids interact with Weeks-Chandler-Andersen (WCA) potential as,

$$\begin{aligned} U(r) &= 4\epsilon[(\frac{r}{\sigma})^{12} - (\frac{r}{\sigma})^{6}] + \epsilon \quad \text{for} \quad r < 2^{1/6}\sigma, \\ &= 0 \quad \text{otherwise.} \end{aligned} \tag{4.17}$$

where σ and ϵ are the paremeter to control the diameter of the colloids and the strength of interaction. Here we set them as $\epsilon/k_BT = 40$ and $\sigma = 7.4$. The volume fraction $\Phi = \pi\sigma^3 N/6L^3$ is estimated as ~ 0.001, at which we can expect that theoretical predictions at dilute limite is valid.

Fluid motion: Velocity correlation

We first focus on hydrodynamic motion of a fluid and measure the velocity auto-correlation function (VAF). The translational and rotational VAF in a dilute limit is expected to obey the following relation:

$$\langle \boldsymbol{V}(t) \cdot \boldsymbol{V}(0) \rangle = \frac{3k_BT}{M_{\text{eff}}} \psi^{\text{T}}(\frac{t}{\tau_a}). \tag{4.18}$$

$$\langle \boldsymbol{\Omega}(t) \cdot \boldsymbol{\Omega}(0) \rangle = \frac{3k_BT}{I} \psi^{\text{R}}(\frac{t}{\tau_a}). \tag{4.19}$$

Here $\tau_{\rm a} = a_{\rm h}^2/\nu_\ell$, where $a_{\rm h}$ is the hydrodynamic radius ($a_{\rm h} = 1.04a$ and $1.14a$ for translational and rotational motion respectively) and $\nu_\ell = \eta_\ell/\rho$ is the momentum diffusion constant of the fluid. $\psi^{\rm T}$ and $\psi^{\rm R}$ are the memory functions including hydrodynamic effect for translational and rotational motion respectively. An expression of $\psi^{\rm T}$ and $\psi^{\rm R}$ is given by [159, 49]

$$\psi^{\rm T}(x) = \frac{\alpha_+ w(i\alpha_+\sqrt{x}) - \alpha_- w(i\alpha_-\sqrt{x})}{(\alpha_+ - \alpha_-)}, \tag{4.20}$$

$$\psi^{\rm R}(x) = \frac{(1+z_1)z_1 w(-iz_1\sqrt{x})}{(z_1-z_2)(z_1-z_3)} + \frac{(1+z_2)z_2 w(-iz_2\sqrt{x})}{(z_2-z_3)(z_2-z_1)} + \frac{(1+z_3)z_3 w(-iz_3\sqrt{x})}{(z_3-z_1)(z_3-z_2)}, \tag{4.21}$$

where w is the complex complementary error function, $\alpha_\pm = \frac{3}{2} \pm \frac{\sqrt{3}}{2}i$, and $z_i (i = 1, 2, 3)$ is the solutions of the equation $x^3 + 6x + 15x + 15 = 0$. The asymptotic behavior of $\psi^{\rm T}$ and $\psi^{\rm R}$ in the large x (or, long-time) limit are given by $\psi^{\rm T}(x) \sim \frac{1}{6\sqrt{\pi}} x^{-3/2}$ and $\psi^{\rm R}(x) \sim \frac{1}{60\sqrt{\pi}} x^{-5/2}$, which are widely known as the long-time tails.

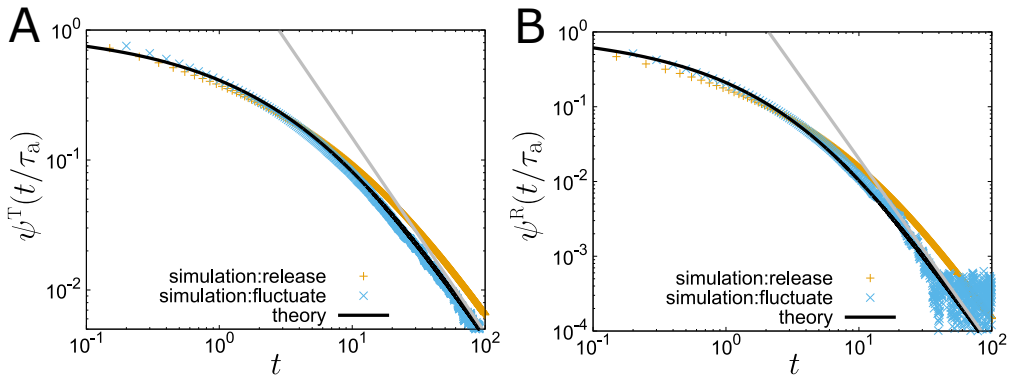

Fig. 4.2 Velocity auto-correlation function (VAF) for translational (A) and rotational (B) motion. Blue symbols are the VAF obtained by the FPD method for particles undergoing thermal Brownian motion at a dilute volume fraction ($\sim 0.1\%$). Brown crosses are the VAF obtained by the FPD method by studying the behavior after removing a external force on a particle from the steady state. The black solid curve is the theoretical prediction (see Eq. (4.20) and Eq. (4.21)). The gray line shows the asymptotic power-law decay function at a long-time limit: $\psi^{\rm T}(x) \sim (6\sqrt{\pi})^{-1} x^{-3/2}$ and $\psi^{\rm R}(x) \sim (60\sqrt{\pi})^{-1} x^{-5/2}$.

In Figs. 4.2 A and 4.2 B, we plot the VAF's for translational and rotational motion calculated by the FPD method together with the above theoretical predictions, respectively. We can see very good agreements between them for both types of motion. In addition, we also check whether our simulation method satisfies the fluctuation-dissipation theorem (FDT). To do so, we first put a particle in the simulation box and externally exert a constant drag force $F_{\rm drag} = 1$ or a constant torque $N_{\rm drag} = 1$ to drag or rotate the particle respectively. After reaching the

steady state, we remove the external force or the torque at $t = 0$ and then monitor the decay of the translational velocity of the particle $V_{\rm l}(t)$ or that of the angular velocity $\Omega_{\rm l}(t)$ respectively. In this situation, the following relations should be held:

$$\langle \boldsymbol{V}(t) \cdot \boldsymbol{V}(0) \rangle = -\frac{3k_{\rm B}T}{F_{\rm drag}} \frac{dV_{\rm l}(t)}{dt},$$

$$\langle \boldsymbol{\Omega}(t) \cdot \boldsymbol{\Omega}(0) \rangle = -\frac{3k_{\rm B}T}{N_{\rm drag}} \frac{d\Omega_{\rm l}(t)}{dt},$$

The brown crosses Figs. 4.2 A and 4.2 B are the VAF's measured with this procedure. The good agreements between the theoretical predictions and the VAF's evaluated by the two different methods indicate that our method well reproduces the FDT including the memory effect of hydrodynamic origin.

Brownian motion of a particle

Next, we examine the thermal Brownian motion of a colloid particle. First we focus on the translational motion of the particle. From Eq. (4.20) and the following identity of the VAF, $\langle \boldsymbol{V}(t) \cdot \boldsymbol{V}(0) \rangle = \frac{1}{2}\frac{d^2}{dt^2}\langle |\Delta \boldsymbol{R}|^2 \rangle$, where $\Delta \boldsymbol{R}(t) = \boldsymbol{R}(t) - \boldsymbol{R}(0)$ is the displacement vector of the particle, we obtain the following expression for the temporal evolution of the mean square displacement (MSD) of a free Brownian particle including hydrodynamic memory effects:

$$\frac{\langle |\Delta \boldsymbol{R}(t)|^2 \rangle}{a^2} = \frac{t}{\tau_{\rm B}} h(\frac{t}{\tau_{\rm a}}). \tag{4.22}$$

Here $\tau_{\rm B}$ is the Brownian time $\tau_{\rm B} = a_{\rm h}^2/6D^{\rm T}$, where $D^{\rm T}$ is the translational diffusion constant of a free particle given by $D^{\rm T} = k_{\rm B}T/(\lambda^{\rm T} 6\pi\eta_{\rm l} a_{\rm h})$, and the function h can be given by [159]

$$h(x) = 1 - \frac{2}{\sqrt{\pi}} x^{-1/2} + \frac{2}{3} x^{-1} + 3x^{-1} \frac{\alpha_+^{-3} w(i\alpha_+\sqrt{x}) - \alpha_-^{-3} w(i\alpha_-\sqrt{x})}{\alpha_+ - \alpha_-}. \tag{4.23}$$

The asymptotic behavior of $h(x)$ is given by $h(x) \to 3x/2$ $(x \to 0)$ and $h(x) \to 1$ $(x \to \infty)$ for the ballistic and diffusive regimes, respectively. Thus, we can obtain from Eq. (4.22) the following expressions for the short-time and long-time behavior: $\langle |\Delta \boldsymbol{R}(t)|^2 \rangle = (3k_B T/M_{\rm eff})t^2$ and $\langle |\Delta \boldsymbol{R}(t)|^2 \rangle = 6D^{\rm T}t$ respectively. The argument of h in Eq. (4.22) can be rewritten as $t/\tau_{\rm a} = S_{\rm c} t/6\tau_{\rm B}$, where $S_{\rm c}$ is called the "Schmidt number" and defined as $S_{\rm c} = \nu_\ell / D^{\rm T}$. $S_{\rm c}$ is the ratio between the momentum and particle diffusion constants, and determines the relation between the time unit of our simulation, τ, and the crossover time from the ballistic to the diffusive motion of a particle.

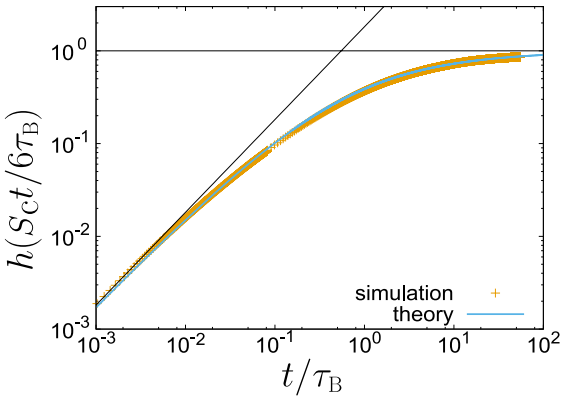

Fig. 4.3 Crossover behavior from the ballistic to diffusive motion of a Brownian particle. We plot the function, h, given by Eq. (4.22). The blue solid curve is the theoretical prediction (see Eq. (4.23)), which can be approximated as $h \sim S_c t/4\tau_B$ in the short-time ballistic limit (shown by the black tilted line) whereas as $h \sim 1$ in the long-time diffusive limit (shown by the black horizontal line). Brown symbols are the results obtained by the FPD method for particles undergoing thermal Brownian motion at a dilute volume fraction ($\sim 0.1\%$).

In Fig. 4.3, we plot the function h obtained by analyzing the results of FPD simulations with the time unit as τ_B and compare it with Eq. (4.23). We can see that our simulation method precisely reproduces Brownian motion covering from the ballistic to the diffusive regime. Here we stress that in the time regime of $t/\tau_B \gtrsim 1$, h is close to 1. This indicates that the Brownian motion in this simulation can be regarded to be almost in the over-damped regime. This situation is realized by choosing the strength of thermal fluctuation such that S_c is to be larger than 1 (in this particular simulation we set S_c=8.0). This can be easily understood from the tilted straight line in Fig. 4.3, $h = S_c t/4\tau_B$: This line is shifted upward and downward with decreasing and increasing the value of S_c respectively. For simulations with $S_c \ll 1$, the ballistic motion becomes dominant even around the time regime $t/\tau_B \sim 1$. We note that the time unit of our simulation is set to the characteristic momentum diffusion time over ξ, and thus increasing S_c requires a longer simulation time to reach the diffusive regime of the Brownian motion.

Next, we examine the rotational Brownian diffusion of a colloid particle. Here we use a parameter $\Delta\boldsymbol{u}(t) = \frac{1}{2}\sum_{i=1,2,3} \boldsymbol{u}_i(0) \times \boldsymbol{u}_i(t)$ to measure the displacement of rotational motion of the particle [160], where $\boldsymbol{u}_i(t)$ $(i = 1, 2, 3)$ are three unit vectors fixed on the particle that are orthogonal with each other. Time evolution of $\boldsymbol{u}_i(t)$ is implemented by using normalized quaternion (see, e.g. [157]). Denoting the axis of rotation of the particle from time 0 to t as $\hat{\boldsymbol{n}}$ and the right-handed rotational angle as θ, we can obtain $\Delta\boldsymbol{u}(t) = \sin(\theta)\hat{\boldsymbol{n}}$. Then the "rotational mean square displacement" (RMSD) can be written as $\langle|\Delta\boldsymbol{u}(t)|^2\rangle = \langle\sin^2\theta\rangle$. In the diffusive regime, it can be calculated as $\langle|\Delta\boldsymbol{u}(t)|^2\rangle = \int_0^\pi \sin^2\theta P(\theta)d\theta = 1/2 - (5e^{-6D^R t} - 3e^{-2D^R t})/4$, where

$P(\theta)$ is the probability density of θ [161]:

$$P(\theta) = \pi^{-1} \sum_{n=0}^{\infty} e^{-n(n+1)D^{\mathrm{R}}t}(2n+1)\{\cos(n\theta) - \cos((n+1)\theta)\}. \qquad (4.24)$$

Here D^{R} is the rotational diffusion constant: $D^{\mathrm{R}} = k_{\mathrm{B}}T/(\lambda^{\mathrm{R}} 8\pi\eta_{\ell} a_{\mathrm{h}}^3)$. In short time, RMSD can be approximated as $\langle|\Delta\boldsymbol{u}(t)|^2\rangle \sim \langle|\theta|^2\rangle \sim \langle|\boldsymbol{\Omega}|^2\rangle t^2 = 3k_{\mathrm{B}}Tt^2/I$, which can be regarded as the ballistic regime. In Fig. 4.4, we plot RMSD and we can see that our simulation method exhibits the ballistic and diffusive behavior also for the rotational Brownian motion, following the theoretical predictions.

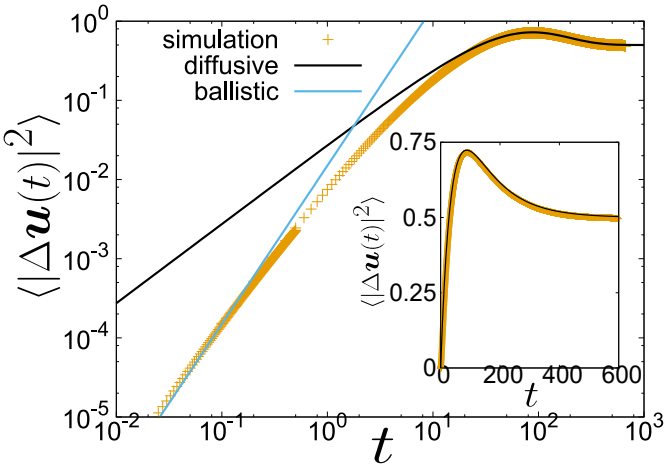

Fig. 4.4 The rotational mean-square displacement (RMSD) of a Brownian particle. Brown symbols are RMSD obtained by the FPD method for particles undergoing thermal Brownian motion at a dilute volume fraction ($\sim 0.1\%$). The blue line and black curve are predictions for the short-time ballistic regime ($\langle|\Delta\boldsymbol{u}(t)|^2\rangle = 3k_{\mathrm{B}}T_{\mathrm{p}}^{\mathrm{R}}t^2/I$) and for the long-time diffusive regime ($\langle|\Delta\boldsymbol{u}(t)|^2\rangle = 1/2 - (5e^{-6D^{\mathrm{R}}t} - 3e^{-2D^{\mathrm{R}}t})/4$).

4.2.3 Verification of FPD method for many-body problems

We have seen so far that FPD method successfully reproduces the diffusion motion of colloidal particles in a dilute limit. Since the aim of our study is to gain a better understanding for the dynamic coupling among colloids and solvent, it is important to verify the validity of FPD method in a situation where many-body interactions play a crucial role, and also clarify under what conditions the numerical predictability can be achieved. We discuss this point in the 'Results' section later, but here we briefly summarize the related previous studies.

In section 8.1.2, where we study the dynamics of hard-sphere-like colloidal suspensions, we checked that the results by FPD method precisely follow the equation of states for all types of equilibrium states (liquid, crystal, and the coexistent states), indicating that our simulation method is valid in terms of thermodynamics.

In the section 5.3.1, we show that FPD method reproduces two-body hydrodynamic interactions, which has been checked by comparing the frictional coefficient between FPD results and theoretical predictions. This implies that our method can properly deal with hydrodynamic interactions at a short distance.

In section 5.4, we consider the effects of the Schmidt number S_c on the colloidal dynamics, which is the ratio between the key timescale of colloids and that of solvent. We note that in order to study phase ordering dynamics of colloidal suspensions by hydrodynamic simulations it is inevitable to apply a small Schmidt number ($S_c < 10$), which is largely different from the one in real colloidal systems ($S_c \sim 10^7$). Despite this discrepancy, we find that FPD simulation can well reproduce the kinetic pathway of colloidal phase separation experimentally observed with confocal microscopy. We have shown that this agreement should be retained as long as $S_c \gtrsim \mathcal{O}(1)$, and provided its physical reason. From these, we may conclude that under a proper setting of the Schmidt number, FPD simulation can reproduce out of equilibrium dynamics of colloidal suspensions including many-body hydrodynamic interactions.

Chapter 5

Scale-invariant nature and numerical predictability of colloidal phase separation

5.1 Motivation

5.1.1 Scale-invariant nature in colloidal phase separation

There are all sorts of colloidal suspensions, and thus their macroscopic properties differ from each other, depending on the microscopic details such as chemical structures of colloids, the type of molecules constituting the solvent that the colloids are suspended, and the intermolecular interactions among them. In section 1.3, we have seen that the static phase behaviors of colloidal suspension can be understood by classical statistical mechanics. Here we emphasize that this is a very powerful tool to comprehensively classify the colloidal systems. In the framework of the statistical mechanics, all we need to know is the interaction among colloids, and we may forget all the microscopic information other than it. For example, if we set a scaling function g for the intercolloid potential U as $U(r) = \epsilon g(r/\sigma)$, we can calculate the thermodynamic functions and determine the phase diagram only by two control parameters, the scaled inverse temperature ($\beta\epsilon$) and the volume fraction (ϕ). In this case, the phase diagrams of the colloidal systems whose interaction potential is written as above can be mapped on a single phase diagram. Roughly speaking, if the interaction potential has a similar shape, the phase diagram should be almost the same. This is often called as the law of corresponding state [38, 39, 40]. Here we note that the above macroscopic parameters $\beta\epsilon$ and ϕ are dimensionless variables, which include ϵ and σ respectively. In this context, we may say that the static phase diagram is scale-invariant in terms of σ and ϵ.

The main aim of our study is to obtain a deeper understanding of dynamic coupling among colloids and solvent. Here a naive question is whether such dynamic coupling can be systematically understood as in the case of the thermodynamic behavior, more specifically, out-of-equilibrium processes of colloidal suspension also have a scale-invariant nature.

To consider this point, in this chapter we focus on colloidal phase separation as a prototype example of nonequilibrium phenomena. Here we consider some characteristic features of colloidal phase separation, through its comparison with phase separation in other classes of materials. For ordinary binary liquid mixtures (a dynamically symmetric mixture), the physics of phase separation is rather well understood on the basis of the concept of dynamic scaling [5], and thus we can predict the process theoretically and numerically. This success is a consequence of the presence of the unique characteristic length and time scales in the problem, the correlation length and lifetime of critical composition fluctuations respectively. For dynamically asymmetric mixtures, on the other hand, it is not so obvious whether we can extract such unique length and time scales controlling dynamic phenomena. For example, in polymer solutions there is no scale invariant nature for dynamics [162, 81, 82], although the static phase diagram can be scaled after a proper scaling [57, 5]; more specifically, it is known that for polymer solutions the effective dynamic critical exponent and the pattern evolution during phase separation are significantly influenced by the degree of polymerization N of polymers [162, 81, 163, 82]. This is a consequence of a non-universal relation between the characteristic lifetime of composition fluctuations $\tau_\xi \sim 6\pi\eta\xi^3/(k_\mathrm{B}T)$, where ξ is the correlation length of composition fluctuations and η is the viscosity, and the structural (or rheological) relaxation time of the system τ_α: the ratio τ_ξ/τ_α crucially depends on the size of polymer (N) [162, 81, 163, 82], since the internal degrees of polymers act differently for the two types of relaxations.

For colloidal suspensions, on the other hand, there is no internal degrees of freedom in a colloidal particle. This implies that any characteristic time scales corresponding to collective motions of colloids should be proportional to that of single-particle diffusion (in other words, τ_ξ/τ_α is independent of the colloidal size), from which we can expect that scale-invariant nature should hold in colloidal dynamics.

5.1.2 Numerical predictability of colloidal phase separation

Importance of precise comparison between experiments and simulations

This scale-invariant nature of colloidal dynamics is also crucial for numerical prediction of dynamical phenomena since we can match the experimental and simulation conditions by scaling arguments without complicated experimental inputs such as the details of their rheological properties.

To study out-of-equilibrium processes of colloidal suspensions, many numerical simulation methods have been developed over past three decades and actively applied to study nonequilibrium phenomena [164, 165, 166, 7, **?**, 167, 168, 169, 62, 65, 103, 104]. For phase demixing, it was found that colloids tend to form more elongated aggregates upon phase separation in simulations with HI than those without [7, 170, 43, 44]. This feature further affects whether a structure formed has a percolated-network or a disconnected-cluster pattern [7, 43, 45, 46]. For cluster formation in dilute suspensions, it was shown [102] that the collision rate in the early stage of aggregation estimated by simulations coincides relatively well with a theoretical prediction that takes HI up to a two-body level into account [74]. Furthermore, the border between cluster and network formations was compared

between experiments and simulations only with "long-range" HI and a good agreement was reported [46].

As noted above, the importance of HI on colloidal phase separation has been demonstrated by numerical simulations, which has contributed significantly to our understanding of the physical mechanism. Furthermore, it has been recognized that numerical simulation is a very useful tool to make predictions for various problems such as aging dynamics [171], mechanical stability [172], and rhological properties [173]. However, there has so far been no parameter-free numerical prediction of such nonequilibrium structural formation, or no direct comparison of the structural evolution between numerical and experimental results *on the basis of the particle-level information*. Such comparison is crucial for establishing a rigorous numerical predictability of structural formation.

In this chapter, we show that such a rigorous numerical prediction of experimental results without any arbitrary parameters is indeed possible for colloidal phase separation, which may be regarded as a typical example of nonequilibrium self-organization of colloidal matter.

Difficulty in numerical prediction

In order to precisely predict the kinetics of colloidal suspensions, we need a model with which we can perform simulation within a realistic computational time while retaining the essential physical laws governing the phenomena. Here, the main difficulty arises from how to deal with the motion of colloids and solvent, whose time and length scales are extremely different. This immediately implies that we have to cover extremely large length and time ranges. This has been overcome by a coarse-grained description of the solvent. For example, Brownian dynamics simulations (more specifically, overdamped Langevin equation with white noise) are one of the most commonly used coarse-grained methods. However, BD simulations ignore the momentum conservation law, which should be satisfied for both colloids and solvent, and the resulting many-body hydrodynamic interactions between colloids, which have recently been shown to play crucial roles in structural formation in colloidal phase separation [7, 43, 44, 45, 102, 46]. For fluid dynamics, we have a very reliable equation describing the momentum conservation, i.e. the Navier-Stokes equation. Thus, we can dynamically integrate out the molecular degrees of freedom while retaining the essential feature coming from the momentum conservation.

However, even after integrating out the microscopic degrees of freedom of solvent molecules, there is a huge gap between the time scale of momentum diffusion of a solvent and colloid diffusion. The momentum diffusion constant of a solvent is given by the kinetic viscosity $\nu = \eta/\rho$, where η is the fluid viscosity and ρ is the density, whereas the diffusion coefficient of an isolated colloidal particle of diameter σ is given by $D = k_{\mathrm{B}}T/(3\pi\eta\sigma)$. The ratio $S_{\mathrm{c}} = \nu/D$ is known as the Schmidt number. In typical colloidal systems, these two diffusion coefficients differ by many orders of magnitude (for example, $S_{\mathrm{c}} \sim 10^6$ for μm-size colloids suspended in water at room temperature), and this condition ($S_{\mathrm{c}} \gg 1$) is widely assumed in the physical laws associated with the dynamics of colloids, such as the Stokes-Einstein relation. In other words, the equilibration of the momentum degrees of freedom is a necessary condition to have the scale invariance of the phenomena in the diffu-

sive regime. For such a large Schmidt number, however, numerically accessing the diffusive time regime, in which structural ordering of colloids takes place, starting from the ballistic regime, is almost impossible with current computational power. Indeed, in most of simulation studies, the Schmidt number has been set to modest values ($S_c < 10$) [174]. Thus, it might look almost hopeless to realize numerical simulations with a predictive power, or to retain the scale invariance, while incorporating full hydrodynamic interactions and thermal noise (see Fig. 5.7A). In this chapter we show that it is actually possible.

5.2 Method

To verify numerical predictability of our simulation scheme, the experimental data that we can precisely compare with the simulation results on a quantitative level is essential. To this end, we experimentally study the kinetic pathway of phase demixing of colloids interacting with reversible and short-range attractions at semi-dilute volume fractions ($\phi = 2\% \sim 10\%$) by three-dimensional (3D) confocal microscopy observation. To confirm the scalability of the phenomena experimentally, we compare experimental results for two types of colloids with different particle diameters but with almost the same interaction range with respect to the colloid size (see below). Then we compare the experimental results with those of two types of simulations, BD and FPD [7, 8]. The system size of our simulations are commonly set as $(L/\sigma)^3 = 34.6^3$. The intensity of thermal noise, as far as not mentioned, is set as $k_B T = 14.3$ and the corresponding Schmidt number is $S_c = 8.0$. See section 4.2.1 for the other setting parameters in FPD method.

5.2.1 Samples

In our experiments, we use PMMA colloids. The average diameter of colloids are $\sigma = 1.9$ μm(EXP1) and 2.9 μm (EXP2), and both have approximately 3% size polydispersity (see section 3.1.2 in more detail). Then, a short-range attractive depletion interaction [21] was induced by dissolving polystyrene with a molecular weight of 8.4×10^6 Da (the gyration radius $R_g = 120$ nm) for EXP1 and 2.0×10^7 Da ($R_g = 180$ nm) for EXP2. Thus, the interaction range parameter $\Delta = 2R_g/\sigma \sim 0.13$ is almost the same for both experiments. The concentration of the polymer, C_p, is used as the control parameter to change the strength of the attraction $\beta\epsilon$. In order to observe the aggregation process of colloids from the very beginning without perturbation by mixing flow, we used a salt-injection method (see section 3.1.3). The definition of the onset time of phase demixing ($t_w = 0$) and the validity of this salt injection method are described in section 3.1.4.

5.2.2 Matching of the thermodynamic condition between experiments and simulations

In order to compare experiments (EXP) and simulations (SIM) in a rigorous manner, we need to precisely match the interaction potentials between them with a

reliable method. In our simulations we used the Morse potential. We determine the interaction range by the method based on the second Virial coefficient and the relation between $C_{\rm p}$ and $\beta\epsilon$ by matching the composition fluctuation of an equilibrium fluid between EXP and SIM. By the precise matching of the interaction potential between EXP and SIM, we successfully predict the equilibrium phase diagram precisely. In this section, we explain the detailed procedure.

The interaction potential used in our simulations

First we explain how we match the interaction potential between experiments and simulations. More specifically, we explain how to determine the interaction potential and its parameters used in our simulations to approximate the real intercolloid potential due to depletion attraction. In our simulations, we assume that the interparticle interaction is pairwise additive and approximated by the Morse potential:

$$U(r) = \epsilon \exp\{\rho_{\rm M}(\sigma_{\rm M} - r)\}(\exp\{\rho_{\rm M}(\sigma_{\rm M} - r)\} - 2),$$

where ϵ is the depth of the attractive potential, $\sigma_{\rm M}$ is the length at which $U(\sigma_{\rm M}) = \epsilon$, and $\rho_{\rm M}$ is a parameter controlling the interaction range. This potential is useful in the sense that it does not have any singularity and we can control its depth and range independently. The validity of this potential to represent the depletion interaction has been examined in Ref. [41]. We determined $\sigma_{\rm M}$ and $\rho_{\rm M}$ so that the reduced second birial coefficient [41, 40, 42],

$$b_2 = \frac{3}{\sigma^3}\int_0^\infty dr\, r^2\{1 - \exp(-\beta U(r))\},$$

and the effective hard sphere parameter,

$$\sigma = \int_{U(r)>0} dr\{1 - \exp\left(\beta U(r)\right)\}$$

are to be the same between the Morse potential and the following Asakura-Osawa potential [21]:

$$\begin{aligned} &= \infty \quad \text{for } \frac{r}{\sigma} < 1, \\ U(r) &= 0 \qquad \text{for } 1 + \Delta < \frac{r}{\sigma}, \\ &= -\epsilon \frac{2(1+\Delta)^3 - 3(1+\Delta)^2(\frac{r}{\sigma}) + (\frac{r}{\sigma})^3}{2(1+\Delta)^3 - 3(1+\Delta)^2 + 1} \quad \text{otherwise.} \end{aligned}$$

Here we set $\Delta = 0.13$ to match this potential with the one in the experiments. The result is shown in Fig. 5.1.

The force acting on particle n is then obtained from the interparticle interaction potential as

$$\boldsymbol{F}_n = \sum_{m(\neq n)} \boldsymbol{F}_{mn},$$

where $\boldsymbol{F}_{mn} = -(\partial/\partial \boldsymbol{R}_n)U(|\boldsymbol{R}_m - \boldsymbol{R}_n|)$ is the force acting on particle n, which interacts with particle m.

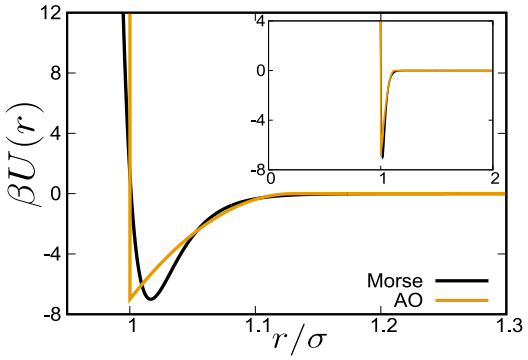

Fig. 5.1 **Comparison of the two interparticle potentials**: Morse (black) and Asakura-Osawa (brown). Here the range and depth of the AO potential are $\Delta = 0.13$ and $\beta\epsilon = 7$ respectively. The controlling parameters of the Morse potential, σ_{M} and ρ_{M}, are determined such that the reduced second virial coefficient and the effective hard sphere parameter are to be the same between the Morse and AO potentials.

Determination of the potential depth parameter and estimation of equilibrium phase diagram

We determine the interaction range to employ the method based on the second Virial coefficient, as described above. We also need to know the relation between C_{p} and $\beta\epsilon$. The easiest way is to directly estimate the form of the interaction potential from the information of polymers added into samples (through C_{p} or R_{g}). However, it is known that this method is not accurate enough to match the locations of the binodal and the spinodal lines between EXP and SIM since the depletion attraction is not pairwise additive and involves many-body interactions [21, 175, 176, 42]. To overcome this problem, we measure the density fluctuation of an equilibrium fluid both in EXP and SIM and compare them directly. Figure 5.2A shows the integral of the scattering function $S(q)$ (see section 3.1.5 for the definition), $I = \int d(q\sigma/2\pi)S(q)$, for various conditions (see above): $(\phi, \beta\epsilon)$ for SIM and (ϕ, C_{p}) for EXP. Here the integration was made over the same q-range, $q\sigma/2\pi \in [1/10, 10]$, for EXP and SIM. Under the constraint that the ratio $\epsilon\beta/C_{\mathrm{p}}$ is to be a constant, we obtain $\epsilon\beta/C_{\mathrm{p}} = 11.8$ for EXP1 and 22.7 for EXP2, for which we have the excellent agreement of the I behavior between EXP and SIM. If we see a monotonic increase in I with time when we increase $\beta\epsilon$ by a small amount, we can judge that state point to enter inside the spinodal line, or in the unstable state. The state points investigated in this manner are summarized in Fig. 5.2B, where black and blue symbols indicate state points in the stable one-phase equilibrium region and in the coexisting region respectively. In this way we have succeeded in precisely matching the interaction potential between EXP and SIM.

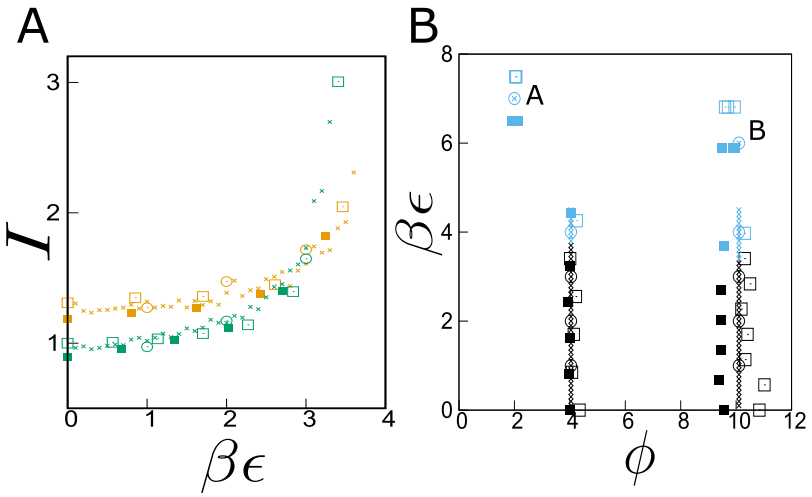

Fig. 5.2 **Estimation of equilibrium phase diagram.** **A**, The intensity of density fluctuation in equilibrium fluids for various strengths of the attraction (C_{p} in EXP, $\beta\epsilon$ in SIM) at two volume fractions, $\phi \sim 4\%$ (brown) and 10% (green). **B**, The state diagram. Black and blue symbols indicate thermodynamically stable and unstable state points respectively. Closed and open square symbols represent the results of two experiments, EXP1 and EXP2, respectively. Cross and circle symbols represent the results of BD and FPD simulations respectively. At point A ($\phi \cong 2\%$, $\beta\epsilon \cong 7$) and point B ($\phi \cong 10\%$, $\beta\epsilon \cong 6$), we observed disconnected isolated clusters and interconnected network structures as the final states ($t_{\mathrm{w}} \gtrsim 300\tau_{\mathrm{B}}$) respectively.

5.3 Results

Now we turn our attention to the dynamics of phase separation taking place at two state points, point A ($\phi \cong 2\%$, $\beta\epsilon \cong 7$) (see Fig. 5.3) and point B ($\phi \cong 10\%$, $\beta\epsilon \cong 6$) (see Fig. 5.5), where we observe respectively the formation of isolated aggregates (clusters) and percolated network structures (gels) at the end of the phase-separation processes. In the following analysis results, we take an average over three independent phase demixing processes in both EXP and SIM for gaining high statistical accuracy.

5.3.1 Cluster formation in a dilute suspension

First we discuss cluster-forming phase separation in a dilute suspension at point A ($\phi \cong 2\%$, $\beta\epsilon \cong 7$). To quantitatively characterize the coarsening dynamics during phase separation, we calculate the temporal change of the characteristic wavenumber of the structure factor $S(q, t_{\mathrm{w}})$ as its first moment: $\langle q(t_{\mathrm{w}})\rangle = \int dq\ qS(q, t_{\mathrm{w}}) / \int dq\ S(q, t_{\mathrm{w}})$. The results are shown in Fig. 5.4A. First we can see that the two sets of experimental results with different sizes of colloids (EXP1 and EXP2) exhibit almost identical coarsening behaviour after scaling the length and time by σ and τ_{B} respectively, implying that colloidal phase separation with

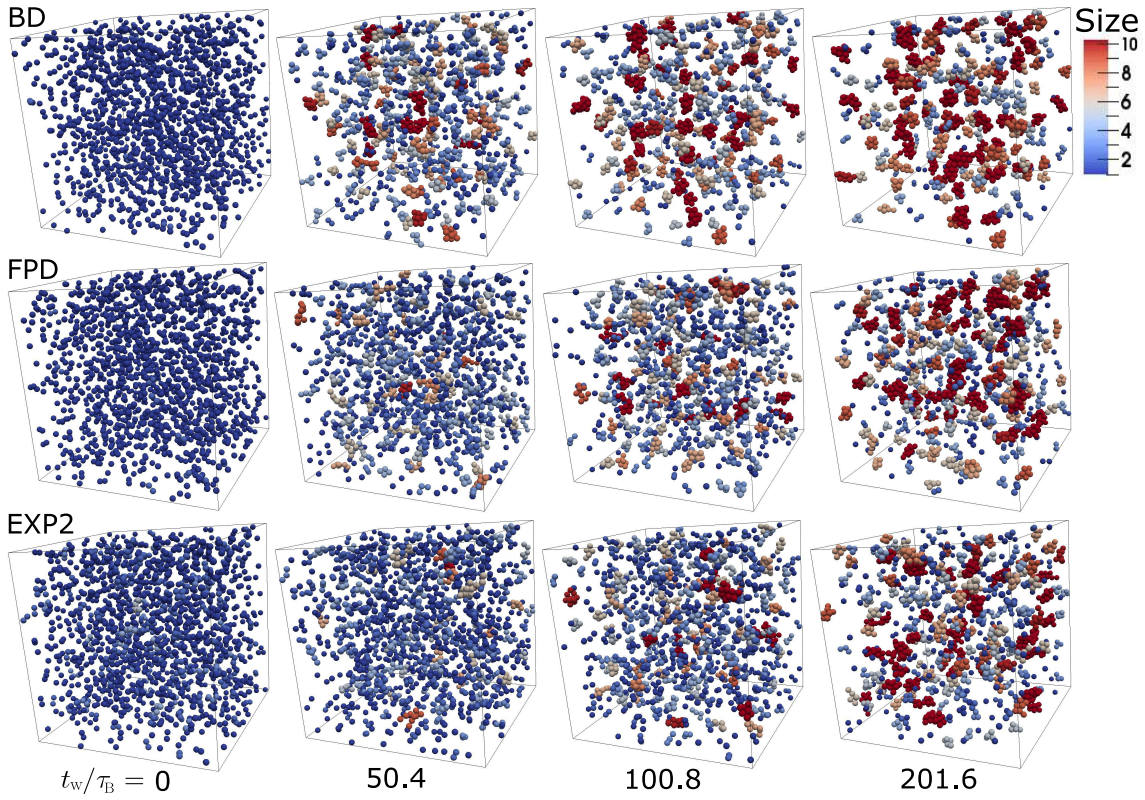

Fig. 5.3 **Cluster-forming phase separation at state point A ($\phi \cong 2\%$, $\epsilon\beta \cong 7$).** We compare the time development of 3D structures obtained from BD and FPD simulations and confocal microscopy observation in EXP2 at $t_w/\tau_B \simeq 0, 50.4, 100.8, 201.6$. The particle colour represents the size of the clusters (see the colour bars on the top right side); for example, clusters involving more than 10 particles appear red. The box sizes are commonly set as $L/\sigma = 34.6$.

a short-range attraction is scale-invariant for the same set of $(\phi, \beta\epsilon, \Delta)$, for which the equilibrium phase diagrams can also be scaled [21]. This result is a direct experimental support for the scale invariance of the phenomena.

Next we can see clearly that FPD almost perfectly reproduces the experimental data, but BD fails even qualitatively (see Fig. 5.3). This strongly indicates not only the numerical predictability of our FPD simulation but also the crucial role of the hydrodynamic degrees of freedom of the solvent, or hydrodynamic interactions, in the kinetic process of phase demixing of a colloidal suspension and the resulting colloidal aggregation. We can also see that $\langle q \rangle$ decreases with time t_w as $\langle q \rangle \propto t_w^{-\alpha}$ (α: the domain growth exponent) with $\alpha \cong 0.33$ for $\phi \cong 2\%$ for both EXP and FPD, but the exponent is smaller for BD. The growth exponent $\alpha \sim 1/3$ seen at $\phi \cong 2\%$ is characteristic of Smoluchowski's Brownian coagulation mechanism [74, 102] (see the gray line in Fig. 5.4), indicating that the phase demixing observed belongs to spinodal decomposition with droplet morphology.

In the above, we see the significance of hydrodynamic interactions in the macro-scale coarsening process of colloidal phase separation. Next we focus on the micro-

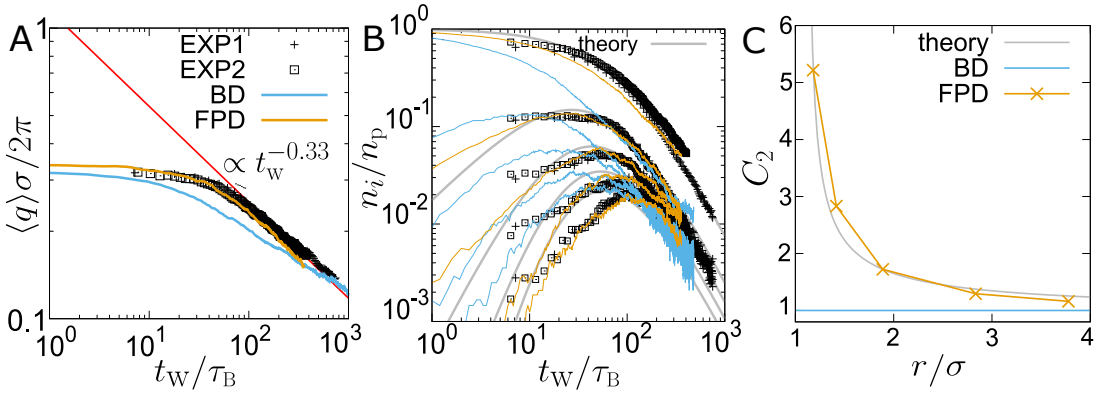

Fig. 5.4 **Analysis of cluster-forming phase separation. A** The temporal change of the characteristic wave number estimated from the structure factor, $\langle q\rangle$. **B** The temporal change of the fraction of clusters of size i, $n_i/n_{\rm p}$. Gray curves are the theoretical predictions of Eq. (5.1) [74]. Five curves and different symbols correspond to $i = 1 \sim 5$ from top to bottom. In both panels a and b, we compare experiments and simulations: EXP1 (black cross), EXP2 (black square), BD (blue curve) and FPD (brown curve). **C** The dependence of the viscous drag coefficient for two particles approaching with each other, normalized by that of a free isolated particle, C_2, on the interparticle distance r scaled by σ. Brown cross symbols are the results calculated by FPD method. The gray curve is the theoretical prediction [60]. Here r is chosen as $r = r_s + \sigma_{\rm H}$, where r_s is the distance between the surfaces of the two colloids and $\sigma_{\rm H}$ is the hydrodynamic radius of the colloids ($\sigma_{\rm H} = 1.1\sigma$). In the BD simulation, $C_2 = 1$ (blue line) since hydrodynamic interactions are ignored.

scopic process of aggregation to make a more rigorous comparison between experiments, simulations, and theory. We identify clusters by regarding particles to be connected and belong to the same cluster if the inter-particle distance is less than $(1 + \Delta)\sigma$. According to Smoluchowski's Brownian coagulation theory [74, 102](see Sec. 2.1.4 on the details), the number of clusters with size i at time t per unit volume, $n_i(t)$, can be given by

$$n_i(t)/n_{\rm p} = (n_{\rm p}Kt)^{i-1}(1 + n_{\rm p}Kt)^{-i-1}, \tag{5.1}$$

where $n_{\rm p}$ $(= n_1(0))$ is the total number of particles per unit volume and K is the so-called coagulation rate. Here we employ K as a fitting parameter to the experimental data. In Fig. 5.3B, we plot $n_i(t)/n_{\rm p}$ for different $i(= 1 \sim 5)$ for EXP and SIM. We can see that FPD again well reproduces the experimental data of each type of cluster. By fitting Eq. (5.1) to the experimental data, we obtain $K/K_{\rm s} = 0.50, 0.93, 1.2, 1.4, 1.7$ respectively for $i = 1, 2, 3, 4, 5$ (gray lines in Fig. 5.3B). Here we use $K_{\rm s} = 4k_{\rm B}T/3\eta$, which is the collision rate derived by Smoluchowski, as a value to normalize K. Note that $n_i(t)/n_{\rm p} \sim (n_{\rm p}Kt)^{-2}$ for a long-time limit and the height of the asymptotic behaviour is proportional to K^{-2}. The rate of collision between two equal-size spherical particles, which interact with the potential $U(r)$,

in a viscous liquid is given by [74] (see Eq. 2.20 on the details)

$$\frac{K}{K_{\mathrm{s}}} = \{\int_{\sigma}^{\infty} dr \frac{\sigma}{r^2} C_2(r) e^{\beta U(r)}\}^{-1}, \tag{5.2}$$

where $C_2(r) = \zeta_2(r)/\zeta_2(\infty)$ is the ratio between the viscous drag coefficient for two particles at the center-of-mass distance z approaching each other ($\zeta_2(r)$) to the one for a single spherical particle ($\zeta_2(\infty)$). Estimating the collision rate with relation (5.2), we obtain $K/K_{\mathrm{s}} = 0.56$, which is reasonably close to the experimental result for $i = 1$ ($K/K_{\mathrm{s}} = 0.50$ (see above)). Collision rates for $i \geq 2$ are higher than this value, likely reflecting the aspherical shape of clusters of $i \geq 2$. Such details of cluster morphology and the resulting modification of hydrodynamic interactions make theoretical predictions of the collision rate extremely challenging.

Figure 5.3C also shows that there is a huge mismatch between BD and EXP and the aggregation speed is much faster for BD than for EXP. In BD, the collision rate for $i = 1$ is $K/K_{\mathrm{s}} \sim 1$, which is almost equivalent to the one for the case where hydrodynamic interactions are completely neglected (if we assume $C_2(r) = 1$ in Eq. (5.2), we get $K/K_{\mathrm{s}} = 1.1$). These results clearly indicate that collisions between colloids are strongly hindered by hydrodynamic interactions. In Fig. 5.3C, we plot the functional form of $C_2(r)$ obtained by FPD together with the theoretical prediction [60], which show an excellent agreement. We can see that there is a steep increase in the friction coefficient between the two particles (or, the "strength" of hydrodynamic interactions between them) for $r/\sigma \lesssim 2$. This tells us that hydrodynamic effects at such a "short-range" distance, or "lubrication effects", are responsible for the significant suppression of the collision rate. We note that the results of BD can never be mapped on those of EXP (FPD) by rescaling time by other time units, which is obvious from the difference in the growth exponent between BD and EXP (FPD).

5.3.2 Gel formation via spinodal decomposition in a semi-dilute suspension

As the volume fraction of colloids increases, it is expected that the many-body nature of hydrodynamic interactions plays a more important role. Now we focus on network-forming phase separation in a semi-dilute suspension (see Fig. 5.5). To check how precisely FPD can capture such effects, we make detailed comparison between EXP and SIM at the volume fraction $\phi \cong 10\%$ (point B), where space-spanning network structures were formed. This formation of space-spanning network structures of the minority colloid-rich phase in phase separation is characteristic of viscoelastic phase separation [81, 82]. It is worth stressing here that all the quantities we measured (see Fig. 5.6A-D) are almost the same between EXP1 and EXP2, which is a direct experimental support of the scale invariance of the phenomena.

Considering the hierarchical nature of network structures, we perform structural analysis at various length scales. First we examine the temporal change in the characteristic wave number $\langle q \rangle$ during phase separation. The results are shown

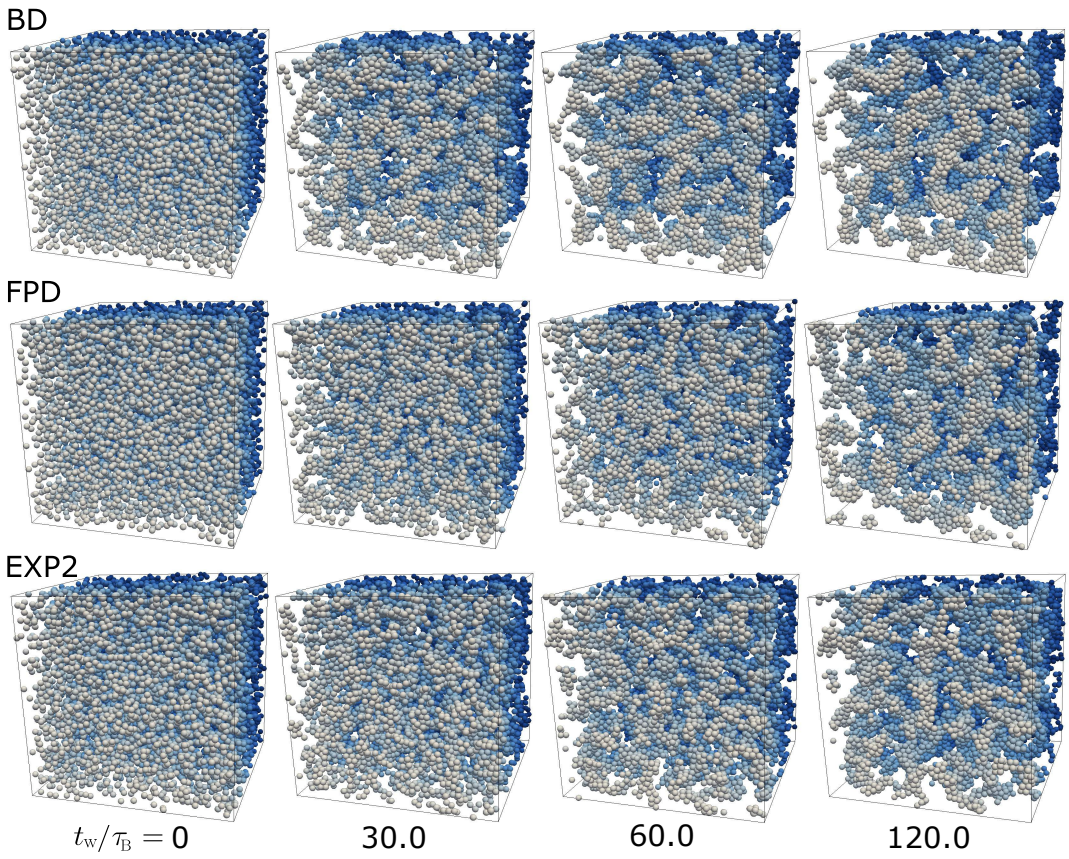

Fig. 5.5 **Network-forming phase separation at state point B ($\phi \cong$ 10%, $\epsilon\beta \cong 6$).** We compare the time development of 3D structures obtained from BD and FPD simulations and confocal microscopy observation in EXP2 at $t_w/\tau_B \simeq 0, 30, 60, 120$. A clear network structure is already formed at $t_w/\tau_B = 30$ for BD, but not for EXP2 and FPD. Particles are coloured to distinguish front particles from back ones.

in Fig. 5.6A. We can see that FPD almost perfectly reproduces the experimental data, but BD fails even qualitatively. This strongly indicates again the numerical predictability of our FPD method and the crucial role of the hydrodynamic degrees of freedom of the solvent and the resulting many-body hydrodynamic interactions in the kinetic process of phase demixing of a colloidal suspension.

We discuss the coarsening dynamics observed in the wave-number apace in more detail.

In Sec. 3.1.5, Fig. 3.5B, we analyze the early stage of phase separation in an experiment and confirm that in the initial stage the scattering intensity grows exponentially with time for every wave number, which are characteristic of the Cahn's linear regime of spinodal decomposition in a thermodynamically unstable state [5]. In Sec. 3.1.5, Fig. 3.5A, we also show the time evolution of $S(q, t_w)$ in the experiment, where we can see that the scattering peak appears in the very early stage, then its position continuously shifts towards a lower wave number with time. Consistently, we can see in Fig. 5.6A that for both EXP and FPD, after the initial

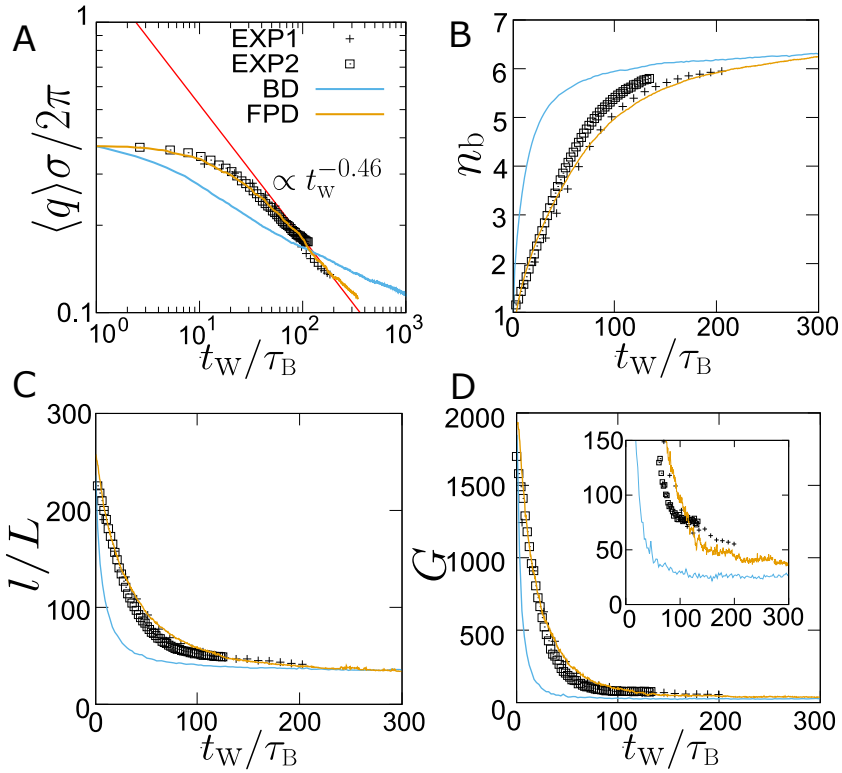

Fig. 5.6 **Structural analysis for network-forming phase separation.** We compare the time evolution of structures between experiments and simulations, EXP1 (black cross), EXP2 (black square), BD (blue curve) and FPD (brown curve): the characteristic wave number (**A**), the number of bonds per particle (**B**), the total length of the skeleton l (**C**), and the Genus number of the skeleton (**D**). We made network analyses for the box whose side length is $L/\sigma = 34.6$ in common for experiments and simulations.

stage, where $\langle q\rangle$ is almost constant with time, $\langle q\rangle$ starts to decrease by obeying a power law $\langle q\rangle \propto t_{\rm W}^{-\alpha}$ ($\alpha \cong 0.46$). This domain growth exponent α is different from the well-known exponents for ordinary spinodal decomposition in a binary critical mixture, $\alpha = 1/3$ for the Brownian coagulation mechanism and $\alpha = 1$ for Siggia's hydrodynamic coarsening mechanism [5]. The physical meaning of $\alpha \sim 0.5$ is unclear at this moment, which we examine in Chap. 7. Here we emphasize that network formation at $\phi \cong 10$ % clearly indicates that phase separation of colloidal suspensions does not belong the dynamical universality class of binary mixtures of simple liquids (model H [5]). We also note that $\langle q\rangle$ deviates from the power law in the late stage. This behaviour may reflect the dynamic arrest due to gelation, but we do not focus on this trend here since it is out of scope of this work [*1].

Next we study the aggregation process at the particle scale. Figure 5.6B shows the temporal change of the number of interparticle bonds per particle, $n_{\rm b}$, where the bond definition is the same as the one for clusters. The time development of $n_{\rm b}$

[*1] In Appendix D, we show experimental results regarding this phenomenon.

is almost identical between EXP and FPD, but again shows much faster increase, or faster contraction, for BD (see Fig. 5.6). We can also see that in the entire time range of the observation $n_{\mathrm{b}} < 7$ (note that $n_b \sim 12$ for a compact structure in 3D), indicating that most particles are located in the domain interface. This lack of separation between the domain size and the interface thickness makes a coarse-grained theoretical description of phase separation quite difficult.

Now we turn our attention to the topological characteristics of network structures in real space. For further characterization of the network structures, we coarse-grain a phase-separated structure by operating Gaussian blurring of each particle, extract the network domain by binarization, and then extract the skeleton of the network structure by applying a skeletonization procedure (see Appendix C on the details). For skeleton structures obtained by this protocol, we first calculated the total length of the skeleton, l. Figure 5.6C shows the temporal change of l normalized by the size of the box L. To capture the topological feature of a network, we also calculated the Genus number G (Fig. 5.6D), which is equivalent to the total number of holes (or pores) existing in the network structure, by analyzing the connectivity of the skeleton (see Appendix C on the details). All these results show excellent agreements between EXP and FPD. On the other hand, the results of BD exhibits much faster changes than EXP and FPD, again reflecting the lack of hydrodynamic ubrication effects as in the dilute system (at point A). In the late stage of the inset of Fig. 5.6D, we can see that the G value of BD is approximately half of EXP and FPD. This clearly indicates that the presence and absence of hydrodynamic interactions have a significant influence on the kinetic pathway and the resulting topological characteristics of the final network structures. We stress that it is these topological features that control the physical properties of network materials, such as elastic, transport, and surface properties.

5.4 Validation of FPD method with a moderate Schmidt number

In the above, we have found excellent agreements of dynamical pattern evolution between EXP and FPD by carefully matching the intercolloid potential and point on the phase diagram. Here we consider the physics behind this excellent predictability of FPD in more detail. In the FPD simulation, we deal with the time revolution of the Navier-Stokes equation, and the time unit is set to be the time scale of the momentum diffusion of the solvent over a lattice size. To access a time scale over which colloid-rich domains coarsen within an accessible simulation time, it is inevitable to apply rather strong thermal stress noise. Accordingly, the Schmidt number $S_{\mathrm{c}} = \nu/D = 3\pi\eta^2\sigma_{\mathrm{H}}/\rho k_{\mathrm{B}}T$, which is the ratio of the momentum diffusivity of the solvent to the colloid diffusivity, is smaller by many orders of magnitude in FPD than in EXP: $S_{\mathrm{c}} = 8.0$ for our typical FPD simulations and $S_{\mathrm{c}} \sim 10^7$ for EXP. This means that we effectively deal with a much higher temperature, a lower viscosity of the solvent, and/or a smaller diameter of colloids in FPD than in EXP.

5.4.1 A free particle diffusion

In order to validate the setting employed in FPD carefully, we first examine the diffusive behavior of a free particle by using the mean square displacement (MSD):

$$\langle |\boldsymbol{R}(t) - \boldsymbol{R}(0)|^2 \rangle = 6Dt\ h(\frac{S_\mathrm{c}}{6}\frac{t}{\tau_\mathrm{B}}). \tag{5.3}$$

Here $\boldsymbol{R}$ is the center-of-mass position vector of a free particle and h is the scaling function of MSD including hydrodynamic memory (see Eq. 4.23 for the functional form). In section 4.2.2, we have checked that under the current setting of $S_\mathrm{c}(= 8.0)$ FPD method reproduces the theoretical prediction almost completely. In Fig. 5.7B, we show the behavior of $h(\frac{S_\mathrm{c}}{6}\frac{t}{\tau_\mathrm{B}})$ as a function of t/τ_B for $S_\mathrm{c} = 10^7$ (EXP) and 8.0 (FPD). The gray shaded region in Fig. 5.7A indicates the time span over which we compare the coarsening behavior between EXP and FPD. In this time region, needless to say, h in EXP shows the diffusive behavior ($h = 1$). On the other hand, although we may claim that h in FPD is close to 1, it is not easy to make a rigorous justification that our simulation completely reaches the diffusive regime. This means that the Brownian time determined in the parameter setting of FPD we employed in this study is not large enough compared to the time scale over which the velocity profile surrounding a particle fully reaches the steady state via momentum diffusion. This is a typical problem of colloid simulations [174].

5.4.2 Colloidal diffusion at a finite volume fraction

Here we introduce a characteristic time required for the momentum of the solvent to dissipate over a distance l_c, which can be given by $\tau_\nu = 24(l_\mathrm{c}/\sigma)^2 S_\mathrm{c}^{-1}\tau_\mathrm{B}$. We obtain $l_\mathrm{c}/\sigma \sim 1$ for $\tau_\nu/\tau_\mathrm{B} \sim 1$ and $S_\mathrm{c} \sim 10$. Thus, many-body hydrodynamic interactions at short-range distance are properly incorporated in our simulation method (see Fig. 5.7B).

To justify the above argument, we examine how the velocity profile is equilibrated for two particles whose center-of-mass distance is given by r. To do so, we applied small constant forces on two particles along the directions for them to approach with each other, and measured the resulting drag coefficient $\zeta_2(r,t)$. For this two-body problem, the exact solution of the velocity field in a steady state is known [60]. In Fig. 5.8A, we plot the time evolution of the normalized diffusion constant $\tilde{D}_2(r,t) = D_2(r,t)/D$, where $D_2(r,t)$ is obtained by $D_2(r,t) = k_\mathrm{B}T/\zeta_2(r,t)$. Here we can see that, for $r/\sigma \lesssim 1.4$, $\tilde{D}_2(r,t)$ becomes almost constant around $t \sim \tau_\mathrm{B}$, which is roughly consistent with the above estimation.

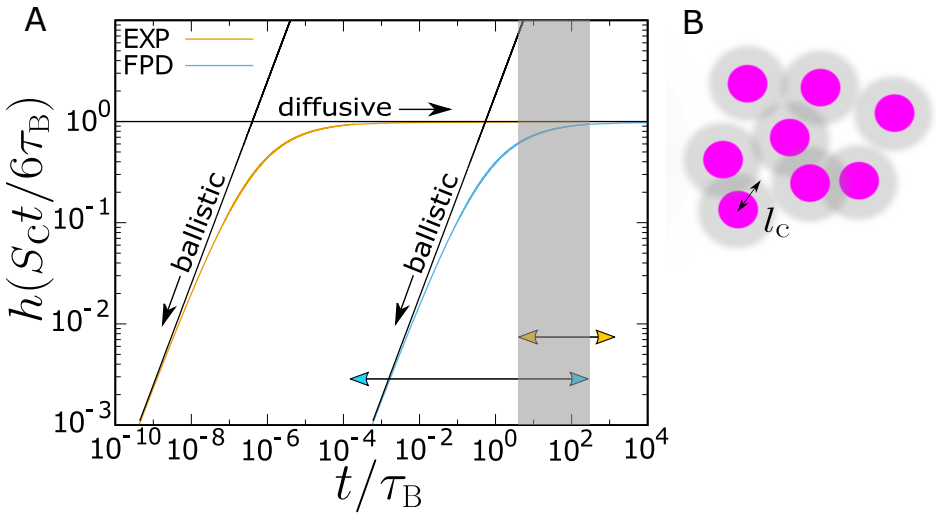

Fig. 5.7 **Difference in the Schmidt number S_c between experiments and simulations. A** The scaling functions of the mean square displacement of *a free particle*, h for experiments (EXP) ($S_c \sim 10^7$: brown curve) and FPD simulations (FPD) ($S_c = 8.0$: blue curve). The blue and brown arrows represent the time scales covered by EXP and FPD respectively. The gray shaded region is the time span over which we compare the coarsening behavior between EXP and FPD. In this time region, needless to say, h in EXP shows the diffusive behavior ($h = 1$). On the other hand, although we may claim that h in FPD is close to 1, it is not easy to make a rigorous justification that our simulation completely reaches the diffusive regime. **B** An estimation of the characteristic length l_c over which the momentum diffusion of a solvent takes place within τ_B. For $S_c \sim 10$, which is a typical value in FPD method, we obtain $l_c/\sigma \sim 1$.

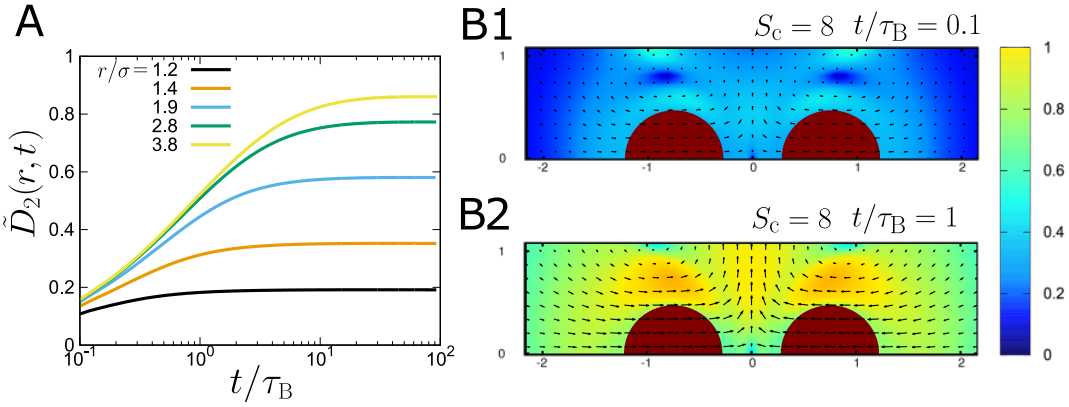

Fig. 5.8 **A**, The ratio of the viscous drag coefficient between the case of two particles approaching with each other to that of a free isolated particle by FPD at $S_c = 8.0$. **B** Flow profile in the situation where two equal-size spheres are approaching. Panels B1 and B2 are the results of FPD method with $S_c = 8.0$ for different time, $t_w/\tau_B = 0.1$ and 1, respectively. The arrows represent the velocity vector fields. The color represents the ratio of the result of FPD simulation to the exact solution in the steady state [60].

In Fig. 5.8B, we show the flow vector field (see arrows), $\boldsymbol{v}(\boldsymbol{r},t)$, at $t = 0.1\tau_B$ for $r/\sigma = 1.4$ together with the relative amplitude of $\boldsymbol{v}(\boldsymbol{r},t)$ to the exact solution [60] (see color), both of which are obtained by the FPD method for $S_c = 8.0$. There we can see from the color that $\boldsymbol{v}(\boldsymbol{r},t)$ is far from the steady state one even at positions close to the particles, obviously implying that hydrodynamic interactions are not properly introduced in such a short time scale. In Fig. 5.8C, on the other hand, we also show the flow field (see arrows), $\boldsymbol{v}(\boldsymbol{r},t)$, at $t = \tau_B$ for $r/\sigma = 1.4$. We can see from the color that the velocity profile of the FPD method is almost fully relaxed near the particles already around τ_B, i.e. the FPD method properly reproduces the velocity profile in a viscous liquid.

5.4.3 Breakdown of the scale invariance of phase separation dynamics at small S_c

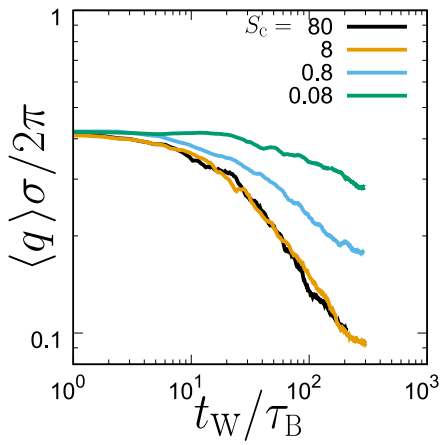

Fig. 5.9 The temporal change of the characteristic wave number $\langle q \rangle$ for four different Schmidt numbers during phase separation at point B in the phase diagram. Here we perform simulations with a smaller system size ($(L/\sigma)^3 = 17.3^3$) than the one used in the other FPD simulations ($(L/\sigma)^3 = 34.6^3$), to access a large Schmidt number ($S_c = 80$).

It is also interesting to check under what condition the agreement in the time development of $\langle q \rangle$ during phase separation between EXP and FPD breaks down. In Fig.5.9, we show the temporal change of the characteristic wave number $\langle q \rangle$ at state point B ($\phi \cong 10\%, \beta\epsilon = 6$) for different Schmidt numbers: $S_c = 0.08, 0.8, 8, 80$. We can clearly see that $\langle q \rangle$ is almost identical when the Schmidt number satisfies $S_c > 1$. Figure 5.8B also provides a physical insight into the above break down of the scaling of $\langle q \rangle$. Given that the typical time scale of momentum diffusion of the solvent is written as $\tau_\nu(r) = 24(r/\sigma_c)^2 S_c^{-1}\tau_B$, the velocity profile at $t/\tau_B = 0.1$ for $S_c = 8$ can be translated as that at $t/\tau_B = 1$ for $S_c = 0.8$. In other words, under the condition where S_c is set as 0.8, the effect of hydrodynamic interactions do not reach the steady state at least in a two-body problem, which should result in the mismatch in $\langle q \rangle$ for $S_c \lesssim 1$. In short, the successful prediction of colloidal phase

separation processes (both structure and kinetics) by FPD is possible at least if the momentum degree of freedom is equilibrated in the time scale of the relevant elementary process of structure formation. We note that this condition is nothing but a requirement to retain the scale invariance of the phenomena.

5.5 Summary

To summarize, we systematically study the phase-separation process of colloidal suspensions by comparing single-particle-level time-resolved 3D confocal microscopy observation, BD simulations without hydrodynamic degrees of freedom and FPD simulations with many-body hydrodynamic interactions. We find that the coarsening dynamics of cluster-forming and network-forming phase separation in the experiments using colloids with two different sizes can be almost perfectly reproduced by FPD simulations without any adjustable parameters after careful matching of the intercolloid potential and the temperature (or, thermal noise), but cannot at all by BD simulations. This finding demonstrates the fundamental importance of many-body hydrodynamic interactions in the dynamical structural formation of colloidal suspensions. More importantly, it indicates that simulation methods based on direct computation of the Navier-Stokes equation including FPD simulation has a high predictive power for nonequilibrium processes in colloidal suspensions, which may significantly contribute to not only the basic physical understanding of these phenomena but also the computer-aided design of colloidal materials.

Chapter 6

Volume fraction dependence of coarsening behavior

As we see in Chap. 2, in phase separation of an ordinary binary mixture close to the symmetric composition, where network (or bicontinous) structures are formed, the growth of domain is governed by Siggia's hydrodynamic mechanism, whereas in an off-symmetric mixture, where cluster (or droplet) domain is formed. Brownian coagulation mechanism plays a major role in the coarsening process [*1]. In this section, we aim to clarify how the coarsening behavior in colloidal phase separation depends on the volume fraction.

6.1 Two types of percolation mechanisms

In this section, we study phase separation dynamics of colloids interacting with short-range attraction by using the same experimental setup described in Sec. 5.2.1 (EXP1) and simulation methods (BD and FPD). In Sec. 5.3.1 and 5.3.2, we observed growth exponent $\alpha \sim 1/3$ and $1/2$ for cluster-forming ($\phi \sim 2\%$) and network-forming phase separation ($\phi \sim 10\%$), respectively. Here we fix the strength of attraction as $\beta\epsilon \sim 6$ and examine the volume-fraction dependence on the coarsening behavior in more details.

6.1.1 Percolation in the early stage of spinodal decomposition

We first examine the volume fraction dependence of the time when percolation happens, $t_{\rm p}$, since the connectivity of domains is expected to have a great influence on the coarsening mechanism. We define $t_{\rm p}$ as the time when $2R_{\rm g}^{\rm max}/L$ first becomes larger than 1, where $R_{\rm g}^{\rm max}$ is the largest gyration radius the clusters (see Sec. 5.3.1 for identification of the clusters) and L is the size length of the scanned

[*1] As a coarsening mechanism in a mixture whose composition is strongly asymmetric ($\phi \lesssim 0.01$, for example), the evaporation-condensation (or Lifshitz-Slyozov-Wagner) mechanism [68] is widely known. In the region of the phase diagram where we studied colloidal phase separation, we do not observe such a mechanism involving detachment of colloidal particles from the colloid-rich clusters. Thus, we do not discuss the mechanism in this thesis.

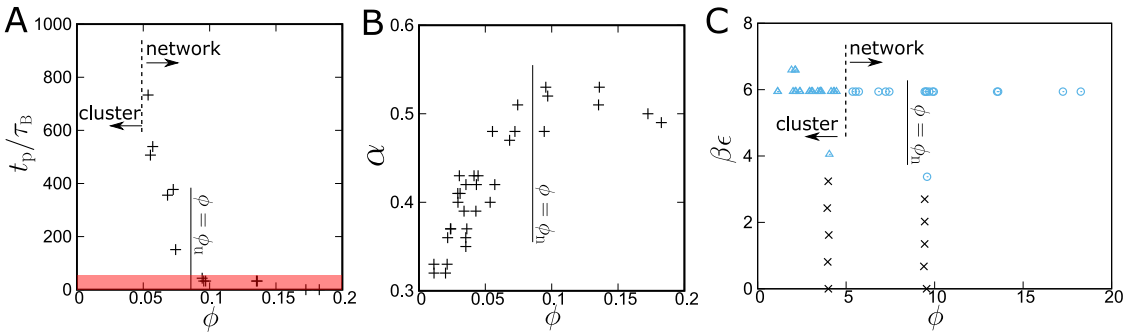

Fig. 6.1 **A.** Volume fraction dependence of the time when percolation takes place, t_p. We observe connected network structures in $\phi \gtrsim \phi_p := 0.05$ and disconnected cluster structures in the other ϕ region. Note that this percolation boundary $\phi \sim \phi_p$ (see the dotted line in the figure) depends on the time window of the observation ($t_w/\tau_B \lesssim 1000$ in this experiment). The red shaded region corresponds to the time region before which we can see a power law decay in the temporal change of the characteristic wave number. We refer the ϕ region where percolation takes place within the red time regime to "network region", and define its lower composition bound as $\phi = \phi_n$. **B.** Volume fraction dependence of the growth exponent α. **C.** Phase diagram. Black and blue symbols mean that these are located at the outside and inside of the spinodal line, respectively. We show the phase points, where we can see connected structure, as cross symbols and those of disconnected structures as triangle symbols.

box. Figure 6.1A shows t_p as a function of ϕ. There we can see that t_p dramatically increases as the volume fraction approaches to $\phi \sim 0.05$, whereas for $\phi \gtrsim 0.08$ there is no strong ϕ dependence. From this trend, one may determine the percolation boundary volume fraction as $\phi_p \sim 0.05$, but we should mention that there is a possibility that ϕ_p highly depends on the time window of observation ($t < 1000\tau_B$ in this experiment). We discuss the dependence of percolation on the time window of observation later. Here we note the coarsening regime starts around $t_w/\tau_B \lesssim 50$ (see the red shaded region in Fig. 6.1A) and this means that in the latter case mentioned in the above ($\phi \gtrsim 0.08$) percolation takes place in the early stage of demixing, or before the coarsening starts. We determine this boundary value as $\phi_n \equiv \phi \sim 0.08$ as a key volume fraction to classify the coarsening mechanism.

Next, in Fig. 6.1B, we show the ϕ dependence of the growth exponent α (which is determined in the same way as in Secs. 5.3.1 and 5.3.2). Here we can see that crossover behavior of the growth exponent from $\alpha \sim 1/3$ to $1/2$ with an increase in ϕ. For $\phi > \phi_n$, we can commonly see $\alpha \sim 1/2$. We call the ϕ region where we can see $\alpha \sim 1/3$ and $1/2$ as "cluster region" and "network region", respectively, and the region between them as "intermediate region". As discussed in Sec. 5.3.1 $\alpha \sim 1/3$ in the cluster region can be understood in terms of the Brownian coagulation theory, which is the same as the coarsening mechanism of liquid droplets in ordinary binary mixtures. On the other hand, the exponent $1/2$ seen in the network region is different from what has been known in the coarsening of bincontinous structures

(Siggia's hydrodynamic mechanism; $\alpha = 1$). We discuss the physical meaning behind the exponent 1/2 in Chap. 7 and in this Chapter we focus on the case of $\phi < \phi_n$. The presence of the intermediate region in colloidal systems is also quite different from the case of ordinary binary mixtures, where the growth exponent sharply changes from $\alpha = 1/3$ to $\alpha = 1$ in a discontinuous manner as the volume fraction ϕ increases.

6.1.2 Percolation via Brownian diffusion of anisotropic clusters

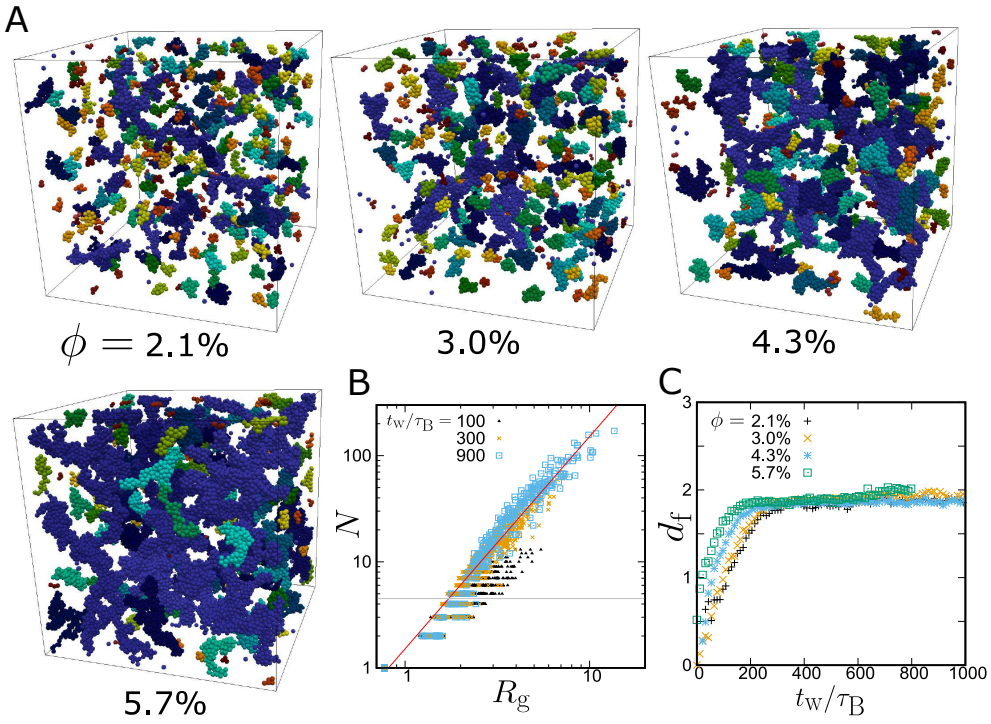

Fig. 6.2 **A.** 3D structures of aggregates at the end of experiment ($t_w/\tau_B \sim 1000$) for various volume fractions $\phi = 0.021, 0.030, 0.043, 0.057$. The particles are colored just to distinguish different clusters. **B.** Mapping of the gyration radius of clusters, R_g, and the size N (the number of particles involved in a cluster). We determine "fractal dimension" d_f by fitting $N \propto R_g^{d_f}$ to the data, where we take statistics for clusters whose size are larger than 5 (the data above the gray line). In this figure, we show an example at $\phi = 0.030$, where black, gray and blue symbols represent the results at $t_w/\tau_B \sim 100, 300$ and 900, respectively. Red line shows the slope with $d_f = 2$. **C.** The temporal change of the fractal dimension for various volume fractions.

To clarify a key difference in the coarsening behavior between binary mixtures and colloidal suspensions, in Fig. 6.2A we show the 3D structures of aggregates at the end of experiment ($t_w/\tau_B \sim 1000$) for various volume fractions ($\phi = 0.021, 0.030, 0.043, 0.057$), where we can clearly see that the aggregates have elongated shape which is in contrast to spherical droplets seen in phase separation of binary liquid mixtures. To characterize the shape of clusters in a qualitative

way, we compute the temporal change of "fractal dimension" $d_{\rm f}$. We obtain $d_{\rm f}$ from the dependence of the number of particles in i-th cluster, $N^{(i)}$, on its radius of gyration, $R_{\rm g}^{(i)}$, by using the relation $N \propto R_{\rm g}^{d_{\rm f}}$ (see Fig. 6.2B). We define $R_{\rm g}^{(i)}$ as $R_{\rm g}^{(i)} = 3(\frac{\sigma}{2})^2/5 + \sum_{j,k=1}^{N^{(i)}} (\boldsymbol{R}_j^{(i)} - \boldsymbol{R}_k^{(i)})^2 / 2{N^{(i)}}^2$, where $\{\boldsymbol{R}_j^{(i)}\}$ is the set of the center-of-mass positions of colloids belonging to i-th cluster [*2]. Figure 6.2C shows the temporal change of $d_{\rm f}$ for various ϕ's, where we can see that $d_{\rm f}$ grows in the early stage but asymptotically approaches the value of approximately 2, which is significantly smaller than the value of spherical aggregates ($d_{\rm f} = 3$).

Based on the morphological information, we reconsider a link between the percolation time and the time window of the experiment. In phase separation of binary liquid mixtures, the self-similarity of the domain morphology is retained in the coarsening regime. Thus, in the systems where no percolated structure is observed at a certain time in the coarsening regime, percolation will never happen in the subsequent time region. In our experiment of colloidal suspensions, on the other hand, *percolation takes place even in the coarsening regime.* This implies that percolation takes place via Brownian diffusion of clusters with anisotropic shapes. In this process, the ratio between the average intercluster distance $l_{\rm rel}$ and the average value for the gyration radius of clusters $R_{\rm g}$, $r = l_{\rm rel}/2R_{\rm g}$ is independent of time. Denoting the number of colloidal particles and clusters per unit volume as $n_{\rm p}$ and $n_{\rm c}$, we can relate these to $l_{\rm rel}$ and $R_{\rm g}$ as $\pi l_{\rm rel}^3 n_{\rm c}/6 = 1$ and $n_{\rm p}/n_{\rm c} = c(2R_{\rm g}/\sigma)^{d_{\rm f}}$, where c is a dimensionless value independent of time. With these relations we obtain,

$$r = n_{\rm c}^{-1/3+1/d_{\rm f}} (\frac{c}{\phi})^{1/3}, \tag{6.1}$$

where we use $\phi = \pi\sigma^3 n_{\rm p}/6$. In the case of self-similar coarsening $d_{\rm f} = 3$, the above relation reduces r =const. Here we assume that $n_{\rm c}$ decays obeying a power law, which we confirm from the long-time behavior of $N_{\rm c}$ shown in Fig. 6.3A; thus, we has the relation of $n_{\rm c} \propto t^{-b}$. Figure 6.3B shows the volume fraction dependence of the exponent b, where we can see $b \sim 1$ for the dilute systems which is consistent with the prediction of Smoluchowski's Brownian coagulation theory (see Sec. 2.1.4). For larger volume fractions, we can see that the crossover behavior from $b \sim 1$ to ~ 2. At the percolation time $t = t_{\rm p}$, we may assume that $r \sim 1$. By substituting these relations into Eq. 6.1, we obtain,

$$t_{\rm p} \propto \phi^{-\frac{d_{\rm f}}{b(3-d_{\rm f})}}. \tag{6.2}$$

When $d_{\rm f} = 2$ and $b = 1$, the above relation becomes $t_{\rm p} \propto \phi^{-2}$. Figure 6.3C shows again the ϕ dependence of $t_{\rm p}$ but in a log-log plot, where we can see that the data in low volume fractions follow the power-law function with the exponent of -2 (see the red line in the figure), which supports our discussion in the above. From this, we can expect that percolation takes place even in an extremely dilute solvent (e.g., less than 1% in volume fraction) as long as the fractal dimension keeps

[*2] We include the moment of inertia for spherical rigid body with diameter σ in the definition of the gyration radius because we regard a cluster as not a set of mass points but a domain.

the same value. To satisfy this condition, the characteristic time required for the morphological relaxation should be slow enough compared to that for intercluster collisions.

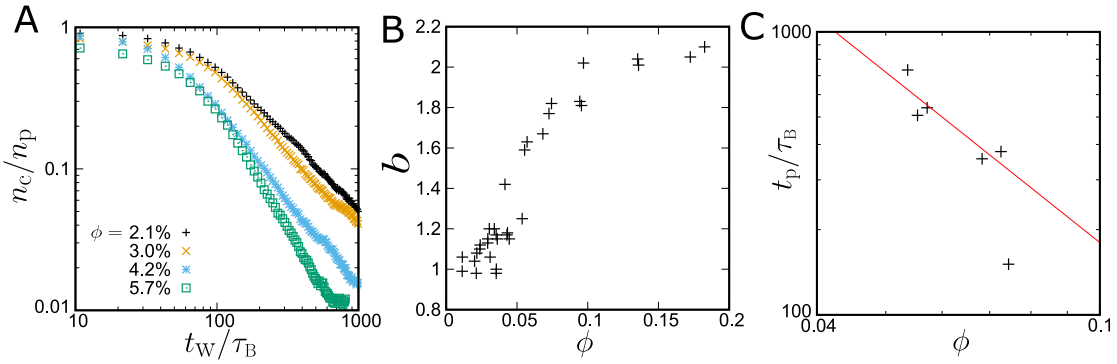

Fig. 6.3 **A.** The temporal change of the number of clusters n_c for various volume fractions. Here we can see a power law decay at large t_w and then we write this trend as $n_c \propto t_w^{-b}$. Panel **B** represents the volume fraction dependence of the exponent b. **C.** Log-log plot of the volume fraction dependence of the percolation time t_p. The red line is a power-law function with the exponent of -2.

6.1.3 Effect of attraction range: Competition between Brownian coagulation and morphological relaxation

We have so far seen that Brownian coagulation among elongated clusters can bring about percolation in the coarsening regime. Here an important question in this context is: Why are such anisotropic clusters formed and how are the shapes retained? Formation of elongated clusters in colloidal suspensions have been pointed out by many experimental and simulation studies. There are at least two physical factors to enhance the formation of anisotropic clusters. One is the hydrodynamic effect [43, 44, 102, 177, 103, 104], and the other is the contribution of attractive interaction [96, 97]. [*3]

In this section, we examine the effect of the range of intercolloid attraction on the structural formation process of colloidal suspensions. For this purpose, we perform FPD simulations for colloidal particles interacting with short-range and long-range attractions. In the former case (SIM-S), we use Morse potential and adjust the interaction range Δ to be the same as in that of the experiment ($\Delta \sim 0.12$). We also perform FPD simulations with Lennard-Jones potential (SIM-L), which can be regard as long-range attraction compared to $\Delta \sim 0.12$. The volume fraction and the inverse temperature are commonly set as $\phi \sim 0.04$ and $\beta\epsilon \sim 6$ for both experiments and simulations.

[*3] It is also known that the presence of electrostatic repulsion also enhances the formation of elongated clusters (see. e.g., [178, 179, 180]), although this may not be relevant in our study.

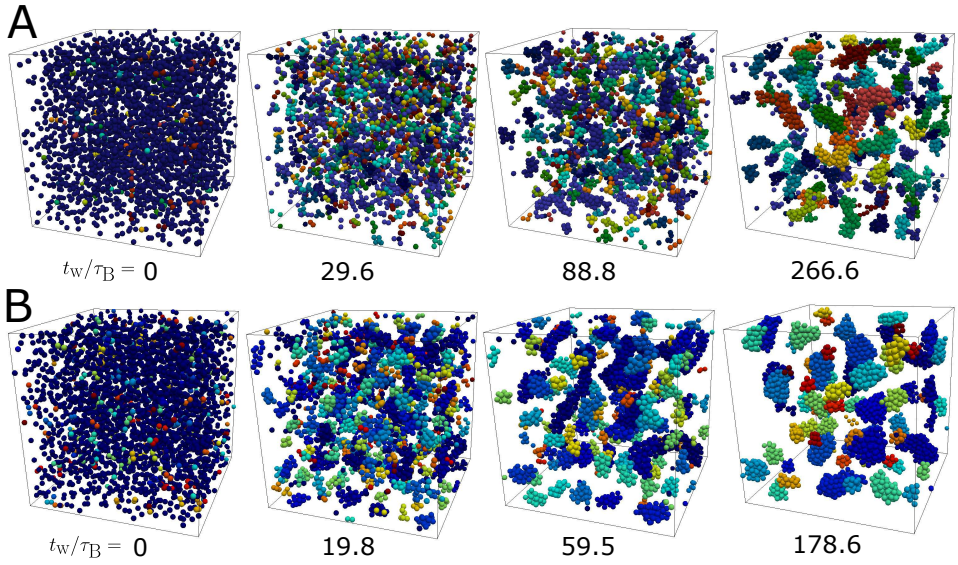

Fig. 6.4 The time evolution of 3D structure of aggregates for the case of short-range attraction (**A**) and long-range attraction (**B**). The particles are colored to distinguish different clusters.

In Fig. 6.4A and B, we show the time evolution of 3D structures for SIM-S and SIM-L, respectively, where we can clearly see that the aggregates seen in SIM-L have more compact structures than those in SIM-S. To see this trend in a qualitative manner, we calculate the temporal change of the fractal dimension for both experiments and simulations (Fig. 6.5A), from which we can confirm the asymptotic behavior at a long time to be $d_f \sim 2$ for short-range attraction and $d_f \sim 3$ for long-range attraction. Here we mention again that there is a good agreement between the experimental and FPD simulation results, supporting the numerical predictability of FPD method for the structural formation process of colloidal suspensions that we argued in Chap. 5. In Fig. 6.5B, we show the time evolution of the gyration radius of the largest clusters R_g^{max}, where we can see that R_g^{max} discontinuously increases at a certain point and decrease after that, reflecting the collision among clusters and the morphological relaxation of clusters, respectively. In the very early stage of SIM-L, we can see the sharp increase of R_g^{max}, but this is due to the formation of sting-like aggregates (see Fig. 6.5C). We do not focus on this particular shape of aggregates here, but we expect that many-body lubrication forces play a key role in the formation process of these aggregates.

From the above, we may conclude that as the attraction range is longer, the morphological relaxation is more likely to take place, leading to the formation of compact clusters. In the case where $d_f \sim 3$, it is expected that the percolation mechanism discussed in Sec. 6.1.2 is no longer operative since the coarsening proceeds while retaining self similarity of the phase-separation structure (Eq. (6.1) becomes r =const., in this case). Such a situation is the case when the morphological relaxation is fast compared to the characteristic time of collisions among

clusters. In other words, in the case where the viscoelastic relaxation time inside the colloid-rich domain is comparable with or longer than the intercluster collision time, such a percolation in the late stage can happen [*4].

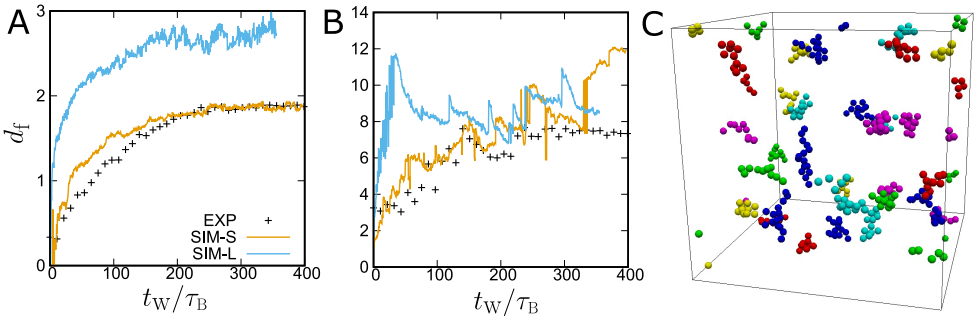

Fig. 6.5 **A.** The temporal change of the fractal dimension. **B.** The time evolution of the gyration radius of the largest cluster. The black cross symbols represent the experimental results of colloids interacting with short-range attraction (the interaction range $\Delta \sim 0.12$). The brown and blue curves are the results obtained by FPD simulations, and correspond to the case where the intercolloid attractions are Morse potential and Lennard-Jones potential respectively. The volume fraction and inverse temperature are set commonly as $\phi \sim 0.04$ and $\beta\epsilon \sim 6$. In the Morse potential, we set the parameters such that the interaction range Δ is the same as that in the experiments. **C.** String-like aggregates seen in the early stage of demixing ($t_w/\tau_B = 5$) in the case of long-range attraction. Here only the clusters which include more than 10 particles are shown. The particles are colored are to distinguish different clusters.

6.2 Crossover behavior of growth exponent

We have mainly discussed phase separation dynamics of colloids interacting with short-range attraction ($\Delta \sim 0.12$) so far, and revealed that there are at least the two types of dynamic path ways to form connected network structure (percolation): one is the case where the connected structure is formed in the early stage of demixing, and the other is where percolation takes place via the diffusion of anisotropic clusters in the coarsening regime. In Fig. 6.1B, we have seen a crossover behavior of the growth exponent with an increase in the volume fraction, which corresponds to the volume fraction region where we can observe the latter percolation mechanism. Furthermore, in Sec. 6.1.3, we argued that in the case where the morphological relaxation of colloidal clusters is fast enough compared to the frequency of cluster-cluster collisions, percolation in the coarsening regime does not take place and there should be no crossover behavior in the growth exponent.

[*4] We may also regard the coarsening of droplets (size R) in ordinary binary mixtures by Brownian coagulation mechanism as the extreme case where the viscoelastic relaxation time ($\sim R\eta/\gamma$) is much faster than the collision time ($\sim 6\pi\eta R^3/k_BT$). The ratio of the former to the latter is the order of $(\xi/R)^2$ (ξ: interface thickness), which is much less than 1.

From the above, we may expect that there may be a link between the crossover behavior of the growth exponent and the formation of clusters of anisotropic shape, which is the main issue that we focus on in this section. More specifically, we examine the following two questions:

(Q1) Why can we still see the growth exponent close to 1/3 even for clusters of anisotropic shape?

(Q2) Is there any link between the crossover behavior of the growth exponent and the formation of clusters of anisotropic shape? If so, how are they related to each other?

6.2.1 Reconsideration of growth exponent 1/3

To examine the above question, we reconsider how the growth exponent 1/3 can be derived from the Smoluchowski equation. In Sec. 2.1.4, we have already introduced a way to derive it under the assumption of the constant collision rate, but here we employ a different approach based on the assumption of a self-similar solution.

In Sec. 2.1.4, we considered the time evolution of the number of clusters of size i per unit volume as $n_i(t)$ by following the Smoluchwski equation (Eq. 6.4). Here we consider the continuous version of the equation for convenience, and denote the number of clusters whose size are between x and $x+dx$ as $n(x,t)dx$. Then, Eq. 6.4 becomes,

$$\frac{\partial}{\partial t}n(x,t) = \frac{1}{2}\int_0^x K(x-y,y)n(x-y,t)n(y,t)dy - \int_0^\infty K(x,y)n(x,t)n(y,t)dy, \tag{6.3}$$

where K is the collision rate. Assuming that the collision radius and the diffusion constant of cluster of size x, R_x and D_x are given by $x \propto R_x^{d_\mathrm{f}}$ and $D_x \propto R_x^{-\lambda}$, we may write K in the following form:

$$K(x,y) \propto (x^{-\lambda/d_\mathrm{f}} + y^{-\lambda/d_\mathrm{f}})(x^{1/d_\mathrm{f}} + y^{1/d_\mathrm{f}}), \tag{6.4}$$

where d_f can be regard as the fractal dimension of the clusters, and λ is an exponent that relates the collision radius of clusters to the diffusion constant. In the case where the clusters have spherical shape, $d_\mathrm{f} = d$ and $\lambda = 1$. If we assume a self-similar solution [*5] $n(x,t) = f(t)F(x/\overline{x}(t))$ for Eq. 6.4, we can find the following relation: [181],

$$f(t) = \overline{x}(t)^{-2}, \tag{6.5}$$

$$\frac{d\overline{x}}{dt} \propto \overline{x}^{\frac{1-\lambda}{d_\mathrm{f}}}, \tag{6.6}$$

where $\overline{x}(t)$ is the characteristic size of clusters at time t. The first relation is easily obtained from the conservation of mass ($\int xn(x,t)dx = \text{const.}$). The second

[*5] We note that the assumption of self-similar solution for $n(x,t)$ does not necessarily require the self-similarity in the domain morphology.

relation is obtained by substituting the self-similar solution into Eq. 6.4. Eq. 6.6 can be rewritten as

$$\overline{x}(t) \propto t^{\frac{d_\mathrm{f}}{d_\mathrm{f}+\lambda-1}}. \tag{6.7}$$

When the Stokes law is valid ($\lambda = 1$), the above relation becomes $\overline{x}(t) \propto t$. Since the total number of clusters per unit volume, n_c, satisfies $n_\mathrm{c}(t) = \int n(x,t)dx \propto \overline{x}(t)^{-1}$, we obtain $n_\mathrm{c} \propto t^{-1}$, which coincides with the solution of the Smoluchwski equation under the assumption of the constant collision rate (see Sec, 2.1.4). In the case of Brownian coagulation of spherical clusters, we may choose the characteristic length $\ell(t)$ of the domain as the mean radius of the clusters, and we obtain $\ell \propto \overline{x}(t)^{1/d_\mathrm{f}}$. In the case of $d_\mathrm{f} = 3$, the growth exponent becomes 1/3.

In the above, we derive the growth exponent $1/d_\mathrm{f}$ based on the assumption of a self-similar solution. Here we summarize important points for considering the correspondence of the aggregation process of colloidal suspensions to this Brownian coagulation mechanism:

(P1) A power law dependence between mass M and collision radius R_c: $M \propto R_\mathrm{c}^{d_\mathrm{f}}$.

(P2) A linear dependence between hydrodynamic radius R_h and collision radius R_c.

(P3) A linear dependence between characteristic length ℓ and mean value of R_c.

The first point (P1) is considered to be the case since fractal dimension approaches to a constant value in a long time: $d_\mathrm{f} \sim 2$ (see Fig. 6.1C). Hereafter we examine validity of P2 and P3.

6.2.2 Relation between hydrodynamic radius and collision radius

To examine P2, we consider a simple problem: diffusive motion of the following ellipsoids: $(\frac{x}{a})^2 + (\frac{y}{pa})^2 + (\frac{z}{pa})^2 = 1$, where p is the aspect ratio and we consider the case of "rod-like" body ($p \leq 1$) rather than "disk-like" body ($p \geq 1$). This simplification seems not to be irrelevant as long as looking at the 3D structures of clusters in Fig 6.4, but it is expected that for further long time beyond our experimental time window the above treatment becomes invalid since the more complicating shape (ramified shape, for example) of cluster can be formed.

The exact expression for the translational diffusion of coefficient of the above ellipsoids is known as

$$D = \frac{k_\mathrm{B}T}{6\pi\eta a} G(p)$$

where $G(p) = \log\left[(1+\sqrt{1-p^2})/p\right]/\sqrt{1-p^2}$, thus the hydrodynamic radius of the body can be expressed as $R_\mathrm{h} = aG(p)^{-1}$. We use the gyration radius $R_\mathrm{g} = \sqrt{(1+2p^2)/5}a$ instead of collision radius R_c, since R_c is expected to be proportional to R_g. Then, if the ratio $g(p) \equiv R_\mathrm{g}/R_\mathrm{h}$ is constant without depending on the aspect ratio p we may conclude that point P3 is valid. The result is shown in Fig 6.6A, where we can see that $g(p)$ dose not strongly depend on aspect ratio

p. For example, the difference between spherical body $p = 1$ and a ellipsoid with $p = 1/3$ is approximately 20%.

From the above, we may conclude that center-of-mass diffusion of elongated body as we observed in current experiments is not crucially affected by the anisotropy of the body. In other word, we may regard that the point P2 is satisfied in our experiment.

We note that the above discussion is based on diffusion motion of a isolated body and is valid only when the suspension is sufficiently dilute. When the clusters are located within a short distance (such that the distance between center-of-mass positions of clusters are comparable with the gyration radius of clusters), the relative diffusion motions of clusters are significantly influenced by the morphology or orientation of clusters due to short-range HI.

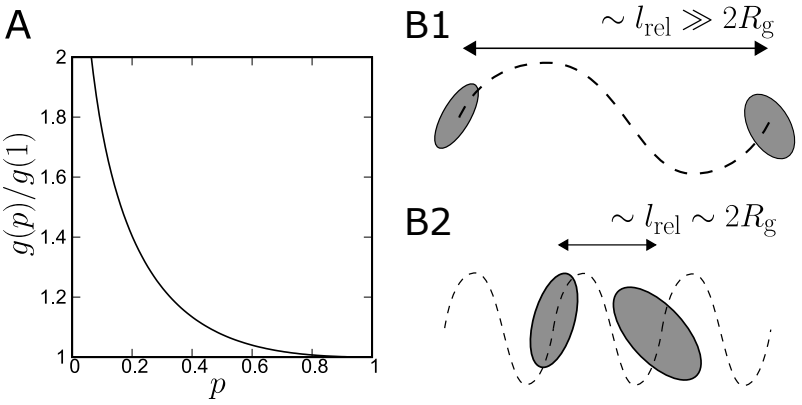

Fig. 6.6 **A.** Aspect ratio dependence of the ratio between hydrodynamic radius and gyration radius $R_{\rm g}$. The function g in the graph is defined by $g(p) = R_{\rm g}/R_{\rm h}$. **B.** The turnover of the characteristic length ℓ between the intercluster distance ($l_{\rm rel}$) and gyration radius ($R_{\rm g}$). In a sufficiently dilute suspension as in B1, we may regard ℓ as $l_{\rm rel}$. In a more dense suspension where $l_{\rm rel} \sim 2R_{\rm g}$, we need to consider the effect of morphology of clusters on ℓ.

6.2.3 What is the length that the characteristic length represents?

Given that P1 and P2 are valid in aggregation kinetics observed in our experiments, we may assume $R_{\rm g} \propto t^{1/d_{\rm f}}$. If we straightforwardly adopt the point P3 (i.e., $\ell \propto R_{\rm g}$) to the above, we immediately obtain $\alpha \sim 1/2$ since $d_{\rm f} \sim 2$ is observed. On the other side, we have observed $\alpha \sim 1/3$ at sufficiently dilute volume fractions ($\phi \lesssim 0.03$, see Fig 6.1B). These two seem conflicting, which is the motivation of the question Q1.

To consider this question, we examine the meaning of point P3 in a careful manner: specifically, here we consider what is the physical quantity that the characteristic length ℓ detects. Since we evaluate ℓ by the first moment of the structure factor, ℓ is considered to reflect the periodicity of the density fluctuation of colloids. Thus, ℓ dose not necessary correspond one-to-one with the characteristic size of the clusters (the mean value of the gyration radius $R_{\rm g}$ of the clusters in the above dis-

cussion). To see this, we reconsider a link between the average intercluster distance $l_{\rm rel}$ and the average value for the gyration radius of clusters $R_{\rm g}$. In a sufficiently dilute suspension such that $l_{\rm rel} \gg 2R_{\rm g}$, as we can see in Fig 6.6B1, the anisotropy of clusters dose not strongly affect the density fluctuation and the average intercolloid distance characterizes the periodicity of domain pattern. Since $\pi l_{\rm rel} n_{\rm c}/6 = 1$ and $n_{\rm c} \propto t^{-1}$, $\ell \propto l_{\rm rel} \propto t^{-1/3}$. Thus, $\alpha \sim 1/3$. This can be the answer for Q1. However, in a more dense suspension where $l_{\rm rel} \sim 2R_{\rm g}$, the gyration radius becomes the substitute for $l_{\rm rel}$. In other word, P3 is the case in this situation and thus we obtain $\alpha \sim 1/2$. The turnover of the characteristic length between $l_{\rm rel}$ and $R_{\rm g}$ can be a part of answer for the question Q2: the crossover behavior of growth exponent from $\alpha \sim 1/3$ to $1/2$. However, it is questionable whether P2 is valid or not in such intermediate volume fractions.

6.3 Summary

We study the volume fraction dependence of phase separation dynamics of colloids interacting with short-range attraction ($\Delta \sim 0.12$). We find that there are at least the two types of dynamic pathways to form connected network structure (percolation): one is the case where the connected structure is formed in the early stage of demixing, and the other is where percolation takes place via the diffusion of anisotropic clusters in the coarsening regime. We also observe that growth exponent α keeps an almost constant value $\alpha = 1/2$ in the former case. In the latter case, on the other hand, α shows crossover behavior from $\sim 1/2$ to $\sim 1/3$ with a decrease in volume fraction, and we confirm that the exponent $1/3$ continues up to the dilute suspensions where we cannot observe the percolated aggregates. By comparing the results with the phase separation dynamics interacting with long-range attractions (LJ potential), we show that the condition that the morphological relaxation time of colloidal clusters is comparable with (or much slower than) the frequency of cluster-cluster collisions is a key in the emergence of the latter case of percolation. We also mention a link between the latter case of percolation and the crossover behavior of growth exponents. These trends confirmed in our study, which is significantly different from those in ordinary binary mixtures, imply the importance of rheological characteristics of colloidal suspensions in phase separation dynamics. To obtain a systematic understanding for this phenomenon, a theoretical framework taking the viscoelastic effects of colloids into account is desirable.

Chapter 7

A universal growth exponent of network-forming phase separation

7.1 Motivation

Background

Phase separation phenomena of soft and bio matter containing liquids such as self-assembly of proteins have been attracting considerable attention from both fundamental and technological viewpoints. For example, quite recently, the formation of membraneless organelles by liquid-liquid phase separation has been a topic of intensive research in biology [182, 183, 184, 185, 17]. In general, phase separation starts from a small scale and then the characteristic size of phase-separated domains grows with time to a macroscopic scale. Thus, it is crucial to understand how phase-separation structures are selected and coarsen with time. This is important not only from a fundamental scientific viewpoint, but also from an applications viewpoint, e.g., the industrial processing of soft materials such as food, cosmetics, and paint industries [186].

Phase separation of liquid mixtures has been studied intensively in 20th century and the power-law growth of the characteristic domain size in the form of $\ell \sim t^{\alpha}$ ($\alpha = 1$ for a symmetric 50:50 mixture, and $\alpha = 1/3$ for an off-symmetric mixture) has been established on the basis of the self-simirality and scaling concept of phase-separation pattern [187, 5] (see Sec. 2.1.1). Later, unconventional phase separation, which is now known as viscoelastic phase separation, was discovered for dynamically asymmetric mixtures such as polymer solutions, whose components have very different dynamics. In this phase separation, the material specific dynamics plays a crucial role and leads to the breakdown of the self-similar growth [81, 82](see Sec. 2.2.2). Thus, after Siggia's seminal work [187] in 1979, there has been no discovery on a new coarsening law of self-similar nature. First we briefly review what we already knew about phase separation of simple fluid mixtures. Phase separation dynamics of a binary mixture of simple liquids with the same viscosity η is now well-understood. The relevant order parameter is the composition, ϕ. The temporal change in ϕ at a certain location $\boldsymbol{r}$ can be caused by both composition diffusion and hydrodynamic flow $\boldsymbol{v}$ under the constraint of the conservation

of the composition and the momentum. In this type of dynamically symmetric mixtures, network-forming phase separation is observed only in a symmetric composition region, where the two phases occupy similar volume. The coarsening of such a bicontinuous structure proceeds with the so-called Siggia's hydrodynamic pumping mechanism: There is the force due to a pressure gradient from a narrow part to a wider part of a tube forming a network structure of the characteristic size of ℓ, $\nabla p \sim \sigma/\ell^2$, ($\sigma$: interface tension). This force is to be balanced with the viscous force $\eta\nabla^2\boldsymbol{v} \sim \eta/\ell^2 d\ell/dt$ (η: viscosity), where $\boldsymbol{v}$ is the fluid velocity. Thus we obtain the above domain coarsening law of $\ell \sim (\sigma/\eta)t$.

However, this mechanism may not work if the slower phase cannot easily flow and shows an elastic response. Such a situation can generally be realized for dynamically asymmetric mixtures [81, 82]. In polymer solutions the slow rheological relaxational time of polymers plays a crucial role in phase separation in addition to the composition diffusion time, leading to the breakdown of self-similar growth. In this case, we can expect neither a simple scaling relation nor a power-law growth of domain size. Such non-universal behavior was indeed observed in both experiments and simulations [81, 82]. The lack of the self-similar growth is a direct consequence of the volume shrinking of the polymer-rich phase even after the formation of the sharp interface between the two phases. This non-universal nature comes from the fact that the slow relaxation of polymer involves complex topological entanglements (see Chap. 2.2.2 for more detail).

Unusual coarsening behavior of network structures in two apparently different types of systems

However, viscoelastic phase separation in colloidal suspensions may be much simpler than that in polymer solutions. This is because the dynamics of colloids can be scaled by the particle radius a alone since it is the only characteristic length of the system, implying a possible self-similar growth of phase-separation pattern. Indeed, we recently noticed that unusual coarsening behavior of network structures has been reported in two apparently different types of systems, (i) gas-liquid phase separation in a single-component system (molecular systems [188, 64, 188, 189]) and (ii) phase separation in soft matter (colloidal suspensions [9, 190, 43, 191], protein solutions[11] and lyotropic liquid crystal [125]). Interestingly, we have recently realized that in these systems phase separation structures with network morphology commonly grow their characteristic network size ℓ as $\ell \propto t^{1/2}$ while retaining their connectivity, although the time range of the power law behavior was rather limited. We note that there are at least two features that these systems have in common, besides the spontaneous formation of a network structure and its preservation during the growth: The first feature is that phase separation dynamics is driven by gas-liquid spinodal instability for both cases. The other is that this exponent is observed only for a sufficiently deep quench. Finally, these systems are very simple in the sense that the dynamics can be related to the unique length scale, i.e., particle size a. These facts imply that there is some universal physical mechanism behind this power-law growth of the particular growth exponent 1/2.

This motivates us to perform extensive simulations to cover a wider time range and confirm the power-law growth of domains. From the theoretical viewpoint,

on the other hand, the key to understand the unusual coarsening behavior is to recognize that for such a mixture under a deep quench the rate of deformation induced by phase separation rather easily exceeds the characteristic rheological time of the slow-component-rich phase. This is because the slow-component-rich phase approaches a glass transition under a deep quench, leading to slow glassy dynamics. If the slow-component-rich phase forms a network structure, a tube of the network structure made of this phase should respond as an elastic body rather than as a fluid to the mechanical force due to a pressure gradient generated by the interface tension. In this chapter, we consider the impact of such elastic response on the coarsening of a network structure during phase separation. We both numerically and theoretically find a new domain coarsening law of $\ell \sim t^{1/2}$. We argue that such coarsening behavior should be generally relevant to colloidal suspensions, protein solutions, and liquid phase separation coupled with glassiness. Understanding the formation process of network-like aggregated structures is significantly important not only fundamentally, but also for materials science, since the nature of network and porous structures drastically affects the functions of soft- and bio- materials such as elastic, surface, and transport properties [98].

7.2 Method

To reveal the mechanism responsible for the unconventional power-law growth, we performed numerical simulations of phase separation in two types of systems. One is phase demixing of a colloidal suspension, and the other is gas-liquid phase separation of a single-component fluid. For the former, we used a hydrodynamic simulation model, fluid particle dynamics (FPD) method [7]. For the latter, we used molecular dynamics simulations.

Simulations of colloidal phase separation

To study colloidal phase separation numerically, we consider a suspension of colloids interacting with a Lennard-Jones (LJ) potential, $U(r) = 4\epsilon_{\rm LJ}[(r/\sigma_{\rm LJ})^{-12} - (r/\sigma_{\rm LJ})^{-6}]$. We define the volume fraction of colloids ϕ as $\phi = \pi\sigma^3 N/6L^3$, where N and L are the number of the colloids and the side length of our simulation box (cubic), and set $\phi = 0.1$, which is a volume fraction dense enough to from network structures upon phase separation. In the data analysis, we use the length unit σ as $\sigma = \sigma_{\rm LJ}$ and the time unit $\tau_{\rm d}$ as $\tau_{\rm d} = 3\pi\eta\sigma^3/\epsilon_{\rm LJ}$, where η is the viscosity of the solvent. $\tau_{\rm d}$ corresponds to the time during which a free colloid under an external constant force of amplitude $\epsilon_{\rm LJ}/\sigma$ moves by its diameter σ. The depth of the LJ potential $\epsilon_{\rm LJ}$ is set such that the "Reynolds number" $Re = \rho\sigma^2/\eta\tau_{\rm d} = 0.8$ (ρ being the density of the solvent).

Here we check whether our simulation reproduce a Stokes flow under this parameter setting. First we consider the motion of a free colloid. Assuming that a constant force $F_{\rm d}$ is applied to the particle at time $t = 0$, the velocity of the particle V can be written as

$$M_{\rm eff}\frac{dV}{dt} = F_{\rm d}\psi^{\rm T}(\frac{t}{\tau_{\rm a}}) \tag{7.1}$$

where $M_{\rm eff} = \frac{3}{2}M$ is the effective mass of the colloid. Then, $\psi^{\rm T}(\frac{t}{\tau_{\rm a}})$ is the memory function for translational motion that takes hydrodynamic effects into account (see Eq. 4.23 for the functioal form). $\tau_{\rm a}$ is the time required for solvent to diffuse over the radius of the colloid and given as $\tau_{\rm a} = (\frac{\sigma}{2})^2/\alpha$, which relates to $\tau_{\rm d}$ by $\tau_{\rm a} = Re\ \tau_{\rm d}/4$.

At the timescale $t \sim \tau_{\rm d}$, $\psi^{\rm T}$ can be estimated as $\psi^{\rm T}(4Re^{-1}) = \psi^{\rm T}(5) \sim 0.0076$. The ratio between the amplidute of momentum of the particle and that of the force is given by

$$\frac{M}{F_{\rm d}}\frac{dV}{dt} = \frac{2}{3}\psi^{\rm T}, \tag{7.2}$$

which is estimated as ~ 0.0051, allowing us to assume that the force acting on the particle is almost perfectly balanced with the viscous drag force, i.e. the inertia term can be neglected.

Simulations of phase separation of a single-component fluid

To study gas-liquid phase separation of molecular systems, we use a single-component Lennard-Jones system and employ the usual Lennard-Jones units (i.e., $\sigma_{\rm LJ}$, $\tau_{\rm LJ} = \sqrt{\sigma_{\rm LJ}^2 m/\epsilon_{\rm LJ}}$, $\epsilon_{\rm LJ}$ for length, time and energy units). We perform molecular dynamics simulation with NVT ensemble by utilizing LAMMPS. We control temperature Nose-Hoover thermostat. We set the number density of particles as $\rho = 0.33$ where we can see the formation of the network structure. The scaled energy is set as $\epsilon_{\rm LJ}\beta = 0.1$, which can bring the system to an elastic regime. We apply the same simulation box size as in the above FPD simulation ($L/\sigma = 69.2$).

7.3 Results

7.3.1 Self-similar coarsening

First we focus on network-forming phase separation in colloidal suspensions. In our previous studies (see Chap. 5), we experimentally observed the growth exponent 1/2 in network-forming phase separations of colloids interacting with short-range depletion attractions, and also found that the dynamic network coarsening process can be almost perfectly reproduced by FPD simulations without any adjustable parameter, thanks to the scale-invariant nature of the phenomena. We also showed that the phase separation kinetics cannot be reproduced by Brownian Dynamics simulations without hydrodynamic interactions. This indicates the crucial role of momentum conservation in this growth mechanism. Here we perform numerical simulations of phase separation of colloidal suspensions by the FPD method without thermal noise, which corresponds to an extreme deep quench to zero temperature. As mentioned above, we note that the growth exponent 1/2 was observed in colloidal suspensions and protein solutions, whose large-size components interact with different types of attractive potentials. Here we consider as an example colloids interacting with a Lennard-Jones (LJ) potential, whose interaction range is longer than the depletion potential.

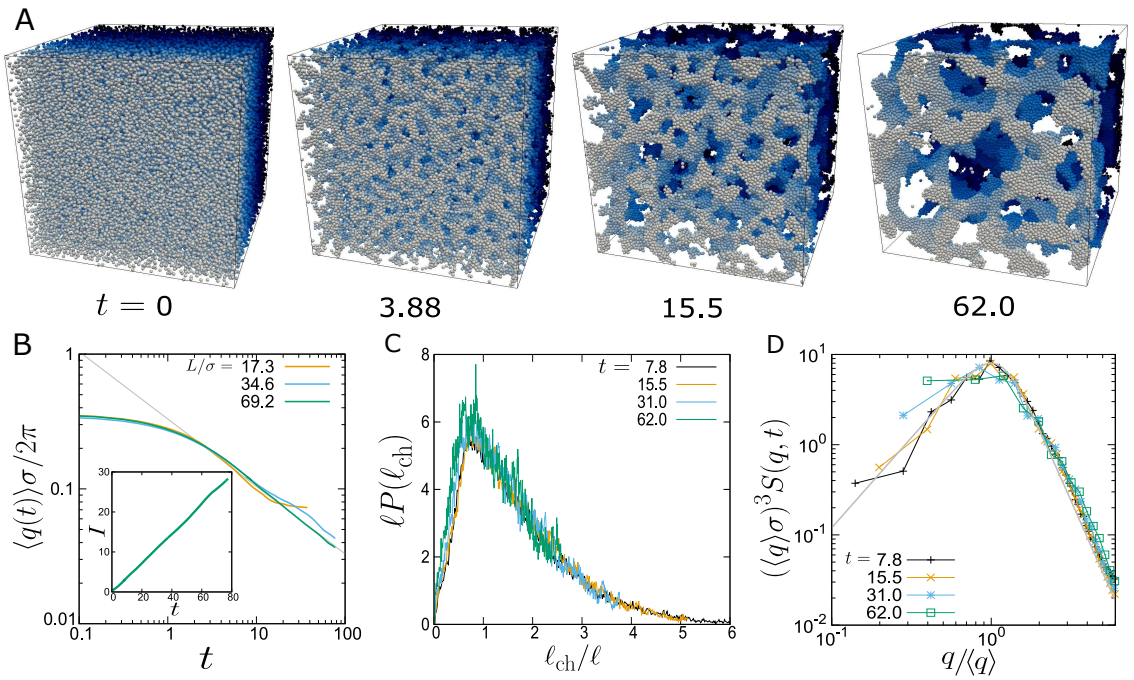

Fig. 7.1 **Coarsening behavior of network-forming phase separation of colloidal suspensions.** **A,** Time evolution of 3D phase-separation structures. Particles are coloured to distinguish front particles from back ones. **B,** Temporal change of the characteristic wave number $\langle q \rangle$ for three different simulation box sizes $L/\sigma = 17.3, 34.6, 69.2$. The gray line represents a power-law decay with exponent 1/2. The inset shows the temporal change of the integrated intensity $I(t)$ of the structure factor $S(q,t)$. **C,** The chord distribution functions $P(\ell_{\rm ch})$ at various times, after scaling the length by the characteristic length $\ell = 2\pi/\langle q \rangle$). **D,** Scaled structure factors, $(\langle q \rangle \sigma)^d S(q,t)$, for various times. The gray line shows a theoretical prediction [192] for the master curve $Ax^2/(\gamma/2 + x^{2+\gamma})$, where $x = q/\langle q \rangle$, $\gamma = d+1$, and A is a constant. All the figures except the main graph of panel a is the results for the largest simulation box ($L/\sigma = 69.2$).

We show in Fig. 7.1A the time evolution of phase-separation structures in the colloidal suspension. There we can clearly see that a space-spanning network structure is spontaneously formed in the early stage and its characteristic length scale grows afterward. On noting that the absence of thermal noise at zero temperature, the coarsening cannot be due to thermal activation, but should be of purely mechanical nature [190]. In order to quantitatively characterize the coarsening behavior, we computed the temporal change of the characteristic wave number, $\langle q(t) \rangle$, defined as the first moment of the structure factor $S(q,t)$: $\langle q(t) \rangle = \int dq\ qS(q,t) / \int dq\ S(q,t)$ (see Sec. 3.1.5 for how to compute $S(q,t)$). This characteristic wave number is inversely proportional to the typical size of the network, $\ell(t) = 2\pi/\langle q(t) \rangle$. To check whether our simulation box is large enough to study the coarsening behavior without suffering from a finite-size effect, here we performed the data analysis for simulation results for three different sizes of the simulation box, $L/\sigma = 17.3, 34.6, 69.2$ (σ:

particle size). We see in Fig. 7.1B that all results show almost identical coarsening behavior in the late stage: $\langle q \rangle \sim t^{-0.5}$. At the same time, however, we see that the results for $L/\sigma = 17.3, 34.6$ deviate from the power-law decay at certain times. In contrast, the one for $L/\sigma = 69.2$ continue to coarsen, obeying the power law over the entire time range of the simulation. This tells us that the deviation from the power law decay is a consequence of the finite size effects. Unlike previous reports [188, 64, 189, 9, 43, 191, 11], this is the first observation of the power-law growth far more than a decade. Hereafter, we focus only on the simulation results with the largest simulation box.

To reveal which length scale of real structures corresponds to ℓ, we also perform the structural analysis in real space by using the chord length distribution function $P(\ell_{\rm ch})$ [98]. Organizing the results based on the dynamic scaling law, we find that the distribution functions characterizing the phase-separation structures are collapsed onto a single master curve after scaling with the growth exponent of 1/2 (see Fig. 7.1c), i.e., $\ell(t)P(\ell_{\rm ch}) = f(\ell_{\rm ch}/\ell(t))$, where $f(\cdot)$ is some function. These results clearly indicates the self-similar nature of the coarsening, showing the presence of a unique physical mechanism behind this coarsening process. In Fig. 7.1c, we can also see that $\ell_{\rm ch}/\ell(t) \sim 1$, meaning that the length $\ell(t)$ obtained by the structure factor corresponds to the characteristic pore size of the network structure. In Fig. 7.1d, we show that $S(q,t)$ is also scaled as $\langle q \rangle^d S(q,t) = g(q/\langle q \rangle)$ (d: the spatial dimension; $g(\cdot)$: some function), also supporting the presence of the self-similarity in pattern evolution. Moreover, denoting q-integral of $S(q,t)$ as $I(t)$, we can directly confirm the following relation, which should hold for self-similarity growth: $I(t) \propto \ell^{d-1} = \ell^2$. In the inset of Fig. 7.1b, we show that $I(t)$ indeed linearly increases with time, suggesting that $\ell \propto t^{1/2}$ as expected.

7.3.2 Dynamic scaling for elastic motion in colloid-rich phase

As shown above, the network coarsening process has self-similarity, indicating that this growth exponent 1/2 continues as long as the condition $\ell \gg \sigma$ is satisfied. This allows us to make a coarse-grained description of the coarsening process. We consider this problem by focusing on the similarity and difference between our problem and the well-known coarsening process of phase separation of an ordinary binary fluid mixture. The fact that in the cluster forming phase separation in a colloidal suspension the growth exponent is about 1/3 rather than 1/2 and the relevant mechanism is the Brownian coagulation mechanism [187, 5] suggests that the connectivity of the network must play a key role in the emergence of the growth exponent of 1/2. As mentioned in Introduction, in a network morphology, the interfacial tension generates a mechanical force on a tube reflecting the spatial variation of its thickness. For the case of a binary liquid mixture, this force is a pressure gradient force, producing hydrodynamic flow along a tube. Thus, the crucial question here is what is the key transport process under such a mechanical force for network coarsening in a colloidal suspension.

To address this problem, we should pay a special attention to slow dynamics of dense colloidal aggregates, which exhibits an elastic response to deformation faster than the rheological relaxation time. First we analyze the strain field $\epsilon_{ij}(\boldsymbol{r}, t)$ by

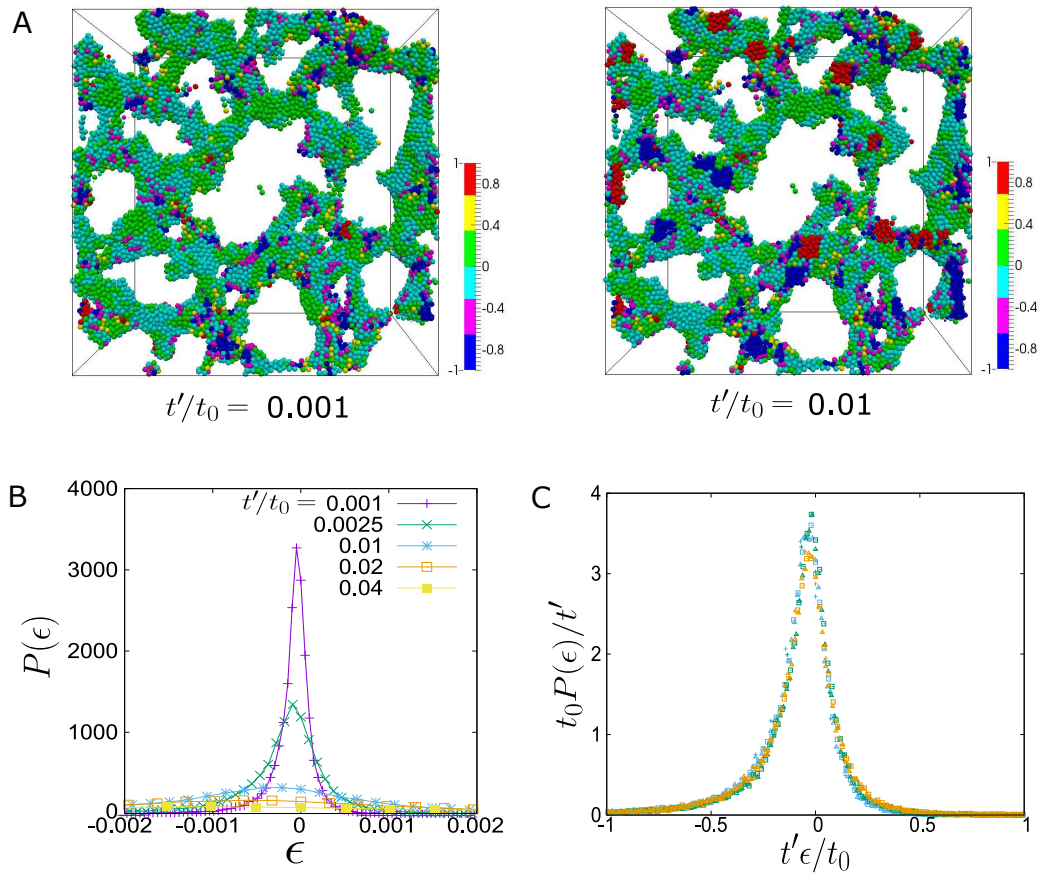

Fig. 7.2 **Bulk strain in the colloid-rich domain. A,** Real-space mapping of the bulk strain around the particles. Colour labelled on the particles represent the value of the scaled bulk strain $t'\epsilon/t_0$. The reference time of strain is chosen as $t_0 = 63.0$. Here we show only particles which are located one quarter on the top side to make the details of structures more visible. **B,** The time evolution of the distribution of bulk strain $P(\epsilon)$. Here t' represents the duration of time from the reference time $t_0 = 62.0$ to measure the strain. **C,** $P(\epsilon)$ after scaling ϵ by t'/t_0. The data are sampled from the data whose reference time is $t_0 = 31.0$ (blue), 46.5 (green), 62.0 (grown symbols). Cross, triangle and square symbols represent the data at $t'/t_0 = 0.001, 0.01, 0.02$, respectively.

coarse-graining the displacements of colloidal particles. We compute the strain field $\epsilon_{\alpha\beta}$ following Ref. [193]. Denoting the displacement of i-th particle from time $t = 0$ to $t = t$ as $\boldsymbol{u}_i(t) = \boldsymbol{R}_i(t) - \boldsymbol{R}_i(0)$, a coarse-grained displacement field $\boldsymbol{u}(\boldsymbol{r}, t)$ can be written as,

$$\boldsymbol{u}(\boldsymbol{r}, t) = \frac{\sum_i \boldsymbol{u}_i(t) g(\boldsymbol{r} - \boldsymbol{R}_i(t))}{\sum_i g(\boldsymbol{r} - \boldsymbol{R}_i(t))}, \tag{7.3}$$

where $g(\boldsymbol{r})$ is a coarse-grain function and we employ the following Gaussian form:

$g(\boldsymbol{r}) = \exp(-\boldsymbol{r}^2/\sigma^2)/(\pi\sigma^2)^{3/2}$. The strain feild $\epsilon_{\alpha\beta}$ is defined as

$$\epsilon_{\alpha\beta}(\boldsymbol{r}, t) = \frac{1}{2}\left(\frac{\partial u_\alpha(\boldsymbol{r}, t)}{\partial r_\beta} + \frac{\partial u_\beta(\boldsymbol{r}, t)}{\partial r_\alpha}\right). \tag{7.4}$$

We sample the strain at the center-of-mass positions of particles which have more than 9 neighbouring particles, and compute the distribution of the strain $P(\epsilon_{\alpha\beta})$. Here we regard two particles as neighbouring ones if the distance of the two particles are less than 1.2σ.

We show in Fig. 7.2b the time evolution of the distribution function $P(\epsilon)$ of bulk (or, volume) strain with respect to the reference time $t_0(= 62.0)$, $\epsilon = \epsilon_{kk}(t_0 \to t_0 + t')$. We can see that the distribution broadens with the increase of t'. Here we stress that the self-similarity and dynamic scalability hold for the phenomena. Thus, if the elastic response of the colloid-rich phase plays an important role, we expect that the dynamical scaling holds for the distribution function of $P(\epsilon, t_0, t')$. Indeed, we find that it can be scaled as $\frac{t'}{t_0}P(\epsilon, t_0, t') = f(t'\epsilon/t_0)$ (see Fig. 7.2c). From this scaling, we may conclude at least two things: Firstly, ϵ is proportional to t' for a certain t_0. This can be understood form the nature of Stokes flow: in a short-time scale in which relative displacements between the center-of-mass positions of colloidal particles are negligible comparing to the particle size, the velocities of colloidal particles should be constant. Therefore, the displacements of particles are to be proportional to the time duration, resulting in the proportionality of the strain to the time duration. Secondly, since $t_0 \propto \ell^2$ and ϵ is a dimensionless and infinitesimal quantity, t' should also be proportional to ℓ^2. This clearly means that the growth exponent $\alpha = 1/2$ reflects the elastic response inside the colloid-rich phase, and the coarse-grained equation governing the elastic behaviour should be the equation in which τ_{e} and length scale ℓ_{e} satisfy $\tau_{\mathrm{e}} \propto \ell_{\mathrm{e}}^2$.

7.3.3 Dynamic couping between elastic motion of colloids and solvent flow: poroelasticity

Now the problem is to elucidate the underlying physical mechanism resposible for this coarsening law. Regarding this, we can get some important insights by recalling the results of our previous work (see Chap. 5). We found that for network-forming colloidal phase separation simulated by FPD, which properly incorporates many-body hydrodynamic interaction between colloids, domains coarsen as $\ell \sim t^{0.5}$, whereas for the one simulated by Brownian Dynamics (BD) method without hydrodynamic degrees of freedom domains coarsen as $\ell \sim t^{0.25}$ even at the same state point as in FPD. Thus, it seems natural to think that the constitutive equation must include some dynamic coupling between colloids and the solvent. This clearly indicates that the coexistence of elasticity and fluidity, or poroelasticity, is the key to this novel coarsening process. Thus, we consider the domain coarsening kinetics under poroelastic effects in two fluid model [76, 77], which can deal with the degree of freedom of both colloids and solvent (see also Sec. 2.2.1).

Denoting the local volume fraction of colloids as ϕ and the velocity field of colloids and solvent as $\boldsymbol{v}_{\mathrm{c}}$ and $\boldsymbol{v}_{\mathrm{s}}$, a basic set of kinetic equations of the viscoelastic model of

colloidal phase separation, whose free energy density $\mathscr{F}_\phi$ scaled by thermal energy is given by $\mathscr{F}_\phi(\phi) = \int d\boldsymbol{r}\left[f(\boldsymbol{r}) + \frac{1}{2}C|\nabla\phi|^2\right]$, are described as follows:

$$\frac{\partial\phi}{\partial t} = -\boldsymbol{\nabla}\cdot(\phi\boldsymbol{v}_\mathrm{c}) = \boldsymbol{\nabla}\cdot((1-\phi)\boldsymbol{v}_\mathrm{s}), \tag{7.5}$$

$$\boldsymbol{v}_\mathrm{s} - \boldsymbol{v}_\mathrm{c} = \frac{(1-\phi)}{\zeta_R}[\boldsymbol{\nabla}\cdot\boldsymbol{\Pi} - \boldsymbol{\nabla}\cdot\boldsymbol{\sigma}_\mathrm{c}], \tag{7.6}$$

$$\rho\frac{\partial\boldsymbol{v}}{\partial t} = -\boldsymbol{\nabla}\cdot\boldsymbol{\Pi} + \boldsymbol{\nabla}\cdot\boldsymbol{\sigma}_\mathrm{c} - \nabla p + \eta\nabla^2\boldsymbol{v}, \tag{7.7}$$

$$\boldsymbol{\nabla}\cdot\boldsymbol{v} = 0. \tag{7.8}$$

where $\boldsymbol{v}$ is the average velocity given as $\boldsymbol{v} = \phi\boldsymbol{v}_\mathrm{c}+(1-\phi)\boldsymbol{v}_\mathrm{s}$, ζ_R is the effective friction constant between colloids and the solvent after coarse-graining and η is the solvent viscosity. Equations (7.5), (7.7) and (7.8) represents the material conservation law, the momentum conservation law, and the incompressible condition, respectively. In the above, $\boldsymbol{\Pi}$ is the osmotic stress tensor, which is related to the thermodynamic force $\boldsymbol{F}_\phi$ as $\boldsymbol{F}_\phi = -\boldsymbol{\nabla}\cdot\boldsymbol{\Pi} = -\phi\nabla(\delta\mathscr{F}_\phi/\delta\phi)$. Then, $\boldsymbol{\sigma}_\mathrm{c}$ is the mechanical stress tensor acting on colloids. Equation (7.6) represents the mechanical balance between these forces and the viscous force resulting from the relative motion between colloids and the solvent.

In order to close the set of the equations described above, we need a constitutive equation describing the temporal change of $\boldsymbol{\sigma}_\mathrm{c}$, but there is no consensus on the form of the constitutive equation for a colloidal system. Fortunately, however, the self-similar network coarsening takes place in an *elastic* regime and thus we need not to consider the relaxation of $\boldsymbol{\sigma}_\mathrm{c}$. However, since the volume fraction ϕ in the late stage ($\sim\phi_0$) reaches its value in the glassy state, or is affected by mechanical rigidity, we need a special care: the elastic properties of the colloid-rich phase cannot be described by the compressibility alone, which is of thermodynamic origin, and we need to consider *additional* elasticity of purely mechanical origin. We assume the additivity of the thermodynamic and mechanical moduli on the basis of a parallel spring model. As we are interested in only small deformation in the elastic regime, we assume that the stress *mechanically* generated on a colloid network is written in the linear order as

$$\sigma_{\mathrm{c},ij} = G_\mathrm{B}(\phi)\epsilon\delta_{ij} + G_\mathrm{S}(\phi)(\epsilon_{ij} + \epsilon_{ji} - \frac{2}{3}\epsilon\delta_{ij}), \tag{7.9}$$

where G_B and G_S are the elastic moduli for bulk and shear deformation respectively.

In such a regime, elastic deformation of the network structure is realized by slow fluid transport through the dense colloid-rich phase, which is the limiting process of the deformation [194]. Such deformation is accompanied by a small local composition change $\delta\phi$ around its average value ϕ_0. We consider this process of elastic deformation controlled by the solvent transport inside the colloid-rich domains. To do so, we set the reference time to t_0 and then consider small deviations of physical quantities such as the local colloid volume fraction $\delta\phi$ and volume deformation ϵ, from the reference state at t_0. Within a linear regime, the osmotic stress can be written as, $\nabla\cdot\Pi \sim -\kappa_\mathrm{OS}(\phi_0)\epsilon$, where $\kappa_\mathrm{OS} = \phi^2\partial^2 f(\phi)\partial\phi^2$ is the osmotic bulk modulus of the colloid-rich phase. Here we use a relation $\delta\phi \sim -\phi_0\epsilon$, which is obtained

from the material conservation law in Eq. (7.5). In the elastic regime, the time and spatial gradient of the average velocity filed is expected to be negligible. Thus, we obtain the following relations:

$$\boldsymbol{v}_{\rm s} - \boldsymbol{v}_{\rm c} = k\boldsymbol{\nabla} p, \tag{7.10}$$

$$0 = \partial_j[(\kappa_{\rm OS} + G_{\rm B})\epsilon\delta_{ij} + G_{\rm S}(\epsilon_{ij} + \epsilon_{ji} - \frac{2}{3}\epsilon\delta_{ij}) - p\delta_{ij}], \tag{7.11}$$

where $k = (1-\phi_0)^2/\zeta_R(\phi_0)$ is the permeability of colloid-rich phase. Eqs. (7.10) and (7.11) has mathematically the same form as the that of the well-known constitutive equation in Biot's poroelastic theory [194], which is often used for describing fluid-saturated elastic materials.

As we are interested in volumetric elastic response of the colloid-rich domain, we consider the bulk part of Eq. (7.11): $0 = \boldsymbol{\nabla}[(\kappa_{\rm OS} + G_{\rm B})\epsilon - p]$. By substituting these relations into Eqs. (7.5), (7.6) and (7.11), we obtain the following diffusion-type equation for ϵ:

$$\frac{\partial}{\partial t}\epsilon \cong D_{\rm P}\nabla^2\epsilon, \tag{7.12}$$

where

$$D_{\rm P} = k\left[\kappa_{\rm OS}(\phi_0) + G_{\rm B}(\phi_0)\right] \tag{7.13}$$

is the poroelastic diffusibility. Here we find that $D_{\rm p}$ is deterimend by the permeability of sovlent for colloid-rich phase and the elastic moduli of the colloid-rich phase.

This diffusion-type equation describes the temporal change of the local colloid composition upon structural evolution driven by the interfacial force: this process proceeds, under the elastic force balance, via fluid transport through densely packed colloids driven by local pressure gradient. Although the average colloid composition in the colloid-rich phase is ϕ_0 and does not change in time, the local composition change is necessary for elastic deformation to take place. Its temporal change obeys the above diffusion-type equation. In Fig. 7.3, we show that the volume fraction of the colloid-rich domain is indeed almost constant in the scaling regime as $\phi_0 = 0.54 \pm 0.03$. In Fig. 7.2a, we show the 3D structures of the colloid-rich network together with real-space mapping of bulk strain ϵ. Here we can clearly see that the locations where compression or dilation takes place are not randomly distributed, but distributed with the characteristic length scale of the network structures ℓ. This together with the self-similar nature of the domain growth justifies the choice of the length scale ℓ as the space unit of the Laplacian in front of $\delta\phi$ in Eq. (7.12). Thus, we obtain the following domain coarsening law:

$$\ell^2 \cong D_{\rm P} t, \tag{7.14}$$

which reproduces growth exponent $\alpha = 1/2$.

In Fig. 7.2C, we show that the distributions of the bulk strain at different times can be mapped on a master curve. However, for large deformation at $t'/t_0 \gtrsim 0.05$, the scaling relation starts to break. This means that the linear elastic description

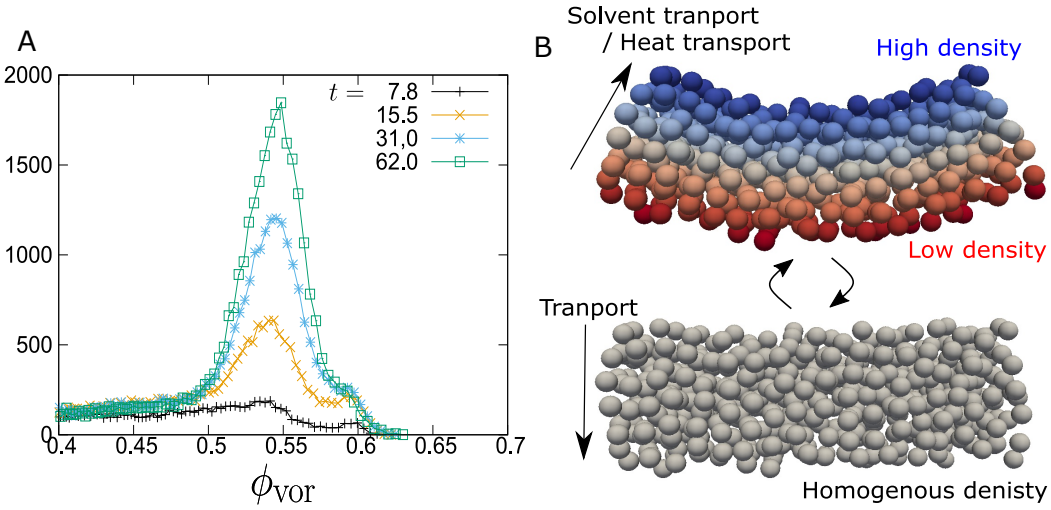

Fig. 7.3 **A**, The distribution of local volume fraction $\phi_{\rm vor} = \pi\sigma^3/6V_{\rm vor}$ where $V_{\rm vor}$ is the volume of Voronoi cell. In the early stage, since the most of particles are located at the interface of the colloid-rich phase, or having only a few neighbouring particles (~ 6) than in bulk (~ 12), the distribution is very flat. But in the late stage ($t \gtrsim 31.0$), we can see a rather sharp peak. The local volume fraction in the colloid-rich phase in the late stage is estimated approximately as $\phi_{\rm vor} = 0.54 \pm 0.03$. **B**, A schematic illustration of the poroelastic and thermoelastic deformation. Elastic volumetric deformation of dense colloidal domain involves solvent transport inside of the domain. For example, in the case of bending deformation of rod-like domain as shown in the figure, where the volume fraction increases/decreases in the upper/lower part of the domain, solvent contained in the domain should transport from the upper part to the lower part. In a single-component molecular system, heat transport takes place in stead of solvent transport. The solvent and heat transport are the limiting process of viscoelastic phase separation in colloidal and molecular systems, respectively.

is no longer valid in this large deformation regime. To discuss such a large deformation accompanying ruptures of the network arms and merges of the pores (see the red or blue parts of Fig. 7.2A), we need to develop a constitutive equation fully incorporating viscoelastic relaxation modes of dense colloidal suspension.

7.3.4 Correspondence with a single-component fluid: thermoelasticity

Next we turn our attention to network formation in a deeply quenched single-component fluid [188, 64, 189], which also shows the domain growth exponent of 1/2. Firstly, we check whether this domain growth law really exists and there is self-similarity during the coarsening. To this end, we performed molecular dynamics simulation with NVT-ensemble for gas-liquid phase separation of a single-component Lennard-Jones fluid. In Fig. 7.4A, we show the temporal change of characteristic wave number $\langle q \rangle$. We find that $\langle q \rangle$ indeed decays with a power-law exponent close to 1/2 in a wide range of temperature (at least $2 \leq \beta_{\rm LJ}\epsilon \leq 100$). In the very late stage of the coarsening, we observe the formation and growth of crys-

tals in the dense liquid phase. Since such a crystallization process during gas-liquid demixing is out of scope in this research, we only focus on the time regime where the fraction of crystals is less than 3%.

Now we consider the physical mechanism responsible for this network coarsening dynamics in a phase-separating single-component fluid. We have seen in the above that the exponent 1/2 in colloidal systems can be explained by the slow transport of a liquid component in a dense colloid-rich phase, which controls elastic deformation of the colloid-rich network. Similarly, to colloidal suspensions, a deep quench leads to phase separation of a fluid to dense liquid and dilute gas phases, whose characteristic rheological relation times are quite different. Then, the typical deformation rate produced by phase separation can exceed the relaxation rate of the dense liquid phase. This leads to viscoelastic phase separation, or the emergence of elastic behavior. We note that for a single-component fluid there is no two-fluid nature, which plays a crucial role in slow elastic deformation of the dense colloid-rich phase through its coupling to slow fluid transport, but there is a slow mode associated with thermal transport.

To elucidate the coarsening mechanism, we consider hydrodynamic equations for a single-component fluid [5]. A basic set of hydrodynamic equations corresponding to mass, momentum and energy conservation can be expressed as the following equations of time evolution for mass density ρ, velocity $\boldsymbol{v}$ and entropy density s:

$$\frac{\partial \rho}{\partial t} = -\nabla \cdot (\rho \boldsymbol{v}) \tag{7.15}$$

$$\frac{\partial}{\partial t}(\rho \boldsymbol{v}) = -\nabla \cdot \boldsymbol{\Pi} + \nabla \cdot \boldsymbol{\sigma} \tag{7.16}$$

$$\rho T \frac{\partial s}{\partial t} = -\rho T \nabla \cdot (s\boldsymbol{v}) + \nabla \cdot (\lambda \nabla \boldsymbol{T}) + \Phi, \tag{7.17}$$

where T and λ are the local temperature and the heat conductivity respectively. $\boldsymbol{\Pi}$ is the pressure tensor, which is given by the thermal-energy-scaled free energy functional $\mathscr{F}$ via $\nabla \boldsymbol{\Pi} = \rho \nabla \frac{\delta \mathscr{F}}{\delta \rho}$. $\boldsymbol{\sigma}$ is the viscoelastic stress and Φ is the dissipation function. In the late stage of coarsening, elastic deformation is induced by a small local change of ρ, $\delta\rho$ around the average value, ρ_0. ρ_0 is roughly kept constant during the scaling regime as in the case of colloidal phase separation, which is the origin of the self-similarity. The presence of self-similarity during the phase separation process has been demostrated in Ref. [188, 64, 189]. Focusing on such small composition change, we only consider the volumetric deformation ϵ for viscoelastic stress: $\nabla \cdot \sigma = G_{\mathrm{B}}(\rho_0)\nabla\epsilon$, where $G_{\mathrm{B}}(\rho)$ is the bulk elastic modulus of purely mechanical origin, which originates from the glassiness of the high density phase, as in the case of colloidal phase separation. Such a local volumetric change is expected to produce a deviation of the entropy density from its average value s_0 in a short timescale (i.e. in a time scale faster than thermal transport). Then, such a change in entropy is slowly homogenized by heat transfer. The deviation of entropy δs can be estimated as $\delta s = (C_V/T_0)\delta T - (\alpha\kappa/\rho_0)\delta\rho$, where C_V, $\kappa = \rho^2(\partial^2 f/\partial\rho^2)$ and α is the specific heat capacity at constant volume, the bulk modulus and the thermal expansion constant respectively. Therefore, here we may write the free energy

density in the elastic regime as

$$\mathscr{F} = \mathscr{F}_\rho + \int d\boldsymbol{r} \frac{\alpha\kappa}{\rho_0} \delta\rho\delta T + \mathscr{F}_T, \tag{7.18}$$

where the functional form of $\mathscr{F}_\rho$ is the same as $\mathscr{F}_\phi$ introduced in the above. $\mathscr{F}_T$ is the extra term regarding temperature. From the above, the pressure tensor is calculated as $\nabla \cdot \boldsymbol{\Pi} \sim \rho_0(\frac{\partial^2 f}{\partial \rho^2}|_{\rho=\rho_0})\nabla\delta\rho + \alpha\kappa\nabla T$. By neglecting the viscous dissipation (Φ) and the convective terms in Eqs. (7.16) and (7.17) and by canceling temperature, we obtain the following diffusion equation regarding ϵ,

$$\frac{\partial}{\partial t}\epsilon \cong D_{\mathrm{T}}\nabla^2\epsilon, \tag{7.19}$$

where

$$D_{\mathrm{T}} = \frac{\lambda}{\rho_0 C_p} \frac{1 + G_{\mathrm{B}}/\kappa}{1 + \gamma^{-1} G_{\mathrm{B}}/\kappa}, \tag{7.20}$$

is the thermal diffusion coefficient, C_p is the specific heat capacity at constant pressure, and $\gamma = C_p/C_V$ are the specific heat ratio, respectively. In the above, we use a thermodynamic relation, $\alpha^2\kappa T = C_p - C_V$. In the case where the relaxation of mechanical bulk stress is sufficiently fast and we can neglect G_{B}, D_{T} becoms $\lambda/\rho_0 C_p$, which coincides with the thermal diffusibility of ordinary single-component fluids [5]. from which we can derive the growth exponent 1/2 as in the case of colloidal suspensions.

To check the above mechanism based on the slow thermal transport is really a relevant mechanism or not, we calculate the effective temperature, or the kinetic energy of each particles, $K_i(t) = \frac{1}{2}m\langle \boldsymbol{V}_i^2\rangle(t)$, where the ensemble average for the velocity of i-th particle, $\boldsymbol{V}_i$ is taken over the time span $[t - \tau_{\mathrm{LJ}}/2, t + \tau_{\mathrm{LJ}}/2]$. Figure 7.4D shows an example of the real-space distribution of K_i, where we can clearly see that the particles with high/low kinetic energy are not randomly distributed, but heterogeneously with the characteristic length scale of the network structure ℓ. This observation strongly supports the above proposed mechanism.

7.3.5 Importance of dynamical asymmetry and dimension dependence of coarsening behavior

In the above, we have shown that the power-law domain of the exponent 1/2 in network-forming gas-liquid phase separation of colloidal suspensions and atomic (or molecular) systems is a consequence of slow elastic motion of the dense phase, whose limiting process is liquid transport (poroelasticity) and thermal transport (thermoelasticity) respectively. Here we examine in more detail under what conditions this coarsening behavior is to be observed. We need a sufficiently deep quench to induce strong enough dynamic asymmetry between the two phases. However, we note that the growth exponent of 1/2 is not observed for ordinary binary liquid mixtures. In Fig. 7.4B, we show the temperature dependence of the coarsening behaviour for a binary liquid mixture. We can see that the growth exponent significantly decreases with a decrease in temperature. By contrast, in a single-component

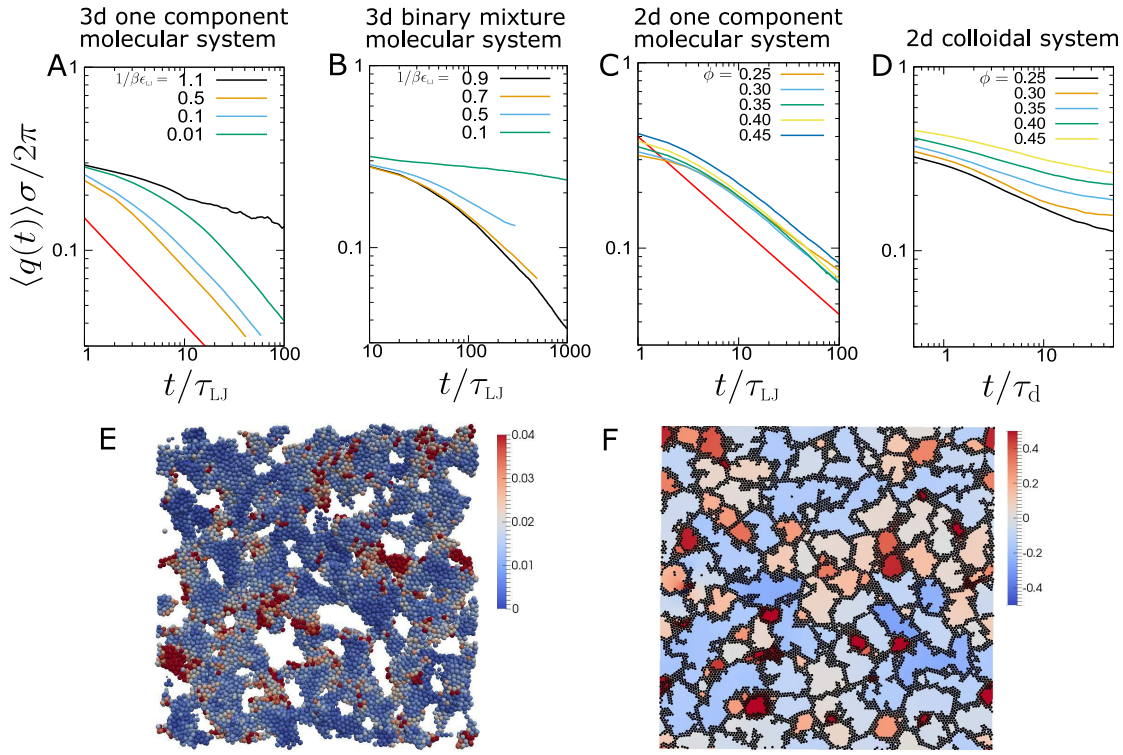

Fig. 7.4 **Comparison of coarsening behaviour among various systems. A-D,** The temporal changes of characteristic wave number $\langle q\rangle$ in various systems: **A** one component molecular system in 3d ($\rho = \rho_{\rm c}, 1/\beta\epsilon_{\rm LJ} = 0.01, 0.1, 0.5, 1.1$, $\beta_{\rm c}\epsilon_{\rm LJ} \sim 1.2$), **B** 50-50 mixture of two component molecular system in 3d ($\rho = 1.0, 1/\beta\epsilon_{\rm LJ} = 0.1, 0.5, 0.7, 0.9$, critical temperature is $\beta_{\rm c}\epsilon_{\rm LJ} \sim 1.4$), **C** one component molecular system in 2d, **D** colloidal system in 2d at zero temperature. **E** Real space mapping of kinetic energy in one component molecular system in 3d. Here we show a snapshot at time $t = 45$. The thermodynamic variables are chosen as $\rho = 0.33$ and $1/\beta\epsilon_{\rm LJ} = 0.01$. Color labeled on particles represents the kinetic energy of the particle. Here we take a time-average over [t-$\tau_{\rm LJ}$/2, t+$\tau_{\rm LJ}$/2]. **F**, a snapshot of colloidal system in 2d at zero temperature ($\phi = 38\%, t = 500$). Here we show pressure feild of sovlent together with the position of colloids.

fluid (Fig. 7.4A), the characteristic domain size grows more slowly at a lower temperature yet with the same power law exponent ($\alpha \sim 0.58$) over a wide range of temperature (at least $0.5 \leq \beta\epsilon \leq 0.01$). At the lowest temperature for the binary mixture ($\beta\epsilon = 0.1$), a logarithmic-like decay of $\langle q(t)\rangle$ is observed, implying that the system is arrested into a nonergodic state where both phases suffer from dynamic arrest. In single-component systems, such a situation never takes place: elastic deformation of the dense phase can proceed without being influenced by the dilute gas phase. This is because the relaxation time of the gas phase is much faster than the time scale of elastic deformation of the dense liquid phase even at a low temperature. A huge gap in the dynamics between the dilute gas and dense liquid phases

is necessary. This is also the case for colloidal suspensions: although a colloidal suspension should be regarded as a binary mixture, the large size difference between colloids and solvent molecules leads to strong dynamic asymmetry between the two phases. We may safely assume that the structural relaxation time of a solvent is infinitely fast comparing to that of colloids.

From the above, we may conclude that the growth exponent of 1/2 observed in network-forming phase separation originates from slow dissipative elastic motion of the dense phase under a condition that this process is not hindered by the other phase. This condition requires strong dynamic asymmetry between the two phases. This conclusion is valid for 3 dimensional (3D) systems. However, it may not be necessary the case for 2D systems. This is because there is an intrinsic topological difference in a percolated structure: in 2D, a bicontinous network structure can never be formed unlike in 3D. In the above, we see the limiting process of elastic deformation is a slow transport described by a diffusion-like equation. In thermoelasticity, the limiting process is heat transfer, which takes place at any dimensions in the same manner. This is confirmed in Fig. 7.4C: The domain coarsening exponent is 0.5 even for 2D. In poroelasticity, on the other hand, the limiting process is fluid flow through the dense colloid-rich phase, which obeys Darcy's law, in which the gradient of fluid pressure induces the flow of the solvent relative to colloids. For a network structure in 2D, the solvent-rich phase cannot have connectivity, as shown in Fig. 7.4E. In this situation, isolated solvent-rich domains cannot change their volume easily because of the incompressible condition, which does not allow the volume deformation of the solvent. The only way to change the volume is to exchange the solvent between neighboring solvent-rich domains through the colloid-rich network. In Fig. 7.4E, we show a pressure distribution in the solvent-rich domains together with the network of the colloid-rich phase during phase separation of a 2D colloidal suspension. We can see from the pressure distribution that the solvent transfers from a domain to its neighboring ones. This situation imposes a strict boundary condition on the interfaces of the colloid-rich domain, i.e., the elastic deformation of the colloid-rich network. In Fig. 7.4D, we show the volume fraction dependence of the temporal change of the characteristic wave number during network-forming colloidal phase separation in 2D. We can see that the growth exponent strongly depends on the volume fractions, as a consequence of complex coupling between the solvent exchange between solvent-rich domains under the constraint of the incompressibility.

7.4 Summary

In summary, we discover a novel coarsening law for network-forming phase separation of dynamically asymmetric mixtures. The phase-separation pattern coarsens with time in a self-similar manner and obeys the universal coarsening law of exponent 1/2. We show both theoretically and numerically that this law is a consequence of diffusional transport of mass or heat that controls elastic volume deformation. We expect that this new mechanism is valid for any network-forming phase separation, in which the strong dynamic asymmetry between the two phases makes the

dynamic behaviour of the slower phase elastic, and thus this mechanism should be valid for a wide class of materials, a mixture of any materials with largely different glass transition temperatures, soft and bio matter containing a liquid component. Porous structures are ubiquitous in nature and industry. From applications viewpoint, our coarsening law will provide a useful guide to control pore sizes of porous materials.

Chapter 8

Crystallization process of hard-sphere suspensions

8.1 Method

8.1.1 Identification of crystal structures

We study the crystallization kinetic of hard-sphere colloidal systems based on local bond order parameter analysis developed by Steinhart et al. [195]. Denoting the orientation vectors that particle i at the center makes with its neighboring particles $j = 1, ..., N_{\rm b}(i)$ as $\hat{\boldsymbol{r}}_{ij}$, we can introduce the following $2l + 1$ dimensional complex vector $\boldsymbol{q}_l$ by using spherical harmonics Y_{lm}.

$$q_{lm}(i) = \frac{1}{N_{\rm b}(i)} \sum_{j=1}^{N_{\rm b}(i)} Y_{lm}(\hat{\boldsymbol{r}}_{ij}), \tag{8.1}$$

where l is a positive integer parameter and $m = -l, ..., l$. The average of $q_{lm}(i)$ over the neighboring particles is often used as an indicator to identify crystal symmetries accurately [196]:

$$\bar{q}_{lm}(i) = \frac{1}{N_{\rm b}(i) + 1} \left[\sum_{k=1}^{N_{\rm b}} q_{lm}(j) + q_{lm}(i) \right]. \tag{8.2}$$

With this, local bond order parameters which satisfy the rotational invariance can be constructed as follows:

$$Q_l(i) = \sqrt{\frac{4\pi}{2l+1}} |\bar{\boldsymbol{q}}(i)|, \tag{8.3}$$

$$W_l(i) = \sum_{m_1+m_2+m_3=0}^{l} \begin{pmatrix} l & l & l \\ m_1 & m_2 & m_3 \end{pmatrix} \frac{\bar{q}_{lm_1}(i)\bar{q}_{lm_2}(i)\bar{q}_{lm_3}(i)}{|\bar{\boldsymbol{q}}(i)|^3}, \tag{8.4}$$

where the above bracket indicates Wigner $3j$ symbol.

As thermodynamically stable crystal structures of a hard-sphere system are closed-packed structures, we set the number of neighboring particle as $N_{\rm b} = 12$. We choose 12 particles in terms of the distance from particle i and regard them as the neighboring particles. Regarding the identification of crystal structures, we follow the methods emplyed Frenkel and his coworkers [197, 198]. We define that particle i and j are bonded if $\boldsymbol{q}_6(i)/|\boldsymbol{q}_6(i)|\cdot\boldsymbol{q}_6(j)/|\boldsymbol{q}_6(j)| > 0.7$, and regard particle i as crystal-like if the particle i is bonded with more than 7 particles and as fluid-like otherwise.

We classify the type of crystal structures, following Ref. [140]. Specifically, we define that if $W_6(i) > 0$, particle i has body centered cubic (bcc) structure, else if $W_4 > 0$ i has face centered cubic (fcc) structure, and otherwise i has hexagonal close packing (hcp) structure.

8.1.2 Mapping on the hard sphere systems

In this study, we approximate the hard-sphere potential by the Weeks-Chandler-Andersen (WCA) potential:

$$\begin{aligned} U(r) &= 4\epsilon\left[(\frac{\sigma}{r})^{12} - (\frac{\sigma}{r})^{6} + \frac{1}{4}\right] \quad \text{for} \quad \frac{r}{\sigma} < 2^{1/6} \\ &= 0 \quad \text{otherwise}, \end{aligned} \tag{8.5}$$

where ϵ is the parameter to determine the steepness of the repulsive potential and we set $\beta\epsilon = 40$ following Ref. [136, 199]. σ is the parameter corresponding to the diameter of colloids and we determine the effective hard-sphere diameter $\sigma_{\rm eff}$ by the following relation [200, 201]:

$$\sigma_{\rm HS} = \frac{2^{1/6}}{(1 + 1/\sqrt{\beta\epsilon})^{1/6}}\sigma. \tag{8.6}$$

With this diameter, we define the volume fraction $\phi = \pi\sigma_{\rm HS}^3 N/6V$, where N and V are the number of the particles and the volume of the system respectively.

8.1.3 The validity of our simulation: measurement of virial pressure

Some time ago, Auer & Frenkel found a huge discrepancy in the crystal nucleation rate I of hard-sphere colloids between results of light scattering experiments and those of the umbrella sampling method. Their study shows that the theoretical values of I change largely by a small change in the volume fraction: for example, I at $\phi = 52.8\%$ differs from that at 53.4% by at least 4 orders of magnitude. Thus, in order to study this dynamic phenomena, we need to precisely estimate the volume fraction.

Here we are interested in studying the impact of hydrodynamic interactions on the crystal nucleation rate by using our FPD simulation method. In FPD, we treat a solid particle as an underformable liquid droplet, whose shape is described by a continuous field, and distribute the interaction force acting on colloids to the lattice

using that shape field. So it is not so clear how we should define the volume fraction of hard-sphere-like colloids. Therefore, we first need to check how precisely FPD method reproduces the thermodynamic behavior of this phenomena [*1]

To confirm the validity of our simulation method, we measured osmotic pressure at equilibrium states via virial pressure:

$$p = \frac{Nk_{\mathrm{B}}T}{V} - \frac{1}{3V}\sum_{i>j} r_{ij}\frac{\partial U(r_{ij})}{\partial r_{ij}}. \tag{8.7}$$

As explained in Sec. 1.3.1, thermodynamically stable states in a hard-shpere system are liquid states for $\phi < \phi_{\mathrm{liq}} \sim 0.494$, fcc crystal states for $\phi > \phi_{\mathrm{cry}} \sim 0.545$ and the coexistence state between them. We prepared the configuration of particles at a liquid state just by randomly distributing the particles and equilibrating them in a thermal bath, where we employ a cubic box with the side length $L/\sigma = 17.297$ and we control ϕ by changing N. For a crystal state, on the other hand, we first made an ideal fcc crystal with $N = 4000$ [*2] and equilibrate it in a thermal bath. Here we employ a cubic box and we control ϕ by changing L. For a coexistence state, we used a cuboid box with $L_x = 2L_y = 2L_z$ to stabilize the interface between the liquid and crystal phase to be parallel to the yz plane. Here L_y needs to be an integer multiple of the lattice constant. Otherwise, an artificial stress due to the finite size effect is induced on the crystal phase, leading to error in measuring the pressure. We note that in FPD simulation we cannot perform a constant-pressure simulation since FPD simulation imposes the imcompressibe condition to the fluid.

Here we explain how to prepare a coexistence state. We prepared the configuration of particles at a coexistence state by molecular dynamics (MD) simulation. We first make an fcc crystal with 2048(:= N_1) particles in a cubic box and performed a constant-pressure (NPT ensemble) MD simulation for this configuration. We change the pressure p with 0.00125 increment (in the Lennard-Jonnes unit). Then, we connected the configuration of the crystal state to that of a liquid state with 1952(=: N_2) particles in a cuboid box. We performed a constant-volume MD simulation for this configuration and monitored the fraction of crystal-like particles. Thus, we found a configuration where we can see little change in the fraction of crystal-like particles, and determined the coexistence pressure p_{coex} as the pressure of this configuration ($p_{\mathrm{coex}} = 0.22125 \pm 0.00125$). As a result, we obtained $L_x/\sigma = 13.772$, and the density at the melting point and freezing point were $N\sigma^3/V = 0.784$ and 0.711 (i.e., $\phi = 0.4889$ and 0.5391), which are very close to the values 0.785 and 0.712 reported by Filion et al. [199].

Following the above procedure, we made configurations in coexsistent states (see Fig. 8.1B) at various volume fractions (which is controlled by changing N_2). Figure 8.1A shows that the fraction of crystal particles as a function of the volume fraction ϕ. Our results fall on a line, as expected from the lever rule, except when

[*1] Although we have seen a good agreement in phase diagram of attractive colloids between FPD and experiments.

[*2] The number of particle should satisfy $N = 4n^3$ (n: integer) when fcc crystal is in a cubic box.

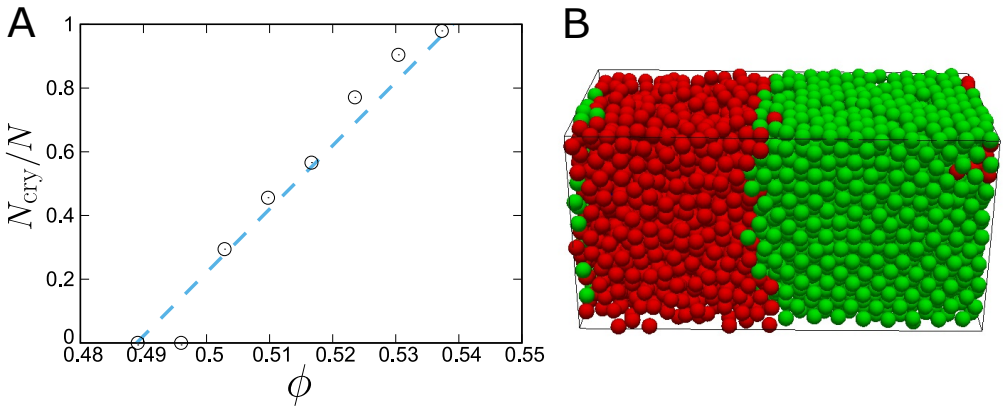

Fig. 8.1 **Identification of liquid-crystal coexistence states. A** Volume fraction (ϕ) dependence of the fraction of crystal-like particles $N_{\rm cry}$. The dashed line represents lever rule, i.e., $(\phi - \phi_{\rm m})/(\phi_{\rm f} - \phi_{\rm m})$. **B** A snapshot of a 3D structure at $\phi = 0.5157$. Liquid-like and crystal-like particles are colored red and green respectively.

the system is too close to the melting and freezing points (the reason is simply because simulations cannot stabilize very thin layers of liquid or solid phases). The line is slightly displaced from the one we estimate from the coexistence points (dashed line), but this is likely due to the fact that the fraction of crystals depends on the choices of the threshold of the order parameter to distinguish the crystal and liquid states.

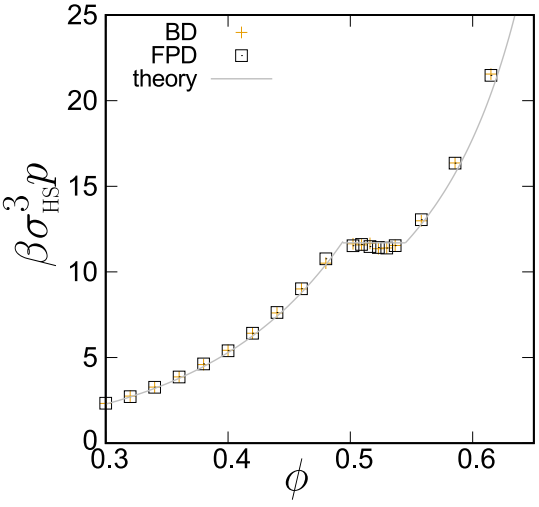

Fig. 8.2 **Virial pressure in equilibrium states.** Cross and square symbols represent the results obtained by BD and FPD simulations, respectively. Gary curve is the theoretical prediction for a hard sphere system.

With the configurations in coexsistence states, we measure the virial pressure in equilibrium states. Figure 8.2 shows the volume fraction dependence of the virial

pressure obtained by BD and FPD simulations, where we can see almost perfect agreement between them. This matching justifies the validity of the thermodynamic modeling based on FPD method. In Fig. 8.2, we also show theoretical predictions (the Carnahan-Starling equation of state (see Eq. 1.11) for the liquid phase and the Speedy equation of state for the solid phase [202, 203]).

8.1.4 Estimation of the free energy barrier

The crystal nucleation process that we study is a rare event and thus it is hard to obtain enough configurations to precisely compute the statistical variables during the activation process. To compute the free energy cost required for crystal nucleation of hard-sphere colloids, we use Umbrella Sampling method [204]. This method is based on Metropolis Monte Carlo simulation but perform the sampling with multiplying a bias $W(\boldsymbol{q}) = \exp[-\beta w(\boldsymbol{q})]$ on the Boltzmann factor, where $\boldsymbol{q}$ represents configuration and $w(\boldsymbol{r})$ is the so-called "biasing potential". In general, the average of any quantity A is related to the statistical values under biased sampling as

$$\langle A \rangle = \frac{\langle A/W(\boldsymbol{q}) \rangle_{\text{bias}}}{\langle 1/W(\boldsymbol{q}) \rangle_{\text{bias}}}, \tag{8.8}$$

where $\langle A \rangle$ and $\langle A \rangle_{\text{bias}}$ represent ensemble average under un-biased and biased sampling, respectively.

The Gibbs free energy barrier for formation of a crystal nucleus with size n, $\Delta G(n)$ can be determined by taking a statistics for the number of the nucleus N_n through the following relation [128]:

$$\langle N_n \rangle / N = \exp[-\beta \Delta F(n)]. \tag{8.9}$$

By performing Monte Carlo simulation with the above biasing and computing the average for $A = N_n$ by Eq. 8.8, we can obtain $\Delta F(n)$. In the study of crystal nucleation, a harmonic potential $w(\boldsymbol{q}) = \frac{1}{2}k(n(\boldsymbol{q}) - n_0)^2$ is often used as the biasing potential, where n_0 is the targeted cluster size and k is a coupling parameter. To ensure high statistical performance generating the crystal nuclei with independent configurations is desirable. However, with the above procedure using the harmonic potential is expected to severely constrain the rearrengement of crystal structures, we need to run the independent simulations. To obtain the functional profile of the free energy barrier over a wide range of n, we also need to run the simulations for various n_0. In this study, we use a variation of Umbrella Sampling method introduced in Ref. [205]. This method (CNT-US method) uses the following biasing potential on the basis of Classical Nucleation Theory:

$$w(\boldsymbol{r}^N) = -|\Delta\mu| n^{2/3} \left(\frac{3}{2} n_{\text{c}}^{1/3} - n^{1/3}\right), \tag{8.10}$$

where $|\Delta\mu|$ is the chemical potential difference between the fluid and crystal phases, which we can determine by the thermodynamic integration. n_{c} is the critical nucleus size, which is the only control parameter in this simulation scheme. Given that the real free energy in n space has a functional profile similar to Eq. 8.10, it is expected

that, as n_c approaches the real critial nucleus size, the biased free energy profile as a function of n becomes flatter, leading to large fluctuations of n. Therefore, we may choose n_c as the one at which we can see large fluctuations in n. See Supplementary Information of Ref. [205] for the further detail of this method.

8.1.5 Normalization of nucleation rate

In dense suspensions where liquid-crystal transition takes place, the structural relaxation of colloids is significantly suppressed by stric hinderance among the colloids, but in the presence of solvent such a slowing down of structural relaxation is also brought about by deformation of fluid field of solvent among the colloids. To examine the effects of hydrodynamic interaction (HI) on crystallization kinetics, we perform BD and FPD simulations and compare the resulting nucleation rates. To do so, we need to consider the above difference arising from the presence and absence of HI.

In Fig 8.3A, we show the volume fraction dependence of mean square displacement (MSD) obtained by FPD simulations, where we can see that the diffusive motions of colloids are suppressed as volume fraction increases. At $\phi = 0.54$, we can see that MSD shows a non-linear dependence in early time and asymptotically approaches to linear behavior, which reflects the casing effect characteristic in super-cooled liquids. From the long time diffusive behavior of MSD, we determined the long time diffusion coefficients D_L. Fig 8.3B shows the volume fraction dependence of D_L for BD and FPD simulations. Here we can see that D_L deviates from the diffusion coefficient for a free particle D_0 for large ϕ but the deviation in FPD is stronger than that in BD, which obviously originates from the difference in the presence or absence hydrodynamic interactions. For example, we can see that

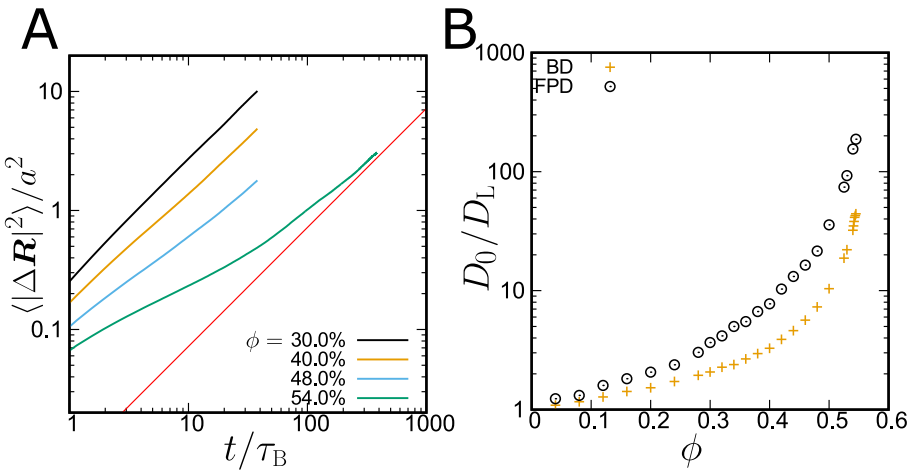

Fig. 8.3 **A.** Mean square displacement for various volume fractions. The red line is a linear line. Here we only show the results by FPD simulations. **B.** Volume fraction dependence of long time diffusion constant D_L scaled by that in dilute limit D_0. Cross and cricle symbols represent the results obtained by BD and FPD simulation respectively.

D_L in BD is approximately four time larger than that in FPD at $\phi = 0.54$.

The main interest of our study is whether such a effect of HI is also significant in crystallization kinetics, and specifically we are interested in difference in nucleation rate over several order of magnitude. Thus, we normalize the hydrodynamic effects as in the above on a unit time, i.e., we normalize I by a time unit $\tau_{\rm L} = \sigma_{\rm HS}^2/6D_{\rm L}$ and a length unit $\sigma_{\rm HS}$. Such a normalization of nucleation rate is widely applied in the previous studies on crystallization of colloidal suspensions [6].

8.2 Results

8.2.1 Determination of nucleation rate via brute force simulations

We perform BD and FPD simulations for various volume fractions: $0.54 \leq \phi \leq 0.545$. The systems size is set commonly as $L/\sigma = 17.3$ and the number of the particle are approximately $N \sim 4000$ in the above volume fractions. According to a study using BD simulation [136], there is few finite-size effect on nucleation rate under the above simulation scale. In FPD simulation, the Schmidt number is set as $S_{\rm c} = 8.0$. In Chap. 5, we have shown that phase separation dynamics of colloid interacting with short-range interactions experimentally observed by confocal microscopy can be reproduced almost perfectly by FPD simulation under the Schmidt number.

To determine the nucleation rate, we simulate the time evolution of colloidal suspensions in metastable liquid state at time $t = 0$ and monitor the temporal change of largest crystal nucleus, $n(t)$. An example of formation process of crystal nuclei is shown in Fig. 8.5. We continue simulations until $n(t)$ exceeds the critical nucleus size $n_{\rm c}$ within our simulation resource (see Fig 8.4A). Denoting the average time to form critical nucleus as $\langle t_{\rm inc} \rangle$, we determine the nucleation rate I by

$$I = \frac{1}{V \langle t_{\rm inc} \rangle}, \tag{8.11}$$

where V is the volume. In BD and FPD simulations, we performed 16 of independent simulations for each volume fractions, $\phi = 0.540, 0.541, ..., 0.545$ and $\phi = 0.540, 0.5425, 0.545$, respectively. In BD simulation, we confirmed the crystallization for all the runs. On the other hand, we couldn't continue FPD simulations until all the runs crystallize due to computational cost [*3] : specifically, 2, 9 and 16 runs crystallized for $\phi = 0.540, 0.5425$ and 0.545, respectively. For the statistical significance, hereafter we only discuss the results with $\phi = 0.5425, 54.5$.

In Fig. 8.4B, we show the results of nucleation rates together with MD result reported by Filion et al [131]. Here we cannot see a huge difference among the different simulation methods in the rage of volume fraction.

[*3] The total simulation time in Brownian time corresponds to approximately $5.0 \times 10^4 \tau_{\rm B}$ for each volume fractions.

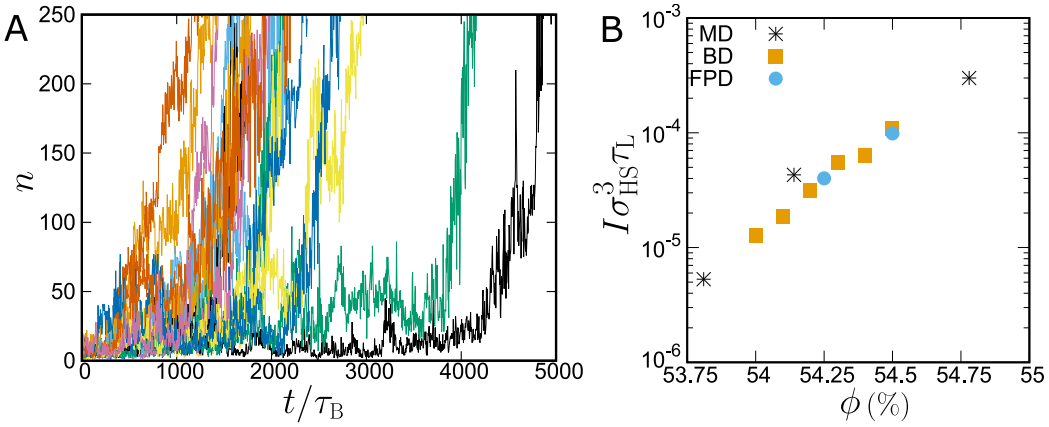

Fig. 8.4 **A** Time evolutions of largest cluster size for 16 independent runs at $\phi = 0.545$ in FPD simulation. **B** A comparison of the crystal nucleation rates determined by BD and FPD methods. Here we also show the MD result by Filion et al [131].

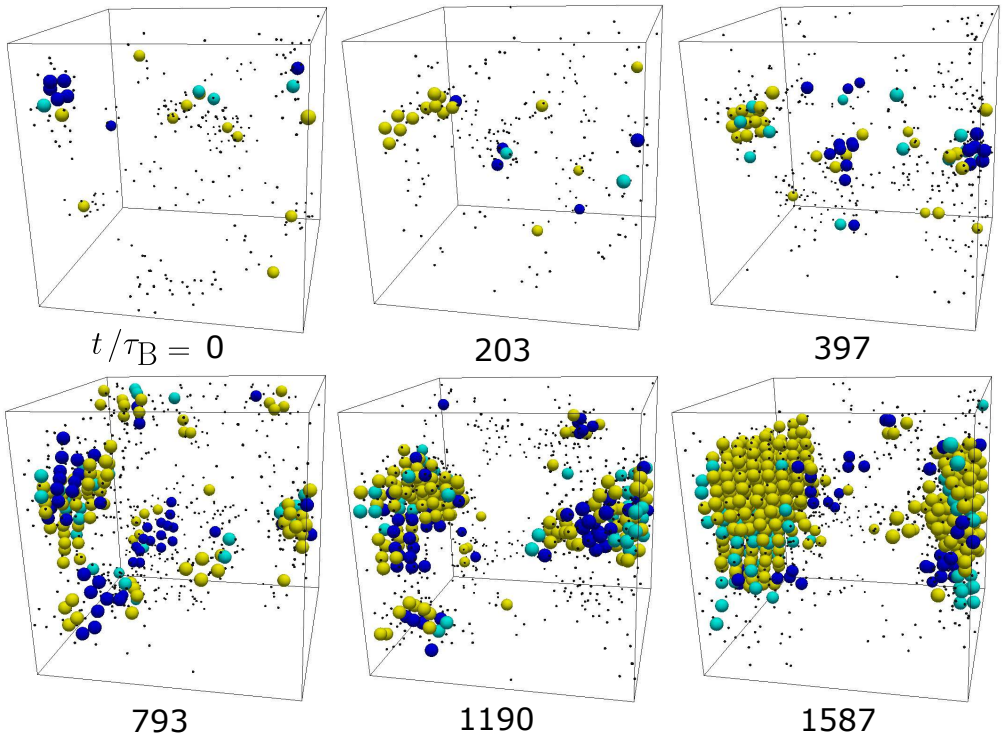

Fig. 8.5 **Formation of a crystal nuclei from metastable liquid**. Here we show an example of the time evolution of crystal nuclei at $\phi = 54.5$ obtained by FPD simulation. The large shperes represents the positions of crystalline particles and the particle color is labeled depending on the type of crystals: Blue, bcc; Right blue, hcp; Yellow, fcc. Black small dots are the particles whose $Q_6 > 0.27$.

8.2.2 Time evolution of critical nucleus: estimation of kinetic factor

In the above, we have compared the nucleation rate at $\phi \sim 0.54$ between BD and FPD simulations but no remarkable difference was confirmed. However, at this volume fraction it is not so obvious how large mismatch in nucleation rates between experiments and simulations exists. One reason is that uncertainty of experimental results is typically huge in this phenomenon. For example, it is known that precise determination of diameter of colloids is not so easy task in experiments [206] and even 1% error in measurement of the diameter can produce difference in nucleation rate over several oder of magnitudes. Furthermore, a huge mismatch in nucleation rates between experiments and simulations over around 10 order of magnitude has been reported in rather more dilute volume fractions ($\phi \sim 0.52$ or less, see Fig 2.11). For the reasons, we cannot judge from current results that there is no effect of hydrodynamic interactions on the crystallization kinetics.

However, it is impossible to access the nucleation events at the lower volume fractions by FPD simulation with current computational power, from the metastable liquid state to the birth of critical nucleus. To examine the behavior of nucleation rates at the lower volume fractions, we employ an approach by Auer and Frankel [127]. Specifically, we make a critical nucleus in the systems and evolve these by BD and FPD simulations. By monitoring the growing or shrinking behavior of the nucleus, we can determine the kinetic factor of nucleation rates (see Sec.2.3.2).

Preparation of critical nuclei

Following the strategy, we study the time evolution of the critical nucleus at $\phi = 0.5183$, at which we can see a huge mismatch in nucleation rates between experiments and simulations (at least 8 order of magnitude). To prepare the nucleus with critical size we first calculate the free energy barrier by the US method. Fig. 8.6 shows the result obtained under setting the *input* critical size as $n_c = 458$, where we can see the maximum of ΔF is located near $n = 458$. The height of the barrier, $\beta\Delta F(n_c)$ and the second derivative, $\beta\Delta F''(n_c)$ obtained by fitting are 70.6 and -3.3×10^{-4}, respectively [*4] We made 10 of the independent initial configurations including a nucleus with $n = 458$ and run 10 simulation for each initial conditions (thus 100 runs in total). We then measured the number of runs to go to the crystalline basin and the ratio obtained was 0.40. We repeated the same procedure but for nucleus with $n = 465$ and the ratio obtained was 0.52. Thus, we can regard $n = 465$ as sufficiently close value to the the real value of critical nucleus size. In the below we consider the time evolution of the nuclei of 465 particles.

Determination of kinetic factor

We performed BD and FPD simulations for 12 of independent initial conditions with a nucleus of 465 particles. We run 4 independent simulations for each initial conditions (thus 48 runs in total) and measure the the means square displacement

[*4] We perform the same simulation at $\phi = 0.545\%$, and obtain the following results: $n_c = 29$, $\beta\Delta F(n_c) = 11.3$, $\beta\Delta F''(n_c) = -5.8 \times 10^{-3}$.

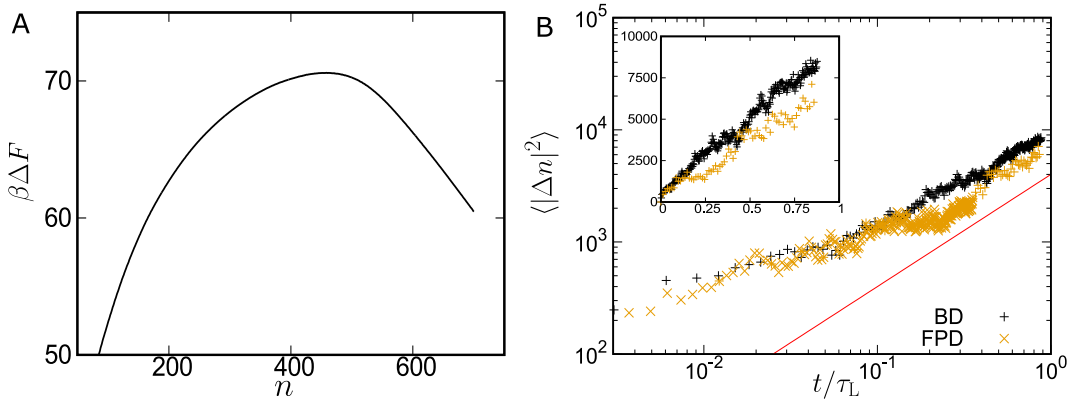

Fig. 8.6 **A**. Free energy barrier at $\phi = 51.83$ computed by the US method. **B**. The means square displacement for nucleus size $\langle|\Delta n(t)|^2\rangle$ at the same volume fraction.

(MSD) for nucleus size $\langle|\Delta n(t)|^2\rangle$ where $\Delta n(t) = n(t) - n(0)$. Fig. 8.6B shows the result where we can see that MSD increases linearly with time. As $n(0) \sim n_c$ we can expect $\langle|\Delta n(t)|^2\rangle \sim 2f_+(n_c)t$ (see Sec. 2.3.2). From the relation, we determine the diffusion coefficient and the result obtained is $f_+(n_c)\tau_L \sim 10000$ and 8000 for BD and FPD, respectively, which cannot be a reason of the huge discrepancy in nucleation rate between experiments and simulations.

8.3 Summary

In summary, to examine the influence of hydrodynamic interactions (HI) on crystallization kinetics of hard-sphere colloids we performed numerical simulation with HI (FPD method) and without (BD method). We simulated the crystallization kinetics of colloids from metastable liquid to formation of critical nucleus at $\phi \sim 0.54$, and no remarkable difference in nucleation rate between BD and FPD was confirmed. We also compared the kinetic factor by monitoring the growing or shrinking behaviors of critical nucleus at more dilute volume fraction $\phi \sim 0.52$, but we could not see a significant difference between BD and FPD results. However, this analysis based on the assumption that the morphology of critical nucleus dose not influenced by HI. To make a rigorous conclusion, we need to conduct further study including the above point.

Chapter 9

Appendix

A Synthesis of PMMA collloid

We synthesized monodisperse poly-methyl methacrylate (PMMA) colloids, combining the methods in Ref. [207, 208, 209]. We dissolve monomers (methyl methacrylate:MMA and Methacrylic acid:MA) into reaction solvent (a mixture of hexane and dodecane). We also mix Azo-bis-isobutyronitrile (AIBN) and octanethiol as initializer and inhibiter of polymerization. We use rhodamin as a fluorescent dye. We functionalize rhodamin to make a chemical bond with PMMA by reacting aminosylene and rhodamine B isothiocyanate in dimethylsrhooxyside (DMSO) at a ratio of 50:50 in number of molecules for two days. In order to avoid addhision between surface of colloids, we add dimethylpolysiloxane (PDMS: specifically, we use one with functional group equivalent weight 3,900 g/mol) as a steric stabilizier. The wight of the above chemicals are summerized in Fig. 1. The above mixture is placed in a flask and heated to 80 °C with a magnetic stirrer. The reaction is completed within 2 hours. After synthesis, PMMA colloids are rinsed with petroleum ether for multiple (roughly 10) times.

The diameter of colloids obtained with the recipe in Fig. 1 was $\sigma \sim 2\mu$m. The size of colloids can be controlled by changing the ratio of monomer to reaction solvent. Specifically, we can synthesize larger colloids by increasing the ratio of MA, MMA

Material	Weight (g)	Role
MMA	19.6	monomer
MA	0.04	monomer
PDMS	1	steric stablizer
AIBN	0.2	initializer
Octanethiol	0.12	inhibiter
RAS	0.1	dey
DMSO	1	solvent
Hexane	14	solvent
Dodecane	7	solvent

Fig. 1 Recipe of PMMA colloid

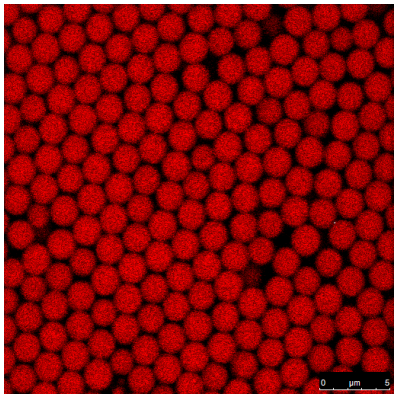

Fig. 2 An image of PMMA colloid

and PDMS (while keeping their mass ratio constant) to the total amount of mixture. For example, the mass ratio of MA, MMA and PDMS in Table 1 is approximately 50%, but if we increase it to 56% we can get colloids with $\sigma \sim 3\mu$m.

Synthesis of core-shell type PMMA collloid

In the situation where colloids are closely packed, fluorescent signals of different particles can overlap, which can cause tracking error of particles. For example, the image of multiple particles can be detected as a single particle. Furthermore, confocal image tends to be elongated along z-axis (direction orthogonal to focal plane), and thus the image corresponding to a single particle is sometimes detected as multiple particles. Such a tracking error is a troublesome problem especially when we need to track the trajectories of particles.

To overcome the above problem, we synthesize core-shell type PMMA colloids (particles with a fluorescent core and nonfluorescent shell) [210, 211]. Since only center part of particles fluoresces, the particles are easily distinguished even in close-packing arrangements.

A recipe for core-shell type PMMA colloids is listed in Table 1. We first redisperse PMMA colloids labeled with RAS which is prepared by the above protocol in a mixture mainly composed of Hexane and Dodecane (see *FLASK*), and heat the mixture to 80°C in a flask with a magnetic stirrer. Then, we add a solvent including monomers (see *DROP*) into the flask. Here we drop the solvent slowly over 90 min with a syringe pump. After finishing the drop, we wait for the reaction for extra 1 hour. We rinse the colloids obtained in the same way as in the above. The diameter of colloids that we obtained with the recipe in Table A was $\sigma \sim 2.6\mu m$ (see Fig. 3).

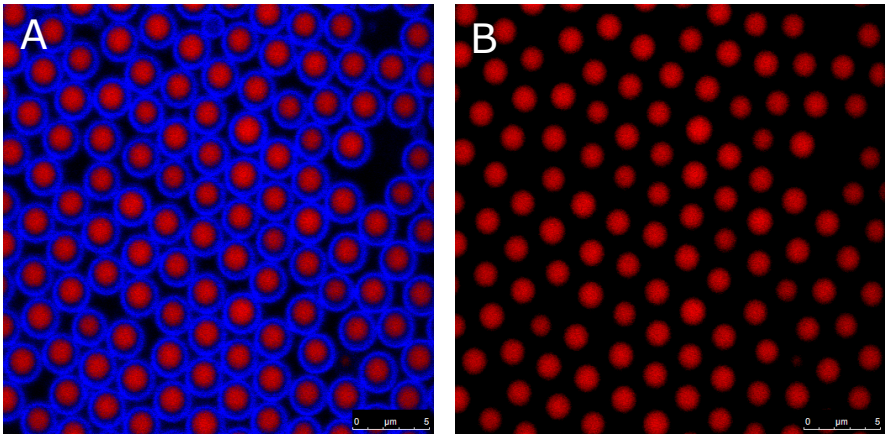

Fig. 3 **A** An image of core-shell type PMMA colloid and **B** one that we show only core part. One may see that the center of the core part and shell part are slightly misaligned, but this is probably due to optical aberration resulting from difference excitation wavelengths.

Table 1 Recipe of core-shell type PMMA colloid

Material	Weight (g)	Role
FLASK		
PMMA colloid ($\sigma \simeq 1.9\mu$m)	6.0	core
AIBN	0.2	initializer
Octanethiol	0.12	inhibiter
Hexane	64	solvent
Dodecane	32	solvent
DROP		
MMA	14.7	monomer
MA	0.3	monomer
PDMS	1.5	steric stablizer
CAS	0.02	dey
DMSO	1.5	solvent
Octanethiol	0.12	inhibiter

B Implementation of FPD method

In Chap. 4, we have mentioned a concept, modeling and physical fundation of Fluid Particle Dynamics (FPD) method. Here we provide detailed information about how to implement this simulation method. In the below, firstly, we explain how to normalize and discretize the basic set of euqations in FPD simulation. Next we explain in what order the calculation is performed. Finally, we mention some important points to improve the computational efficiency.

B.1 Normalization and discretization

We normalize the time and length by $\tau \equiv \rho l^2/\eta_{\rm s}$ and $l \equiv \xi$ as $t = \tau\widetilde{t}$, $\boldsymbol{r} = l\widetilde{\boldsymbol{r}}$, which means that we use the interfacial length of ϕ as a length unit and the time requried for momentum of solvnet to diffuses over the length as a time unit. We also choose $\rho l^3(l/\tau)^2$ as a every unit. As a result, Navier-Stokes euqation (Eq. B.1) rewriten into the following equation:

$$(\frac{\partial}{\partial\widetilde{t}} + \widetilde{\boldsymbol{v}}\cdot\widetilde{\nabla})\widetilde{\boldsymbol{v}} = \widetilde{\boldsymbol{f}} + \widetilde{\nabla}\cdot(\widetilde{\boldsymbol{\sigma}} + \widetilde{\boldsymbol{\sigma}}^{\rm R}), \tag{1}$$

with

$$\widetilde{\nabla}\widetilde{\boldsymbol{v}} = 0. \tag{2}$$

Corresponding to the units described in the above, the other physical quantities are normalized in the following way: $\rho = \rho\widetilde{\rho}$ (i.e., $\widetilde{\rho} = 1$), $\boldsymbol{v} = \frac{l}{\tau}\widetilde{\boldsymbol{v}}$, $\boldsymbol{f} = \frac{\rho l}{\tau^2}\widetilde{\boldsymbol{f}}$, $\boldsymbol{\sigma} = \frac{\rho l}{\tau^2}\widetilde{\boldsymbol{\sigma}}$, $p = \frac{\rho l^2}{\tau^2}\widetilde{p}$, $\eta = \eta_{\rm s}\widetilde{\eta}$, $k_{\rm B}T = \rho l^3(l/\tau)^2\widetilde{k_{\rm B}T}$ Hereafter, we neglect the normalization symbol $\widetilde{*}$ just for simplification. We employ the following temporal discretization for Eq. and : [*1]

$$\boldsymbol{R}_n^{(m+1)} = \boldsymbol{R}_n^{(m)} + \boldsymbol{V}_n^{(m+1)}\Delta t, \tag{3}$$

and

$$\boldsymbol{v}^{(m+1)} = \boldsymbol{v}^{(m)} + \Delta t\,\{\nabla\cdot(-\boldsymbol{v}^{(m)}\boldsymbol{v}^{(m)} + \boldsymbol{\sigma}^{(m)}) + \boldsymbol{f}^{(m)}\} + \nabla\cdot(\sqrt{2\eta k_{\rm B}T\Delta t}\,\boldsymbol{s}^{(m)}), \tag{4}$$

where Δt is the time step and the symbol $*^{(m)}$ means that quantity $*$ is one at m-th time step. The last term in the right-hand side is the sum of $\nabla\cdot\boldsymbol{\sigma}^{\rm R}$ over $m\Delta t < t < (m+1)\Delta t$ and satisfies $\langle \boldsymbol{s}_\alpha\rangle = 0$, $\langle s_{ij,\alpha}^{(m)} s_{kl,\beta}^{(n)}\rangle = (\delta_{ik}\delta_{jl} + \delta_{il}\delta_{jk})\delta_{\alpha\beta}\delta_{mn}$ where α, β are the index to specify the spatial lattice [*2]. Due to the difference in viscosity between solvent and colloid, we need to set a sufficienty small time step to maintain numrical stability. In this thesis, we set $\Delta t = 2.5\times10^{-3}$. The length step

[*1] We use first-order explicit discretization here, which is valid when viscous dissipation plays a prominent role. We cannot find a way to compute with implicit discretization for now, which is expected to significantly accelate the computational speed.

[*2] Specifically, we generate gassuain noise with mean 0 and variance $\sqrt{2}$ for $i = j$, and mean 0 and variance 1 for $i \neq j$, respectively.

is set as $\Delta x = 1$ and spatial difference is performed on staggered lattice (see Fig 4). We empoly periodic boundary condition and use Marker-and-Cell (MAC) method for computation of simultaneous equations 1 and 2 (see Block **e** in the next section). For parameters regarding phase field ϕ, we set as $a = 3.2$, $\xi = 1.0$, $\eta_c/\eta_s = 50.0$.

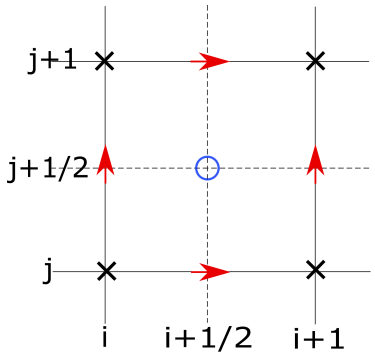

Fig. 4 An illustrative figure of staggered lattice. We define scalar feilds on regular mesh (cross symobol), vector feilds on the mesh which shifts by half lattice size (allow symbol), and diagonal and non-diagonal components of second rank tensor fields on cross symobols and circle symbols, respectively.

B.2 Flowchart of computation

We explain the detail of computation in the below. Fig. 5 schematically describes the procedure of the computation at m-th time step. The blocks of computation aligning horizontally can be performed independently. The quantities written on the left top side of the blockes represent those required to perfrom the computation, and those on the right top side what we obtain by the computation. The flowchart starts with the center-of-mass positions of colloids $\{\boldsymbol{R}_n^{(m)}\}$ and the velocity field $\boldsymbol{v}(\boldsymbol{r})^{(m)}$, and finish when those at the next time step $m+1$ are obtained. In the below, we explain what kind of computation are performed in each blocks.

a. Computation of the order parameters: Compute the order parameters $\{\phi_n(\boldsymbol{r})^{(m)}\}$ from the center-of-mass position of colloids $\{\boldsymbol{R}_n^{(m)}\}$ following Eq. 4.2.

b. Computation of the forces acting on colloids: Compute the forces acting on colloids $\{\boldsymbol{F}_n^{(m)}\}$ from $\{\boldsymbol{R}_n^{(m)}\}$. $\{\boldsymbol{F}_n^{(m)}\}$ are given by the sum of into intercolloid force $\{\boldsymbol{F}_n^{\mathrm{int}(m)}\}$ and external force $\{\boldsymbol{F}_n^{\mathrm{ext}(m)}\}$ as $\boldsymbol{F}_n^{(m)} = \boldsymbol{F}_n^{\mathrm{int}(m)} + \boldsymbol{F}_n^{\mathrm{ext}(m)}$, and the former is expressed by the interaction potential U via,

$$\boldsymbol{F}_n^{\mathrm{int}(m)} = -\sum_{n'(\neq n)} (\partial/\partial \boldsymbol{R}_n^{(m)}) U(|\boldsymbol{R}_{n'}^{(m)} - \boldsymbol{R}_n^{(m)}|). \tag{5}$$

We use Cell linked list method for the calculation of interparticle forces.

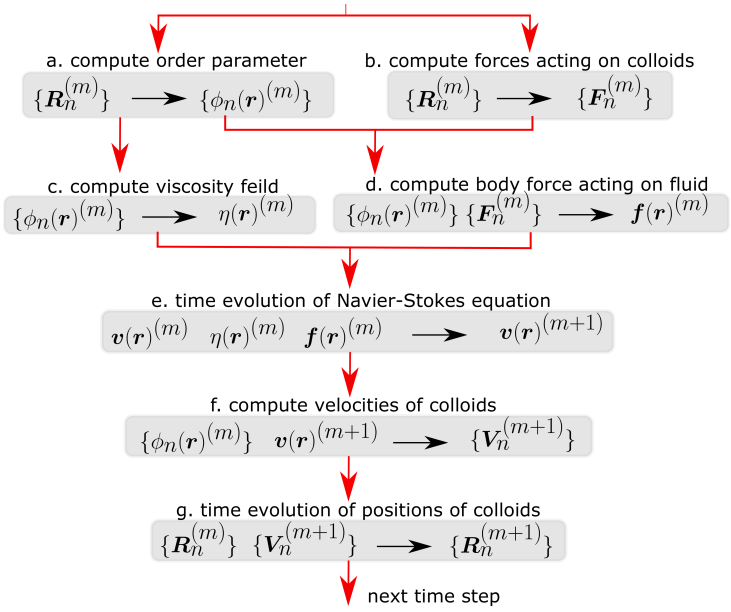

Fig. 5 The flowchart of computation of FPD method

c. Computation of the viscosity feild: Compute $\eta(\boldsymbol{r})^{(m)}$ from $\{\phi_n(\boldsymbol{r})^{(m)}\}$ following Eq. 4.3.

d. Computation of the body force acting on fluid: Compute $\boldsymbol{f}(\boldsymbol{r})^{(m)}$ from $\{\boldsymbol{F}_n^{(m)}\}$ following Eq. 4.5.

e. Time evolution of Navier-Stokes equation: Compute $\boldsymbol{v}(\boldsymbol{r})^{(m+1)}$ from $\boldsymbol{v}(\boldsymbol{r})^{(m)}$, $\eta(\boldsymbol{r})^{(m)}$ and $\boldsymbol{f}(\boldsymbol{r})^{(m)}$. To do so, we need to solve the simultaneous equations 1 and 2. Under periodic boundary conditions, we can employ the Marker-and-Cell (MAC) method: operating $\nabla\cdot$ for the both side of Eq. 4, $\nabla \cdot v(\boldsymbol{r})^{(m+1)}$ is dropped due to incompressibility condition and we obtain the following Poisson equation,

$$\nabla^2 p^{(m)} = c^{(m)}, \tag{6}$$

where [*3]

$$c^{(m)} = \nabla\cdot[\frac{\boldsymbol{v}^{(m)}}{\Delta t}+\nabla\cdot\{-\boldsymbol{v}^{(m)}\boldsymbol{v}^{(m)}+\eta^{(m)}\{\nabla\boldsymbol{v}^{(m)}+(\nabla\boldsymbol{v}^{(m)})^{\mathrm{T}}\}+\sqrt{\frac{2\eta k_{\mathrm{B}}T}{\Delta t}}\boldsymbol{s}^{(m)}\}+\boldsymbol{f}^{(m)}]. \tag{7}$$

Here we denote $p^{(m)}, c^{(m)}$ on the spatial latice $(i,j,k) \in [0, N_x-1]\times[0,N_y-1]\times[0,N_z-1]$ as $p_{ijk}^{(m)}, c_{ijk}^{(m)}$, and the descrite Fourier components as $P_{IJK}^{(m)}, C_{IJK}^{(m)}$. Under periodic boundary condition, Eq 6 can be transformed in

$$P_{IJK}^{(m)} = \frac{C_{IJK}^{(m)}}{-4[\sin^2(2\pi I/N_x)+\sin^2(2\pi J/N_y)+\sin^2(2\pi K/N_z)]} \tag{8}$$

[*3] Here $\nabla\cdot\boldsymbol{v}^{(m)}$ is expected to be zero, but we leave it to suppress numerical error.

We obtain $C_{IJK}^{(m)}$ by performing the Fast Fourier Transform for $c_{ijk}^{(m)}$, and compute $P_{IJK}^{(m)}$ following the above relation. By performing inverse Fourier transform for $P_{IJK}^{(m)}$, we obtain $p_{ijk}^{(m)}$ at time $t = m\Delta t$. By substituting the pressure $p^{(m)}$, $\boldsymbol{f}^{(m)}$ and $\boldsymbol{v}^{(m)}$ in Eq. 1, we finally obtain the velocity field $\boldsymbol{v}^{(m+1)}$.

f. Computation of the velocities of colloids: Compute the center-of-mass velocities of colloids $\{\boldsymbol{V}_n^{(m+1)}\}$ from velocity field $\boldsymbol{v}^{(m+1)}$ following Eq. 3.

g. Time evolution of the positions of colloids: Compute $\{\boldsymbol{R}_n^{(m+1)}\}$ from $\{\boldsymbol{R}_n^{(m)}\}$ and $\{\boldsymbol{V}_n^{(m+1)}\}$ following Eq. 3.

B.3 Important points for implementation

Here we mention important points for speeding up FPD method.

Cutoff for the computational range of order parameter

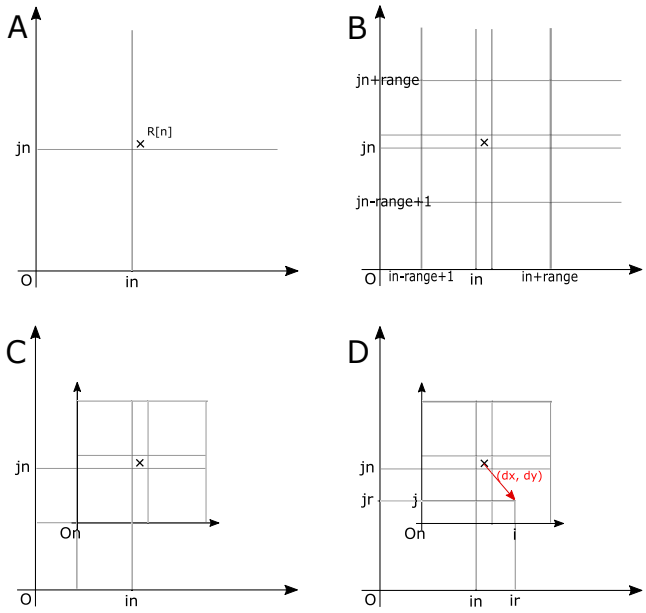

Fig. 6 Relation between the coordinate of n-th support $\mathrm{O_n}$ and the reference coordinate O. **A**, Let the integer part of the center-of-mass position ($\boldsymbol{R}_n$: cross symbol) of n-th particle be (in, jn). **B**, **C**, We take the coordinate of n-th support $\mathrm{O_n}$ such that $\boldsymbol{R}_n$ is to be approximately in the center. **D**, Let a point (i, j) on $\mathrm{O_n}$ and denote the vector $\boldsymbol{R}_n$ to (i, j) as (dx, dy) and the point seen from O as (ir, jr).

As we can see from Fig. 4.1A, ϕ_n is sufficiently close to zero at a point roughly diameter away from the center-of-mass position of n-th particle. Then, for numerical efficiency, we compute ϕ_n only for the points whose distance from $\boldsymbol{R}_n$ is less than the diameter. We call the spatial region as "suport" of n-th particle. Practically,

we implement the cut off for the order parameter in the following way.

Denoting the integer part of $2(a+\xi)$ as range and 2×range as Nrange, we allocate memory of 3-dimensional arrays with size Nrange^3 for every particles, $n = 0, 1, ..., N$ (let the array be phi[n][i][j][k])). We store the values in the array such that the index (i, j, k) for the arrays correspond to the reference coordinate O in the following way: first we define the integer part of $\boldsymbol{R}_n$ as (in, jn, kn) (Fig. 6A). Next we set a coordinate O_n whose origin is to be (in-range+1, jn-range+1, kn-range+1) and call the coordinate for the support of n-th particle (Fig. 6B, C). Denoting arbitray latice point of O_n as (i, j, k), we define the spatial region within (i, j, k)$\in$ [0, Nrange-1]^3 as the support of n-th particle. The above means that we take the supports such that $\boldsymbol{R}_n$ is to be approximately in the center of n-th support (Fig. 6C). Letting the vector from $\boldsymbol{R}_n$ to an arbitrary point A: (i, j, k) on O_n be (dx, dy, dz), we compute the value of order parameter ϕ_n at (i, j, k) by phi[n][i][j][k] $= [\tanh\{(a - dx * dx + dy * dy + dz * dz)/\xi\} + 1]/2$.

Treatment of supports in MPI-parallel programming

In MPI-parallelization, we divide the total lattice (denoting the lattice size as (Nxg, Nyg, Nzg)) along x axis into nump equal parts, where nump is the number of process [*4]. Denoting the size of divided lattice as (Nx, Ny, Nz) $\equiv$ (Nxg/nump, Nyg, Nzg), we let process myid (=0, ... , nump-1) deal with the lattice located in [myid*Nx, (myid+1)*Nx-1]×[0, Ny-1]×[0, Nz-1] (where we take the reference coordinate O). When we compute the order parameters or refer to their values, we only need to consider the overlapped region between the supports of the particles and the lattice that process myid deal with. Fig. 7 schematically shows this, where gray, light blue and dark blue represent the region that process myid deal with, the region that the supports occupy and the overlapped region between them, respectively. Cross symbols represent the center-of-mass positions of particles. As we can see from the figure, the particles that process nump deal with are those whose x coordinates (on O) are in (-range+myid*Nx, range+(myid+1)*Nx-1].

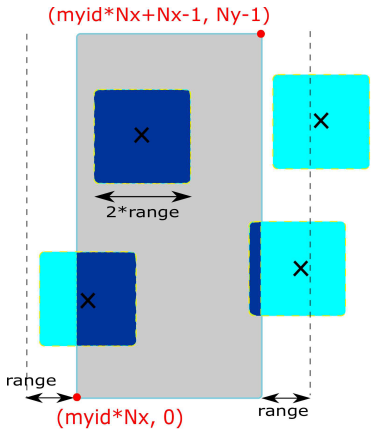

Fig. 7 Relation between the region that process myid deal with and supports.

[*4] We consider the case where Nxg is divisible by nump.

Treatment of supports in GPU-parallel programming

In calculation related to order parameter ϕ_n, we need to perform multi-loop calculation for n and (i, j, k), where n is the index of particles and (i, j, k) is the coordinate on supports. For example, in the case of Block c (or, computation of $\eta(\boldsymbol{r})$ from $\phi_n(\boldsymbol{r})$), a corresponding program in C language can be written as follows:

```
for(int n=0;n<N;n++){
  double Rnx = R[n].x; double Rny = R[n].y; double Rnz = R[n].z;
  int in = (int)Rnx; int jn = (int)Rny; int kn = (int)Rnz;

#pragma acc parallel loop collapse(3)
  for(int i=0;i<N_range;i++){
    int ir = i+in-range_m1; int irP = (ir+Nx)%Nx; double dx = ir - Rnx;
    for(int j=0;j<N_range;j++){
      int jr = j+jn-range_m1; int jrP = (jr+Ny)%Ny; double dy = jr - Rny;
      for(int k=0;k<N_range;k++){
        int kr = k+kn-range_m1; int krP = (kr+Nz)%Nz; double dz = kr - Rnz;
        if(range2<dx*dx+dy*dy+dz*dz) continue;
          eta[irP][jrP][krP] += (eta_c - eta_s)*phi[n][i][j][k];
      }
    }
  }

}
```

where range2=2×range, range_m1=range-1, and eta_s and eta_c are the viscosity of a solvent and colloids, respectively. eta is viscosity field and initialized as eta[i][j][k] = eta_s for all (i, j, k). See the above for the other notations. The number of iteration of this multi-loop calculation is N×N_range^3. For example, in Chap. 8, we typically set N∼4000 and N_range^3 = 16^3 ∼4000. In this case, N×N_range^3 ∼ 10^7. To take advantage of GPU, it is desirable to parallelize the whole of the multi-loop calculation, but we need to be careful upon implementation: Specifically, there is the possibility that the lattice points which the different supports shares can be refereed at the same time (see Fig. 8A2), which is not thread-safe [*5]. The simplest way to avoid this problem may be to parallelize only the inside of the loop for n (see the line where a OpenACC directive is inserted). However, with this parallelization, we cannot expect a sufficiently efficient computation since the parallel number is not large enough (N_range^3 ∼4000).

To solve this problem, we split support into 8 equal-size parts as described in Fig. 8B1, and perform a parallel computation with the parallel number N×N_range^3/8 for each parts. Specifically, we modify the above program as in the below:

```
for(int b=0;b<8;b++){
  int ib = b/4; int jb = (b%4)/2; int kb = b%2;

#pragma acc parallel loop collapse(4)
   for(int n=0;n<N;n++){
     //the same as the above
```

[*5] This problem is also the case for Block d.

```
    for(int i=ib*range;i<(ib+1)*range;i++){
      //the same as the above
      for(int j=jb*range;j<(jb+1)*range;j++){
        //the same as the above
        for(int k=kb*range;k<(kb+1)*range;k++){
        //the same as the above
        }
      }
    }
  }

}
```

where b is a label to specify the 8 divided parts. For example, in the case of b=2, the right blue region in the figure 8C1 is the region refereed during parallel computation. As described in Fig. 8C2, the calculation regions which belong to different supports do not overlap because of repulsive interactions among the colloids, which allows us to perform a thread-safe parallel computation.

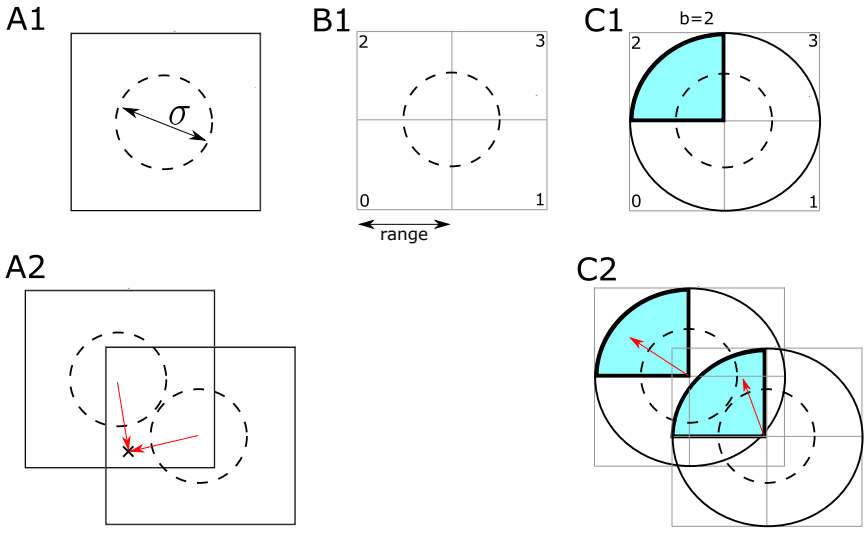

Fig. 8 **A1** shows an illustrative figure of a support. The region where the dashed line surrounds represents the part which the colloid occupies (σ being the diameter of colloids). If we parallelize the whole of the multi-loop calculation, there is the possibility that lattice points can be refereed at the same time from the different supports (**A2**), which is not thread-safe. To avoid this, we divide support into 8 equal-size parts as in **B1**, and we label the 8 divided regions by b=0,1, ..., 7. The right blue region in **C1** represents the calculation region of b=2. As seen in **C2**, the calculation regions which belong to different supports do not overlap because of the repulsive interactions among colloids.

C Analysis of network structures based on a skeletonization method

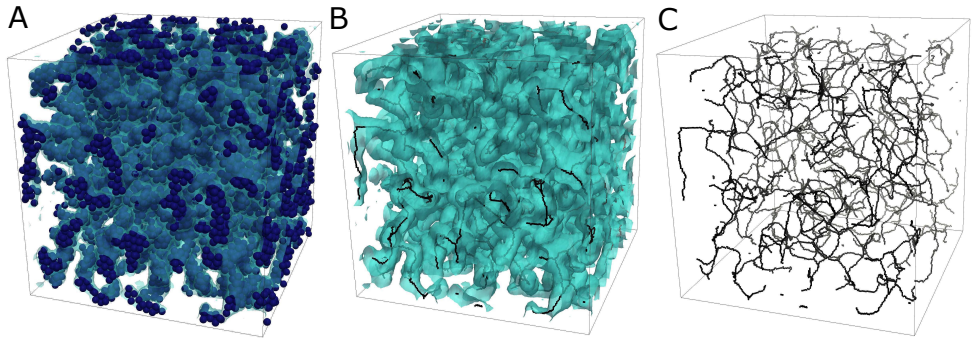

Fig. 9 **A** 3D reconstruction of confocal images in EXP1 at state point B ($\phi \cong 10\%$, $\epsilon\beta \cong 6$) at time $t_w/\tau_B = 108$. The image shows the positions of colloids together with the surface of coarse-grained network structures at various times. We also show an image of the coarse-grained network structure together with the skelton (**B**), and an image of only the skelton (**C**).

One of the distinct features of a colloidal gel is the space-spanning nature of its network structure. In order to capture the topological characteristics of the network, we performed its analysis based on a skeletonization method, as follows. Since our interest is not in the particle-scale structure, we first coarse-grain a phase-separated structure composed of discrete colloidal particles into a continuous field by making Gaussian blurring operation of the particles with the standard deviation of $\sigma/2$. Then we binarized the field by setting the half of the maximum value of the Gaussian function as the threshold and obtained the continuous network domain structure that is occupied by colloidal particles (see Fig. 9A). Next we extract the skeleton of the network structure by applying a skeletonization algorism on the domain (see Fig. 9B, C). Here we utilized a module in python's package (skeletonize_3d in scikit-image [212]) and the analysis was performed in the square lattice with 256^3 pixels. The ratio of the diameter of colloids to the pixel size was set as $\sigma = 7.4$ pixels for all the data (for both experiments and simulations). Denoting the set of the positions of the skeleton as V, we define the total length of the skeleton ℓ as the total number of the elements $\ell = \sum_{i \in V} 1$.

If the distance between two different elements $i, j \in V$ is within $\sqrt{3}\times$ pixel, we regard them as being connected. We denote the number of the connected components as N_c. Finally, we define the connectivity of i-th element, c_i, as the number of elements connected to element i. Then the "Genus number", G, which is the number of holes in the network structure, can be obtained from c_i and N_c as:

$$G = \sum_{i \in V} \frac{c_i - 2}{2} + N_c. \tag{9}$$

D Direct observation of dynamic arrest due to colloidal gelation

This section describes experimental results regarding mechanism of colloidal gelation, which I obtained in my master's research. I show the result here since it is highly related to one of the subject of my phD study: phase separation dynamics of colloidal suspensions.

D.1 Motivation

A gel is generally composed of a percolated network structure and a fluid, which is the origin of the coexistence of elasticity and fluidity. The resulting mechanical and transport properties play a crucial role in various applications, including foods, tissues, inks, and cosmetics. However, the gelation mechanism has not fully understood yet despite intensive researches in the past. Colloid-polymer mixtures are often used as a model system to study this type of gelation, in which we can precisely control the phase behavior in terms of the colloid volume fraction ϕ and the polymer concentration, which determines the strength of the attractive interaction between colloids, ϵ [13, 14, 21]. In the mixture, polymers are a hidden valuable controlling the interaction potential between colloids via the depletion effect [21, 12]. When ϵ is much larger than the thermal energy $k_{\mathrm{B}}T$, gels are formed by cluster-growth percolation [95] and the ratio between the microscpoic structre and the mechanical properties are rather well understood especially for a dilute system ($\phi < 1\%$) [213, 214, 215]. On the other hand, when ϵ is the order of several times of $k_{\mathrm{B}}T$, gels are formed by an out-of-equilibrium process, i.e., arrested spinodal decomposition and thus the resulting gels are in a non-equilibrium state [42].

Since the pioneering work on the phase demixing dynamics of colloid-polymer mixtures [216, 12], many experimental studies have been performed: For example, the important roles of collective dynamics in the colloid-rich domain has recently been pointed out [217, 218, 122]. A recent development of confocal microscopy observation and its applications to colloidal systems allow to observe the gel network structure and dynamics at a single-particle level. For example, microscopic details such as dynamic heterogenities [219] and locally favored structures [101] were successfully accessed. Furthermore, the precise comparison with confocal microscopy observation, theory, and simulations has established that colloidal gelation indeed happened in an unstable state via spinodal decomposition and the volume fraction of the dynamic arrested phase directly measured exceeds ϕ_{g}. Thus, colloidal gel is now a widely recognized as an out-of-equilibrium state resulting from interplay between spinodal decomposition and vitrification: [14, 105, 42]. The most strong evidence for the relevance of glass transition comes from the fact that $\phi > \phi_{\mathrm{g}}$ for the arrested colloid-rich phase and the absence of crystalline order.

However, this is not the end of story since there still remains a few very fundamental questions: First of all, it is not clear how the colloid-rich liquid phase can increase its volume fraction ϕ to reach ϕ_{g}. Furthermore, the concept of a glass is

basically for a bulk system, but the network structure formed in colloidal gels are often thin. Thus, it is not clear whether such a thin network structure can be simply regarded as a glass or not. In this section, we study these problems experimentally by confocal microscopy observation.

D.2 Method

Experimental method

To address the above issues experimentally, we need to follow the phase-demixing process at a single particle level while tracking the trajectories of all particles from the very beginning of demixing to the final dynamic arrest. This is quite challenging experimentally: Firstly it is difficult to follow the phase demixing process just after its initiation since this means that we must initiate the demixing without strong perturbation to the system. Secondly, to follow the trajectories of all particles as a function of time, we need very high spatial and time resolutions.

We have overcome these difficulties as follows. Firstly, we synthesize and use core-shell colloidal particles only whose cores have fluorescent dyes to avoid mis-tracking due to the overlap of fluorescent images (Fig. 3). We also used rather large colloids with a diameter of $\sigma = 2.56\mu$m (the size polydispersity of 3 %) and thus the Brownian time $\tau_{\rm B} = a^2/6D_0$, where D_0 is the free-particle diffusion constant and $a = \sigma/2$ is the radius of the particle, was estimated to be ~ 5.1 sec [*6]. The region observed by confocal microscopy was 53.5 μm^3 (256^3 pixel), and the time required for scanning this region was 8.08 sec ($\sim 1.6\tau_{\rm B}$). This allows us to track the trajectories of all particles continuously without mis-tracking while simultaneously observing the change of the overall network structure. In order to induce controllable attractive interaction (depletion interaction[20, 21]), we mix colloidal suspension with polystyrene with a molecular weight of 8.4×10^6 Da. The the range of the depletion interaction to the colloid diameter, $\Delta \equiv 2R_{\rm g}/\sigma$, is approximately $\Delta \sim 0.08$. We mix colloids, polymers, and a mixture of cis-decalin and cyclohexyl bromide, whose density and refractive index are simultaneously matched with those of colloids. Thus the effects of gravity and the van der Waals interaction between colloids can be ignored.

Secondly, we have employed a salt injection method to initiate phase separation. This protocol allows us to initiate phase demixing almost instantaneously and gently at time zero, without harmful perturbation such as hydrodynamic flow induced by mixing of samples. See Sec. 3.1.3 for the detail of this method and the definition of the onset time of demixing $t_{\rm w} = 0$.

The results shown below are obtained for colloidal suspensions with the volume fraction of $10\% \lesssim \phi \lesssim 20\%$ and the polymer concentration $C_{\rm p} = 0.5$ g/L.

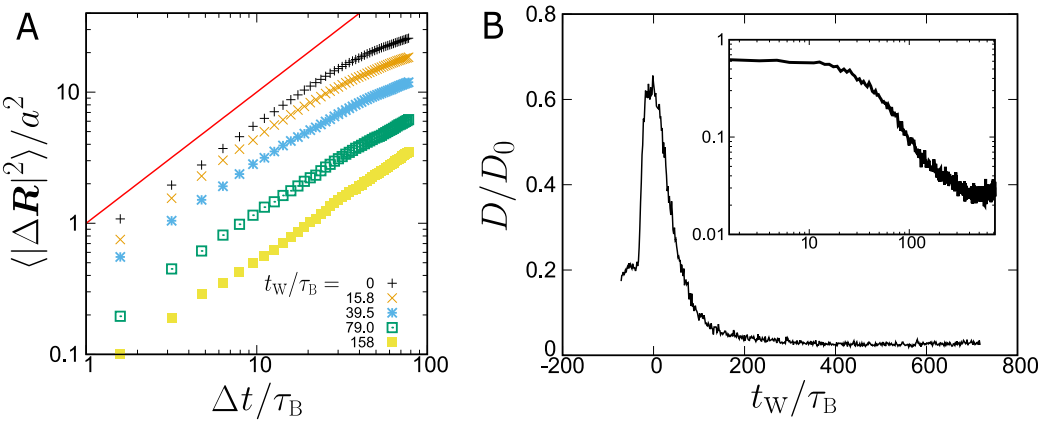

Fig. 10 **The temporal change of "diffusion constant". A.** The mean square displacement (MSD) for different reference time t_w. The red line in the figure is MSD of a free particle. Here we show the experimental result at $\phi = 11.1\%$. Panel **B** shows the temporal change of "diffusion constant" D, obtained by linear fitting for short time behavior of MSD (specifically, $\Delta t/\tau_B < 10$). Here D is scaled by diffusion constant of a free particle, D_0.

Particle tracking and mobility of the system

As we mentioned in the above, we set the time window of the observation as $\Delta t_{scan} = 8.08$ sec, which is around the free diffusion time of the colloid ($\Delta t_{scan}/\tau_B \sim 1.6$). Thus, we can track the trajectories of the colloids throughout the phase-demixing process. We reconstruct the trajectory of the i-th particle by linking the position at time t, $\boldsymbol{R}_i(t)$ with the positions of the particles at the next time step, $\{\boldsymbol{R}_j(t + \Delta t_{scan})\}_j$: Specifically, we identify the j-th particle which minimizes $|\boldsymbol{R}_j(t + \Delta t_{scan}) - \boldsymbol{R}_i(t)|$ with i-th particle.

With the above method, we can obtain the displacements of particles for time interval $\Delta t = n\Delta t_{scan}$ (n being an integer), $\Delta \boldsymbol{R}_i(t) = \boldsymbol{R}_i(t + \Delta t) - \boldsymbol{R}_i(t)$. Here we consider the case of aggregation kinetics at $\phi = 11.1\%$ as an example. Fig. 10A, shows the mean square displacement (MSD) $\langle|\boldsymbol{R}_i(t_w + \Delta t) - \boldsymbol{R}_i(t_w)|^2\rangle$ for various reference time t_w. Here we can see that MSD shows a linear behavior for small Δt, and the perfactor decreases as the reference time increases, which reflects slowing down of the diffusion motions due to aggregation of the particles. For large Δt, we can see that MSD deviates from linear behavior, but this is just because the slow motions of the colloids at late stage are statistically significant in this time regime. From the above, as far as focusing on a relatively short time region such as $n < 10$, we may regard that MSD is proportional to time. Thus, we may use the corresponding diffusion constant, $D(t_w)$ as a physical value to characterize the mobility of the system. Fig. 10B shows the time evolution of $D(t_w)$. At early time

[*6] More precisely, it corresponds to the Brownian time at temperature $T = 26°C$ and the polymer concentration $C_p = 0.5$ g/L. Because we fix T and C_p at these values in this chapter, we may regard τ_B as constant.

of observation ($t_w < 0$), we can see the behavior that D inceases suddenly from a almost constant value, which corresponds to a screening process of electrostatic repulsion (see Sec. 3.1.3). After that D reaches maximum at around $t_w \sim 0$ and decreases with time, from which we can confirm that the definition of the onset time of aggregation discussed in the above works well.

D.3 Results

Three time regimes and introduction of "arrest time"

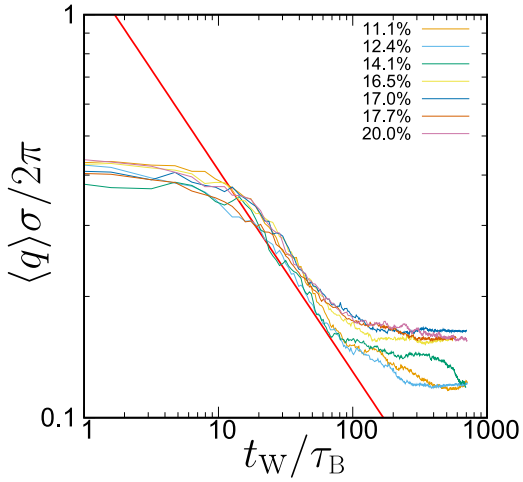

Fig. 11 **Temporal change of the characteristic wavenumber at various volume fractions.** The red line represents a slope with 1/2.

To identify the time when dynamic arrest takes place during the phase demixing process, we first calculate the characteristic wave number $\langle q(t) \rangle$ (see Sec. 5.3.1 and 3.1.5 on the definition of $\langle q(t) \rangle$), which is roughly the inverse of the characteristic size of the phase-separated structure. We show in Fig. 11 the temporal change in $\langle q(t) \rangle$ for various ϕ's. We can see that there are three time regimes: (1) the early stage where $\langle q(t) \rangle$ is almost constant with time. This is characteristic of the early stage of spinodal decomposition known as the Cahn's linear regime [20], supporting the claim that colloidal gelation is initiated by spinodal decomposition. (2) the domain growth (or, coarsening) regime, where $\langle q(t) \rangle$ decreases with time as $t^{-1/2}$. (3) the final arrest regime, where the coarsening slows down and tends to stop and $\langle q(t) \rangle$ approaches a plateau value. The departure from the power-law growth of domains or networks indicates that the coarsening is arrested by some mechanism. Here we define the onset of the dynamical arrest as t_a and refer the time region $t_w > t_a$ to the aging regime.

Visualization of network structure

Now we show the time evolution of the 3D structure of the colloid-rich liquid phase in Fig. 12. To visualize the network structure of colloidal gel, we show the surface of coarse-grained network structure (colloid-rich phase: the blue translu-

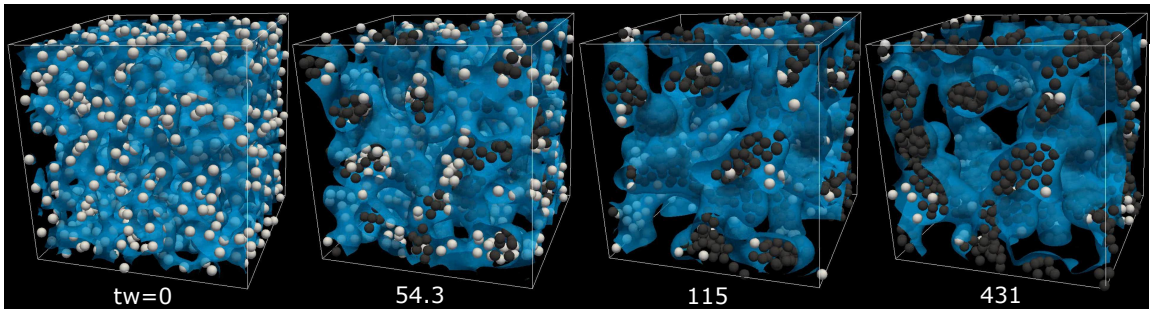

Fig. 12 **The time evolution of 3D structure.** The blue translucent part in the image represents the surface of coarse-grained network structure (colloid-rich phase). The particles which constitute tetrahedral structure are displayed as black spheres (the others being labeled in white).

cent part) together with the positions of colloids (spheres). Here we display the strongly packed particles in black and the others in white. See the later section "Structural analysis" for the detailed definition of labeling of the colors. We constract the colloid-rich phase in the following way: First we replace discrete colloidal particles at positions $\{\boldsymbol{R}_i\}_i$ by continuous Gaussian fields and represent the spatial distribution of colloids by a continuous field Φ. Specifically, we constract Φ as $\Phi(\boldsymbol{r}) = \sum_i \exp(-|\boldsymbol{r} - \boldsymbol{R}_i|^2/2\lambda^2)$. Then, we define "colloid-rich phase" Γ as $\Gamma = \{\boldsymbol{r} \in V | \Phi(\boldsymbol{r}) > \Phi_0\}$ (V being the whole space of the scanned box). Here we set $\Phi_0 = \exp(-\lambda^2/2\lambda^2) = e^{-1/2}$ and $\lambda = 1.23\sigma$, which corresponds to the location of first minima of radial distribution function observed in late stage ($t_\mathrm{a} < t_\mathrm{w}$).

In Fig. 12, we can see that space-spanning network structure is formed at the very beginning of phase demixing, and coarsens with time. From the particle color (or, fraction of the black particles), we can also find that densification in network structure progresses with time [*7].

Cooperativity in particle motion

We can expect that the densification leads to the increase in the cooperativity in particle motion. This we confirm from a snapshot of particle motion. An example is shown in Fig. 13A. To quantify this, we calculate a correlation length ξ related with directions of motion of particles in the following way. We first define "velocities" of particles as $\boldsymbol{V}_i(t_\mathrm{w}) = \Delta\boldsymbol{R}_i(t_\mathrm{w})/\Delta t$. Here we set $\Delta t = \Delta t_\mathrm{scan}$ (or, $n = 1$) [*8]. For a set of $\{(i,j)\}$ satisfied with $r < |\boldsymbol{R}_i(t_\mathrm{w}) - \boldsymbol{R}_j(t_\mathrm{w})| < r + \Delta r$, we take an average on $\cos\theta_{ij} = \hat{\boldsymbol{V}}_i(t_\mathrm{w}) \cdot \hat{\boldsymbol{V}}_j(t_\mathrm{w})$, and just wrote the average as $\langle\cos\theta\rangle(r, t_\mathrm{w})$ where where $\hat{\boldsymbol{V}}_i$ is unit vector of $\boldsymbol{V}_i$. As an example, we show $\langle\cos\theta\rangle$ for $\phi = 11.1\%$ in Fig. 13D,

[*7] The densification process can be confirmed from the time evolution in the fraction of the volume of colloid-rich phase $|\Gamma|/|V|$, where we observe that $|\Gamma|/|V|$ monotonically decreases with time. We don't show the corresponding graph here since Γ is very sensitive to parameter setting (Φ_0 and λ).

[*8] We perform the same analysis for $n = 1, ..., 5$, but no significant difference in ξ has not been confirmed for $t_\mathrm{w} < t_\mathrm{a}$. However, we find that behavior of ξ after arrest time ($t_\mathrm{a} < t_\mathrm{w}$) strongly depends on the choice of n.

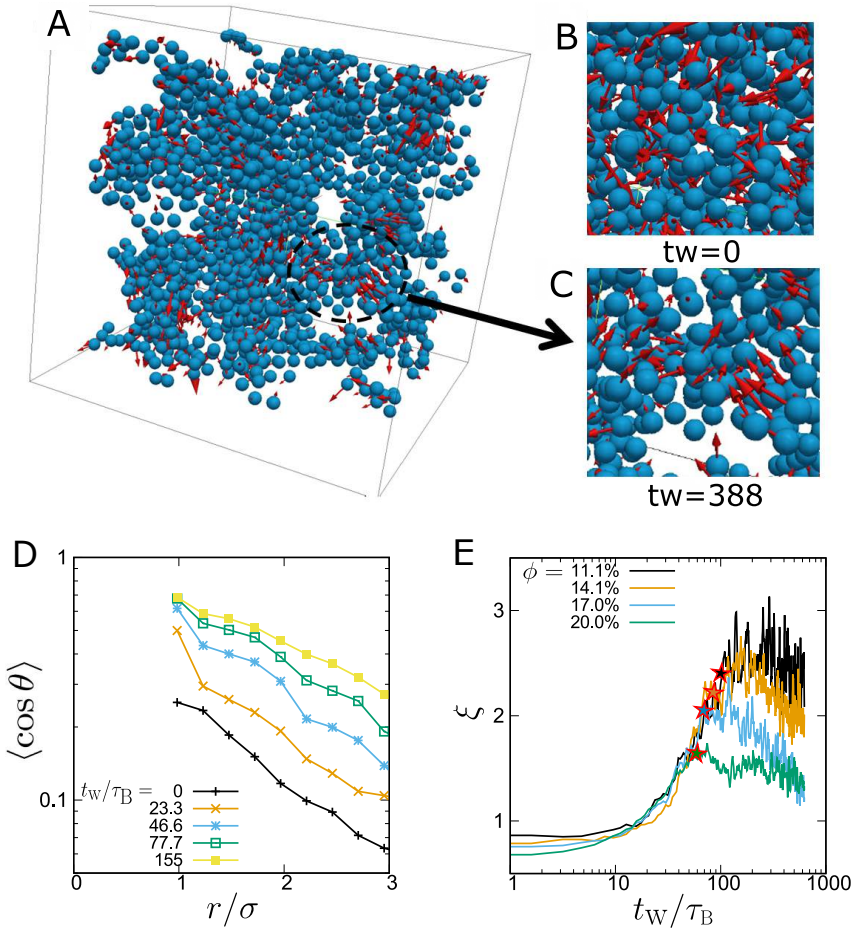

Fig. 13 **Cooperativity in particle motion. A.** An example of 3d structure of colloids ($t_w/\tau_B = 388$). The red arrows shown on each particles represent displacement vectors, $\Delta \boldsymbol{R}_i(t_w)$. For visualization, the length of the arrows is normalized by an arbitrary value. Panel **C** is an enlarged image of the part surrounded by a dashed line in panel **A**, where we can see that particles are moving cooperatively. For comparison, we show the same image at $t_w = 0$ in panel **B**, where we can see that particles are moving randomly. **D.** Spatial correlation of the direction of particle motions. Here we show the result at $\phi = 11.1\%$. **E.** The time evolution of correlation length ξ for various volume fractions.

where we can see that $\langle \cos\theta \rangle$ decays approximately exponentially with respective to r. We determine $\xi(t_w)$ by fitting $\langle \cos\theta \rangle(r, t_w)$ with $\exp(-r/\xi(t_w))$.

We show the temporal change in ξ in Fig. 13E, where we can see that ξ grows rapidly in the early stage but stops growing rather abruptly around the arrest time $t_w \sim t_a$ (indicated by the star symbols). This crossover behavior can be regarded as a manifestation of the freezing of particle motion in the network structure and the resulting emergence of the rigidity.

Structural analysis

To explore the structural origin of the rigidity, we study the local structural arrangement of the network microscopically. Firstly, we show the temporal change of interparticle bonds per particle, n_b. Here we regard that two particles have a bond if the center-of-mass distance is smaller than 1.23σ. The result is shown in Fig. 14A, where we can see that n_b grows before arrest time and the speed of the growth slows down after arrest time. We can also see that in the entire time range

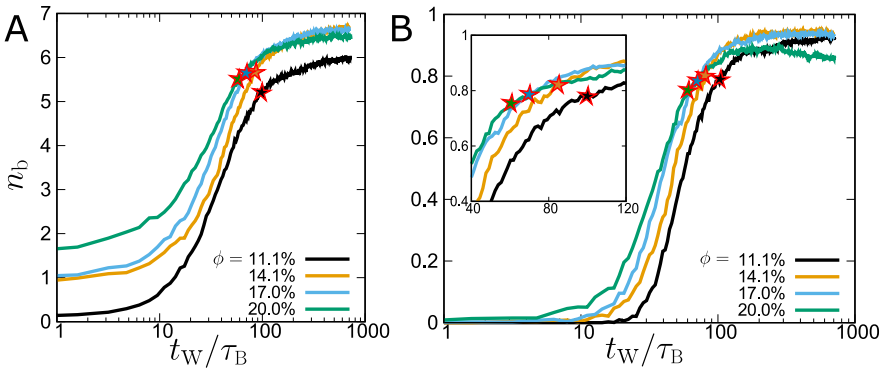

Fig. 14 **Analysis of local structure. A.** The temporal change of interparticle bonds per particle, n_b. **B.** The temporal change of the fraction of particles with tetrahedral structures. The star symbols correspond to arrest time.

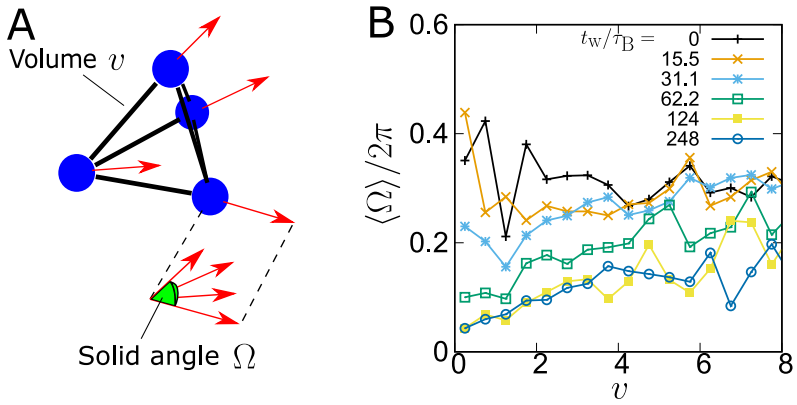

Fig. 15 **Correlation between local packing and mobility of particles. A.** By performing Delaunay tessellation for the center-of-mass positions of particles, we can relate a Delaunay cell to four particles in the corners of the cell (blue spheres). To see link between local packing and mobility of particles in a qualitative way, we consider a solid angle Ω (light green part) which the displacement vectors of four particles (red arrows) constitute, and examine correlation between Ω and the volume of the corresponding cell, v. **B** represents the average of Ω for a constant v at various time. Here v is normalized by the volume of regular tetrahedron with length σ on one side. In this figure, we only show the result at $\phi = 11.1\%$. The arrest time at this volume fraction is $t_\mathrm{a}/\tau_\mathrm{B} \sim 100$.

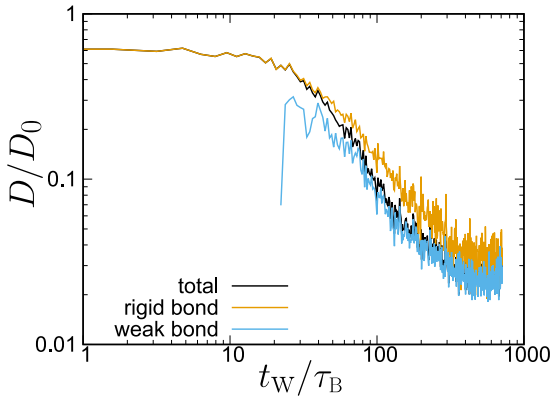

Fig. 16 **Relation between local structure and particle mobility.** The brown and blue line represent the effective diffusion constant D of particles for involved and not involved in tetrahedral structures, respectively. The black line is D for all particles. Here we show the result at $\phi = 11.1\%$ and the corresponding arrest time is $t_a/\tau_B \sim 100$.

of the observation, $n_b < 7$, indicating that most particles are located in the domain interface. This means that analysis methods developed for bulk systems such as the local bond order parameter analysis cannot be applied to our results. Then, we focus on a compact tetrahedral structure made of four mutually bound particles, since it has a smallest rigid structural unit. We show the fraction of particles involved in tetrahedral structures in Fig. 14B. During the process of network coarsening, the fraction of particles in tetrahedral structures grows dramatically, but it is saturated around the arrest time and finally reaches the plateau. This implies that the formation of local structures of mechanical stability plays an important role in the slowing down of macroscopic structural change.

To see this link between structure and dynamics in more detail, we analyze the correlation between the local packing and the mobility of particles. Figure 15B shows the relation between the volume of a Delaunay cell and the coherence of the motion of particles contained in the cell. Here Ω is the solid angle made by the displacement vectors of four particles in the corners of the cell (see Fig. 15A). Thus, the smaller Ω means the higher coherency of the directions of particle motion. The results clearly show that particles packed more densely exhibit more coherent motion. After the arrest time, there is little change in this relationship, indicating that that highly packed dense local structures tend to be retained for a long time, or stable.

Dynamics in aging regime

In the above, we have seen that slowing down of phase separation dynamics is triggered by the formation of locally stable densely-packed structures in colloid-rich phase. Here we mention roles of locally stable structures after the dynamics arrest, i.e., in the aging regime. In Fig. 14B, we can see that the number of particles not in tetrahedral structures decreases with time, but very slowly, in the aging regime. As shown in Fig. 12, the characteristic wave number slowly deceases

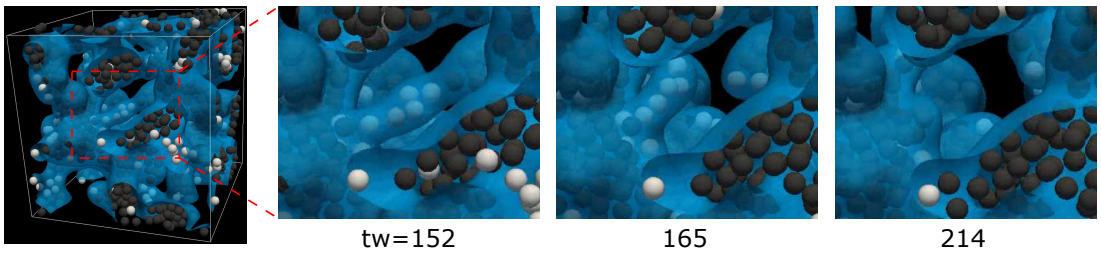

Fig. 17 **Rupture of network arm observed in aging regime.**

in the aging regime, implying that the slow increase in locally stable structures may be related to macroscopic structural change of the network in aging regime.

To see this, we calculate the effective diffusion constant of particles for both involved and not involved in tetrahedral structures. As shown in Fig. 16, particles not in tetrahedral structures are more mobile than the ones in them even after the dynamic arrest. We examine where these highly mobile particles are located in the network and find that a part of them are located in network strands that are under tension and going to be ruptured (see Fig. 17). This rupture is considered to be induced by mechanical tension acting on network arms as a consequence of densification in colloid-rich domain. This suggests that the topological structure of the network is selected mechanically to satisfy the mechanical force balance condition. However, such structural changes in network structure is rare events for our observation window. To gain better understanding of the above mechanism, we need large scale experiments to evaluate these rupture events with statistical significance.

D.4 Summary

To summarize, we have succeeded in following the gas-liquid phase separation and the resulting gelation process of colloidal suspensions interacting with short-range attraction (interaction range: $\Delta = 0.08$) while tracking the trajectories of all particles from the beginning to the final arrested state. We find that there are three regimes: the early linear regime, the coarsening regime characterized by the growth exponent of 1/2, and the aging regime, and successfully identify "arrest time" t_{a}, at which phase separation dynamics significantly slows down. Concerning the final dynamic arrest, we observe that the fraction of locally stable densely packed structures rapidly increases towards arrest time, and the trend slows down after arrest time. This indicates that the dynamic arrest is a consequence of phase separation dynamics hindered by the formation of locally stable rigid structures.

Bibliography

[1] Lekkerkerker, H. N. W., Poon, W. C. K., Pusey, P. N., Stroobants, A. & Warren, P. B. Phase behaviour of colloid+ polymer mixtures. *Europhys. Lett.* **20**, 559 (1992).

[2] Fine, B. M., Pande, J., Lomakin, A., Ogun, O. O. & Benedek, G. B. Dynamic critical phenomena in aqueous protein solutions. *Phys. Rev. Lett.* **74**, 198–201 (1995).

[3] Fine, B. M., Lomakin, A., Ogun, O. O. & Benedek, G. B. Static structure factor and collective diffusion of globular proteins in concentrated aqueous solution. *J. Che. Phys.* **104**, 326–335 (1996).

[4] Rouch, J., Tartaglia, P. & Chen, S. Experimental evidence of nonexponential relaxation near the critical point of a supramolecular liquid mixture. *Physical review letters* **71**, 1947 (1993).

[5] Onuki, A. *Phase Transition Dynamics* (Cambridge University Press, 2002).

[6] Palberg, T. Crystallization kinetics of colloidal model suspensions: recent achievements and new perspectives. *Journal of Physics: Condensed Matter* **26**, 333101 (2014).

[7] Tanaka, H. & Araki, T. Simulation method of colloidal suspensions with hydrodynamic interactions: Fluid particle dynamics. *Phys. Rev. Lett.* **85**, 1338 (2000).

[8] Furukawa, A., Tateno, M. & Tanaka, H. Physical foundation of the fluid particle dynamics method for colloid dynamics simulation. *Soft Matter* **14**, 3738 – 3747 (2018).

[9] Tanaka, H., Nishikawa, Y. & Koyama, T. Network-forming phase separation of colloidal suspensions. *J. Phys.: Condens. Matter* **17**, L143 (2005).

[10] Bailey, A. *et al.* Spinodal decomposition in a model colloid-polymer mixture in microgravity. *Physical review letters* **99**, 205701 (2007).

[11] Tanaka, H. & Nishikawa, Y. Viscoelastic phase separation of protein solutions. *Phys. Rev. Lett.* **95**, 078103 (2005).

[12] Anderson, V. J. & Lekkerkerker, H. N. Insights into phase transition kinetics from colloid science. *Nature* **416**, 811 (2002).

[13] Poon, W. C. K. The physics of a model colloid–polymer mixture. *J. Phys.: Condens. Matter* **14**, R859 (2002).

[14] Zaccarelli, E. Colloidal gels: equilibrium and non-equilibrium routes. *J. Phys.: Condens. Matter* **19**, 323101 (2007).

[15] Larson, R. G. The structure and rheology of complex fluids (topics in chemical engineering). *Oxford University Press, New York Oxford* **86**, 108 (1999).

[16] Marchetti, M. C. *et al.* Hydrodynamics of soft active matter. *Reviews of*

Modern Physics **85**, 1143 (2013).

[17] Banani, S. F., Lee, H. O., Hyman, A. A. & Rosen, M. K. Biomolecular condensates: organizers of cellular biochemistry. *Nature reviews Molecular cell biology* **18**, 285 (2017).

[18] Israelachvili, J. N. *Intermolecular and surface forces* (Academic press, 2011).

[19] Verwey, E. J. W., Overbeek, J. T. G. & Overbeek, J. T. G. *Theory of the stability of lyophobic colloids* (Courier Corporation, 1999).

[20] Asakura, S. & Oosawa, F. On interaction between two bodies immersed in a solution of macromolecules. *J. Chem. Phys.* **22**, 1255–1256 (1954).

[21] Lekkerkerker, H. N. W. & Tuinier, R. *Colloids and the Depletion Interaction*, vol. 833 (Springer, 2011).

[22] Vrij, A. Polymers at interfaces and the interactions in colloidal dispersions. *Pure and Applied Chemistry* **48**, 471–483 (1976).

[23] Eisenriegler, E., Hanke, A. & Dietrich, S. Polymers interacting with spherical and rodlike particles. *Physical Review E* **54**, 1134 (1996).

[24] Ye, X. *et al.* Depletion interactions in colloid-polymer mixtures. *Physical Review E* **54**, 6500 (1996).

[25] Verma, R., Crocker, J. C., Lubensky, T. C. & Yodh, A. Entropic colloidal interactions in concentrated dna solutions. *Physical review letters* **81**, 4004 (1998).

[26] Royall, C. P., Louis, A. A. & Tanaka, H. Measuring colloidal interactions with confocal microscopy. *J. Chem. Phys.* **127**, 044507 (2007).

[27] Alder, B. & Wainwright, T. Phase transition for a hard sphere system. *The Journal of chemical physics* **27**, 1208–1209 (1957).

[28] Wood, W. W. & Jacobson, J. Preliminary results from a recalculation of the monte carlo equation of state of hard spheres. *The Journal of Chemical Physics* **27**, 1207–1208 (1957).

[29] Pusey, P. N. & Van Megen, W. Phase behaviour of concentrated suspensions of nearly hard colloidal spheres. *Nature* **320**, 340 (1986).

[30] Hansen, J.-P. & McDonald, I. R. *Theory of simple liquids* (Elsevier, 1990).

[31] Lennard-Jones, J. E. & Devonshire, A. Critical phenomena in gases-i. *Proc. R. Soc. Lond. A* **163**, 53–70 (1937).

[32] Hoover, W. G. & Ree, F. H. Melting transition and communal entropy for hard spheres. *The Journal of Chemical Physics* **49**, 3609–3617 (1968).

[33] Poon, W. *et al.* An experimental study of a model colloid-polymer mixture. *Journal de Physique II* **3**, 1075–1086 (1993).

[34] Ilett, S. M., Orrock, A., Poon, W. & Pusey, P. Phase behavior of a model colloid-polymer mixture. *Physical Review E* **51**, 1344 (1995).

[35] Muschol, M. & Rosenberger, F. Liquid–liquid phase separation in supersaturated lysozyme solutions and associated precipitate formation/crystallization. *The Journal of chemical physics* **107**, 1953–1962 (1997).

[36] ten Wolde, P. R. & Frenkel, D. Enhancement of protein crystal nucleation by critical density fluctuations. *Science* **277**, 1975–1978 (1997).

[37] Noro, M., Kern, N. & Frenkel, D. The role of long-range forces in the phase behavior of colloids and proteins. *EPL (Europhysics Letters)* **48**, 332 (1999).

[38] Pitzer, K. S. Corresponding states for perfect liquids. *The Journal of Chemical*

Physics **7**, 583–590 (1939).

[39] Guggenheim, E. A. The principle of corresponding states. *The Journal of Chemical Physics* **13**, 253–261 (1945).

[40] Noro, M. G. & Frenkel, D. Extended corresponding-states behavior for particles with variable range attractions. *J. Chem. Phys.* **113**, 2941–2944 (2000).

[41] Taffs, J., Malins, A., Williams, S. R. & Royall, C. P. A structural comparison of models of colloid–polymer mixtures. *J. Phys.: Condens. Matter* **22**, 104119 (2010).

[42] Lu, P. J. *et al.* Gelation of particles with short-range attraction. *Nature* **453**, 499–503 (2008).

[43] Furukawa, A. & Tanaka, H. Key role of hydrodynamic interactions in colloidal gelation. *Phys. Rev. Lett.* **104**, 245702 (2010).

[44] Whitmer, J. K. & Luijten, E. Influence of hydrodynamics on cluster formation in colloid- polymer mixtures. *J. Phys. Chem. B* **115**, 7294–7300 (2011).

[45] Cao, X. J., Cummins, H. Z. & Morris, J. F. Hydrodynamic and interparticle potential effects on aggregation of colloidal particles. *J. Colloid Interface Sci.* **368**, 86–96 (2012).

[46] Varga, Z., Wang, G. & Swan, J. The hydrodynamics of colloidal gelation. *Soft Matter* **11**, 9009–9019 (2015).

[47] Huang, R. *et al.* Direct observation of the full transition from ballistic to diffusive brownian motion in a liquid. *Nature Physics* **7**, 576 (2011).

[48] Alder, B. & Wainwright, T. Decay of the velocity autocorrelation function. *Physical review A* **1**, 18 (1970).

[49] Lisy, V. & Tothova, J. On the (hydrodynamic) memory in the theory of brownian motion. *arXiv preprint cond-mat/0410222* (2004).

[50] Landau, L. & Lifshitz, E. *Course of theoretical physics. vol. 6: Fluid mechanics* (London, 1959).

[51] Chow, T. & Hermans, J. Effect of inertia on the brownian motion of rigid particles in a viscous fluid. *The Journal of Chemical Physics* **56**, 3150–3154 (1972).

[52] Hauge, E. & Martin-Löf, A. Fluctuating hydrodynamics and brownian motion. *Journal of Statistical Physics* **7**, 259–281 (1973).

[53] Bedeaux, D. & Mazur, P. Brownian motion and fluctuating hydrodynamics. *Physica* **76**, 247–258 (1974).

[54] De Zarate, J. M. O. & Sengers, J. V. *Hydrodynamic fluctuations in fluids and fluid mixtures* (Elsevier, 2006).

[55] Hills, B. A generalized langevin equation for the angular velocity of a spherical brownian particle from fluctuating hydrodynamics. *Physica A: Statistical Mechanics and its Applications* **80**, 360–368 (1975).

[56] Kaneda, Y. Brownian motion of an almost spherical drop of viscous fluid and fluctuating hydrodynamics. *Physica A: Statistical Mechanics and its Applications* **101**, 423–430 (1980).

[57] Doi, M. & Edwards, S. F. *The Theory of Polymer Dynamics*, vol. 73 (oxford university press, 1988).

[58] Ermak, D. L. & McCammon, J. Brownian dynamics with hydrodynamic interactions. *The Journal of chemical physics* **69**, 1352–1360 (1978).

[59] Beenakker, C. Ewald sum of the rotne–prager tensor. *The Journal of chemical physics* **85**, 1581–1582 (1986).

[60] Brenner, H. The slow motion of a sphere through a viscous fluid towards a plane surface. *Chem. Eng. Sci.* **16**, 242–251 (1961).

[61] Ichiki, K. Improvement of the stokesian dynamics method for systems with a finite number of particles. *Journal of fluid mechanics* **452**, 231–262 (2002).

[62] Khair, A. S. & Brady, J. F. On the motion of two particles translating with equal velocities through a colloidal dispersion. In *Proc. Royal Soc. London A*, vol. 463, 223–240 (The Royal Society, 2007).

[63] Hu, H. H., Patankar, N. A. & Zhu, M. Direct numerical simulations of fluid–solid systems using the arbitrary lagrangian–eulerian technique. *J. Comput. Phys.* **169**, 427–462 (2001).

[64] Yamamoto, R. & Nakanishi, K. Computer simulation of vapor-liquid phase separation in two-and three-dimensional fluids: Growth law of domain size. *Phys. Rev. B* **49**, 14958 (1994).

[65] Usabiaga, F. B., Delgado-Buscalioni, R., Griffith, B. E. & Donev, A. Inertial coupling method for particles in an incompressible fluctuating fluid. *Computer Methods in Applied Mechanics and Engineering* **269**, 139–172 (2014).

[66] Shimizu, R. & Tanaka, H. Impact of complex topology of porous media on phase separation of binary mixtures. *Science advances* **3**, eaap9570 (2017).

[67] Shimizu, R. & Tanaka, H. A novel coarsening mechanism of droplets in immiscible fluid mixtures. *Nature communications* **6**, 7407 (2015).

[68] Lifshitz, I. M. & Slyozov, V. V. The kinetics of precipitation from supersaturated solid solutions. *Journal of physics and chemistry of solids* **19**, 35–50 (1961).

[69] Siggia, E. D. Late stages of spinodal decomposition in binary mixtures. *Physical review A* **20**, 595 (1979).

[70] Wong, N.-C. & Knobler, C. M. Light scattering studies of phase separation in isobutyric acid+ water mixtures. *The Journal of Chemical Physics* **69**, 725–735 (1978).

[71] Koga, T. & Kawasaki, K. Late stage dynamics of spinodal decomposition in binary fluid mixtures. *Physica A: Statistical Mechanics and its Applications* **196**, 389–415 (1993).

[72] Ahmad, S., Das, S. K. & Puri, S. Crossover in growth laws for phase-separating binary fluids: Molecular dynamics simulations. *Physical Review E* **85**, 031140 (2012).

[73] Melzak, Z. A scalar transport equation. *Transactions of the American Mathematical Society* **85**, 547–560 (1957).

[74] Spielman, L. A. Viscous interactions in brownian coagulation. *J. Colloid Interface Sci.* **33**, 562–571 (1970).

[75] Mewis, J. & Wagner, N. J. *Colloidal suspension rheology* (Cambridge University Press, 2012).

[76] Brochard, F. & De Gennes, P. G. Dynamical scaling for polymers in theta solvents. *Macromolecules* **10**, 1157–1161 (1977).

[77] Doi, M. & Onuki, A. Dynamic coupling between stress and composition in polymer solutions and blends. *J. Phys. (Paris)* **2**, 1631–1656 (1992).

[78] Saito, S., Takenaka, M., Toyoda, N. & Hashimoto, T. Structure factor of semidilute polymer solution under continuous shear flow: Numerical analysis of a two-fluid model and comparison with experiments. *Macromolecules* **34**, 6461–6473 (2001).

[79] Tanaka, H. Unusual phase separation in a polymer solution caused by asymmetric molecular dynamics. *Physical review letters* **71**, 3158 (1993).

[80] Tanaka, H. Phase separation in soft matter: concept of dynamic asymmetry. Tech. Rep. (2013).

[81] Tanaka, H. Viscoelastic phase separation. *J. Phys.: Condens. Matter* **12**, R207 (2000).

[82] Tanaka, H. *Phase separation in soft matter: the concept of dynamic asymmetry*, vol. Soft Interfaces of *Session XCVIII , École de Physique des Houches*, chap. 15, 465–526 (Oxford Univ. Press, 2017).

[83] Sappelt, D. & Jäckle, J. Computer simulation study of phase separation in a binary mixture with a glass-forming component. *Physica A: Statistical Mechanics and its Applications* **240**, 453–479 (1997).

[84] Sappelt, D. & Jäckle, J. Percolation inversion in spinodal decomposition of mixtures with strong kinetic asymmetry. *Polymer* **39**, 5253–5256 (1998).

[85] Onuki, A. Domain growth and rheology in phase-separating binary mixtures with viscosity difference. *EPL (Europhysics Letters)* **28**, 175 (1994).

[86] Tanaka, H. M. Spinodal decomposition of binary fluid mixtures with viscosity difference. *Progress of theoretical physics* **101**, 863–873 (1999).

[87] Bouttes, D., Gouillart, E. & Vandembroucq, D. Topological symmetry breaking in viscous coarsening. *Physical review letters* **117**, 145702 (2016).

[88] Taniguchi, T. & Onuki, A. Network domain structure in viscoelastic phase separation. *Physical review letters* **77**, 4910 (1996).

[89] Tanaka, H. & Araki, T. Phase inversion during viscoelastic phase separation: roles of bulk and shear relaxation moduli. *Physical review letters* **78**, 4966 (1997).

[90] Zhang, J., Zhang, Z., Zhang, H. & Yang, Y. Kinetics and morphologies of viscoelastic phase separation. *Physical Review E* **64**, 051510 (2001).

[91] Luo, K., Gronski, W. & Friedrich, C. Viscoelastic phase separation in polymer blends. *The European Physical Journal E* **15**, 177–187 (2004).

[92] Tanaka, H. Universality of viscoelastic phase separation in dynamically asymmetric fluid mixtures. *Physical review letters* **76**, 787 (1996).

[93] Bibette, J., Mason, T., Gang, H. & Weitz, D. Kinetically induced ordering in gelation of emulsions. *Physical review letters* **69**, 981 (1992).

[94] Dickinson, E. & Golding, M. Depletion flocculation of emulsions containing unadsorbed sodium caseinate. *Food Hydrocolloids* **11**, 13–18 (1997).

[95] Weitz, D. & Oliveria, M. Fractal structures formed by kinetic aggregation of aqueous gold colloids. *Physical Review Letters* **52**, 1433 (1984).

[96] Lu, P. J., Conrad, J. C., Wyss, H. M., Schofield, A. B. & Weitz, D. A. Fluids of clusters in attractive colloids. *Phys. Rev. Lett.* **96**, 028306 (2006).

[97] Griffiths, S., Turci, F. & Royall, C. P. Local structure of percolating gels at very low volume fractions. *The Journal of chemical physics* **146**, 014905

(2017).

[98] Torquato, S. *Random heterogeneous materials: microstructure and macroscopic properties*, vol. 16 (Springer Science & Business Media, 2013).

[99] Chiew, Y. & Glandt, E. Percolation behaviour of permeable and of adhesive spheres. *Journal of Physics A: Mathematical and General* **16**, 2599 (1983).

[100] Eberle, A. P., Wagner, N. J. & Castañeda-Priego, R. Dynamical arrest transition in nanoparticle dispersions with short-range interactions. *Physical review letters* **106**, 105704 (2011).

[101] Royall, C. P., Williams, S. R., Ohtsuka, T. & Tanaka, H. Direct observation of a local structural mechanism for dynamic arrest. *Nature materials* **7**, 556 (2008).

[102] Matsuoka, Y., Fukasawa, T., Higashitani, K. & Yamamoto, R. Effect of hydrodynamic interactions on rapid Brownian coagulation of colloidal dispersions. *Phys. Rev. E* **86**, 051403 (2012).

[103] Delong, S., Usabiaga, F. B., Delgado-Buscalioni, R., Griffith, B. E. & Donev, A. Brownian dynamics without green's functions. *The Journal of chemical physics* **140**, 134110 (2014).

[104] Delmotte, B. & Keaveny, E. E. Simulating brownian suspensions with fluctuating hydrodynamics. *The Journal of chemical physics* **143**, 244109 (2015).

[105] Pham, K. N. *et al.* Multiple glassy states in a simple model system. *Science* **296**, 104–106 (2002).

[106] Sciortino, F. Disordered materials: One liquid, two glasses. *Nature materials* **1**, 145 (2002).

[107] Foffi, G., De Michele, C., Sciortino, F. & Tartaglia, P. Scaling of dynamics with the range of interaction in short-range attractive colloids. *Physical review letters* **94**, 078301 (2005).

[108] Cardinaux, F., Gibaud, T., Stradner, A. & Schurtenberger, P. Interplay between spinodal decomposition and glass formation in proteins exhibiting short-range attractions. *Physical Review Letters* **99**, 118301 (2007).

[109] Zaccarelli, E., Lu, P. J., Ciulla, F., Weitz, D. A. & Sciortino, F. Gelation as arrested phase separation in short-ranged attractive colloid–polymer mixtures. *Journal of Physics: Condensed Matter* **20**, 494242 (2008).

[110] Testard, V., Berthier, L. & Kob, W. Influence of the glass transition on the liquid-gas spinodal decomposition. *Physical review letters* **106**, 125702 (2011).

[111] Puertas, A. M., Fuchs, M. & Cates, M. E. Comparative simulation study of colloidal gels and glasses. *Physical review letters* **88**, 098301 (2002).

[112] Trappe, V., Prasad, V., Cipelletti, L., Segre, P. & Weitz, D. A. Jamming phase diagram for attractive particles. *Nature* **411**, 772 (2001).

[113] Valadez-Pérez, N. E., Liu, Y., Eberle, A. P., Wagner, N. J. & Castaneda-Priego, R. Dynamical arrest in adhesive hard-sphere dispersions driven by rigidity percolation. *Physical Review E* **88**, 060302 (2013).

[114] Tsurusawa, H., Leocmach, M., Russo, J. & Tanaka, H. Direct link between mechanical stability in gels and percolation of isostatic particles (2018).

[115] Sabin, J., Bailey, A. E., Espinosa, G. & Frisken, B. J. Crystal-arrested phase separation. *Phys. Rev. Lett.* **109**, 195701 (2012).

[116] Tsurusawa, H., Russo, J., Leocmach, M. & Tanaka, H. Formation of porous

crystals via viscoelastic phase separation. *Nat. Mater.* **16**, 1022–1028 (2017).
[117] Royall, C. P., Williams, S. R. & Tanaka, H. Vitrification and gelation in sticky spheres. *The Journal of chemical physics* **148**, 044501 (2018).
[118] Lodge, J. F. M. & Heyes, D. M. Brownian dynamics simulations of lennard-jones gas/liquid phase separation and its relevance to gel formation. *Journal of the Chemical Society, Faraday Transactions* **93**, 437–448 (1997).
[119] de Graaf, J., Poon, W. C., Haughey, M. J. & Hermes, M. Hydrodynamics strongly affect the dynamics of colloidal gelation but not gel structure. *Soft matter* (2019).
[120] Poon, W., Pirie, A., Haw, M. & Pusey, P. Non-equilibrium behaviour of colloid-polymer mixtures. *Physica A: Statistical Mechanics and its Applications* **235**, 110–119 (1997).
[121] Bhat, S., Tuinier, R. & Schurtenberger, P. Spinodal decomposition in a food colloid–biopolymer mixture: evidence for a linear regime. *Journal of Physics: Condensed Matter* **18**, L339 (2006).
[122] Gao, Y., Kim, J. & Helgeson, M. E. Microdynamics and arrest of coarsening during spinodal decomposition in thermoreversible colloidal gels. *Soft Matter* **11**, 6360–6370 (2015).
[123] Verhaegh, N. A., van Duijneveldt, J. S., Dhont, J. K. & Lekkerkerker, H. N. Fluid-fluid phase separation in colloid-polymer mixtures studied with small angle light scattering and light microscopy. *Physica A: Statistical Mechanics and its Applications* **230**, 409–436 (1996).
[124] Tanaka, H. Viscoelastic model of phase separation in colloidal suspensions and emulsions. *Phys. Rev. E* **59**, 6842 (1999).
[125] Iwashita, Y. & Tanaka, H. Self-organization in phase separation of a lyotropic liquid crystal into cellular, network and droplet morphologies. *Nature materials* **5**, 147 (2006).
[126] Debenedetti, P. G. *Metastable liquids: concepts and principles* (Princeton University Press, 1996).
[127] Auer, S. & Frenkel, D. Prediction of absolute crystal-nucleation rate in hard-sphere colloids. *Nature* **409**, 1020 (2001).
[128] Auer, S. & Frenkel, D. Numerical prediction of absolute crystallization rates in hard-sphere colloids. *The Journal of chemical physics* **120**, 3015–3029 (2004).
[129] Russo, J. & Tanaka, H. Crystal nucleation as the ordering of multiple order parameters. *J. Chem. Phys.* **145**, 211801 (2016).
[130] Li, B., Zhou, D. & Han, Y. Assembly and phase transitions of colloidal crystals. *Nature Reviews Materials* **1**, 15011 (2016).
[131] Filion, L., Hermes, M., Ni, R. & Dijkstra, M. Crystal nucleation of hard spheres using molecular dynamics, umbrella sampling, and forward flux sampling: A comparison of simulation techniques. *The Journal of chemical physics* **133**, 244115 (2010).
[132] Gasser, U., Weeks, E. R., Schofield, A., Pusey, P. & Weitz, D. Real-space imaging of nucleation and growth in colloidal crystallization. *Science* **292**, 258–262 (2001).
[133] Moroni, D., Ten Wolde, P. R. & Bolhuis, P. G. Interplay between structure

and size in a critical crystal nucleus. *Physical review letters* **94**, 235703 (2005).
[134] Schöpe, H. J., Bryant, G. & van Megen, W. Two-step crystallization kinetics in colloidal hard-sphere systems. *Physical review letters* **96**, 175701 (2006).
[135] Schilling, T., Schöpe, H. J., Oettel, M., Opletal, G. & Snook, I. Precursor-mediated crystallization process in suspensions of hard spheres. *Physical review letters* **105**, 025701 (2010).
[136] Kawasaki, T. & Tanaka, H. Formation of a crystal nucleus from liquid. *Proceedings of the National Academy of Sciences* **107**, 14036–14041 (2010).
[137] Kawasaki, T. & Tanaka, H. Structural origin of dynamic heterogeneity in three-dimensional colloidal glass formers and its link to crystal nucleation. *J. Phys.: Condens. Matter* **22**, 232102 (2010).
[138] Tanaka, H., Kawasaki, T., Shintani, H. & Watanabe, K. Critical-like behaviour of glass-forming liquids. *Nature Mater.* **9**, 324 (2010).
[139] Tanaka, H. Bond orientational order in liquids: Towards a unified description of water-like anomalies, liquid-liquid transition, glass transition, and crystallization. *Eur. Phys. J. E* **35**, 113 (2012).
[140] Russo, J. & Tanaka, H. The microscopic pathway to crystallization in supercooled liquids. *Scientific reports* **2**, 505 (2012).
[141] Russo, J. & Tanaka, H. Selection mechanism of polymorphs in the crystal nucleation of the gaussian core model. *Soft Matter* **8**, 4206–4215 (2012).
[142] Tan, P., Xu, N. & Xu, L. Visualizing kinetic pathways of homogeneous nucleation in colloidal crystallization. *Nature Physics* **10**, 73 (2014).
[143] Lu, Y., Lu, X., Qin, Z. & Shen, J. Experimental evidence for ordered precursor foreshadowing crystal nucleation in colloidal system. *Solid State Communications* **217**, 13–16 (2015).
[144] Auer, S. & Frenkel, D. Suppression of crystal nucleation in polydisperse colloids due to increase of the surface free energy. *Nature* **413**, 711 (2001).
[145] Russo, J., Maggs, A. C., Bonn, D. & Tanaka, H. The interplay of sedimentation and crystallization in hard-sphere suspensions. *Soft Matter* **9**, 7369–7383 (2013).
[146] Ketzetzi, S., Russo, J. & Bonn, D. Crystal nucleation in sedimenting colloidal suspensions. *The Journal of chemical physics* **148**, 064901 (2018).
[147] Radu, M. & Schilling, T. Solvent hydrodynamics speed up crystal nucleation in suspensions of hard spheres. *EPL (Europhysics Letters)* **105**, 26001 (2014).
[148] Roehm, D., Kesselheim, S. & Arnold, A. Hydrodynamic interactions slow down crystallization of soft colloids. *Soft matter* **10**, 5503–5509 (2014).
[149] Crocker, J. C. & Grier, D. G. Methods of digital video microscopy for colloidal studies. *J. Colloid Interface Sci.* **179**, 298–310 (1996).
[150] Vissers, T., Imhof, A., Carrique, F., Delgado, Á. V. & Van Blaaderen, A. Electrophoresis of concentrated colloidal dispersions in low-polar solvents. *J. Colloid Interface Sci.* **361**, 443–455 (2011).
[151] Ohshima, H. Electrical conductivity of a concentrated suspension of spherical colloidal particles. *J. Colloid Interface Sci.* **212**, 443–448 (1999).
[152] Fujitani, Y. Steady stokes flow in and around a droplet calculated using viscosity smoothened across interface. *J. Phys. Soc. Jpn.* **75**, 13401 (2006).

[153] Kodama, H., Takeshita, K., Araki, T. & Tanaka, H. Fluid particle dynamics simulation of charged colloidal suspensions. *Journal of Physics: Condensed Matter* **16**, L115 (2004).
[154] Arai, S. & Tanaka, H. Surface-assisted single-crystal formation of charged colloids. *Nature Physics* **13**, 503 (2017).
[155] Takae, K. & Tanaka, H. Hydrodynamic simulations of charge-regulation effects in colloidal suspensions. *Soft matter* **14**, 4711–4720 (2018).
[156] Araki, T. & Tanaka, H. Colloidal aggregation in a nematic liquid crystal: topological arrest of particles by a single-stroke disclination line. *Physical review letters* **97**, 127801 (2006).
[157] Delong, S., Balboa Usabiaga, F. & Donev, A. Brownian dynamics of confined rigid bodies. *The Journal of chemical physics* **143**, 144107 (2015).
[158] Iwashita, T., Nakayama, Y. & Yamamoto, R. A numerical model for brownian particles fluctuating in incompressible fluids. *Journal of the Physical Society of Japan* **77**, 074007 (2008).
[159] Hinch, E. J. Application of the langevin equation to fluid suspensions. *J. Fluid Mech.* **72**, 499–511 (1975).
[160] Kraft, D. J. *et al.* Brownian motion and the hydrodynamic friction tensor for colloidal particles of complex shape. *Physical Review E* **88**, 050301 (2013).
[161] Furry, W. Isotropic rotational brownian motion. *Physical Review* **107**, 7 (1957).
[162] Tanaka, H., Nakanishi, Y. & Takubo, N. Nonuniversal nature of dynamic critical anomaly in polymer solutions. *Physical Review E* **65**, 021802 (2002).
[163] Furukawa, A. Dynamic critical phenomena of polymer solutions. *J. Phys. Soc. Jpn.* **72**, 1436–1445 (2003).
[164] Brady, J. F. & Bossis, G. Stokesian dynamics. *Annual review of fluid mechanics* **20**, 111–157 (1988).
[165] Ladd, A. Numerical simulations of particulate suspensions via a discretized boltzmann equation. part 1. theoretical foundation. *J. Fluid Mech.* **271**, 285–309 (1994).
[166] Malevanets, A. & Kapral, R. Mesoscopic model for solvent dynamics. *J. Chem. Phys.* **110**, 8605 (1999).
[167] Nakayama, Y. & Yamamoto, R. Simulation method to resolve hydrodynamic interactions in colloidal dispersions. *Physical Review E* **71**, 036707 (2005).
[168] Banchio, A. & Brady, J. Accelerated stokesian dynamics: Brownian motion. *The Journal of chemical physics* **118**, 10323 (2003).
[169] Lobaskin, V., Dünweg, B. & Holm, C. Electrophoretic mobility of a charged colloidal particle: a computer simulation study. *J. Phys.: Condens. Matter* **16**, S4063 (2004).
[170] Yamamoto, R., Kim, K., Nakayama, Y., Miyazaki, K. & R. Reichman, D. On the role of hydrodynamic interactions in colloidal gelation. *J. Phys. Soc. Jpn.* **77**, 084804 (2008).
[171] Bouzid, M., Colombo, J., Barbosa, L. V. & Del Gado, E. Elastically driven intermittent microscopic dynamics in soft solids. *Nature communications* **8**, 15846 (2017).
[172] Padmanabhan, P. & Zia, R. Gravitational collapse of colloidal gels: non-

equilibrium phase separation driven by osmotic pressure. *Soft matter* **14**, 3265–3287 (2018).

[173] Zia, R. N., Landrum, B. J. & Russel, W. B. A micro-mechanical study of coarsening and rheology of colloidal gels: Cage building, cage hopping, and smoluchowski's ratchet. *Journal of Rheology* **58**, 1121–1157 (2014).

[174] Balboa Usabiaga, F., Xie, X., Delgado-Buscalioni, R. & Donev, A. The Stokes-Einstein relation at moderate Schmidt number. *J. Chem. Phys.* **139**, 214113 (2013).

[175] Shah, S. A., Chen, Y. L., Schweizer, K. S. & Zukoski, C. F. Phase behavior and concentration fluctuations in suspensions of hard spheres and nearly ideal polymers. *J. Chem. Phys.* **118**, 3350–3361 (2003).

[176] Dijkstra, M., van Roij, R., Roth, R. & Fortini, A. Effect of many-body interactions on the bulk and interfacial phase behavior of a model colloid-polymer mixture. *Phys. Rev. E* **73**, 041404 (2006).

[177] Tomilov, A. *et al.* Aggregation in colloidal suspensions: Evaluation of the role of hydrodynamic interactions by means of numerical simulations. *The Journal of Physical Chemistry B* **117**, 14509–14517 (2013).

[178] Campbell, A. I., Anderson, V. J., van Duijneveldt, J. S. & Bartlett, P. Dynamical arrest in attractive colloids: The effect of long-range repulsion. *Physical review letters* **94**, 208301 (2005).

[179] Toledano, J. C. F., Sciortino, F. & Zaccarelli, E. Colloidal systems with competing interactions: from an arrested repulsive cluster phase to a gel. *Soft Matter* **5**, 2390–2398 (2009).

[180] Zhang, T. H., Klok, J., Tromp, R. H., Groenewold, J. & Kegel, W. K. Non-equilibrium cluster states in colloids with competing interactions. *Soft Matter* **8**, 667–672 (2012).

[181] Tomita, H. Similarity law in spinodal decomposition. *Progress of Theoretical Physics* **56**, 1661–1663 (1976).

[182] Iborra, F. J. Can visco-elastic phase separation, macromolecular crowding and colloidal physics explain nuclear organisation? *Theor. Biol. Med. Model.* **4**, 15 (2007).

[183] Aguzzi, A. & Altmeyer, M. Phase separation: linking cellular compartmentalization to disease. *Trends in cell biology* **26**, 547–558 (2016).

[184] Feric, M. *et al.* Coexisting liquid phases underlie nucleolar subcompartments. *Cell* **165**, 1686–1697 (2016).

[185] Mitrea, D. M. & Kriwacki, R. W. Phase separation in biology; functional organization of a higher order. *Cell Commun. Signal.* **14**, 1 (2016).

[186] Mezzenga, R., Schurtenberger, P., Burbidge, A. & Michel, M. Understanding foods as soft materials. *Nature materials* **4**, 729 (2005).

[187] Siggia, E. D. Late stages of spinodal decomposition in binary mixtures. *Physical review A* **20**, 595 (1979).

[188] Koch, S., Desai, R. C. & Abraham, F. F. Dynamics of phase separation in two-dimensional fluids: spinodal decomposition. *Phys. Rev. A* **27**, 2152 (1983).

[189] Testard, V., Berthier, L. & Kob, W. Intermittent dynamics and logarithmic domain growth during the spinodal decomposition of a glass-forming liquid.

J. Chem. Phys. **140**, 164502 (2014).

[190] Tanaka, H. & Araki, T. Spontaneous coarsening of a colloidal network driven by self-generated mechanical stress. *Europhys. Lett.* **79**, 58003 (2007).

[191] Tateno, M. & Tanaka, H. Numerical prediction of colloidal phase separation based on its scale invariant nature. *Submitted* (2018).

[192] Furukawa, H. A dynamic scaling assumption for phase separation. *Advances in physics* **34**, 703–750 (1985).

[193] Goldhirsch, I. & Goldenberg, C. On the microscopic foundations of elasticity. *The European Physical Journal E* **9**, 245–251 (2002).

[194] Biot, M. A. General theory of three-dimensional consolidation. *Journal of applied physics* **12**, 155–164 (1941).

[195] Steinhardt, P. J., Nelson, D. R. & Ronchetti, M. Bond-orientational order in liquids and glasses. *Physical Review B* **28**, 784 (1983).

[196] Lechner, W. & Dellago, C. Accurate determination of crystal structures based on averaged local bond order parameters. *The Journal of chemical physics* **129**, 114707 (2008).

[197] Ten Wolde, P. R., Ruiz-Montero, M. J. & Frenkel, D. Numerical evidence for bcc ordering at the surface of a critical fcc nucleus. *Physical review letters* **75**, 2714 (1995).

[198] Rein ten Wolde, P., Ruiz-Montero, M. J. & Frenkel, D. Numerical calculation of the rate of crystal nucleation in a lennard-jones system at moderate undercooling. *The Journal of chemical physics* **104**, 9932–9947 (1996).

[199] Filion, L., Ni, R., Frenkel, D. & Dijkstra, M. Simulation of nucleation in almost hard-sphere colloids: The discrepancy between experiment and simulation persists. *The Journal of chemical physics* **134**, 134901 (2011).

[200] Heyes, D. M. & Okumura, H. Equation of state and structural properties of the weeks-chandler-andersen fluid. *The Journal of chemical physics* **124**, 164507 (2006).

[201] Ahmed, A. & Sadus, R. J. Phase diagram of the weeks-chandler-andersen potential from very low to high temperatures and pressures. *Physical Review E* **80**, 061101 (2009).

[202] Speedy, R. J. Pressure of the metastable hard-sphere fluid. *Journal of Physics: Condensed Matter* **9**, 8591 (1997).

[203] Speedy, R. J. Pressure and entropy of hard-sphere crystals. *Journal of Physics: Condensed Matter* **10**, 4387 (1998).

[204] Torrie, G. M. & Valleau, J. P. Nonphysical sampling distributions in monte carlo free-energy estimation: Umbrella sampling. *Journal of Computational Physics* **23**, 187–199 (1977).

[205] Russo, J., Romano, F. & Tanaka, H. New metastable form of ice and its role in the homogeneous crystallization of water. *Nature materials* **13**, 733 (2014).

[206] Royall, C. P., Poon, W. C. & Weeks, E. R. In search of colloidal hard spheres. *Soft Matter* **9**, 17–27 (2013).

[207] Antl, L. *et al.* The preparation of poly (methyl methacrylate) latices in non-aqueous media. *Colloids and Surfaces* **17**, 67–78 (1986).

[208] Bosma, G. *et al.* Preparation of monodisperse, fluorescent pmma–latex colloids by dispersion polymerization. *Journal of Colloid and Interface Science*

245, 292–300 (2002).

[209] Hu, H. & Larson, R. G. One-step preparation of highly monodisperse micron-size particles in organic solvents. *Journal of the American Chemical Society* **126**, 13894–13895 (2004).

[210] Elsesser, M. T., Hollingsworth, A. D., Edmond, K. V. & Pine, D. J. Large core- shell poly (methyl methacrylate) colloidal clusters: Synthesis, characterization, and tracking. *Langmuir* **27**, 917–927 (2010).

[211] Dullens, R. P., Claesson, M., Derks, D., van Blaaderen, A. & Kegel, W. K. Monodisperse core- shell poly (methyl methacrylate) latex colloids. *Langmuir* **19**, 5963–5966 (2003).

[212] Lee, T.-C., Kashyap, R. L. & Chu, C.-N. Building skeleton models via 3-d medial surface axis thinning algorithms. *CVGIP: Graphical Models and Image Processing* **56**, 462–478 (1994).

[213] Krall, A. & Weitz, D. Internal dynamics and elasticity of fractal colloidal gels. *Physical review letters* **80**, 778 (1998).

[214] Wessel, R. & Ball, R. Fractal aggregates and gels in shear flow. *Physical Review A* **46**, R3008 (1992).

[215] Dinsmore, A., Prasad, V., Wong, I. & Weitz, D. Microscopic structure and elasticity of weakly aggregated colloidal gels. *Physical review letters* **96**, 185502 (2006).

[216] Verhaegh, N. A. M., Asnaghi, D., Lekkerkerker, H. N. W., Giglio, M. & Cipelletti, L. Transient gelation by spinodal decomposition in colloid-polymer mixtures. *Physica A* **242**, 104–118 (1997).

[217] Guo, H., Ramakrishnan, S., Harden, J. L. & Leheny, R. L. Gel formation and aging in weakly attractive nanocolloid suspensions at intermediate concentrations. *The Journal of chemical physics* **135**, 154903 (2011).

[218] Negi, A. S., Redmon, C. G., Ramakrishnan, S. & Osuji, C. O. Viscoelasticity of a colloidal gel during dynamical arrest: Evolution through the critical gel and comparison with a soft colloidal glass. *Journal of Rheology* **58**, 1557–1579 (2014).

[219] Dibble, C. J., Kogan, M. & Solomon, M. J. Structure and dynamics of colloidal depletion gels: Coincidence of transitions and heterogeneity. *Physical Review E* **74**, 041403 (2006).